APPLIED COMPUTATIONAL ELECTROMAGNETICS SOCIETY JOURNAL

December 2013
Vol. 28 No. 12
ISSN 1054-4887

The ACES Journal is abstracted in INSPEC, in Engineering Index, DTIC, Science Citation Index Expanded, the Research Alert, and to Current Contents/Engineering, Computing & Technology.

The illustrations on the front cover have been obtained from the research groups at the Department of Electrical Engineering, The University of Mississippi.

THE APPLIED COMPUTATIONAL ELECTROMAGNETICS SOCIETY
http://www.aces-society.org

EDITOR-IN-CHIEF

Atef Elsherbeni
Colorado School of Mines, EECS Department
Golden, CO 80401, USA

ASSOCIATE EDITORS-IN-CHIEF

Sami Barmada
University of Pisa. EE Dept.
Pisa, Italy, 56126

Fan Yang
Microwave and Antenna Institute
Tsinghua University, Beijing, China

Mohamed Bakr
McMaster University, ECE Dept.
Hamilton, ON, L8S 4K1, Canada

Yasushi Kanai
Niigata Inst. of Technology
Kashiwazaki, Japan

Mohammed Hadi
Kuwait University, EE Dept.
Safat, Kuwait

Mohamed Abouzahra
MIT Lincoln Laboratory
Lexington, MA, USA

Ozlem Kilic
Catholic University of America
Washington DC, 20064, USA

Alistair Duffy
De Montfort University
Leicester, UK

Levent Gurel
Bilkent University
Ankara, Turkey

EDITORIAL ASSISTANTS

Matthew J. Inman
University of Mississippi, EE Dept.
University, MS 38677, USA

Mohamed Al Sharkawy
Arab Academy for Science and
Technology, ECE Dept. Alexandria,
Egypt

EMERITUS EDITORS-IN-CHIEF

Duncan C. Baker
EE Dept. U. of Pretoria
0002 Pretoria, South Africa

Allen Glisson
University of Mississippi, EE Dept.
University, MS 38677, USA

David E. Stein
USAF Scientific Advisory Board
Washington, DC 20330, USA

Robert M. Bevensee
Box 812
Alamo, CA 94507-0516, USA

Ahmed Kishk
University of Mississippi, EE Dept.
University, MS 38677, USA

EMERITUS ASSOCIATE EDITORS-IN-CHIEF

Alexander Yakovlev
University of Mississippi, EE Dept.
University, MS 38677, USA

Erdem Topsakal
Mississippi State University, EE Dept.
Mississippi State, MS 39762, USA

EMERITUS EDITORIAL ASSISTANTS

Khaled ElMaghoub
University of Mississippi, EE Dept.
University, MS 38677, USA

Anne Graham
University of Mississippi, EE Dept.
University, MS 38677, USA

Christina Bonnington
University of Mississippi, EE Dept.
University, MS 38677, USA

DECEMBER 2013 REVIEWERS

Mohamed Abouzahra
Osman Ahmed
Mohamed Al-Sharkaway
Mohamed Bakr
Ahmed Boutejdar
Veysel Demir
Glauco Fontgalland
Ahmad Hosseinbeig
Nikolaos Kantartzis
Rakhesh Kshetrimayum
Mingyu Lu
Hend Malhat
Ivor Morrow
Payam Nayeri
Saad Omar
Zhen Peng
Hassan Ragheb
Vince Rodriguez
P Sampath
Seyyed Sedighy

THE APPLIED COMPUTATIONAL ELECTROMAGNETICS SOCIETY

JOURNAL

Vol. 28 No. 12 December 2013

TABLE OF CONTENTS

© 2013, The Applied Computational Electromagnetics Society

Characterization of Biaxial Materials Using a Partially-Filled Rectangular Waveguide

J. Tang[1], B. Crowgey[1], O. Tuncer[1], E. Rothwell[1], B. Shanker[1], L. Kempel[1], and M. Havrilla[2]

[1] Department of Electrical and Computer Engineering
Michigan State University, East Lansing, MI 48824, USA
rothwell@egr.msu.edu

[2] Department of Electrical and Computer Engineering
Air Force Institute of Technology, Wright-Patterson Air Force Base, OH, 45342
Michael.Havrilla@afit.edu

***Abstract*—** A technique is proposed to measure the permittivity and permeability parameters of a sample of biaxial material placed into a rectangular waveguide. By constructing the material as a cube, only a single sample is required to find all six material parameters. The sample is inserted into the waveguide in multiple orientations, and the transmission and reflection coefficients of the sample region are measured using a vector network analyzer. The material parameters are then found by equating the measured S-parameters to those determined theoretically using a mode-matching technique. The theoretical details are outlined and the extraction process is described. A stacked dielectric cube is characterized experimentally to demonstrate the feasibility of the approach, and results are compared to those obtained using a reduced-aperture waveguide technique.

Index Terms – Anisotropic, biaxial, material measurement, permeability, permittivity, and waveguide.

I. INTRODUCTION

Engineered materials, formed from composites of various constituents with both dielectric and magnetic properties, are gaining interest for use in antenna apertures due to their useful electromagnetic properties [1, 2]. These materials are often anisotropic, and their constitutive parameters are hard to predict theoretically. Thus it is important to develop methods to accurately characterize the behavior of anisotropic materials experimentally, so that the constitutive parameters may be used in the analysis and design of antenna systems.

Rectangular waveguide systems are often used to measure the electromagnetic properties of materials due to high signal strength, ease of sample preparation, and the ability to analyze the sample interaction analytically [3]. The authors have recently developed a method for characterizing the properties of biaxially anisotropic materials using a reduced-aperture waveguide system [4]. By using a sample holder of cubical shape, a single sample of biaxial material may be measured in three different orientations, providing the required number of reflection and transmission measurements to determine the six unique constitutive parameters. The fields in the sample region are computed analytically, and the mode-matching approach is used to determine the theoretical S-parameters of the cascaded system consisting of the sample holder and the empty waveguide transitions. This technique has the drawbacks that the sample must fit tightly within the conducting sample holder (to preclude air gaps), the restricted aperture of the sample holder reduces the energy transmitted through the sample, and a special sample holder must be constructed.

Submitted On: March 25, 2013
Accepted On: Aug. 27 2013

1054-4887 © 2013 ACES

This paper introduces an alternative technique that doesn't require a special sample holder. In this technique a cubical sample is inserted directly into a full-aperture waveguide, leaving spaces on each side of the sample. The sample is centered within the guide cross section, and mode-matching techniques are again used to find the S-parameters. This approach eliminates the presence of gaps along the sidewalls (although not along the top and bottom walls), reduces reflections from the conducting restriction, and does not require a special sample holder. Drawbacks include accurately centering the sample in the guide, and dealing with a more complicated field structure in the sample region, including finding the modal propagation constants by solving a transcendental equation.

II. THEORETICAL S-PARAMETERS FOR A CUBICAL BIAXIAL MATERIAL SAMPLE IN A RECTANGULAR WAVEGUIDE

Dependable extraction of the biaxial properties of a material sample depends on having an accurate model for the theoretical S-parameters of the measurement system. The system considered here is designed in such a way that simple mode-matching techniques can be used to find the S-parameters with a computational accuracy that is easily quantified [5].

Consider the system shown in Fig. 1. A cubical sample of material is centered within the cross-section of a rectangular waveguide such that the cross-sectional view is shown in Fig. 2. The material is assumed to be biaxial along the orthogonal axes A, B, and C, such that the tensor permittivity and permeability are given by,

$$\varepsilon = \varepsilon_0 \begin{bmatrix} \varepsilon_A & 0 & 0 \\ 0 & \varepsilon_B & 0 \\ 0 & 0 & \varepsilon_C \end{bmatrix} \tag{1}$$

and

$$\mu = \mu_0 \begin{bmatrix} \mu_A & 0 & 0 \\ 0 & \mu_B & 0 \\ 0 & 0 & \mu_C \end{bmatrix}, \tag{2}$$

respectively, where ε_A, μ_A, etc., are relative parameters. A TE_{10} rectangular waveguide mode is assumed to be incident upon the sample from the region $z < 0$, as shown in Fig. 3. Due to the material discontinuities at the sample interfaces, an infinite spectrum of empty waveguide modes is reflected back into this region, an infinite spectrum of modes is created in the sample region, $0 \le z \le d$, and an infinite spectrum of modes is transmitted into the region $z > d$. The empty waveguide sections on the sending and receiving ends are assumed to be of sufficient length that only the dominant empty waveguide TE_{10} mode propagates to the ends of the sections. Thus, dominant-mode reflection and transmission coefficients can be measured at these ports using a vector network analyzer, and the S-parameters of the sample determined by shifting these measurements to the sample planes $z = 0$ and $z = d$. To determine the biaxial material properties, the theoretical S-parameters are needed at these planes.

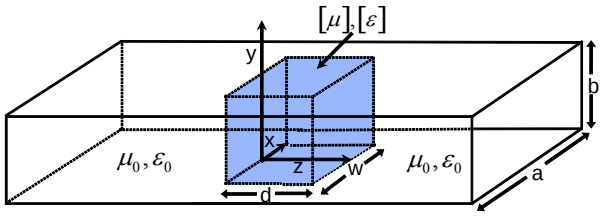

Fig. 1. Cubical sample of biaxial material centered inside a rectangular waveguide.

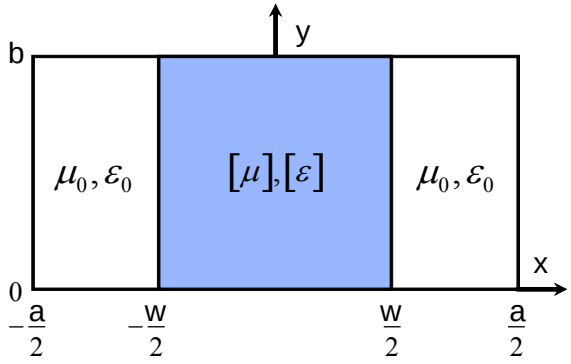

Fig. 2. Cross-sectional view of the sample inside the waveguide.

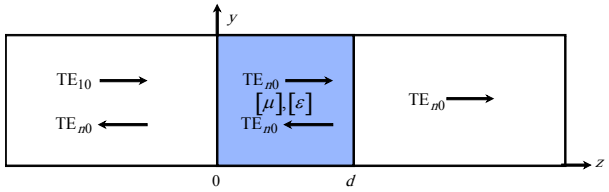

Fig. 3. Side view of the sample inside the waveguide showing the presence of higher-order modes in each region.

Since the electric field of the dominant TE_{10} mode of the empty guide is even about x, the incident field will only couple to modes with a similar symmetry. The field structure of the empty waveguide modes is well known [6], and it is easily seen that only modes of the type TE_{n0} will be excited in the empty guides. Thus, the transverse fields in the region $z < 0$ may be expanded as,

$$E_y(x,z) = a_1^i \bar{E}_1(x) e^{-j\bar{\beta}_1 z} + \sum_{n=1}^{N} a_n^r \bar{E}_n(x) e^{+j\bar{\beta}_n z} \quad (3)$$

$$H_x(x,z) = -a_1^i \bar{H}_1(x) e^{-j\bar{\beta}_1 z} + \sum_{n=1}^{N} a_n^r \bar{H}_n(x) e^{+j\bar{\beta}_n z}, \quad (4)$$

while the field in the region $z > d$ may be written as,

$$E_y(x,z) = \sum_{n=1}^{N} a_n^t \bar{E}_n(x)\, e^{-j\bar{\beta}_n (z-d)} \quad (5)$$

$$H_x(x,z) = -\sum_{n=1}^{N} a_n^t \bar{H}_n(x) e^{-j\bar{\beta}_n (z-d)}. \quad (6)$$

Here a_1^i is the known amplitude of the incident TE_{10} mode, while a_n^r and a_n^t are modal amplitudes to be determined by applying appropriate boundary conditions at the interfaces between the samples and the empty waveguide sections. Once these are found, the theoretical S-parameters are given by,

$$S_{11}^T = \frac{a_1^r}{a_1^i} \quad (7)$$

$$S_{21}^T = \frac{a_1^t}{a_1^i}. \quad (8)$$

In equations (3) to (6), $\bar{\beta}_n$ is the real phase constant of the TE_{n0} mode given by,

$$\bar{\beta}_n = \sqrt{k_0^2 - \bar{k}_{c,n}^2} \quad (9)$$

with $k_0 = \omega\sqrt{\mu_0 \varepsilon_0}$ is the free-space wave number, and $\bar{k}_{c,n}$ the cutoff wavenumber,

$$\bar{k}_{c,n} = \frac{n\pi}{a},\ n = 1,2,3,.... \quad (10)$$

Also in equations (3) to (6), the field structure of the empty waveguide modes is given by,

$$\bar{E}_n(x) = -\frac{j\omega\mu_0}{\bar{k}_{c,n}} \sin\bar{k}_{c,n}\left(x - \frac{a}{2}\right) \quad (11)$$

$$\bar{H}_x(x) = \frac{\bar{E}_n}{\bar{Z}_n}, \quad (12)$$

where $\bar{Z}_n$ is the TE-wave impedance

$$\bar{Z}_n = \frac{\omega\mu_0}{\bar{\beta}_n}. \quad (13)$$

The field structure of the waveguide modes in the sample region is somewhat more complicated. Assuming that the biaxial cube is aligned so that the axes A, B, and C lie along some choice of the directions x, y, and z, the fields within the region $0 \le z \le d$ may be expanded as,

$$E_y(x,z) = \sum_{n=1}^{N}\left[a_n^+ e^{-j\beta_n z} + a_n^- e^{+j\beta_n z}\right] E_n(x) \quad (14)$$

$$H_x(x,z) = \sum_{n=1}^{N}\left[-a_n^+ e^{-j\beta_n z} + a_n^- e^{+j\beta_n z}\right] H_n(x), \quad (15)$$

where a_n^+ and a_n^- are amplitudes to be determined by application of the boundary conditions at $z = 0$ and $z = d$. Here the modal fields are given for $x > 0$ by,

$$E_n(x) = \begin{cases} E_n^I(x), & 0 \le x \le \frac{w}{2} \\ E_n^{II}(x), & \frac{w}{2} < x \le \frac{a}{2} \end{cases} \quad (16)$$

$$H_n(x) = \begin{cases} H_n^I(x), & 0 \le x \le \frac{w}{2} \\ H_n^{II}(x), & \frac{w}{2} < x \le \frac{a}{2}, \end{cases} \quad (17)$$

where

$$E_n^I(x) = \frac{j\omega\mu_z}{k_{c,n}^I}\cos\left(k_{c,n}^I x\right), \quad (18)$$

$$E_n^{II}(x) = -\frac{j\omega\mu_0}{k_{c,n}^{II}}\sin\left(k_{c,n}^I \frac{d}{2}\right)\frac{\sin k_{c,n}^{II}\left(x - \frac{a}{2}\right)}{\cos k_{c,n}^{II}\left(\frac{d-a}{2}\right)}, \quad (19)$$

$$H_n^I(x) = \frac{E_n^I(x)}{Z_n^I},\ H_n^{II}(x) = \frac{E_n^{II}(x)}{Z_n^{II}}, \quad (20)$$

with

$$Z_n^I = \frac{\omega\mu_x}{\beta_n},\ Z_n^{II} = \frac{\omega\mu_0}{\beta_n}. \quad (21)$$

These fields are found by solving the wave equation for a biaxial medium [7],

$$\left[\frac{\partial^2}{\partial x^2} + \frac{\mu_z}{\mu_x}\left(\omega^2\mu_x\varepsilon_y - \beta^2\right)\right] H_z(x,z) = 0 \quad (22)$$

and applying the boundary conditions at the interfaces $x = a/2$ and $x = w/2$. Note that because of symmetry, the boundary conditions at $x = -a/2$ and $x = -w/2$ are satisfied automatically.

The complex propagation constants β_n are found by solving the transcendental equation,

$$\mu_0 k_{c,n}^I \sin\left(k_{c,n}^I \frac{w}{2}\right)\sin\left(k_{c,n}^{II}\frac{a-w}{2}\right) = \mu_z k_{c,n}^{II}\cos\left(k_{c,n}^I \frac{w}{2}\right)\cos\left(k_{c,n}^{II}\frac{a-w}{2}\right) \quad (23)$$

where the cutoff wavenumbers are related to the complex propagation constants by,

$$\begin{aligned}\left(k_{c,n}^{I}\right)^2 &= \tfrac{\mu_z}{\mu_x}\left(\omega^2\mu_x\varepsilon_y - \beta_n^2\right)\\ \left(k_{c,n}^{II}\right)^2 &= k_0^2 - \beta_n^2\,.\end{aligned} \tag{24}$$

It is not as straightforward to number the modes in the partially-filled guide as it is to number the modes in the empty waveguide extensions. One approach is to start with the solution for β_n under the condition $w = 0$, which is given by equations (9) and (10) since the sample region is empty, and then slowly increase the width of the sample, solving for β_n at each step using the previous solution as an initial guess. Then the modes can be numbered according to the starting empty waveguide mode. This is the approach suggested in [8] for thin samples. However, as the sample width increases, modes may switch between propagating and evanescent, and solving equation (23) using previous results as initial guesses becomes problematic. Instead, when the material loss is not too high, the following approach can be used. First the imaginary parts of the material constants are set to zero (implying a lossless material). Then the real values of β are found by looking for zero crossings of equation (23) between $\beta = 0$ and $\beta = \omega\sqrt{\mu_x\varepsilon_y}$. These are the propagating modes, and are assigned the index n according to the order of the zero crossing. Next β is replaced by $-j\delta$ in equation (23), and real values of δ are found by looking for zero crossings starting from $\delta = 0$ and continuing until a prescribed number of modes have been found. These are the evanescent modes, and they are numbered continuing after the highest order propagating mode. Finally, the imaginary parts of the material parameters are restored, and the zero crossing values found earlier for β and δ are used as initial guesses in a Newton's method root search (possibly with a small imaginary perturbation) to find the complex propagation constants for both the propagating and the evanescent modes.

The unknown modal amplitudes are found by enforcing continuity of E_y and H_x at the interfaces $z = 0$ and $z = d$,

$$a_1^i\bar{E}_1(x) + \sum_{n=1}^{N} a_n^r\bar{E}_n(x) = \sum_{n=1}^{N}[a_n^+ + a_n^-]E_n(x) \tag{25}$$

$$-a_1^i\bar{H}_1(x) + \sum_{n=1}^{N} a_n^r\bar{H}_n(x) = \sum_{n=1}^{N}[-a_n^+ + a_n^-]H_n(x), \tag{26}$$

$$\sum_{n=1}^{N}\left[a_n^+\mathrm{e}^{-j\beta_n d} + a_n^-\mathrm{e}^{+j\beta_n d}\right]E_n(x) = \sum_{n=1}^{N} a_n^t\bar{E}_n(x), \tag{27}$$

$$\sum_{n=1}^{N}\left[-a_n^+\mathrm{e}^{-j\beta_n d} + a_n^-\mathrm{e}^{+j\beta_n d}\right]H_n(x) = -\sum_{n=1}^{N} a_n^t\bar{H}_n(x). \tag{28}$$

Note that, for convenience, the same number of modes, N, is used in the empty waveguide and sample holder regions.

Equations (25) to (28) are a system of functional equations. They may be transformed into a system of linear equations by applying appropriate testing operators as follows. First, equation (25) is multiplied by $\bar{E}_m(x)$ and integrated between 0and $a/2$. Next, equation (26) is multiplied by $\bar{H}_m(x)$ and integrated between 0and $a/2$. Then equation (27) is multiplied by $\bar{E}_m(x)$ and integrated between 0and $a/2$. Finally, equation (28) is multiplied by $\bar{H}_m(x)$ and integrated between 0 and $a/2$. Note that all integrals can be computed in closed form. The result is a linear system of $4N \times 4N$ equations of the form,

$$\begin{bmatrix} -C_{mn} & D_{mn} & D_{mn} & 0 \\ E_{mn} & F_{mn} & -F_{mn} & 0 \\ 0 & D'_{mn} & D''_{mn} & -C_{mn} \\ 0 & -F'_{mn} & F''_{mn} & E_{mn} \end{bmatrix}\begin{bmatrix} a_n^r \\ a_n^+ \\ a_n^- \\ a_n^t \end{bmatrix} = a_1^i\begin{bmatrix} C_{m1} \\ E_{m1} \\ 0 \\ 0 \end{bmatrix} \tag{29}$$

where each of the quantities C_{mn}, D_{mn}, etc., are $N \times N$ submatrices, and a_n^r, a_n^+, etc., are the unknown modal coefficients. Once the matrix of equation (29) has been solved, equations (7) and (8) can be used to compute the desired S-parameters.

III. EXTRACTION PROCEDURE

Since there are six independent complex quantities to determine, $(\varepsilon_A, \varepsilon_B, \varepsilon_C, \mu_A, \mu_B, \mu_C)$, the extraction process requires a minimum of six complex measurements. These may be obtained by measuring S_{11} and S_{21} with the material axes A, B, and C aligned along three properly chosen directions. Consider the orientations,

$$(A, B, C) \rightarrow (x, y, z) \tag{30}$$

$$(A,B,C) \rightarrow (z,x,y), \quad (31)$$

$$(A,B,C) \rightarrow (y,z,x). \quad (32)$$

Measurement under these orientations gives the S-parameters $(S_{11,1}^{\text{meas}}, S_{21,1}^{\text{meas}})$, $(S_{11,2}^{\text{meas}}, S_{21,2}^{\text{meas}})$, $(S_{11,3}^{\text{meas}}, S_{21,3}^{\text{meas}})$, respectively. The material parameters can be found by solving the system of six nonlinear equations in six complex unknowns,

$$S_{11,n}^{\text{thy}}(\varepsilon_A, \varepsilon_B, \varepsilon_C, \mu_A, \mu_B, \mu_C) - S_{11,n}^{\text{meas}} = 0 \quad n = 1,2,3 \quad (33)$$

$$S_{21,n}^{\text{thy}}(\varepsilon_A, \varepsilon_B, \varepsilon_C, \mu_A, \mu_B, \mu_C) - S_{21,n}^{\text{meas}} = 0 \quad n = 1,2,3. \quad (34)$$

It may be difficult to solve this set of equations using standard methods such as Newton's method, since extremely accurate initial guesses may be required. Alternatively, a subset of the material parameters may be found using fewer equations and then these parameters may be used as known quantities to solve for the remaining parameters. This approach is possible since only the three parameters ε_y, μ_x, and μ_z appear at any given orientation.

Although many possible measurement combinations are possible, the results shown here were obtained using a three-step process. First, measurements are made with the orientations,

$$(A,B,C) \rightarrow (x,y,z) \quad (35)$$

$$(A,B,C) \rightarrow (-z,y,x), \quad (36)$$

giving the S-parameters $(S_{11,1}^{\text{meas}}, S_{21,1}^{\text{meas}})$ and $(S_{11,2}^{\text{meas}}, S_{21,2}^{\text{meas}})$, respectively. The first of these orientations is labeled 1 in Fig. 4. The second orientation corresponds to a rotation of the cube by 90° and is labeled 2 in Fig. 4. The measured S-parameters only implicate ε_B, μ_A, and μ_C, which can be found by solving the set of simultaneous equations,

$$S_{11,n}^{\text{thy}}(\varepsilon_B, \mu_A, \mu_C) - S_{11,n}^{\text{meas}} = 0, n = 1 \quad (37)$$

$$S_{21,n}^{\text{thy}}(\varepsilon_B, \mu_A, \mu_C) - S_{21,n}^{\text{meas}} = 0, n = 1,2, \quad (38)$$

using Newton's method. Next, a measurement is made using orientation 3 in Fig. 4,

$$(A,B,C) \rightarrow (y,-x,z) \quad (39)$$

giving $(S_{11,3}^{\text{meas}}, S_{21,3}^{\text{meas}})$. This measurement implicates ε_A, μ_B, and μ_C. However, μ_C is now known, so ε_A and μ_B may be found by solving,

$$S_{11,3}^{\text{thy}}(\varepsilon_A, \mu_B) - S_{11,3}^{\text{meas}} = 0 \quad (40)$$

$$S_{21,3}^{\text{thy}}(\varepsilon_A, \mu_B) - S_{21,3}^{\text{meas}} = 0, \quad (41)$$

using Newton's method. Finally, a measurement is made under orientation 4 of Fig. 4,

$$(A,B,C) \rightarrow (z,x,y) \quad (42)$$

implicating ε_C, μ_A, and μ_B. Since both μ_A, and μ_B are now known, ε_C can be found by solving,

$$S_{21,4}^{\text{thy}}(\varepsilon_C) - S_{21,4}^{\text{meas}} = 0 \quad (43)$$

using Newton's method. Note than when both reflection and transmission data is available, but only one S-parameter is required, a choice is made to use transmission data since experience shows that it is more robust.

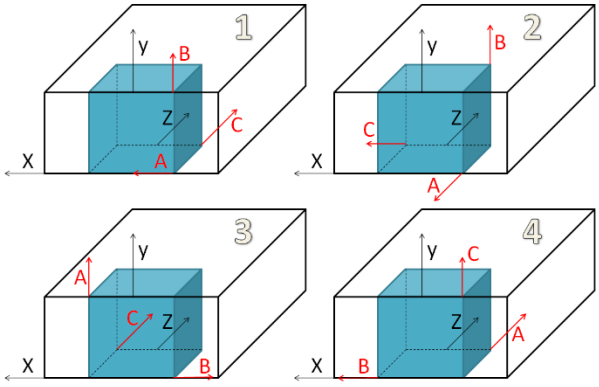

Fig. 4. Four cube orientations used in the three-step process.

IV. MEASURED RESULTS

A. Experimental setup

Demonstration of the partially-filled waveguide technique is undertaken by performing appropriate measurements at S-band and employing the extraction algorithm developed in the previous section. The waveguide system consists of two 5 inch (12.7 cm) long sections of WR-284 rectangular guide with coaxial transitions connected at the ends. These are attached through test port cables to an Agilent E5071C vector network analyzer (VNA); the assembled system is shown in Fig. 5. The VNA is calibrated at the open ends of the waveguide sections using a through-reflect-line (TRL) method. A cubical material sample is inserted in the end of one of the

waveguide sections so that its surface is flush to the open-ended waveguide surface and centered between the walls, as shown in Fig. 6. The two sections of guide are then assembled and the reflection coefficient S_{11}, and transmission coefficient, S_{21}, are measured. Assembly is done using precision alignment pins to ensure high repeatability between measurements. The measurement process is repeated with the sample inserted into the appropriate orientations described in section III. Note that the S-parameters must be phase corrected to account for the fact that the rear surface of the cube is not located at the calibration plane. All measurements were made with a -5dBm source power, 64 averages, and a 70 kHz IF bandwidth.

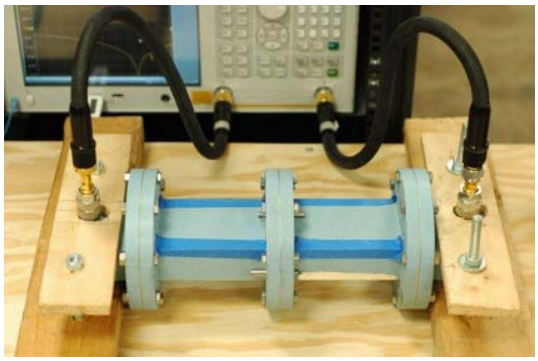

Fig. 5. Assembled S-band waveguide system.

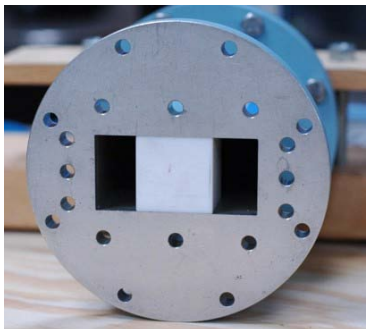

Fig. 6. Cubical sample inserted into waveguide section.

B. Experimental results

To test the characterization procedure using an anisotropic material, a cube was constructed by gluing together Rogers RO3010 circuit board substrate and Rogers RT/duroid 5870 substrate. The 3010 board has a thickness of $t_1 = 1.27$ mm, a dielectric constant of $\varepsilon_{r1}^{'} = 10.2$ and a loss tangent of $\tan\delta_1 = 0.0022$. The 5870 board has a thickness of $t_2 = 3.4$ mm, a dielectric constant of $\varepsilon_{r2}^{'} = 2.33$, and a loss tangent of $\tan\delta_2 = 0.0012$. The resulting cube, shown in Fig. 7, has uniaxial dielectric properties and isotropic magnetic properties. If the B direction is chosen to be aligned perpendicular to the layer interfaces, then it is expected that ε_A and ε_C should be identical, but different from ε_B. The sample was constructed approximately 0.01 mm larger than the inner dimensions of the sample holder so that when inserted it would compress slightly and eliminate air gaps between the MUT and the sample holder walls.

The simple geometry of the uniaxial cube allows ε_A, ε_B, and ε_C to be estimated using closed-form expressions. At the highest frequency considered in the measurements, the free-space electrical length of the stack period is $k_0(t_1 + t_2) = 0.387$. Since $k_0\sqrt{\varepsilon_{r1}^{'}}(t_1 + t_2) \ll 2\pi$, the following approximate formulas may be used to determine the biaxial material constants [9],

$$\varepsilon_B = \left[\frac{1}{\varepsilon_{r2}} - \frac{\varepsilon_{r1}-\varepsilon_{r2}}{\varepsilon_{r1}\varepsilon_{r2}}\frac{t_1}{t_1+t_2}\right]^{-1} \quad (44)$$

$$\varepsilon_A = \varepsilon_C = \varepsilon_{r2} + (\varepsilon_{r1} - \varepsilon_{r2})\frac{t_1}{t_1+t_2} \quad (45)$$

where $\varepsilon_{r1} = \varepsilon_{r1}^{'}(1 - j\tan\delta_1)$ and $\varepsilon_{r2} = \varepsilon_{r2}^{'}(1 - j\tan\delta_2)$. Using the board parameters gives $\varepsilon_B = 2.95 - j0.0038$ and $\varepsilon_A = \varepsilon_C = 4.47 - j0.0081$. Because of internal reflections, the results of [10] suggest deviations of up to 10% between these approximations and the values measured using the partially-filled waveguide. Also, the slight anisotropy of the boards themselves suggests that ε_A should differ slightly from ε_C [11].

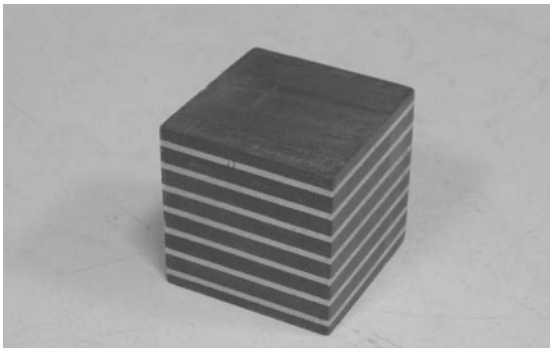

Fig. 7. Layered cube constructed from alternating layers of Rogers substrates.

The S-parameters of the uniaxial cube were measured 10 separate times, recalibrating between the measurements, and the material parameters were extracted using the 3-step procedure outlined in section III. The average values are shown in Figs. 8 and 9.

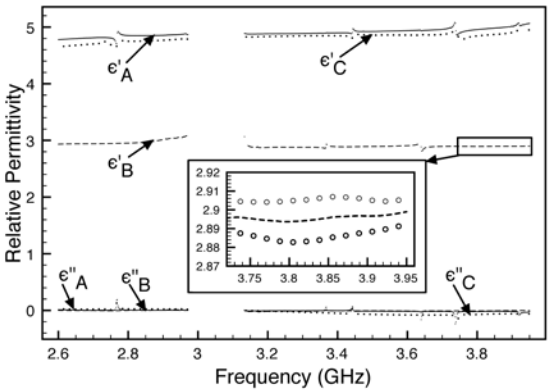

Fig. 8. Relative permittivities (mean values) of the uniaxial cube extracted using 10 measurement sets. Inset shows 2-σ confidence interval.

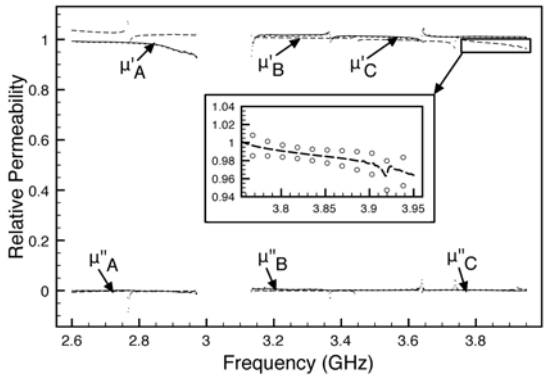

Fig. 9. Relative permeabilities (mean values) of the uniaxial cube extracted using 10 measurement sets. Inset shows 2-σ confidence interval.

The results for ε_A and ε_C are slightly higher than predicted by the closed-form expression (36), while ε_B is very close to the predicted value. The extracted values of μ_r are all close to unity, as expected, since the cube is non-magnetic. Note that the variance between measurement sets is quite small, such that showing the error bars in the figures would be distracting. Instead, the smaller insets in the figures show 95% (2-σ) confidence intervals for portions of the data sets; these intervals are typical across the entire frequency range.

The narrow confidence intervals suggest that noticeable variations in the extracted parameters are due to systematic errors, such as imperfect machining and alignment of the sample layers, or the presence of glue between sample layers, or air gaps between the sample and the waveguide walls, accentuated in certain frequency ranges by an ill-conditioning of the extraction process. This can be observed as gaps in the data in the frequency range 3 GHz - 3.15 GHz. There is amplified propagation of experimental uncertainties near frequencies where the sample is a half-wavelength long, a problem inherent to all guided-wave techniques in which both permittivity and permeability are determined (including the Nicolson-Ross-Wier closed-form method for isotropic materials [12-13]). Typically, the propagated error becomes so large that extraction is completely unreliable. This is a drawback of using a cubical sample holder, since the thickness of the material cannot be reduced below a half-wavelength. Experience has shown that a frequency range within approximately ±5% of the half-wavelength frequency should be avoided, and data within that range is not displayed in the figures, producing the observed gaps. It is possible, however, to interpolate the values of the parameters in the gaps. Figures 10 and 11 show the extracted parameters obtained by fitting a fifth-order polynomial to the data.

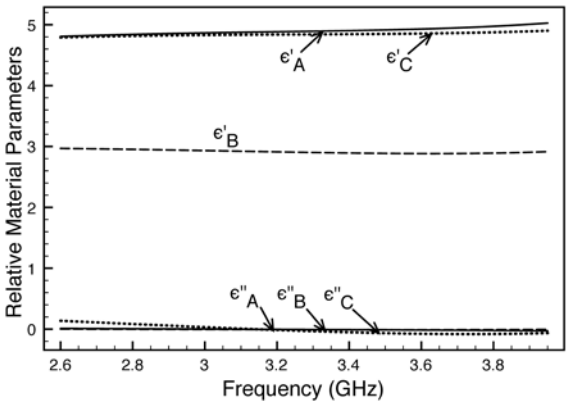

Fig. 10. Extracted relative permittivities of the uniaxial cube fitted to a fifth-order polynomial.

The extracted values of permittivity and permeability are quite similar to those obtained using the reduced-aperture waveguide described in [4]. To provide a direct comparison, the material

parameters ε_A and $\varepsilon_B$extracted using both methods are directly compared in Figs. 12 and 13, while a comparison for the parameter μ_A is shown in Fig. 14. Results for the parameters ε_C, μ_B, and μ_C are quite similar. Note that the reduced-aperture waveguide technique also has difficulties near half wavelength frequencies, but because the propagation constants of the modes are different than those for the partially-filled guide, the gaps appear in the range 3.55 GHz - 3.75 GHz, and do not coincide with those of Figs. 8 and 9. This suggests that combining data from both techniques may ameliorate the half-wavelength issue.

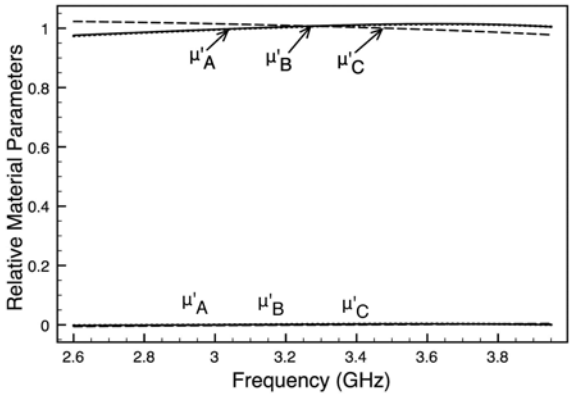

Fig. 11. Extracted relative permeabilities of the uniaxial cube fitted to a fifth-order polynomial.

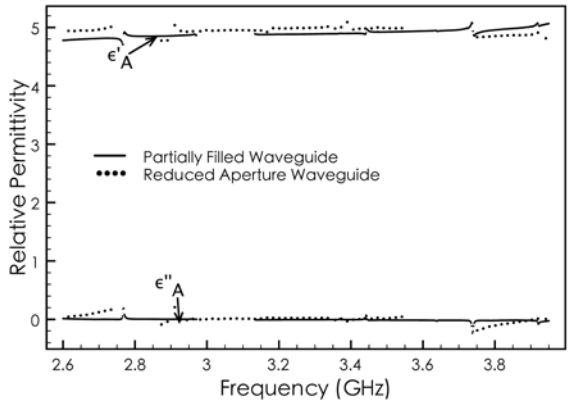

Fig. 12. Comparison of ε_A for the uniaxial cube extracted using the partially-filled waveguide technique and the reduced-aperture waveguide technique [4].

V. CONCLUSION

This paper introduces a method for measuring the electromagnetic properties of a biaxial material using a partially-filled rectangular waveguide. The proposed technique is validated using experimental data, and its accuracy is found to be commensurate with that of the reduced-aperture waveguide technique, without the need for a special sample holder, and with less worry about air gaps between the sample and the waveguide walls. The drawback to the method is the need for a more complicated theoretical analysis. A combination of both techniques may provide a means for overcoming the difficulties with accurately extracting the parameters near frequencies where the sample is a half wavelength in thickness.

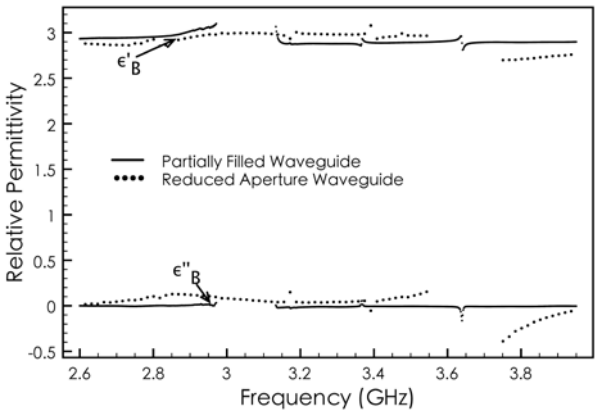

Fig. 13. Comparison of ε_B for the uniaxial cube extracted using the partially-filled waveguide technique and the reduced-aperture waveguide technique [4].

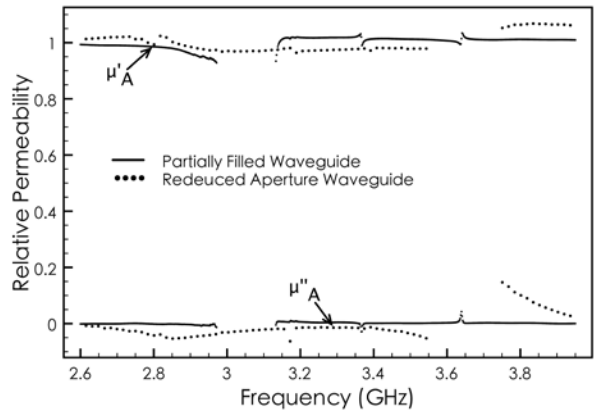

Fig. 14. Comparison of μ_A for the uniaxial cube extracted using the partially-filled waveguide technique and the reduced-aperture waveguide technique [4].

ACKNOWLEDGMENT

The research reported in this paper was supported by the US Air Force Office of Scientific Research under grant FA9550-09-1-0182.

REFERENCES

[1] Y. Ma, P. Wang, X. Chen, and K. Ong, "Near-field plane-wave-like beam emitting antenna fabricated by anisotropic metamaterial," *Applied Physics Letters*, vol. 94, no. 4, pp. 044107, 2009.

[2] G. Mumcu, K. Sertel, and J. Volakis, "Miniature antennas and arrays embedded within magnetic photonic crystals," *IEEE Antennas and Wireless Propagation Letters*, vol. 5, no. 1, pp. 168-171, Dec. 2006.

[3] B. Crowgey, O. Tuncer, E. Rothwell, B. Shanker, and L. Kempel, "Development of numerical techniques for simulated characterization of anisotropic materials," *28th Annual Review of Progress in Applied Computational Electromagnetics (ACES)*, pp. 553-557, Columbus, Ohio, April 2012.

[4] B. Crowgey, E. Rothwell, S. Balasubramaniam, L. C. Kempel, O. Tuncer, and M. Havrilla, "Characterization of biaxial anisotropic material using a reduced aperture waveguide," *IEEE AP-S International Symposium and URSI Radio Science Meeting*, Spokane, WA, July 3-8, 2011.

[5] Á. Gómez, I. Barba, A. Cabeceira, J. Represa, G. Molina-Cuberos, M. Núñez, J. Margineda, Á. Vegas, and M. Solano, "Theoretical and experimental analysis of rectangular waveguides with isotropic chiral media," *23rd Annual Review of Progress in Applied Computational Electromagnetics (ACES)*, pp. 1140-1144, Verona, Italy, March 2007.

[6] S. Ramo, J. Whinnery, and T. Duzer, *Fields and Waves in Communications Electronics*, 3rd ed., John Wiley & Sons, New York, 1994.

[7] B. Crowgey, R. Ouedraogo, E. Rothwell, L. Kempel, and S. Balasubramaniam, "Measurement of the electromagnetic properties of biaxial anisotropic materials using a waveguide technique," *Inverse Problems Symposium (IPS)*, East Lansing, MI, June 2010.

[8] A. Bogle, M. Havrilla, D. Nyquist, L. Kempel, and E. Rothwell, "Electromagnetic material characterization using a partially-filled rectangular waveguide," *J. Electromagnetic Waves Applications*, vol. 19, no. 10, pp. 1291-1306, 2005.

[9] R. Collin, "A simple artificial anisotropic dielectric medium," *IRE Transaction on Microwave Theory and Techniques*, pp. 206 - 209, April 1958.

[10] D. Killips, L. Kempel, D. Nyquist, and E. Rothwell, "Analysis of layering dielectrics on effective permittivity using wave matrices," *IEEE Antennas and Propagation Society International Symposium*, Washington, D.C., vol. 3A, pp. 212-215, July 3-8, 2005.

[11] J. Rautio, "Measurement of uniaxial anisotropy in Roger RO3010 substrate material," *COMCAS*, 2009.

[12] A. Nicolson and G. Ross, "Measurement of the intrinsic properties of materials by time-domain techniques," *IEEE Trans. Instrum. Meas.*, vol. 19, no. 4, pp. 377-382, Nov. 1970.

[13] W. Weir, "Automatic measurement of complex dielectric constant and permeability at microwave frequencies," *Proc. IEEE*, vol. 62, no. 1, pp. 33-36, Jan. 1974.

Junyan Tang was born in Hangzhou, China in 1986. He received the B.S. degree from Zhejiang University, Hangzhou, China, and the M.S. degree in electrical engineering from Michigan State University, East Lansing, MI. He is currently working toward the Ph.D. degree at Michigan State. His research interests include metamaterials, antennas and material characterization.

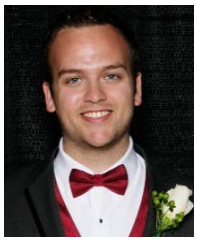

Benjamin R. Crowgey was born in Iron River, MI, on July 17, 1985. He received the B.S. degree and M.S. degree in electrical engineering from Michigan State University, East Lansing, in 2007 and 2009, respectively. He is currently working on his Ph.D. at Michigan State University with a current expected date of graduation during summer of 2013.

His current research interests include anisotropic material characterization, self-structuring antennas, traveling wave antennas, electromagnetic radiation, and scattering.

Ozgur Tuncer received the B.Sc. degree in electrical and electronics engineering from the Middle East Technical University, Ankara, Turkey, in 2003, the M.Sc. degree in electrical engineering and information technology from the Technische Universität Mu¨nchen,

Munich, in 2005, and the Ph.D. degree in electrical engineering from Michigan State University, East Lansing, in 2012.

In 2006, he worked as a system engineer at Infineon Technologies, Munich, on the modelling of 3G mobile communication products for HSDPA/HSUPA. From 2007 to 2012, he was a research assistant at Michigan State, where he worked on the development of the generalized finite element methods. He is currently working at ANSYS as a research and development engineer. His research interests include all aspects of theoretical and computational electromagnetics, particularly the finite element methods.

Edward J. Rothwell was born in Grand Rapids, MI, on September 8, 1957. He received the B.S. degree in electrical engineering from Michigan Technological University, Houghton, in 1979, the M.S. degree in electrical engineering and the degree of electrical engineer from Stanford University, Stanford, CA, in 1980 and 1982, and the Ph.D. degree in electrical engineering from Michigan State University, East Lansing, MI, in 1985, where he held the Dean's Distinguished Fellowship.

He worked for Raytheon Co., Microwave and Power Tube Division, Waltham, MA, from 1979-1982 on low power traveling wave tubes, and for MIT Lincoln Laboratory, Lexington, MA, in 1985. He has been at Michigan State University from 1985-1990 as an assistant professor of electrical engineering, from 1990-1998 as an associate professor, and from 1998 as professor. He is co-author of the book *Electromagnetics* (Boca Raton, FL: CRC Press, 2001; 2nd edition 2008). His current interests include electromagnetic theory, antennas, and material characterization.

Dr. Rothwell received the John D. Withrow award for teaching excellence from the College of Engineering at Michigan State University in 1991, 1996, 2006, and 2012, the Withrow Distinguished Scholar Award in 2007, the MSU Alumni Club of Mid Michigan Quality in Undergraduate Teaching Award in 2003, and the MSU Distinguished Faculty Award in 2013. He was a joint recipient of the Best Technical Paper Award at the 2003 Antenna Measurement Techniques Association Symposium, and in 2005 he received the Southeast Michigan IEEE Section Award for Most Outstanding Professional. He is a member of Phi Kappa Phi, Sigma Xi, ACES, and Commission B of URSI, and is a Fellow of the IEEE.

B. Shanker received his B'Tech degree from the Indian Institute of Technology, Madras, India in 1989, and the M.S. and Ph.D degrees in 1992 and 1993, respectively, from the Pennsylvania State University. From 1993 to 1996 he was a research associate in the Department of Biochemistry and Biophysics at Iowa State University where he worked on the Molecular Theory of Optical Activity. From 1996 to 1999 he was with the Center for Computational Electromagnetics at the University of Illinois at Urbana-Champaign as a Visiting Assistant Professor, and from 1999-2002 with the Department of Electrical and Computer Engineering at Iowa State University as an Assistant Professor. Currently, he is a Professor in the Department of Electrical and Computer Engineering at Michigan State University.

He has authored/co-authored over 300 journal and conferences papers and presented a number of invited talks. His research interest include all aspects of computational electromagnetics (frequency and time domain integral equation based methods, multi-scale fast multipole methods, fast transient methods, higher order finite element and integral equation methods), propagation in complex media, mesoscale electromagnetics, and particle and molecular dynamics as applied to multiphysics and multiscale problems.

Dr. Shanker was an Associate Editor for IEEE Antennas and Wireless Propagation Letters (AWPL), is an Associate Editor for IEEE Transactions on Antennas and Propagation, and is a full member of the USNC-URSI Commission B. He is Fellow of IEEE, elected for his contributions in computational electromagnetics. He has also been awarded the Withrow Distinguished Junior scholar (in 2003), Withrow Distinguished Senior scholar (in 2010) and the Withrow teaching award (in 2007).

Leo C. Kempel was born in Akron, OH, in October 1965. He earned his B.S.E.E. at the University of Cincinnati in 1989 as well as the M.S.E.E. and Ph.D. degrees at the University of Michigan in 1990 and 1994, respectively.

After a brief Post-Doctoral appointment at the University of Michigan, Dr. Kempel joined Mission Research Corporation in 1994 as a Senior Research Engineer. He led several projects involving the design of conformal antennas, computational electromagnetics, scattering analysis, and high power/ultrawideband microwaves. He joined Michigan State University in

1998. Prof. Kempel's current research interests include computational electromagnetics, conformal antennas, microwave/millimeter wave materials, mixed-signal electromagnetic interference techniques, and measurement techniques. Prof. Kempel has been awarded a CAREER award by the National Science Foundation and the Teacher-Scholar award by Michigan State University in 2002. He also received the MSU College of Engineering's Withrow Distinguished Scholar (Junior Faculty) Award in 2001. He served as an IPA with the Air Force Research Laboratory's Sensors Directorate from 2004-2005 and 2006-2008. He was the inaugural director of the Michigan State University High Performance Computing Center. He was the first Associate Dean for Special Initiatives in the College of Engineering at Michigan State University for 2006-2008 and is now serving as the Associate Dean for Research, also in the College of Engineering at Michigan State University. He was appointed to the US Air Force Scientific Advisory Board in October 2011.

Dr. Kempel served as the technical chairperson for the 2001 Applied Computational Electromagnetics Society (ACES) Conference and technical co-chair for the Finite Element Workshop held in Chios, GREECE in 2002. He was a member of the Antennas and Propagation Society's Administrative Committee and was a member of the ACES Board of Directors. He served as an Associate Editor for the *IEEE Transactions on A ntennas and P ropagation*. He is currently the Fellow Evaluation Committee Chairperson for the IEEE Antennas and Propagation Society. He is an active reviewer for several IEEE publications as well as JEWA and Radio Science. He co-authored *The Finite Element Method for Electromagnetics* published by IEEE Press. Dr. Kempel is a member of Tau Beta Pi, Eta Kappa Nu, and Commission B of URSI, and is a Fellow of the IEEE.

Michael J. Havrilla received B.S. degrees in Physics and Mathematics in 1987, the M.S.E.E degree in 1989 and the Ph.D. degree in electrical engineering in 2001 from Michigan State University, East Lansing, MI. From 1990-1995, he was with General Electric Aircraft Engines, Evendale, OH and Lockheed Skunk Works, Palmdale, CA, where he worked as an electrical engineer. He is currently a Professor in the Department of Electrical and Computer Engineering at the Air Force Institute of Technology, Wright-Patterson AFB, OH.

He is a member of URSI Commission B, a senior member of the IEEE, and a member of the Eta Kappa Nu and Sigma Xi honor societies. His current research interests include electromagnetic and guided-wave theory, electromagnetic propagation and radiation in complex media and structures and electromagnetic materials characterization.

Wideband Measurements of the Forward RCS and the Extinction Cross Section

C. Larsson[1,2] and M. Gustafsson[1]

[1]Department of Electrical and Information Technology, Lund University,
P.O. Box 118, S-221 00 Lund, Sweden
Christer.Larsson@eit.lth.se, Mats.Gustafsson@eit.lth.se

[2] Saab Dynamics, S-581 88 Linköping, Sweden

Abstract ─ This paper describes the development of a method based on measurements of the radar cross section (RCS) amplitude and phase in the forward direction to determine the extinction cross section for the 2.5 GHz - 38 GHz frequency range using the optical theorem. Forward RCS measurements are technically complicated due to that the direct signal has to be subtracted from the total signal at the receiving antenna in order to extract the forward RCS. The efficiency of this subtraction as a function of time is evaluated. A traditional calibration method using a calibration target and a second method that does not require a calibration target are investigated and compared. The accuracy of the forward RCS measurements is determined using small spheres of different sizes. The spheres have a forward RCS that is straight forward to calculate with good accuracy. The method is also extended to polarimetric measurements on a small helix that are compared with method-of-moments calculations to validate the method.

Index Terms - Bistatic, calibration, extinction cross section, forward RCS, measurement, method of moments, and polarimetry.

I. INTRODUCTION

This study treats the development of a method to determine the extinction cross section for the 2.5 GHz-38 GHz frequency range. The method is based on measurements of the radar cross section (RCS) in the forward direction in a conventional anechoic chamber designed for monostatic measurements. The extinction cross section is then calculated from the measured forward RCS using the optical theorem. The motivation for this work is to develop an experimental method that can be used to verify theoretical work, which shows that the extinction cross section integrated over all frequencies is related to the static properties of the scatterer [1-4].

Most radar applications in use today are monostatic. One comparative advantage of bistatic radar is that it can be used to detect objects, which have a low monostatic radar signature [5], but bistatic systems are, in general, more complicated than monostatic systems. Some applications that use scattering in the forward direction are systems for ground target identification [6], radar fences [5], and Beyond the line-of-sight HF-radar [7]. The relative lack of applications where forward scattering is used also means that most RCS ranges are set up for monostatic measurements. A system where the RCS in the forward direction can be measured is described in [8]. That system operates in the 2 GHz-12.4 GHz range with a measurement accuracy of 1 dB at a level of -18 dBsm for the forward RCS [8].

Forward RCS measurements are technically complicated due to the large direct contribution from the transmitting antenna to the received signal. The direct signal has to be subtracted from the total signal at the receiving antenna in order to extract the forward RCS. The efficiency of this subtraction is evaluated in this study by performing long time measurements leading to an estimation of subtraction accuracy as a function of the time between the two measurements.

Submitted On: March 8, 2013
Accepted On: Aug. 27, 2013

1054-4887 © 2013 ACES

Two calibration methods are investigated. The first method is the traditional calibration method used in most RCS measurements. It uses a target with known RCS as a calibration target to calibrate the target measurement. The second method that is described here uses only a direct path measurement of the signal to calibrate the target measurement without any calibration object. To the best of our knowledge, the latter method is not in frequent use in the RCS community.

The method described here is also extended to polarimetric measurements of the forward RCS and hence, the possibility to determine the extinction cross section for arbitrarily polarized incident radiation. This is tested using measurements on a small helix coil and comparing with method of moments calculations. More details of the experimental methods that are presented in this paper can be found in [9-11].

II. THEORY

Consider the direct scattering problem of a time harmonic plane electromagnetic wave impinging in the $\hat{\boldsymbol{k}}$-direction on a bounded scatterer. The bistatic RCS, $\sigma(f,\hat{\boldsymbol{r}})$, in the $\hat{\boldsymbol{r}}$ direction at the frequency f is then defined as [12],

$$\sigma(f,\hat{\boldsymbol{r}}) = \lim_{r\to\infty} 4\pi r^2 \frac{\left|\boldsymbol{E}_{\mathrm{s}}(\boldsymbol{r})\right|^2}{\left|\boldsymbol{E}_{\mathrm{i}}\right|^2} \tag{1}$$

where $\boldsymbol{E}_{\mathrm{i}}$ denotes the incident electric field, $\boldsymbol{E}_{\mathrm{s}}$ denotes the scattered electric field and $r = |\boldsymbol{r}|$ denotes the magnitude of the position vector $\boldsymbol{r} = r\hat{\boldsymbol{r}}$. Introduce the complex-valued bistatic RCS amplitude, $\boldsymbol{A}(f,\hat{\boldsymbol{r}})$, in the $\hat{\boldsymbol{r}}$ direction. $\boldsymbol{A}(f,\hat{\boldsymbol{r}})$ is similar to the scattering dyadic usually used in scattering theory. $\boldsymbol{A}(f,\hat{\boldsymbol{r}})$ preserves the phase information in the measurement and it is defined as,

$$\boldsymbol{A}(f,\hat{\boldsymbol{r}}) = \lim_{r\to\infty} 2\sqrt{\pi} r \frac{\boldsymbol{E}_{\mathrm{s}}(\boldsymbol{r})}{\left|\boldsymbol{E}_{\mathrm{i}}\right|} \mathrm{e}^{-\mathrm{i}kr} \tag{2}$$

where it is assumed that the time convention is $\mathrm{e}^{-\mathrm{i}\omega t}$ for the time harmonic wave and $k=2\pi f/c_0$. c_0 is the phase velocity of light in free space. $\sigma(f,\hat{\boldsymbol{r}})$ and $\boldsymbol{A}(f,\hat{\boldsymbol{r}})$ are then related by,

$$\sigma(f,\hat{\boldsymbol{r}}) = \left|\boldsymbol{A}(f,\hat{\boldsymbol{r}})\right|^2. \tag{3}$$

In practice, the two polarization components of $\boldsymbol{A}(f,\hat{\boldsymbol{r}})$ are measured separately for an incident wave that is transmitted with a defined polarization. This means that measured RCS data usually is presented as a function of the transmitted and received polarizations, e.g., σ_{VH} and $\boldsymbol{A}_{\mathrm{VH}}$ are the notations for the recorded RCS and RCS amplitude component, respectively, for vertical transmitting and horizontal receiving linear polarizations.

The scattering cross section, $\sigma_{\mathrm{s}}(f)$, is the average of the bistatic RCS over all angles,

$$\sigma_s(f) = \frac{1}{4\pi}\int_{\Omega} \sigma(f,\hat{\boldsymbol{r}})\mathrm{d}\Omega, \tag{4}$$

where Ω and $\mathrm{d}\Omega$ denote the unit sphere and the surface element of the unit sphere, respectively. The extinction cross section, $\sigma_{\mathrm{ext}}(f)$, also designated the total cross section [13], is defined as

$$\sigma_{\mathrm{ext}}(f) = \sigma_{\mathrm{s}}(f) + \sigma_{\mathrm{a}}(f), \tag{5}$$

where $\sigma_{\mathrm{a}}(f)$, is the absorption cross section. The extinction cross section can be determined using equation (5) by measuring the bistatic RCS at all angles and the absorption cross section. However, a more straight forward method is to measure the RCS amplitude in the forward direction, $\boldsymbol{A}(f,\hat{\boldsymbol{r}})$, and use the optical theorem to determine $\sigma_{\mathrm{ext}}(f)$ [14],

$$\sigma_{\mathrm{ext}}(f) = \frac{c_0}{\sqrt{\pi} f} \mathrm{Im}\, A_{\mathrm{ii}}(f,\hat{\boldsymbol{k}}) \tag{6}$$

where $A_{\mathrm{ii}}(f,\hat{\boldsymbol{k}})$ is the component of $\boldsymbol{A}(f,\hat{\boldsymbol{k}})$ that is co-polarized with the incident electric field, $\boldsymbol{E}_{\mathrm{i}}$, *i.e.*,

$$A_{\mathrm{ii}}(f,\hat{\boldsymbol{k}}) = \boldsymbol{A}(f,\hat{\boldsymbol{k}}) \cdot \frac{\boldsymbol{E}_{\mathrm{i}}^*}{\left|\boldsymbol{E}_{\mathrm{i}}\right|}. \tag{7}$$

III. MEASUREMENTS

Forward RCS measurements are performed in an anechoic chamber originally designed for monostatic RCS measurements. A pair of wideband ridged horn antennas are positioned facing each other at a distance of 6.80 m with the sample placed on an expanded polystyrene (EPS) column at the midpoint, see Fig. 1. The measurement uses a performance network analyzer (PNA) transmitting a continuous wave without online hard or software gating. The source

power from the PNA is set to 1 mW for the measurements described here. The power output from the antenna is significantly lower mainly due to cable losses. Two separate measurements using different antennas are performed for each sample in the frequency intervals 1 GHz-22 GHz and 16 GHz-40 GHz. Each interval is swept using 4000 frequency points. Eight such sweeps are averaged for each of the sample measurement, background measurement, and calibration measurement. Calibration measurements are performed using the two methods described in section A.

The sample is measured and the direct path data is subtracted from the sample data. The processed sample data is then calibrated with the calibration vectors obtained using the two calibration methods. The calibrated data is finally gated with a 3.3 ns window in the time domain, chosen to acquire the entire target response and to minimize the influence of the background. The time domain filtering, as well as a large antenna beam width at low frequencies, reduces the useful frequency range to 2.5 GHz-38 GHz.

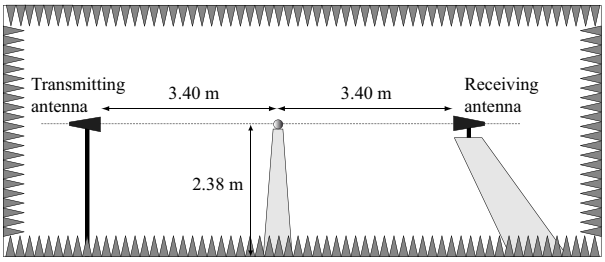

Fig. 1. The figure shows the experimental setup in the anechoic chamber.

IV. RESULTS AND DISCUSSION

A. Calibration

The first calibration method described here using a calibration target is the standard method for RCS calibration [8]. The RCS amplitude is determined from the difference between a measurement with the scattering target present and a measurement without target. The RCS amplitude component A_{ij} defined previously with i and j transmitted and received polarizations, respectively, is then given by

$$A_{ij} = v_{ij}(V_{ij,r} - V_{ij,d}), \tag{8}$$

where v_{ij} is the complex-valued calibration vector for the setup, $V_{ij,r}$ is the complex-valued amplitude as measured at the receiver with a scattering target, and $V_{ij,d}$ is the complex-valued amplitude as measured at the receiver without a scattering target. In this method v_{ij} is determined in a calibration measurement using a target with known RCS amplitude, $A_{ij,cal}$,

$$v_{ij} = \frac{A_{ij,cal}}{(V_{ij,r,cal} - V_{ij,d})} \tag{9}$$

where $V_{ij,r,cal}$ is the measured amplitude at the receiver for the calibration target.

Spheres are ideal forward RCS calibration objects for several reasons. The RCS is easy to calculate to very good accuracy using the Mie series, see [9]. The symmetry of a sphere means that it is straight forward to align the setup. A sphere has also a much larger forward RCS than its monostatic RCS. In fact, a sphere's forward RCS is similar to the forward RCS of a flat plate with the same cross section area.

It is also of interest to find a method that does not require a calibration target. This alternative method is based on measuring the direct signal from transmitting to receiving antenna and using it to calibrate. It is used to calibrate forward scattering measurements from different terrain types [11] and to calibrate the measurements in an outdoors bistatic RCS range [12]. The method is also evaluated and discussed in great detail in [13].

The transmitting and receiving antennas are positioned facing each other at distance r_d between the antenna phase centers so that the direct path signal can be measured. Assuming that the transmitting antenna generates a spherical wave and an ideal receiving antenna, the measured amplitude component at the receiving antenna for an empty setup can be written as,

$$V_{ij,d} = \frac{F_0 e^{ikr_d}}{2\sqrt{\pi} r_d} \tag{10}$$

where F_0 is the complex far field amplitude of the transmitting antenna and r_d is the distance between the antenna phase centers. The incident field at the object position r_t is,

$$E_0 = \frac{F_0 e^{ikr_t}}{2\sqrt{\pi} r_t} \tag{11}$$

and the far field amplitude of the scattered field is $F = SE_0$, where S is the scattering coefficient for the co- and cross-polarized components. The received signal with the object present is,

$$V_{\mathrm{ij,r}} = V_{\mathrm{ij,d}} + \frac{SE_0 \mathrm{e}^{\mathrm{i}kr_\mathrm{r}}}{2\sqrt{\pi} r_\mathrm{r}} = V_{\mathrm{ij,d}} + \frac{SF_0 \mathrm{e}^{\mathrm{i}kr_\mathrm{d}}}{2\sqrt{\pi} r_\mathrm{t} r_\mathrm{r}} \qquad (12)$$

where r_r is the distance between the target and the receiving antenna, $r_\mathrm{r} + r_\mathrm{t} = r_\mathrm{d}$. We can then solve for the scattering coefficient as,

$$S = \frac{V_{\mathrm{ij,r}} - V_{\mathrm{ij,d}}}{V_{\mathrm{ij,d}}} \frac{2\sqrt{\pi} r_\mathrm{t} r_\mathrm{r}}{r_\mathrm{d}}. \qquad (13)$$

This expression is equal to the complex valued RCS amplitude for the object, A_{ij}, and can be used to calculate the RCS using equation (3) and the extinction cross section using equation (6). The calibration vector, v_{ij}, can be identified as,

$$v_{\mathrm{ij}} = \frac{2\sqrt{\pi} r_\mathrm{t} r_\mathrm{r}}{r_\mathrm{d} V_{\mathrm{ij,d}}}. \qquad (14)$$

A comparison between the two methods is made by performing forward RCS measurements on small metal spheres, with different radii a and calibrating the measured data with both calibration methods. The results of these measurements are shown in Fig. 2. The first calibration method using a calibration target gives a more accurate result than the second method. In fact, the data calibrated in this way is so close to the theoretical results that the curve is hard to distinguish from the theoretical curve in the figure. A calibration with the second calibration method using the direct path measurement to obtain a calibration vector results in a forward RCS that deviates up to 0.7 dB from the Mie result. It is not clear what causes the discrepancies for the second calibration method. Further studies are needed in order to investigate this.

Equation (6) is used to determine the extinction cross section for horizontally polarized incident electric field from the forward RCS amplitude, shown in Fig. 2, with similar results.

B. Background subtraction

Consecutive background measurements of the forward scattering amplitude, $A_{\mathrm{bg}}(f, \hat{\boldsymbol{k}})$, are performed to determine the efficiency of the background subtraction as a function of time. $A_{\mathrm{bg,0}}(f, \hat{\boldsymbol{k}})$ is the forward scattering amplitude measured at $t = t_0$ and $A_{\mathrm{bg,n}}(f, \hat{\boldsymbol{k}})$ is the forward scattering amplitude measured at $t = t_\mathrm{n}$ with $t_\mathrm{n} > t_0$. The subtraction efficiency is defined according to equation (15). Here $\eta(f_0, t_\mathrm{n})$ is the subtraction efficiency for the frequency $f = f_0$ at time $t = t_\mathrm{n}$. The efficiency is obtained by averaging over a frequency interval centered at $f = f_0$ with k frequency points,

$$\eta(f_0, t_\mathrm{n}) = \frac{1}{k} \sum_\mathrm{i} \left| \frac{A_{\mathrm{bg,n}}(f_\mathrm{i}, \hat{\boldsymbol{k}}) - A_{\mathrm{bg,0}}(f_\mathrm{i}, \hat{\boldsymbol{k}})}{A_{\mathrm{bg,n}}(f_\mathrm{i}, \hat{\boldsymbol{k}})} \right|^2. \qquad (15)$$

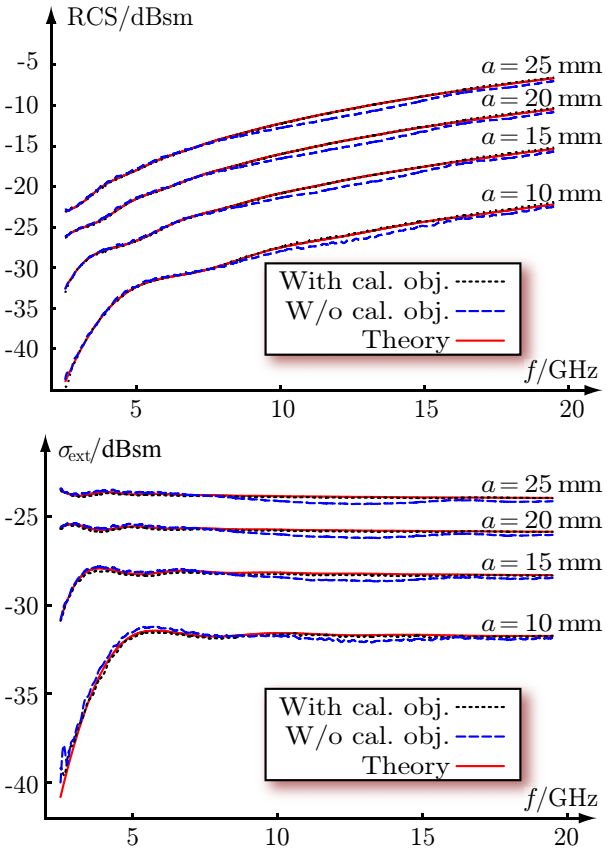

Fig. 2. Comparison between results from forward RCS measurements on metal spheres using the two calibration methods described (top figure). The corresponding results for the extinction cross section are shown in the bottom figure. The results obtained from a Mie series calculation are shown as a reference.

Figure 3 shows the subtraction efficiency, η, as a function of time for six different, 2 GHz wide, frequency bands. The bands with 6 GHz, 12 GHz, and 18 GHz center frequencies are measured at the same time and the bands with 24 GHz, 30 GHz, and 36 GHz center frequencies are measured at the same time but on another day. As expected and seen in the figure, the subtraction is most efficient

at low frequencies. With reduced wavelength the effect of displacements becomes larger. The losses also increase with increased frequency, which means a reduced signal to noise ratio (SNR). The reduced SNR also reduces the efficiency of the subtraction. The figure shows that the background subtraction is most efficient if the subtraction is performed within a few minutes relative to t_0. Focusing on the first 4 h of the measurements it is seen that the curves are not monotonically increasing. Instead, the subtraction is more efficient at t = 4 h than at t = 2 h.

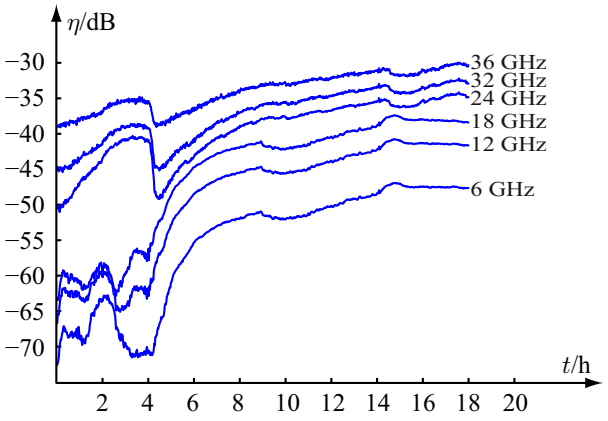

Fig. 3. The figure shows the subtraction efficiency as a function of time, in hours, for Δf = 2 GHz wide frequency bands. The curves are labeled with the center frequencies of the frequency bands.

This is interpreted as due to a change in distance between transmitting and receiving antenna. This interpretation is confirmed by a corresponding phase shift in the background measurement data. It is likely that this change in distance is caused by small chamber contractions or expansions due to temperature changes. Estimates of the temperature changes that are required to obtain these results can be made assuming a 6.8 m antenna to antenna distance, a chamber steel support structure and a coefficient of linear expansion of $11.7 \cdot 10^{-6}$/°C for steel [14]. The subtraction efficiency is –63 dB for the 6 GHz curve at t=2 h and –30 dB for the 36 GHz curve at t=3 h. Assuming that the background subtraction efficiency is limited by relative displacements of the antennas, displacements of 5.6 μm and 24 μm are calculated for 6 GHz and 36 GHz, respectively. Using the antenna to antenna distance and the coefficient for linear expansion for steel, the error levels correspond to temperature changes of 0.07 °C and 0.3 °C, respectively. This means that it is extremely important to maintain a stable temperature if a good background subtraction efficiency is desired.

The result of a forward RCS measurement of the empty chamber is shown in Fig. 4. The figure also shows the results after coherent background subtraction and time domain gating. The performed background subtraction suppresses the background by more than 70 dB, which gives a background level of less than –55 dBsm at the lower frequencies. The background suppression becomes gradually less efficient with increasing frequency and gives a background of less than –25 dBsm at the highest frequencies. Time domain gating reduces the background by another 5 dB for the lower frequencies and 20 dB for the higher frequencies, see Fig. 4.

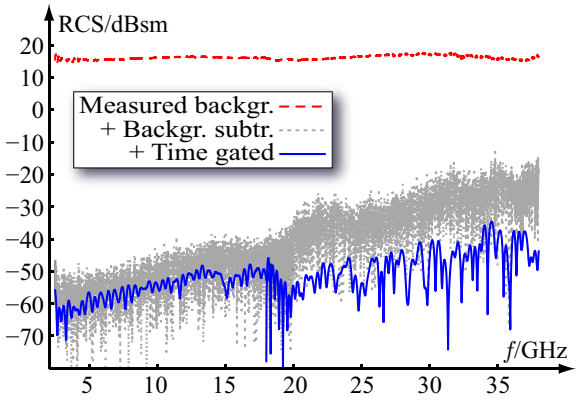

Fig. 4. Measurement of the background. The figure shows calibrated raw data from a background measurement, data after subtracting another background measurement, and after additional time gating.

C. Polarimetric measurements

The cross-polarization distortion in the transmit and receive channels can be estimated measuring the background signal using the setup in Fig. 1 without a target. Figure 5 shows the results from such a measurement of the calibrated background signal for the HH and HV components. The suppression, *i.e.*, the difference between the two curves, varies from approximately 20 dB to more than 30 dB depending on frequency.

The forward RCS of a helix is measured with the incident wave direction, $\hat{\boldsymbol{k}}$, along the axis of the helix. A helix is chosen because it is expected to give different extinction cross sections for different circular polarizations of the incident wave. The four linearly polarized components, HH, VV, HV, and VH, of the forward RCS obtained from a measurement of the helix sample are shown in Fig. 6. The linearly polarized components of the RCS amplitude can then be used to determine the circular polarized components.

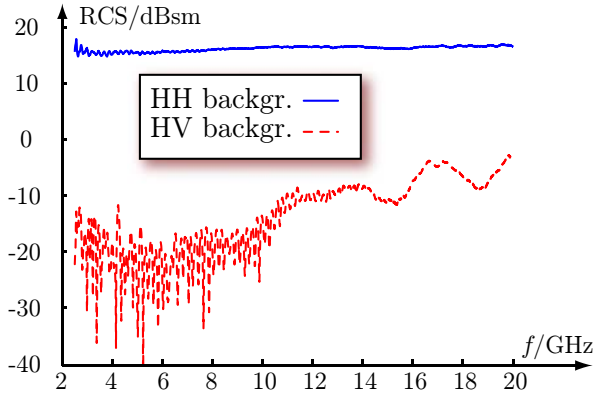

Fig. 5. The measured calibrated backgrounds for HH and HV polarizations before background subtraction.

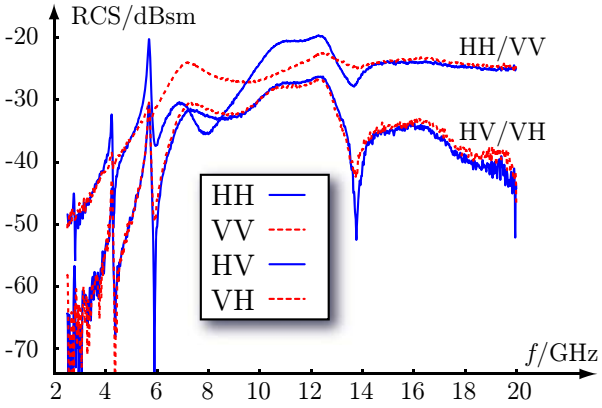

Fig. 6. The measured linearly polarized forward RCS components.

The determined circular polarized forward RCS amplitude components are used with equation (6) to obtain extinction cross sections for circular polarized incident waves. The resulting extinction cross sections for the helix for left circular polarized incident wave and for a right circular polarized incident wave are shown in Fig. 7. There is also, as expected, a large difference between the two polarizations due to the geometry of the helix. The results are compared with method-of-moments calculations to validate the method. It is found that the measured and calculated results qualitatively agree well.

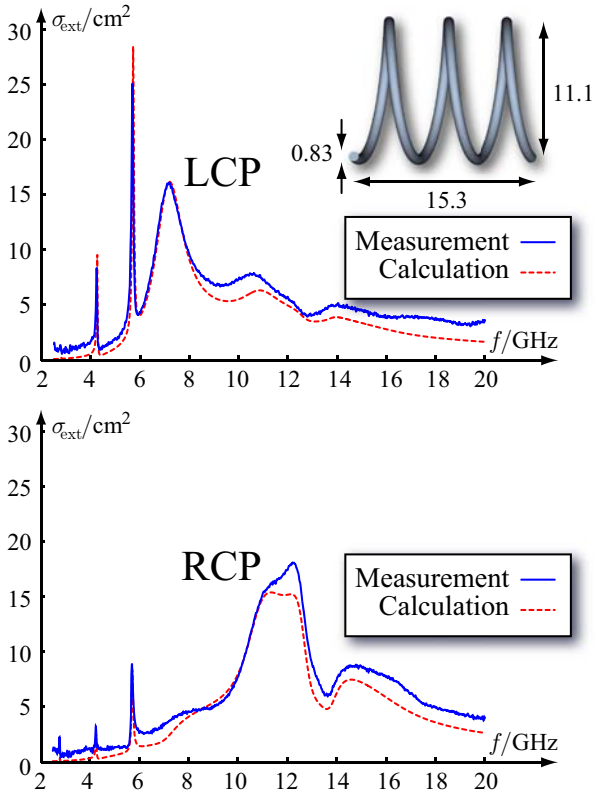

Fig. 7. The figure shows the extinction cross sections, $\sigma_{\text{ext}}(f)$, for left circular (LCP) (top) and right circular (RCP) (bottom) polarization of the incident wave determined from experiments and calculations. A drawing of the helix (dimensions in mm) used in the experiments is shown as an insert.

Polarimetric calibration to reduce the effect of cross-polarization distortion in the transmit and receive channels is considered for future development of the method presented in this paper. One could *e.g.*, use methods analogous to polarimetric calibration methods suggested for monostatic measurements, see *e.g.*, [15, 16]. However, finding a calibration object for broadband forward scattering polarimetric

calibration is more complicated than in the monostatic case.

V. CONCLUSIONS

A method to determine the extinction cross section utilizing forward RCS measurements is developed. It can be used to determine the extinction cross section in the frequency range 2.5 GHz-38 GHz. It is found that a calibration using a calibration target is more accurate than an alternative calibration method that does not require a calibration target. It is concluded that the alternative method needs further analysis to be useful for this purpose.

It is suggested that changes in the relative distance from transmitting antenna to receiving antenna are the limiting factor for the background subtraction efficiency. It is found that the combined effect of coherent background subtraction and time domain gating is to suppress the background by 75 dB at low frequencies and by 50 dB at high frequencies. This results in a remaining background level of -60 dBsm at low frequencies and -35 dBsm at high frequencies for a forward RCS measurement.

The method is validated by measuring small metal spheres with known extinction cross sections. The measurements show that the extinction cross section can be measured with good accuracy down to a level of -30 dBsm for the investigated frequency range. Measurements of the RCS amplitude linear polarization components can be used to calculate the extinction cross section for a circular polarized incident wave.

ACKNOWLEDGMENT

The financial support by the Swedish Foundation for Strategic Research and the Swedish Defense Materiel Administration is gratefully acknowledged.

REFERENCES

[1] C. Sohl, M. Gustafsson, and G. Kristensson, "Physical limitations on broadband scattering by heterogeneous obstacles," *J. Phys. A : Math. Theor.*, vol. 40, pp. 11165-11182, 2007.

[2] C. Sohl, C. Larsson, M. Gustafsson, and G. Kristensson, "A scattering and absorption identity for metamaterials: experimental results and comparison with theory," *J. Appl. Phys*., vol. 103, no. 5, pp. 054906, 2008.

[3] M. Gustafsson, C. Sohl, and G. Kristensson, "Illustrations of new physical bounds on linearly polarized antennas," *IEEE Trans. Antennas Propagat.*, vol. 57, no. 5, pp. 1319-1327, May 2009.

[4] M. Gustafsson, I. Vakili, S. Keskin, D. Sjöberg, and C. Larsson, "Optical theorem and forward scattering sum rule for periodic structures," *IEEE Trans. Antennas Propagat*., vol. 60, no. 8, pp. 3818-3826, 2012.

[5] C. Larsson, M. Gustafsson, and G. Kristensson, "Wideband microwave measurements of the extinction cross section — experimental techniques," Lund University, Department of Electrical and Information Technology, P.O. Box 118, S-221 00 Lund, Sweden, Tech. Rep. LUTEDX/(TEAT-7182)/1–22/, 2009, http: // www. eit.lth.se.

[6] C. Larsson, M. Gustafsson, and G. Kristensson, "Polarimetric measurements of the extinction cross section," *International Conference on Electromagnetics in Advanced Applications (ICEAA)*, Turin, Italy, pp. 311-314, September 14–18 2009.

[7] C. Larsson, M. Gustafsson, and G. Kristensson, "Calibration methods for wideband forward RCS measurements," *Proceedings of the Fourth European Conference on Antennas and Propagation (EuCAP)*, pp. 1-5, 2010.

[8] E. Knott, J. Shaeffer, and M. Tuley, *Radar Cross Section.* 5601 N. Hawthorne Way, Raleigh, NC 27613: SciTech Publishing Inc., 2004.

[9] G. Ruck, D. Barrick, W. Stuart, and C. Krichbaum, *Radar Cross-Section Handbook*. New York: Plenum Press, vol. 1 and 2, 1970.

[10] R. Newton, "Optical theorem and beyond," *Am. J. Phys*, vol. 44, pp. 639-642, 1976.

[11] P. Beckmann and A. Spizzichino, *The Scattering of Electromagnetic Waves from Rough Surfaces.* Oxford: Pergamon, 1963.

[12] F. Daout, A. Khenchaf, and J. Saillard, "Calibration of bistatic polarimetric scatterometers," *International Geoscience and Remote Sensing Symposium*, *(IGARSS) , Remote Sensing for a Sustainable Future*, vol. 1, pp. 746-648, May 1996.

[13] E. Zdansky, A. Örbom, and J. Rahm, "Object-free calibration and procedures for bistatic wideangle ISAR measurements of clutter reflectivity at the Lilla Gåra (Sweden) test range," *Proceedings of the Antenna Measurement Techniques Association (AMTA)*, pp. 1-6, 2011.

[14] D. Lide, *CRC Handbook of Chemistry and Physics: A Ready-Reference Book of Chemical and Physical Data. Ed. 88 (2007-2008).* Boca Raton, Florida: CRC Press, 2008.

[15] W. Wiesbeck and D. Kähny, "Single reference, three target calibration and error correction for monostatic, polarimetric free space measurements," *Proc. IEEE*, vol. 79, no. 10, pp. 1551-1558, 1991.

[16] B. Welsh, B. Kent, and A. Buterbaugh, "Full polarimetric calibration for radar cross-section measurements: Performance analysis," *IEEE Trans. Antennas Propagat*., vol. 52, no. 9, pp. 2357-2365, 2004.

Christer Larsson received the B.Sc. degree in Physics from Uppsala University, Uppsala, Sweden in 1981, the Ph.D. degree in Physics from the Royal Technical Institute, Stockholm, Sweden in 1990, was appointed Adjunct Professor in 2007 at Lund University, Lund, Sweden and Docent in 2010 at Lund University. Prof. Larsson is a senior specialist in radar signatures at Saab Dynamics, Linköping, Sweden. His research interests are in the electromagnetic properties of materials, radar cross section, and inverse synthetic aperture radar.

Mats Gustafsson received the M.Sc. degree in Engineering Physics 1994, the Ph.D. degree in Electromagnetic Theory 2000, was appointed Docent 2005, and Professor of Electromagnetic Theory 2011, all from Lund University, Sweden. His research interests are in scattering and antenna theory and inverse scattering and imaging with applications in microwave tomography and digital holography. He has written over 60 peer reviewed journal papers and over 75 conference papers. He cofounded the company Phase holographic imaging AB in 2004. Prof. Gustafsson received the best antenna poster prize at EuCAP 2007 and the IEEE Schelkunoff Transactions Prize Paper Award 2010. He serves as an AP-S Distinguished Lecturer for 2013-15.

A Three Dimensional FDTD Algorithm for Wave Propagation in Cold Plasma Media using Forth-Order Schemes

M. Pourbagher[1] and S. Sohafi[2]

[1] Department of Electrical Engineering, Urmia University
armanpurbaqer@yahoo.com

[2] Department of Electrical Engineering, Semnan University

***Abstract*—** A fourth-order accurate in space and second-order accurate in time, finite-difference time-domain (FDTD) scheme for wave propagation in cold plasma media is presented. The formulation of Maxwell's equations is fully described and an elaborate study of the stability and dispersion properties of the resulting algorithm is conducted. The efficiency of the proposed FDTD (2, 4) technique in cold plasma media compared to its conventional FDTD (2, 2) counterpart is demonstrated through numerical results.

***Keywords*-** FDTD algorithm, cold plasma, and Routh-Hurwitz.

I. INTRODUCTON

The finite difference time domain (FDTD) method [1, 2] has prevailed in the computational electromagnetics area as an accurate numerical technique for the direct integration of Maxwell's equations. Its evolution has ensued from several technological developments, resulting in the emergence of various algorithms that extend the method's implementation to various modern applications. A major group of such problems involves pulse propagation inside dispersive materials. Representative examples are the simulation of light propagation in optical devices, soil modeling in ground penetrating radar (GPR) problems [3], and study of potential effects of human tissue exposure to electromagnetic radiation. The techniques that render the FDTD method suitable for dispersive media modeling are grounded on an appropriate formulation of either the equation of motion of charged particles, or the local constitutive relation connecting the dielectric displacement to the electric field. In the former occasion a differential equation, which describes the electric field dependence on the polarization current density, is derived and discretized via regular differencing rules [4, 5]. For the latter case three popular approaches have been presented. The auxiliary differential equation (ADE) [6] technique translates the frequency-dependent constitutive relation in the time domain, by inverse Fourier transform, leading to an ordinary differential equation. The *Z*-transform based method [7] concludes in a similar differential equation, assuming the complex permittivity in the *Z*-domain to be a transfer function. Finally, in the recursive convolution (RC) [1] formulation the convolution integral corresponding to the time domain constitutive relation is approximated by a discrete summation, which is then properly calculated using a recursive procedure. The accuracy of the aforementioned efforts for expanding the FDTD method to frequency dependent materials is controlled by the choice of the spatial increment. Specifically, Yee's scheme is characterized by numerical dispersion errors, which accumulate in time and contaminate the solution. This side-effect is limited by using very fine discretization. Considering the fact that FDTD techniques for dispersive media introduce auxiliary variables or store field values from previous time steps, the fine mesh is translated into excessive memory demands. Furthermore, the achievement of high frequency resolution requires elongated simulations. An obvious way to restrict the memory needs and total computational times is the use of higher-order schemes [8-12]. A fourth-

Submitted On: March 27, 2013
Accepted On: Aug. 16, 2013

1054-4887 © 2013 ACES

order accurate in time and space FDTD approach for propagation in collisionless plasma has been presented in [13-24]. Despite the accuracy and memory savings achieved, the proposed method is restricted to lossless dispersive media. Recently, in [14, 25-31], a novel higher order method for modeling lossy media has been presented. In this paper, a staggered fourth-order accurate in space and second-order accurate in time FDTD scheme for the simulation of lossy dispersive materials is proposed. The media considered are second- and *N*th-order Lorentz, first- and *M*th-order Debye, and second-order Drude. The algorithm is based on the ADE technique [6, 12, 21], while a material-independent perfectly matched layer (PML) [15-18] is utilized for the reflectionless truncation of the computational domain. The stability and numerical dispersion characteristics of the proposed technique, examined for the (2, 2) case in [16, 19, 27, 29, 31], are investigated through the derivation of an appropriate stability criterion as well as a dispersion relation for each material.

II. HIGHER-ORDER FDTD SCHEMES FOR DISPERSIVE MEDIA

The key premise of the proposed FDTD (2, 4) method is the discretization of the spatial and temporal derivatives using fourth-order and second-order approximations, respectively. In order to present a more compact methodology for wave propagation in dispersive media, temporal central finite difference- (δ_t,δ_{2t},δ_t^2), central average- (μ_t,μ_{2t}), and central spatial-operators δ_β are defined in tables I and II. In the context of this paper the spatial derivative $\partial/\partial\beta$ is substituted by the fourth-order spatial operator,

$$\frac{1}{\Delta\beta}\delta_\beta F_m = \frac{1}{24\Delta\beta}$$

$$(F_{m-\frac{3}{2}} - 27F_{m-\frac{1}{2}} + 27F_{m+\frac{1}{2}} - F_{m+\frac{3}{2}}) \quad (1)$$

where the index m corresponds to β coordinate, unless stated otherwise.

The simulation of dispersive materials is founded on the ADE technique. Wave propagation inside the medium is fully described by the two Maxwell's laws, which are discretized using the FDTD (2, 4) scheme, and the frequency-dependent constitutive relation $\boldsymbol{D}(\boldsymbol{r},\omega) = \epsilon(\omega)\boldsymbol{E}(\boldsymbol{r},\omega)$, where $\epsilon(\omega)$ is the complex permittivity defining the material's dispersion properties. Taking the inverse Fourier transform of the previous constitutive relation, an ordinary differential equation is derived, which is then discretized utilizing a central differencing scheme in time. Assuming an *N*th-order dispersion, the process, which has been just described, results in [8-12],

$$E^{n+1} = \mathcal{F}\,(E^n,\ldots,\ E^{n-N+1},\ D^{n+1},\ D^n,\ldots,\ D^{n-N+1}). \quad (2)$$

The two discretized Maxwell's equations along with equation (2) constitute the overall computation model.

Table I: Temporal approximations.

	Time Domain	Z Domain	ω Domain
$\delta_t F^n$	$F^{n+\frac{1}{2}} - F^{n-\frac{1}{2}}$	$Z^{1}/_{2} - Z^{-1}/_{2}$	$2j\sin(\frac{\omega\Delta t}{2})$
$\delta_{2t} F^n$	$\frac{1}{2}(F^{n+1} - F^{n-1})$	$\frac{1}{2}(Z - Z^{-1})$	$j\sin(\omega\Delta t)$
$\mu_t F^n$	$\frac{1}{2}(F^{n+\frac{1}{2}} + F^{n-\frac{1}{2}})$	$\frac{1}{2}(Z^{1}/_{2} + Z^{-1}/_{2})$	$\cos(\frac{\omega\Delta t}{2})$
$\mu_{2t} F^n$	$\frac{1}{2}(F^{n+1} + F^{n-1})$	$\frac{1}{2}(Z + Z^{-1})$	$\cos(\omega\Delta t)$
$\delta_t^2 F^n$	$F^{n+1} - 2F^n + F^{n-1}$	$Z + Z^{-1} - 2$	$-4\sin^2(\frac{\omega\Delta t}{2})$

A. Cold plasma media

Cold plasma media is described by the following permittivity function [2, 6, 19, 20],

$$\epsilon(\omega) = \epsilon_0\left[1 + \frac{\omega_p^2}{\omega(j\nu_c - \omega)}\right] \quad (3)$$

where ω_p is the radian plasma frequency and ν_c is the collision frequency. The governing differential equation is,

$$\nu_c\frac{\partial D}{\partial t} + \frac{\partial^2 D}{\partial t^2} = \epsilon_0\,(\omega_p^2 E + \nu_c\frac{\partial E}{\partial t} + \frac{\partial^2 E}{\partial t^2}) \quad (4)$$

which is written in difference notation as,

$$[\, v_c \frac{\delta_{2t}}{\Delta t} + \frac{\delta_t^2}{(\Delta t)^2} \,] D^n =$$

$$\epsilon_0 \,[\, \omega_p^2 \mu_{2t} + v_c \frac{\delta_{2t}}{\Delta t} + \frac{\delta_t^2}{(\Delta t)^2} \,] E^n, \qquad (5)$$

and solved for E^{n+1} to obtain,

$$E^{n+1} = \frac{1}{\epsilon_0}\{\frac{4\epsilon_\infty E^n - \epsilon_0[\omega_p^2(\Delta t)^2 - v_c\Delta t + 2]E^{n-1}}{[\omega_p^2(\Delta t)^2 + v_c\Delta t + 2]} + \frac{1}{\epsilon_0}\{\frac{(2 + v_c\Delta t)D^{n+1} - 4D^n + (2 - v_c\Delta t)D^{n-1}}{[\omega_p^2(\Delta t)^2 + v_c\Delta t + 2]}\}. \qquad (6)$$

Table II: Spatial approximations.

	$\delta_\beta F^m$	Eigenvalues
2nd-order	$F_{m+\frac{1}{2}} - F_{m-\frac{1}{2}}$	$2j \sin(k_{num,\beta} \frac{\Delta\beta}{2})$
4th-order	$-\frac{1}{24}(F_{m+\frac{3}{2}} - F_{m-\frac{3}{2}}) + \frac{9}{8}(F_{m+\frac{1}{2}} - F_{m-\frac{1}{2}})$	$2j\,[\frac{9}{8}\sin(k_{num,\beta}\frac{\Delta\beta}{2}) - \frac{1}{24}\sin(3k_{num,\beta}\frac{\Delta\beta}{2})]$
6th-order	$\frac{3}{640}(F_{m+\frac{5}{2}} - F_{m-\frac{5}{2}}) - \frac{25}{384}(F_{m+\frac{3}{2}} - F_{m-\frac{3}{2}}) + \frac{75}{64}(F_{m+\frac{1}{2}} - F_{m-\frac{1}{2}})$	$2j\,[\frac{75}{64}\sin(k_{num,\beta}\frac{\Delta\beta}{2}) - \frac{25}{384}\sin(3k_{num,\beta}\frac{\Delta\beta}{2}) + \frac{3}{640}\sin(5k_{num,\beta}\frac{\Delta\beta}{2})]$

III. STABILITY ANALYSIS

Among the principal properties of the FDTD method, inherent in explicit differential equation solvers, is the conditional stability. In the conventional Yee's scheme the unbounded growth of errors is eluded by the proper choice of the time step size dictated by the Courant condition. The stability characteristics of the proposed higher-order algorithm are investigated using the methodology presented in [17-21, 28-36], which combines the Von Neumann method with the Routh-Hurwitz criterion. It is presumed that the error present in the computation of any field quantity F is described by a single term of a Fourier series expansion,

$$F^n = F_0 Z^n e^{j\sum_{\beta=x,y,z} k_{num,\beta} m\Delta\beta} \qquad (7)$$

where the complex variable Z corresponds to the growth factor of the error. Under this assumption, the temporal differencing and averaging operators as well as the spatial differencing operators are evaluated as shown in tables I and II. The time-dependent wave equation in a source-free homogeneous dispersive medium is,

$$\mu \frac{\partial^2 D}{\partial t^2} - \nabla^2 E = 0 \qquad (8)$$

and approximated by,

$$\mu \frac{\delta_t^2}{(\Delta t)^2} D^n - \sum_{\beta=x,y,z} \frac{\delta_\beta^2}{(\Delta\beta)^2} E^n = 0 \qquad (9)$$

where δ_β, ($\beta = x, y, z$) denotes the central spatial difference operator of arbitrary order with respect to the coordinate indicated by the subscript. Solutions of the form in equation (7) are substituted in equation (9) leading to a polynomial in Z. The stability of the finite difference scheme is assured if the roots of this characteristic polynomial are located inside or on the unit circle in the Z-plane, namely $|Z| \leq 1$. The bilinear transformation,

$$Z = \frac{r+1}{r-1} \qquad (10)$$

is then applied to the stability polynomial. In this way, the exterior of the unit circle in the Z-plane is mapped on the right-half of the r-plane. In order to examine whether the root of the polynomial with respect to r are nonnegative, the Routh table is created. If the values of all the elements in the first column are positive or zero, the algorithm is stable. The enforcement of the stability constraint regarding the specified entries of the Routh table results in certain inequalities relating the parameters of the FDTD scheme. Following the procedure, which has just been described, equation (9) is formulated, with the use of tables I and II as,

$$(Z-1)^2 D_0 + 4Z\epsilon_\infty v^2 E_0 = 0 \qquad (11)$$

where,

$$v^2 = (c_\infty \Delta t)^2 \sum_{\beta=x,y,z} \frac{1}{(\Delta\beta)^2} [\frac{9}{8}\sin(k_{num,\beta}\frac{\Delta\beta}{2}) - \frac{1}{24}\sin(k_{num,\beta}\frac{3\Delta\beta}{2})]^2 \qquad (12)$$

for fourth-order accuracy in space and $c_\infty = 1/\sqrt{\mu\epsilon_\infty}$. A formula similar to equation (12) can be derived in a straight forward manner for any spatial approximation order [29-34]. The spatial discretization operators are shown in table II for the case of second- and sixth-order. Next, the stability properties of the FDTD (2, 4) scheme for

the three aforementioned cold plasmas media will be examined. In the case of the Drude model the methodology will be presented in detail, while for the Debye and Lorentz models only the final results will be provided. The constitutive relation in the *Z*-domain for the Drude model is,

$$\{ [\frac{v_c}{2\Delta t} + \frac{1}{(\Delta t)^2}] Z^2 - \frac{2}{(\Delta t)^2} Z + \frac{1}{(\Delta t)^2} - \frac{v_c}{2\Delta t} \} D_0 = \epsilon_0 \{ [\frac{\omega_p^2}{2} + \frac{v_c}{\Delta t} + \frac{1}{(\Delta t)^2}] Z^2 - \frac{2}{(\Delta t)^2} Z + \frac{\omega_p^2}{2} - \frac{v_c}{\Delta t} + \frac{1}{(\Delta t)^2} \} E_0 \quad (13)$$

Solving equation (11) for D_0 results in,

$$D_0 = -\frac{4Z\epsilon_0 v^2}{(Z-1)^2} E_0 . \quad (14)$$

Substituting in equation (13) the characteristic stability polynomial is derived,

$$S(Z) = [\frac{2}{(\Delta t)^2} + \frac{v_c}{\Delta t} + \omega_p^2] Z^4 + [\frac{8(1-v^2)}{(\Delta t)^2} - \frac{2v_c(1-2v^2)}{\Delta t} - 2\omega_p^2] Z^3 + [\frac{12}{(\Delta t)^2} + 2\omega_p^2 - \frac{16v^2}{(\Delta t)^2}] Z^2 + [\frac{8(1-v^2)}{(\Delta t)^2} - \frac{2v_c(1-2v^2)}{\Delta t} - 2\omega_p^2] Z + \frac{2}{(\Delta t)^2} - \frac{v_c}{\Delta t} + \omega_p^2 . \quad (15)$$

After applying the billinear transformation, we obtain,

$$S(r) = \frac{2v^2 v_c}{\Delta t} r^3 + [\omega_p^2 + \frac{4v^2}{(\Delta t)^2}] r^2 + \frac{2v_c}{\Delta t} (1- v^2) + \omega_p^2 + \frac{4}{(\Delta t)^2} - \frac{4v^2}{(\Delta t)^2} \quad (16)$$

and the corresponding Routh table is built.

Table III: Routh-Hurwithz table.

$\frac{2v^2 v_c}{\Delta t}$	$\frac{2v_c}{\Delta t}(1- v^2)$
$\omega_p^2 + \frac{4v^2}{(\Delta t)^2}$	$\omega_p^2 + \frac{4}{(\Delta t)^2} - \frac{4v^2}{(\Delta t)^2}$
c_3	0
c_5	0

where,

$$c_3 = \frac{2\omega_p^2 v_c}{\Delta t} \frac{1-2v^2}{\omega_p^2 + \frac{4v^2}{(\Delta t)^2}}, \; c_5 = \omega_p^2 + \frac{4(1-v^2)}{(\Delta t)^2} . \quad (17)$$

Enforcing the entries of the first column to be nonnegative we get,

$$v^2 \le 1/2 . \quad (18)$$

In order to derive the numerical dispersion relation, the following discrete solution is assumed,

$$F^n (I, J, K) = F_0 \, exp [j (n\omega\Delta t + Ik_{num,x}\Delta x + Jk_{num,y}\Delta y + Kk_{num,z}\Delta z)] \quad (19)$$

where $\boldsymbol{F}$ represents the electric or magnetic field, indexes *I, J, K* denote the position of the nodes in the mesh, $\Delta\beta$ (β=*x, y, z*) are the sizes of the discretization cell, and $k_{num,\beta}$ (β = *x, y, z*) the wave numbers of the discrete modes in the β-direction. Similarly to the continuous case, we replace in Maxwell's equations $\partial/\partial t$ with $j\omega_{num}$ and ∇ with $-j\boldsymbol{k}_{num}$, where $\omega_{num} = \frac{2}{\Delta t}\sin(\frac{\omega\Delta t}{2})$. Given ω_{num} and $\boldsymbol{k}_{num}$, Maxwell's equations can be written in discrete form as,

$$\omega_{num}\,\mu_0 H_0 = \boldsymbol{k}_{num} \times E_0 \quad (20\text{-a})$$

$$\omega_{num}\,\epsilon_{num}(\omega_{num})E_0 = -\boldsymbol{k}_{num} \times H_0, \quad (20\text{-b})$$

where ϵ_{num} is the discrete permittivity function defined below. The numerical wave number $\boldsymbol{k}_{num}$ derived for the second-order spatial approximation is,

$$\boldsymbol{k}_{num} = \sum_{\beta=x,y,z} \frac{2}{\Delta\beta} \sin(\frac{k_{num,\beta}\Delta\beta}{2}) \alpha_\beta \quad (21)$$

and for the fourth-order spatial approximation,

$$\boldsymbol{k}_{num} = \sum_{\beta=x,y,z} \frac{2}{\Delta\beta} [\frac{9}{8} (\frac{k_{num,\beta}\Delta\beta}{2}) - \frac{1}{24} \sin(\frac{3k_{num,\beta}\Delta\beta}{2})] \alpha_\beta \quad (22)$$

where α_β is the unit vector in β-direction (see table II). The previous definitions can be extended to any order of spatial approximation. The central operator of *N*-order (*N*: even number) has the general form,

$$\delta_\beta F_m = \sum_{j=1(jodd)}^{N-1} c_j^N (F_{m+\frac{j}{2}} - F_{m-\frac{j}{2}}) \quad (23)$$

with the coefficients c_j calculated through Taylor series expansions and given in a closed form [18-24] by,

$$c_j^N = \frac{(-1)^{\frac{j-1}{2}}}{2(\frac{j}{2})^2} \frac{[(N-1)!!]^2}{(N-1-j)!!(N-1+j)!!} j = 1, 3, 5, \ldots, N-1 \quad (24)$$

where,

$$n!! = \begin{cases} n.(n-2)\ldots 5.3.1 & n > 0, odd \\ n.(n-2)\ldots 6.4.2 & n > 0, even \\ 1 & n = -1, 0. \end{cases}$$

Applying the previous formula, the coefficients $c_1^2 = 1$ for Yee's scheme, $c_1^4 = 9/8$ and $c_3^4 = -1/24$ for Fang's fourth-order scheme, and $c_1^6 = 75/64$, $c_3^6 = -25/384$, $c_5^6 = 3/640$ for a sixth-order scheme are yielded. It can be easily proven that the numerical wave number for the *N*th-order accurate scheme is,

$$\boldsymbol{k}_{num} = \sum_{\beta=x,y,z} \frac{2}{\Delta\beta} \sum_{j=1(jodd)}^{N-1} c_j^N \sin\left(\frac{j k_{num,\beta} \Delta\beta}{2}\right) \alpha_\beta . \quad (25)$$

The numerical wave number $\boldsymbol{k}_{num}$ is defined as,

$$\boldsymbol{k}_{num} = k_{num} (\sin\theta\cos\emptyset\, a_x + \sin\theta\sin\emptyset\, a_y + \cos\theta\, a_z). \quad (26)$$

The discrete counterpart of the continuous permittivity function, called numerical permittivity, is defined as the ratio of the discrete values of D and E, i.e., $\epsilon_{num} = D^n / E^n$. Similar to the continuous dispersion relation the discrete one is,

$$\mu_0 \epsilon_{num}(\omega_{num}) \omega_{num}^2 = \boldsymbol{k}_{num} \cdot \boldsymbol{k}_{num} \quad (27)$$

Using the discrete form of the constitutive equation and the temporal operators shown in the third column of table I, which are derived by setting $Z = \exp(j\omega t\Delta t)$, the discrete expression of the complex permittivity function for the cold plasma medium,

$$\epsilon_{num} = \epsilon_0 \left[1 + \frac{\omega_{p,num}}{\omega_{num}(j\nu_{c,num} - \omega_{num})}\right] \quad (28)$$

where $\omega_{p,num} = \omega_p \sqrt{\cos(\omega\Delta t)}$, $\omega_{num} = \frac{2}{\Delta t}\sin(\frac{\omega\Delta t}{2})$ and $\nu_{c,num} = \nu_c \cos(\frac{\omega\Delta t}{2})$. Restricting ourselves to one-dimensional problems, without loss of generality, it is obtained for the FDTD (2, 2) case,

$$k_{num} = \frac{2}{\Delta} sin^{-1}\left(\frac{\Delta}{2}\omega_{num}\sqrt{\mu_0\epsilon_{num}}\right) \quad (29)$$

for the FDTD (2, 4),

$$\frac{2}{\Delta}\left[\frac{9}{8}\sin\left(\frac{k_{num}\Delta}{2}\right) - \frac{1}{24}\sin\left(\frac{3k_{num}\Delta}{2}\right)\right] = \omega_{num}\sqrt{\mu_0\epsilon_{num}} \quad (30)$$

and for the FDTD (2, 6),

$$\frac{2}{\Delta}\left[\frac{75}{64}\sin\left(\frac{k_{num}\Delta}{2}\right) - \frac{25}{384}\sin\left(\frac{3k_{num}\Delta}{2}\right) + \frac{3}{640}\sin\left(\frac{5k_{num}\Delta}{2}\right)\right] = \omega_{num}\sqrt{\mu_0\epsilon_{num}}. \quad (31)$$

To investigate the dispersive features for both second- and fourth- order schemes we consider the following example in a second order Lorentz medium; let $\epsilon_\infty = 2.25\epsilon_0$, $\epsilon_s = 3\epsilon_0$, $\omega_0 = 2\pi f_0$, $f_0 =$ 200 MHz and $\delta_0 = 0.1\omega_0$. Figure 1 shows the normalized phase velocity $c_{num}/c = k/Re\{k_{num}\}$ for the second-order case with $\Delta = 0.005$ m, $Q = 0.6$ and the fourth- and sixth-order with $\Delta = 0.01$ m, $Q = 0.1$ where the Courant number Q is defined as $Q = c_0\Delta t/\Delta$. The superior performance of the higher-order schemes is evident, even for larger Δ.

IV. NUMERICAL RESULTS

The efficiency of the proposed FDTD (2, 4) scheme compared to the conventional second-order accurate technique has been extensively investigated through numerical results. An analytical reference solution has been developed in order to precisely define the potential errors of each method [21-23]. The two schemes have been tested in one-dimensional wave propagation problems in homogeneous and inhomogeneous geometries involving materials of diverse dispersion types. In all the examined cases, the new algorithm has been found to be superior, achieving higher accuracy in modeling dispersive characteristics for equal spatial discretization, or allowing a less dense lattice to be used, while the same level of accuracy is ensured [33-36].

In the first case studied a Lorentz-type medium slab is placed in free space. The resonant frequency of the material is set to $\omega_0 = 2 \times 10^9\, rad/sec$, the damping coefficient is equal to $\delta_0 = 0.1\omega_0$, whereas $\epsilon_\infty = 2.25\epsilon_0$ and $\epsilon_s = 3\epsilon_0$ [22-27]. The wideband reflection coefficient at the interface between air and the dispersive dielectric is calculated by the FDTD (2, 2) and FDTD (2, 4)

ADE techniques. The computational domain consists of 2000 cells and the dielectric slab occupies the region from the 700th cell to 750th cell. For the FDTD (2, 4) scheme the spatial step size is set to Δx = 0.005 m, Q = 0.1 and the total number of time steps N_t = 14250. Two sets of parameters are selected for the FDTD (2, 2) simulations, namely (a) Δx = 0.005 m, Q = 0.95 and N_t= 1500 and (b) Δx = 0.0025 m, Q = 0.95, N_t= 3000 where the number of cells is doubled. The results for the first case are depicted in Fig. 1, along with the reference solution. It is clearly observed that the FDTD (2, 4) scheme is far more accurate obtaining only slight deviations from the exact reflection coefficient function even for frequencies high above the resonant one [25-27]. Contrarily, its (2, 2) counterpart generates significant errors. The reflection coefficient for the latter group of parameters is illustrated in Fig. 2. The graphs corresponding to the two schemes almost coincide introducing minor shifts in the peaks locations compared to the analytical solution. However, it should be reminded that in the FDTD (2, 2) case a two times denser grid is utilized.

In the next simulation, the propagation of the modulated Gaussian pulse $f(t) = \exp\left\{-(t-t_0)^2/T^2\right\}\cos(2\pi f_s t)$ where t_0= 8×10−9 sec, T = 10−9 sec and f_s= 600 MHz, inside a Lorentz-type dispersive medium is explored. The parameters of the material are ω_0= 2π 200×10^6 rad/sec, δ_0= 0.1ω_0, ϵ_∞= 2.25ϵ_0 and ϵ_s= 3ϵ_0. For the FDTD (2, 2) scheme two different uniform grids are considered: (a) Δx = 0.01 m, Q = 0.5 for 5000 time steps and (b) Δx = 0.05 m, Q = 0.5 for 1000 time steps. The respective parameters for the FDTD (2, 4) scheme are Δx = 0.05m and Q = 0.1.

In Fig. 3, the time domain electric field located 0.2 m away from the excitation point is illustrated for the three aforementioned cases along with the exact solution. For an easier observation a detail of the previous graphs is shown in Fig. 4. It is evident that the higher order algorithm achieves the same level of accuracy as the FDTD (2, 2) with the first set of parameter values, but with a five times coarser grid. In table III, the three methods are compared in terms of maximum error and total computational time. It is noted that the proposed higher order technique is more accurate and computationally efficient.

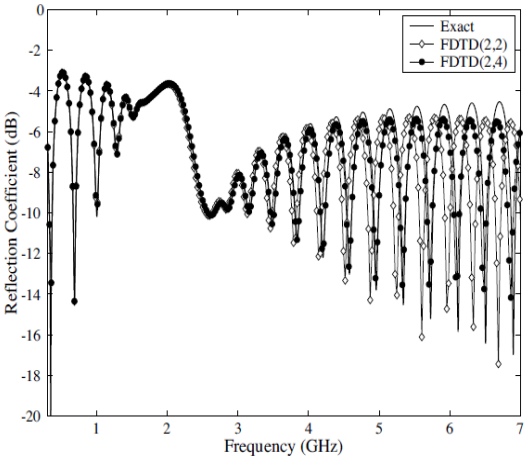

Fig. 1. The reflection coefficient as a function of frequency. Comparison is made between the exact data, FDTD (2, 4) and FDTD (2, 2) with Δx = 0.005 m.

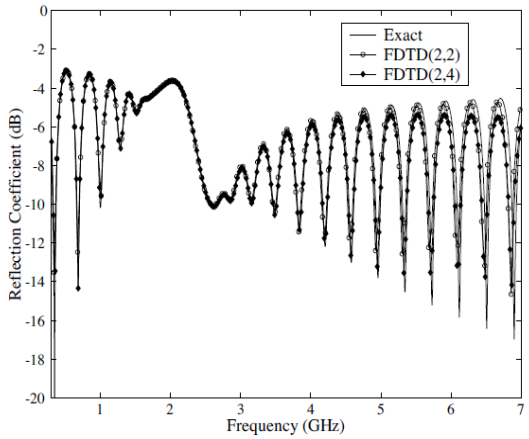

Fig. 2. The reflection coefficient as a function of frequency. Comparison is made between the exact data, FDTD (2, 4) Δx = 0.05 m and FDTD (2, 2) with Δx = 0.0025 m.

Finally, the air-slab problem is solved by the FDTD (2, 2) and FDTD (2, 4) algorithms assuming that the slab is filled with a third order Debye dispersive material. The characteristic parameters of the three poles are ϵ_{s1}= 3ϵ_0, τ_1= 9, 4×10^{-9}sec, ϵ_{s2}= 2ϵ_0, τ_2= 10^{-10}sec, and ϵ_{s3}=ϵ_0, τ_3 = 10^{-6} sec, while the infinite permittivity is set equal to 2.25 ϵ_0. In both cases, the computational space consists of 2000 cells, the spatial step size is 0.01m and Q = 0.8. The electric

field function in the time-domain is presented in Fig. 5. It is again obvious that the proposed higher order scheme accomplishes better accuracy.

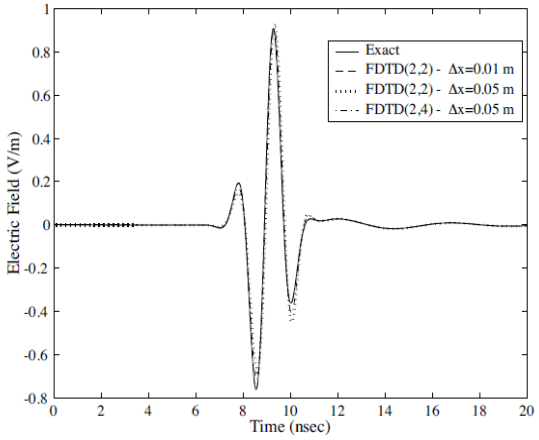

Fig. 3. Electric field waveforms of the exact, FDTD (2, 4) and FDTD (2, 2) with two different grids.

Having verified that FDTD (2, 4) can be efficiently extended to cold plasma medias, it is applied to wave scattering by an infinite height cylinder made of cold plasma placed in air. The computational space consists of 200×200 cells. The cylinder is excited by a plane wave. The wave front is assumed to be a modulated Gaussian pulse centered at 20 GHz. The excitation frequency is stable, while for the plasma frequency of the cold plasma three values have been selected, namely 28.7 GHz, 5.74 GHz, and 0.287 GHz.

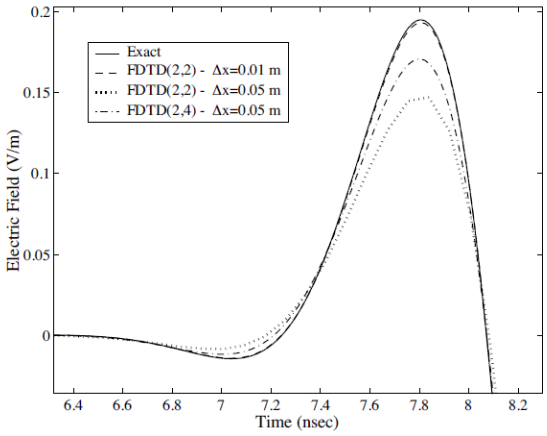

Fig. 4. Details of Fig. 3, observed that the proposed technique produces an acceptable close to the (2, 2) scheme result but with a five-times coarser grid.

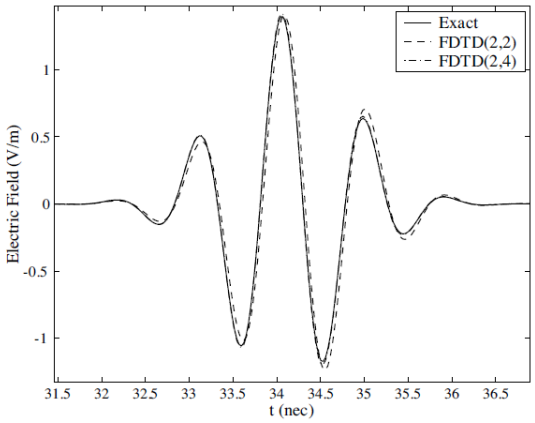

Fig. 5. Electric field waveforms of the exact, FDTD (2, 4) and FDTD (2, 2).

V. CONCLUSION

A novel FDTD (2, 4) scheme for the simulation of wave propagation inside cold plasma media has been presented. Its stability properties for three specific models have been investigated and appropriate stability conditions have been derived. Additionally, the numerical dispersion characteristics have been examined and for the case of a second-order Lorentz medium, it has been verified that the proposed algorithm is more powerful than the conventional second-order technique, as expected. The efficiency of the FDTD (2, 4) algorithm has also been explored in various numerical examples, where it has been compared to the FDTD (2, 2) method and an analytical solution. In all the cases considered, it has been proven that the former achieves better accuracy when the same grid is used or the same level of accuracy for coarser grids. Additionally, the presented method accomplishes minimum errors, while reducing the overall computational time.

REFERENCES

[1] K. Kunz and R. Luebbers, *The Finite Diference Time Domain Method for Electromagnetics*, CRC, Boca Raton, FL, 1993.

[2] A. Taflove and S. Hagness, *Computational Electrodynamics: The Finite-Difference Time-Domain Method*, 2nd ed., Artech House, Boston, MA, 2000.

[3] F. Teixeira, W. Chew, M. Straka, M. Oristaglio, and T. Wang, "Finite-difference time-domain simulation of ground penetrating radar on dispersive, inhomogenous, and conductive soils,"

IEEE Trans. Geosci. Remote Sensing, vol. 36, pp. 1928-1937, Nov. 1998.

[4] J. Young, "Propagation in linear dispersive media: Finite difference time-domain methodologies," *IEEE Trans. Antennas Propagat.*, vol. 43, pp. 422-426, Mar. 1995.

[5] S. Cummer, "An analysis of new and existing FDTD methods for isotropic cold plasma and a method for improving their accuracy," *IEEE Trans. Antennas Propagat.*, vol. 45, pp. 392-400, Mar. 1997.

[6] R. Joseph, S. Hagness, and A. Taflove, "Direct time integration of Maxwell's equations in linear dispersive media with absorption for scattering and propagation of femtosecond electromagnetic pulse," *Opt. Lett.*, vol. 16, pp. 1412-1414, Sept. 1991.

[7] D. Sullivan, "Frequency-dependent FDTD methods using Z transforms," *IEEE Trans. Antennas Propagat.*, vol. 40, pp. 1223-1230, Oct. 1992.

[8] J. Fang, *Time Domain Finite Difference Computation for Maxwell's Equations*, Ph.D. dissertation, University California, Berkeley, CA, 1989.

[9] N. Kantartzis and T. Tsiboukis, "A generalized methodology based on higher-order conventional and non standard FDTD concepts for the systematic development of enhanced dispersionless wide-angle absorbing perfectly matched layers," *International Journal of Numerical Modelling: Electronic Networks, Devices and Fields*, vol. 13, pp. 417-440, 2000.

[10] J. Young, D. Gaitonde, and J. Shang, "Toward the construction of a fourth-order difference scheme for transient EM wave simulation: Staggered grid approach," *IEEE Trans. Antennas Propagat.*, vol. 45, pp. 1573-1580, Nov. 1997.

[11] A. Yefet and P. Petropoulos, "A staggered fourth-order accurate explicit finite difference scheme for the time-domain Maxwell's equations," *J. Comput. Phys.*, vol. 168, pp. 286-315, 2001.

[12] S. Georgakopoulos, C. Birtcher, C. Balanis, and R. Renaut, "Higher-order finite-difference schemes for electromagnetic radiation, scattering, and penetration, Part I: Theory," *IEEE Antennas Propag. Mag.*, vol. 44, pp. 134-142, Feb. 2002.

[13] J. Young, "A higher order FDTD method for EM propagation in a collisionless cold plasma," *IEEE Trans. Antennas Propagat.*, vol. 44, pp. 1283-1289, Sept. 1996.

[14] K. Prokopidis and T. Tsiboukis, "Higher-order FDTD (2, 4) scheme for accurate simulations in lossy dielectrics," *Electron. Lett.*, vol. 39, no. 11, pp. 835-836, 2003.

[15] P. Petropoulos, L. Zhao, and A. Cangellaris, "A reflectionless sponge layer absorbing boundary condition for the solution of Maxwell's equations with high-order staggered finite difference schemes," *J. Comput. Phys.*, vol. 139, pp. 184-208, 1998.

[16] P. Petropoulos, "Stability and phase error analysis of FDTDin dispersive dielectrics," *IEEE Trans. Antennas Propagat.*, vol. 42, pp. 62-69, Jan. 1994.

[17] J. Pereda, L. Vielva, A. Vegas, and A. Prieto, "Analyzing the stability of the FDTD technique by combining the von Neumann method with Routh-Hurwitz criterion," *IEEE Trans. Microwave Theory Tech.*, vol. 49, pp. 377-381, Feb. 2001.

[18] M. Ghrist, *Finite Difference Methods for Wave Equations*, Ph.D. Thesis, University of Colorado at Boulder, Boulder, CO, 2000.

[19] L. Prokopeva, A. Kildishev, J. Fang, J. Borneman, M. Thoreson, V. Shalaev, and V. Drachev, "Nanoplasmonics FDTD simulations using a generalized dispersive material model," *27th Annual Review of Progress in Applied Computational Electromagnetics (ACES)*, pp. 963-968, Williamsburg, Virginia, March 2011.

[20] J. Chen and A. Zhang, "A frequency-dependent hybrid implicit-explicit FDTD scheme for dispersive materials," *Applied Computational Electromagnetics Society (ACES) Journal*, vol. 25, no. 11, pp. 956-961, Nov. 2010.

[21] J. Chen and J. Wang, "A frequency-dependent weakly conditionally stable finite-difference time-domain method for dispersive materials," *Applied Computational Electromagnetics Society (ACES) Journal*, vol. 25, no. 8, pp. 665-671, August 2010.

[22] A. Greenwood, "FDTD model for magnetized plasma," *25th Annual Review of Progress in Applied Computational Electromagnetics (ACES)*, pp. 612-616, Monterey, California, March 2009.

[23] A. Greenwood, A. Schulz, and K. Cartwright, "Hybrid modeling of electromagnetic plasmas," *20th Annual Review of Progress in Applied Computational Electromagnetics (ACES)*, Syracuse, NY, April 2004.

[24] M. pourbagher, J. Nourinia, and N. Pourmahmud, "Reconfigurable plasma antennas," *Indian Journal of Science and T echnology*, vol. 5, no. 6, June 2012.

[25] M. pourbagher, J. Nourinia, and N. Pourmahmud, "Development of a three-dimensional magnetic-field-independent absorbing boundary condition (MFIABC) for cold magneto plasma," *International Journal of Modern Engineering Research*, vol. 2, no. 4, pp. 2880-2884, July 2012.

[26] D. Lawrence and K. Sarabandi, "Electromagnetic scattering from vibrating penetrable objects using a general class of time-varying sheet boundary conditions," *IEEE Trans. Antennas Propagat.*, vol. 54, no. 7, pp. 2054-2061, July 2006.

[27] J.-H. Chang and A. Taflove, "Three-dimensional diffraction by infinite conducting and dielectric wedges using a generalized total-field/scattered-field FDTD formulation," *IEEE Trans. Antennas Propagat.*, vol. 53, no. 4, pp. 1444-1454, April 2005.

[28] S. Tseng, A. Taflove, D. Maitland, and V. Backman, "Pseudospectral time-domain simulations of multiple light scattering in three-dimensional macroscopic random media," *Radio Science*, vol. 41, RS4009, doi:10.1029/2005RS003408, 2006.

[29] J. Simpson and A. Taflove, "Three dimensional FDTD modeling of impulsive ELF propagation about the earth-sphere," *IEEE Trans. Antennas Propagat.*, vol. 52, no. 2, pp. 443-451, Feb. 2004.

[30] J. Simpson, R. Heikes, and A. Taflove, "FDTD modeling of a novel ELF radar for major oil deposits using a three-dimensional geodesic grid of the earth-ionosphere waveguide," *IEEE Trans. Antennas Propagat.*, vol. 54, no. 6, pp. 1734-1741, June 2006.

[31] J. Simpson and A. Taflove, "A review of progress in FDTD Maxwell's equations modeling of impulsive subionospheric propagation below 300 kHz," *IEEE Trans. Antennas Propagat.*, vol. 55, no. 6, pp. 1582-1590, June 2007.

[32] S.-C. Kong, J. Simpson, and V. Backman, "ADE-FDTD scattered-field formulation for dispersive materials," *IEEE Microwave and Wireless Comp. Lett.*, vol. 18, no. 1, pp. 4-6, Jan. 2008.

[33] Y. Yu and J. Simpson, "An E-J collocated 3-D FDTD model of electromagnetic wave propagation in magnetized cold plasma," *IEEE Trans. Antennas Propagat.*, vol. 58, no. 2, pp. 469-478, Feb. 2010.

[34] L. Prokopeva, A. Kildishev, J. Fang, J. Borneman, M. Thoreson, V. Shalaev, and V. Drachev, "Nanoplasmonics FDTD simulations using a generalized dispersive material model," *27th Annual Review of Progress in Applied Computational Electromagnetics (ACES)*, pp. 963-968, Williamsburg, Virginia, March 2011.

[35] J. Chen and A. Zhang, "A frequency-dependent hybrid implicit-explicit FDTD scheme for dispersive materials," *Applied Computational Electromagnetics Society (ACES) Journal*, vol. 25, no. 11, pp. 956-961, November 2010.

[36] J. Chen and J. Wang, "A frequency-dependent weakly conditionally stable finite-difference time-domain method for dispersive materials," *Applied Computational Electromagnetics Society (ACES) Journal*, vol. 25, no. 8, pp. 665-671, August 2010.

A Cone Shaped Tapered Chamber for Antenna Measurements Both in Near Field and Far Field in the 200 MHz to 18 GHz Frequency Range and Extension of the Quiet Zone using an RF Lens

V. Rodriguez[1], S. Matitsine[2,3], T.-T. Chia[3,4], P. Lagoiski[2], L. Matytsine[2], M. Matytsine[2], and P.-K. Tan[3]

[1] ETS-Lindgren L.P.
1301 Arrow Point Dr. Cedar Park TX 78613 USA
Vince.Rodriguez@ets-lindgren.com

[2] Matsing Pte Ltd.
31 Kaki Bukit Road 3, #06-21 Techlink, Singapore 417818
smatitsine@matsing.com, pavel@matsing.com, leo@matsing.com, michael@matsing.com

[3] Temasek Laboratories, National University of Singapore
T-Lab Building, 5A, Engineering Drive 1, #09-02, Singapore 117411
tslms@nus.edu.sg, tslctt@nus.edu.sg, tsltpk@nus.edu.sg

[4] DSO National Laboratories
20 Science Park Drive, Singapore 118230
ctsetong@dso.org.sg

Abstract–Traditionally, tapered chambers are constructed using a square based pyramidal shaped taper. The taper is then shaped into an octagon and finally transformed into a cylindrical launch section. This approach is related to the manufacturability of different absorber cuts. This paper introduces a chamber where the conical shape of the launch in continued throughout the entire length of the tapered chamber. The results of the free space VSWR test over a 1.5 m diameter quiet zone (QZ) are presented at different frequencies. The conical taper appears to have a better illumination wave front and better QZ levels even at frequencies above 2 GHz than the standard traditional approach. This design was implemented in Singapore and the actual chamber was designed to have a secondary near field range for planar and spherical scans. As with all antenna chambers, as the frequency increases, the usable or far field illuminated QZ is reduced. At a 12 m distance from the feed to the turntable, the quiet zone at 8 GHz is reduced to 45 cm. The chamber includes a near to far field range to allow the use of the chamber at higher frequencies when testing electrically large antennas. Another solution implemented to extend the quiet zone at high frequency is to use a large dielectric lens to improve the phase distribution of the field. A light weight, broadband lens with a diameter of 2 m was developed by Matsing Pte Ltd. The parameters of the lens were specially customized for the tapered chamber built. The RF lens, weighing just 35 kg, has a focal length of 10 m. It was installed in front of the turn table. The performance of the tapered chamber with the RF lens is presented. The usable far field QZ was increased by using a dielectric RF lens that allows for electrically larger antennas to be measured in the tapered range of the chamber.

Index Terms–Antenna range design, metamaterials, quiet zone, RF lens, and tapered chamber.

Submitted On: April 1, 2013
Accepted On: Oct. 14, 2013

1054-4887 © 2013 ACES

I. INTRODUCTION

Tapered anechoic chambers have been around for almost 50 years [1-2]. The reason for the introduction of these chambers was the issues present on rectangular chambers at frequencies below 500 MHz [3-4]. At lower frequencies, the antennas used in an antenna measurement range become physically very large. These antennas can be difficult to handle inside an anechoic chamber. Less directive antennas are used. These less directive antennas will radiate more energy to the side walls, ceiling and floor of the chamber. To reduce the reflections, thicker absorbers are required. To accommodate the thicker absorbers, the chamber must be larger. Tapered anechoic chambers were introduced to solve this low frequency issue. Instead of trying to eliminate the specular reflections into the quiet zone, the specular area is brought closer to the measuring antenna and the specular reflections are used to create the illumination in the QZ [2, 5]. Traditionally, tapered anechoic chambers were built having a square based pyramid as the taper (see Figs. 1 and 2). To better accommodate different feed antennas, the square section may be changed to a cylindrical cross section taper. These changes in cross section require a lot of special cuts of absorber to make the transition from the conical section to the square section as smooth as possible. As was reported in [2-5], the absorber reflections are used to create the illumination in the QZ.

Fig. 1. A typical tapered anechoic chamber.

The concept presented in this paper introduces a conical taper. The entire tapered structure maintains a constant angle and a circular cross section. Figure 3 shows a picture of the conical tapered chamber of the new type of chamber. The tapered section shown in Fig. 3 is about 10 m in total length. The results for the free-space VSWR [6] of the range are presented in the next section where they are compared with similar chambers that use the traditional design.

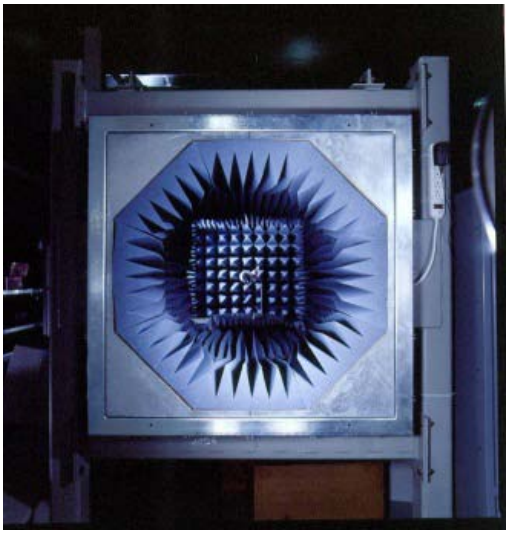

Fig. 2. Shaping from square to octagonal cross-section at the feed section.

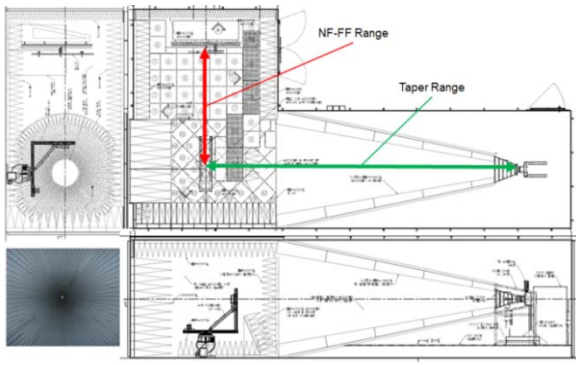

Fig. 3. The conical tapered anechoic range.

II. MEASURED RESULTS

The manufactured chamber, using the conical taper, had its QZ scanned using the free space VSWR tests [6]. The tests were performed at a series of frequencies from 200 MHz up to 18 GHz. The chamber was lined with 60" (152 cm) curvilinear absorbers on the back (i.e., receive) wall and a combination of 24" (61 cm) pyramidal absorbers and 36" (91.44 cm) on the sidewalls, floor and ceiling. The tapered section has a specially cut wedge material that lines the tapered

section from the feed location to the QZ area. The wedges ranged from 18" (45.72 cm) at the QZ end to 8" (20.32 cm). Figure 4 shows a picture of the conical treatment.

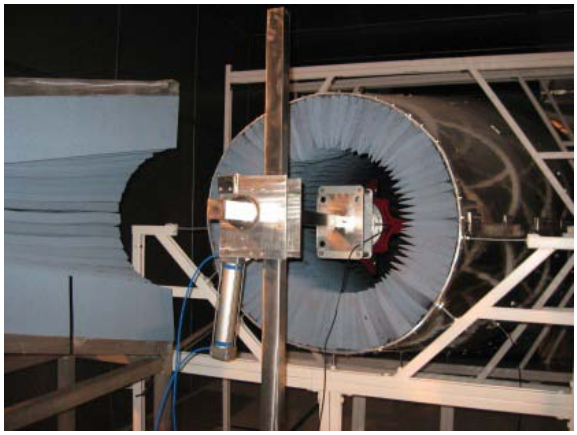

Fig. 4. The tapered section seen from the feed location. The tapered section was built inside an RF shielded room to avoid outside interference during measurements.

The source antenna was an ETS-Lindgren model 3164-06 dual linearly polarized open boundary quad-ridge horn [7], rated from 300 MHz to 6 GHz. In this application, the antenna was used from 200 MHz. Attenuators were used at the feed of the antenna to reduce the effects of the high VSWR. The QZ was scan with an ETS-Lindgren model 310 6B dual ridge horn. The scanning antenna and source antenna are shown in Fig. 5.

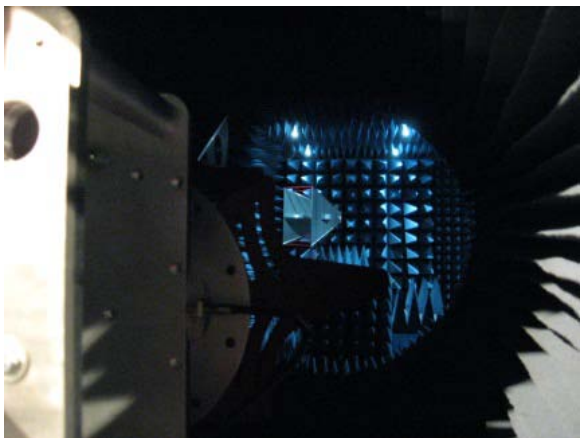

Fig. 5. The scanning antenna at the QZ viewed from a point right behind the source antenna at the apex of the taper.

Figure 6 shows the reflectivity levels of the QZ versus direction for horizontal and vertical polarizations. Results are shown for 200 MHz, 400 MHz, 800 MHz, and 1,000 MHz. All these results were measured with the source antenna at a fixed position in the apex of the taper. Commonly, the antenna is moved as frequency changes to maintain the phase center close to the reflections and keep a QZ illumination free of ripples [3-4].

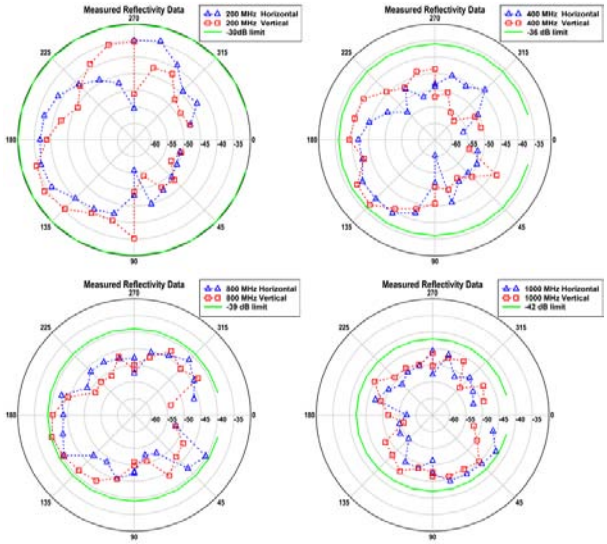

Fig. 6. Reflectivity results for the conical tapered chamber.

For frequencies above 2 GHz, a different horn, an ETS-Lindgren 3164-05 dual linearly polarized open boundary quad-ridge horn, rated from 2 GHz to 18 GHz, was used. For scanning the QZ, a series of standard gain horns were used with gains ranging from 10 dBi to 20 dBi. Additionally, since a smaller horn was used as the source, the horn was positioned inside an extension of the conical taper. Figure 4 shows one of the two halves that made up this high frequency extension.

Figure 7 shows the results of the scans at high frequencies. As discussed in [5], tapered chambers are better suited for low frequencies and care must be taken to properly position the source antenna. However, it is possible to use them at these high frequencies once the chamber is properly characterized.

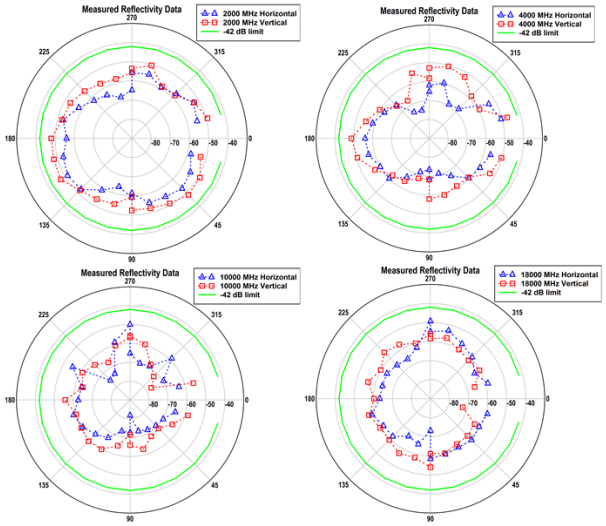

Fig. 7. Reflectivity levels in the QZ versus angle at four different frequencies.

III. COMPARISON WITH TRADITIONAL CHAMBERS

Comparison with traditional chambers is difficult. There are no two identical chambers with the exact same absorber treatment with the only difference being the taper geometry. So a qualitative comparison is done. When compared with traditional chambers, there seem to be some advantages in the new design. In traditional chambers, antennas with gains of 16 dBi and above are required to get adequate illumination at the QZ. It appears to be one of the advantages of the conical taper that lower gain antennas can be used to illuminate the QZ. At 10 GHz, the source antenna has a directivity of 12 dBi [7]. On the other hand, the conical quad ridge horn used in many traditional tapered anechoic chambers has a directivity of 14 dBi at 10 GHz.

The open boundary ridge horn was successfully used in the conical chamber design. However, in the past, when it was used in a traditional chamber, a smooth amplitude taper was not achieved as seen in Fig. 8. In Fig. 9, a comparison of the reflectivity of the conical tapered chamber and a traditionally implemented chamber is shown for 400 MHz. At this frequency, there is a slight difference on the back wall reflectivity between the chambers (180°) but this is related to the difference in absorber treatment between the chambers. One can notice the large variation in horizontal polarization as the direction changes from 15° to 60° on either side of the source antenna. The reflectivity swings by about 10 dB. These variations are not seen in the conical tapered chamber.

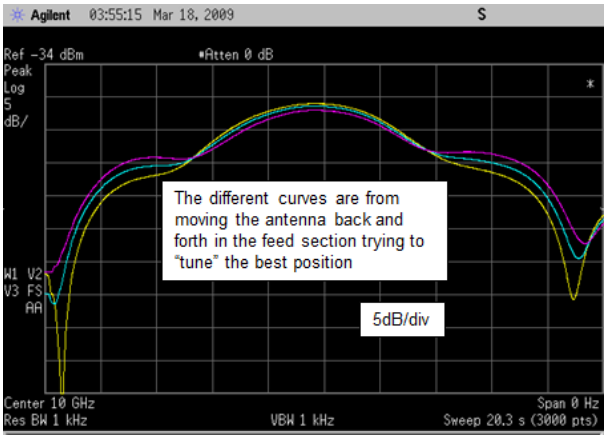

Fig. 8. Data for a transverse scan of a traditional chamber using the same horn used in the conical design.

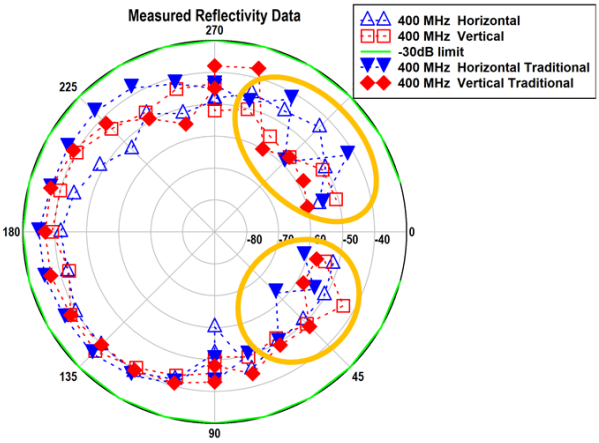

Fig. 9. Comparison with a traditional chamber.

The chamber was implemented with two ranges, a far field tapered range and an NF-FF planar and spherical range. Figure 3 shows the chamber plan with the two ranges. The antenna under test uses the same positioner for both ranges, and the QZ is the same for both ranges. For the spherical range the probe is located between the QZ and the planar scanner on the opposite wall. The planar scanner can be used for testing high gain arrays. These arrays can be positioned at the QZ or closer to the scanner mounted on a tripod depending on the frequency of operation or the size of the scanner.

IV. INCREASING THE QZ SIZE

As mentioned above, the tapered chamber is used to overcome some of the limitations of the standard rectangular chamber for antenna testing at lower frequencies. However, like in rectangular chamber, the size of the quiet zone in a tapered chamber reduces significantly as the frequency increases. For example, the tapered chamber installed at the National University of Singapore (NUS) has a quiet zone of 1.4 m at 500 MHz but only 45 cm at 8 GHz. To increase the quiet zone at the higher frequencies, it was proposed to integrate a customized RF lens inside the chamber. The authors are not aware of other methods to increase the quiet zone without physical alterations to the original chamber.

V. DESIGN OF THE RF LENS

The design of the RF lens is based on the principle of optical refraction to transform a spherical wave from a point source to a planar wave. By precisely controlling the dielectric constant of the lens, the focal length of the lens can be customized based on the lens aperture.

A plano-convex RF lens was designed and integrated into tapered chamber at NUS (see Fig. 10). Its focal length, *f*, of 10 m is equal to the distance between the source antenna and the end of the tapered section of the chamber. The diameter of the lens was chosen to be 2 m in order to cover a large area of the aperture of the tapered chamber while allowing easy mobility of the lens inside the chamber.

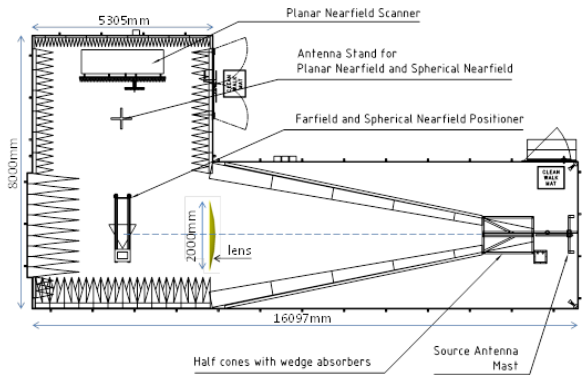

Fig. 10. Placement of lens in tapered chamber.

The lens has a comparatively high ratio of the size of the planar wave front to the lens diameter (a factor of about 0.7 *D*, where *D* is the diameter of the lens). Hence, a 2 m diameter lens can produce a 1.4 m plane wave-front. The profile $P(x,y)$ of the lens was designed using the following equations [8],

$$x = \frac{r}{\tan\theta_m} - \frac{y}{\tan\theta} \quad (1)$$

where

$$y = \rho \sin\theta, \quad (2)$$

and

$$\rho = \frac{f(\sqrt{\varepsilon}-1)}{\sqrt{\varepsilon}\cos\theta - 1}, \quad (3)$$

with

$$h = \frac{r}{\sqrt{\varepsilon}-1}\left(\frac{1}{\sin\theta_m} - \frac{1}{\tan\theta_m}\right). \quad (4)$$

The variables are defined in Fig. 11.

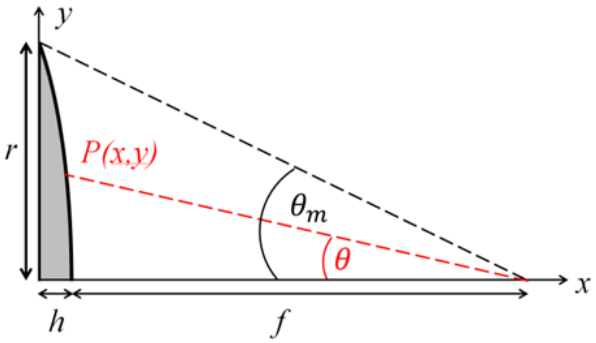

Fig. 11. Lens geometry.

Due to the proposed size of the RF lens (2 m), the lens cannot be manufactured with traditional dielectric materials as it will be difficult to control the dielectric permittivity throughout the lens to a high degree of accuracy. Furthermore, if the lens is manufactured with traditional dielectric material, it will be extremely heavy (≈ 1,000 kg), making it difficult to install and requiring a special support structure, which may cause undesirable diffractions.

To overcome these challenges, a new low-loss, light weight metamaterial manufactured by Matsing Pte Ltd was used. The material allows the control of the dielectric permittivity to a high degree of accuracy. It has extremely low-loss ($\varepsilon'' < 10^{-4}$). It slow density (40 kg/m^3) means that the 2 m lens weighs only 35 kg, allowing the lens to be portable and easily installed. Furthermore, the material is isotropic and broadband, so that the lens is operable for both vertical and horizontal polarizations on a range of frequencies.

VI. NUMERICAL ANALYSIS

The performance of the designed lens was first evaluated using FEKO. A half-wavelength dipole was placed at the focal length of the 2 m lens. The focal length corresponds to the distance (of 10 m) between the feed and aperture of the tapered chamber. The field was observed at a vertical plane at 2 m (corresponding to the quiet zone region) on the other side of the lens. For simplicity, the lens and the dipole were simulated in free-space without the tapered chamber as the primary aim of the simulation was to ensure that for the given length of the taper, the lens would provide the best possible illumination. Including the chamber with its absorbers in the simulation model would drastically increase the problem size and complexity beyond the capability that the numerical package could handle at these high frequencies.

Figure 12 shows the predicted fields (for a quadrant) at 8 GHz. The circles in the plots represent the outline of the 2 m lens. Cuts of the fields along the lens diameter are shown in Figs.13 and 14 for 2 GHz and 8 GHz, respectively. The fields of the dipole in the absence of the lens are superimposed in the figures for reference. For ease of comparison, the magnitudes are normalized to their respective mean values while the phase without the lens is normalized to its peak value and the phase with the lens is normalized to its mean value. From these figures, it is observed that the field with the lens deviates slightly from the dipole field due to mainly diffraction from the lens. However, the lens reduces significantly the large phase variation of the dipole field. Thus, the designed lens was shown to produce a reasonably good plane wave in the vicinity of the quiet zone of the tapered chamber.

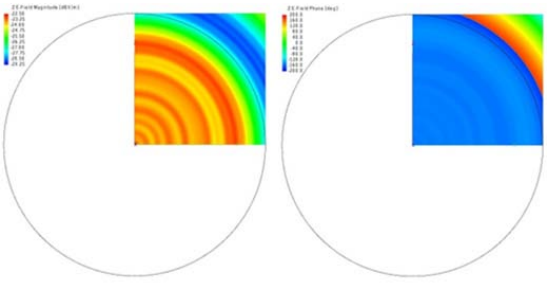

Fig. 12. Predicted field distribution at 8 GHz, both in (a) magnitude and (b) phase.

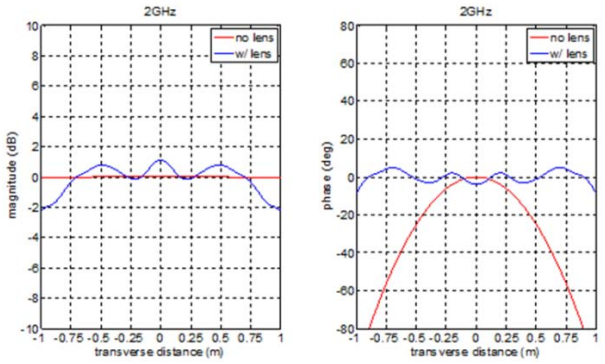

Fig. 13. Computed field distribution at 2 GHz.

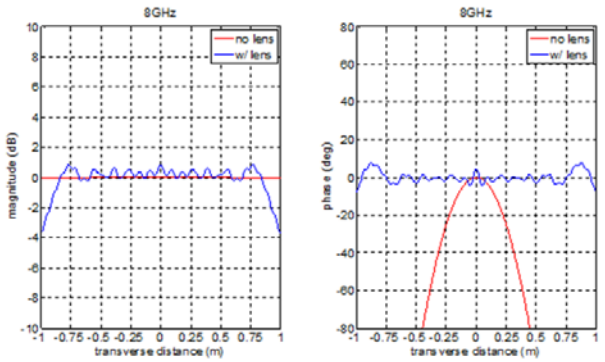

Fig. 14. Computed field distribution at 8 GHz.

VII. MEASURED PERFORMANCE

The manufactured lens is installed at the aperture of the tapered chamber as shown in Fig. 15. A special frame was made from low reflection material to hold and easily place the lens in the tapered chamber.

For the field measurement of the quiet zone of the tapered chamber, a simple linear scanner was set up as shown in Fig. 16. A broadband dual-ridged horn was used as the probe antenna. The field was measured along an axis transverse to the lens axis at about 2 m from the lens. The lens was then removed and the measurement repeated.

The results at 2 GHz and 8 GHz are shown in Figs. 17 and 18, respectively. The magnitudes and phases are "normalized" in the same manner as the numerical results were. Note that the transverse distance in these figures, unlike that of Figs.13 and 14, is relative to the start of the measurement position at 0 m. The plots show that the lens has indeed improved the phase significantly without adversely affecting the amplitude. The size of the quiet zone for ±10° phase variation with and without lens is summarized in Table I. Thus, the

lens has significantly improved the phase performance of the tapered chamber.

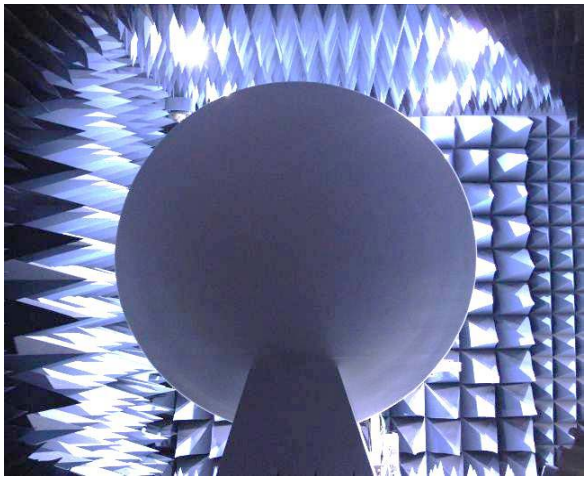

Fig. 15. View of the lens from the source antenna.

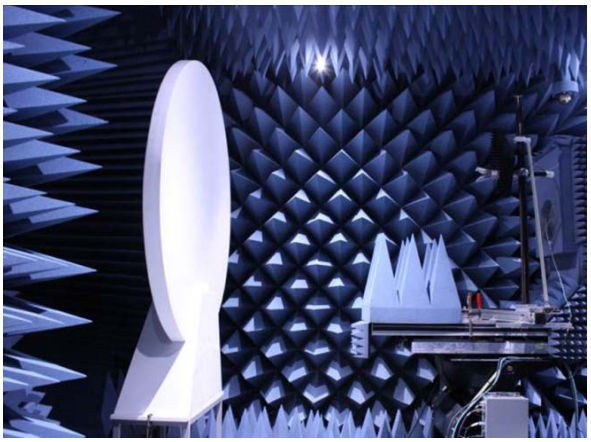

Fig. 16. The QZ scanned with the lens in place at the end of the taper section.

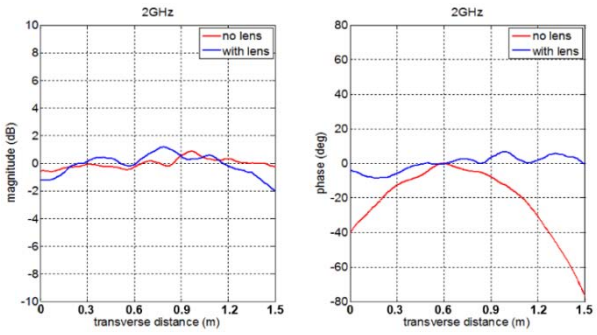

Fig. 17. Measured field distribution at 2 GHz.

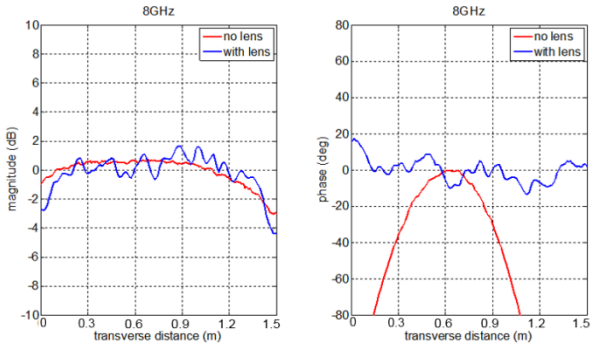

Fig. 18. Measured field distribution at 8 GHz.

Measurements were also done from 500 MHz to 1 GHz to confirm that the lens did not affect the original quiet zone of the chamber at low frequency.

Table I: Size of quiet zone (in cm) for ±10° phase variation with and without lens.

***f* (GHz)**	**2**	**4**	**6**	**8**	**10**
Without lens	95	65	55	45	40
With lens	140	140	140	140	140

VIII. CONCLUSION

The paper has introduced a new approach to the manufacturing of tapered anechoic chambers. This approach has shown that it provides good QZ reflectivity results over wide frequency ranges. Additionally, the new design appears to allow the use of lower directivity antennas than the ones used in traditional chambers. These lower directivity antennas provide a smaller amplitude taper across the QZ, which reduces the errors during gain measurements. With the addition of the RF lens, the phase of the quiet zone of the tapered chamber at higher frequency (2 GHz–10 GHz) has been improved significantly. The lens provides a quick and easy way to enhance the performance of the tapered chamber, allowing the user to easily install it due to its light-weight construction. The NUS tapered chamber with the RF lens is now capable of far-field measurement of relatively large antennas from 0.3 MHz to 10 GHz.

REFERENCES

[1] W. Emerson and H. Sefton “An improved design for indoor ranges,” *Proceedings of the IEEE*, vol. 53, no. 8, pp. 1079-1081, 1965.

[2] H. King, F. Shiukuro, and J. Wong, "Characteristics of a tapered anechoic chamber," *IEEE Trans. Antennas Propagat.*, vol. 15, no. 3, pp. 488-490, 1967.
[3] L. Hemming, *Electromagnetic Anechoic Chambers: A Fundamental Design and Specification Guide*, Wiley-Interscience, John Wiley and Sons and IEEE Press. Piscataway, New Jersey, 2002.
[4] V. Rodriguez, "Using tapered chambers to test antennas," *Evaluation Engineering*, vol. 43, no. 5, pp. 62-68, 2004.
[5] V. Rodriguez and J. Hansen, "Evaluate antenna measurement methods," *Microwaves and RF*, pp. 61-67, Oct. 2010.
[6] R. Hiatt, E. Knott, and T. Senior, "A study of VHF absorbers and anechoic rooms," *Technical Report 5391-1-F*, The University of Michigan, Feb. 1963.
[7] ETS-Lindgren horn; http: //www.ets-lindgren. com /pdf/3164-05.pdf.
[8] J. Kraus and R. Marhefka, *Antennas for All Applications*, 3rd ed., McGraw-Hill, 2001.

Vicente Rodriguez Attended Ole Miss, in Oxford MS, where he obtained his B.S.E.E in 1994, his M.Sc. in 1996 and a Ph.D. in 1999. Dr. Rodriguez joined ETS-Lindgren as an RF and Electromagnetics engineer in 2000. In 2004 Dr. Rodriguez became Senior Principal Antenna Design Engineer, placing him in charge of the development of new antennas. In 2006 Dr. Rodriguez became Antenna Product Manager placing him in charge of development, marketing and maintenance of the antenna product line.

Dr. Rodriguez is the author of more than fifty publications. Dr. Rodriguez holds patents for hybrid absorber and dual ridge horn antennas. Dr. Rodríguez is a Senior Member of the IEEE and several of its technical societies, including the EMC society where he serves as Distinguished Lecturer of the Society for the years 2013 and 2014. He is also a Senior Member of the Antenna Measurements Techniques Association (AMTA). He served as Meeting Coordinator and Vice-President in the board of directors of AMTA. Dr. Rodriguez is an active member of the Applied Computational Electromagnetic Society (ACES). He is an Associate Editor of the ACES Journal and has served as a reviewer for the ACES Journal and for the Journal of Electromagnetic Waves and Applications (JEWA). Dr. Rodriguez currently serves as the Dean Appointee to the School of Engineering Advisory Board at the University of Mississippi. Dr. Rodriguez is a Full member of the Sigma Xi Scientific Research Society and of the Eta Kappa Nu Honor Society.

Serguei Matitsine graduated with honors from the Moscow Institute of Physics and Technology in 1979 and received his PhD in 1982. From 1982-1984 he held the position of senior researcher at the Institute of Radio-Engineering and Electronics of the Russian Academy of Sciences. From 1984 until 1995 he has held several positions including senior researcher, Head of Electromagnetic Laboratory and Deputy Director at the Institute of Theoretical and Applied Electromagnetics of Russian Academy of Sciences.

In 1995 Dr. Matitsine joined the research and development group at Singapore Technologies Aerospace as Technical Director and later holding the position of Chief Engineer. In parallel, since 2001, Dr. Matitsine has also been working at Temasek Laboratories of the National University of Singapore as an Adjunct Senior Principal Research Scientist. He is also the Chairman and Technical Director of MatsingPte Ltd.

His research interests include electromagnetic materials, metamaterials, smart materials, multi-beam antennas, antenna measurement techniques, and most recently, lightweight, large-size RF Lenses. He has more than 60 publications in these areas, including four patents.

Tse-Tong Chia received the B.Eng. with 1st Class Honours in 1986 from the National University of Singapore, Singapore, and the M.Sc. and Ph.D. in 1991 and 1994, respectively, from The Ohio State University, USA. He has been with the DSO National Laboratories, Singapore, since 1986, where he is currently a Distinguished Member of Technical Staff. He was a laboratory head from 1995 till 2010 when he stepped down to focus on research. He is also a Principle Research Scientist in the Temasek Laboratories at the National University of Singapore. His current research interests include computational methods for electromagnetic scattering and installed antenna performance, as well as the use of lenses for antenna applications.

Pavel Lagoiski received his B.S E.E. from the National University of Singapore in 2010. Since then he has held the position of Engineer at Matsing Pte Ltd. His current research interests include antenna measurement system and RF Lenses.

Leo Matytsine received his B.Sc. from the University of Southern California in 2009 and his MBA from the Australian Global School of Management in 2013. He has been with Matsing Pte Ltd since 2009 and currently holds the position of Director. His interests include RF convex lenses and antenna measurement systems.

Michael Matytsine received his B.A from Chapman University in 2006 as well as his MBA from La Verne University in 2010. He has been with Matsing Pte Ltd since 2006 and currently holds the position of Director. His interests include Luneburg and convex RF lenses.

Peng-Khiang Tan received his diploma on Electronic and Computer Engineering from Ngee Ann Polytechnic in 1999 and the Bachelor of Technology in Electronics Engineering (2nd Class Hons) from the National University of Singapore in 2008. He currently works as a laboratory technologist within the Antenna Group at the Temasek Laboratories of the National University of Singapore.

A Model-Based Technique with ℓ_1 Minimization for Defect Detection and RCS Interpolation from Limited Data

Ivan J. LaHaie, Steven M. Cossmann, and Michael A. Blischke

Integrity Applications, Inc. (IAI)
900 Victors Way, Suite 220, Ann Arbor, MI 48108
ilahaie@integrity-apps.com, scossmann@integrity-apps.com, mblischke@integrity-apps.com

Abstract ─ Method of moments (MoM) codes have become increasingly capable and accurate for predicting the radiation and scattering from structures with dimensions up to several tens of wavelengths. In an earlier work, we presented a network model (NM) algorithm that uses a Gauss-Newton iterative nonlinear estimation method in conjunction with a CARLOS-3D™ MoM model to estimate the "as-built" materials parameters of a target from a set of backscatter measurements. In this paper, we demonstrate how the NM algorithm, combined with the basis pursuits (BP) ℓ_1 minimization technique, can be used to locate unknown defects (dents, cracks, etc.) on a target from a limited set of RCS pattern measurements. The advantage of ℓ_1 minimization techniques such as BP is that they are capable of finding sparse solutions to underdetermined problems. As such, they reduce the requirement for a priori information regarding the location of the defects and do not require Nyquist sampling of the input pattern measurements. We will also show how the BP solutions can be used to interpolate RCS pattern data that is undersampled or has gaps.

Index Terms - ℓ_1 minimization, method of moments, RCS measurement.

I. INTRODUCTION

Recently, there has been an interest in the use of computational electromagnetics (CEM) prediction codes to improve the quality, efficiency, and utility of RCS measurements. This is especially true at lower frequencies (electrically small targets) where multiple interactions and narrow bandwidths limit the effectiveness of ISAR imaging for mitigation of measurement errors such as multipath and/or target support contamination or the detection of defects or changes on a target. Furthermore, these CEM-aided measurement techniques have applications beyond those of conventional imaging, including estimating the as-built values of surface impedances, near field-to-far field transformation, and interpolating RCS pattern data that is undersampled or has gaps.

Over the last several years, IAI staff have developed a specific implementation of a CEM-aided measurement technique known as the network model (NM) algorithm [1]. The NM algorithm is a model-based estimation technique that uses a full-wave method of moments (MoM) CEM code to predict the induced currents on the structure and associated radiated/scattered field patterns as part of the estimation process (although it can be extended in principle to other types of rigorous CEM codes). As such, the algorithm includes both single and multiple interactions and is applicable to both convex and concave shaped targets. The NM algorithm has been used in the past to mitigate illumination and multipath errors [2], [3] and to estimate the "as-built" equivalent surface impedance of non-PEC features and/or treatments of a target from a set of backscatter (RCS) measurements [4].

In this paper, which is an expansion of our 2012 AMTA Proceedings paper [5], we apply the NM algorithm to the problem of RF target diagnostics. Specifically, we demonstrate how the NM algorithm, combined with the basis pursuits (BP) ℓ_1 minimization technique, can be used to locate ***unknown*** defects (dents, cracks,

Submitted On: April 6, 2013
Accepted On: Aug. 27, 2013

1054-4887 © 2013 ACES

etc.) on a target from a limited set of RCS pattern measurements. The advantage of ℓ_1 minimization techniques such as BP is that they are capable of finding sparse solutions to underdetermined problems. As such, they reduce the requirement for a priori information regarding the location and/or characteristics of the defects and do not require Nyquist sampling of the input pattern measurements. The fact that NM algorithm does not require specific knowledge or models of the defects makes it more generally applicable than methods where a "library" of one or more defect models is required (see, for example, the method described earlier in this journal [6]). We will also show how the BP solutions can be used to interpolate RCS pattern data that is undersampled or has gaps.

In Section II of this paper, we derive the iterative network model (NM) algorithm and briefly discuss its convergence properties. Section III provides numerical simulations of its performance for a simple canonical RCS shape using the CARLOS-3D™ MoM code [7]. The paper concludes with a summary and list of references in Sections 0 and V, respectively.

II. NETWORK MODEL ALGORITHM FORMULATION

The network model (NM) algorithm is a model-based technique for bringing a method-of-moments (MoM) scattering prediction into agreement with a corresponding set of measurements [1]-[5]. The formulation of the NM algorithm begins with the familiar matrix equation that arises in all MoM prediction codes [8], namely

$$\mathbf{Z}(\boldsymbol{\eta})\mathbf{j} = \mathbf{v}\,, \tag{1}$$

Here, $\mathbf{Z}$ is the target impedance matrix, written explicitly as a function of a vector of target model parameters $\boldsymbol{\eta}$, $\mathbf{j}$ is the vector of coefficients for the basis functions used to represent the induced (electric and magnetic) currents on the target, and $\mathbf{v}$ is the vector of excitation coefficients used to represent the incident field on the target. We will assume throughout that the incident field is a plane wave with a given polarization and direction of incidence (i.e., far-field illumination), but the derivation presented herein can be straightforwardly extended to arbitrary scattering and/or radiation measurements in the near or far field. Note that all of the quantities in Eq. (1) are implicit functions of frequency *f*.

Given the incident field and a model for the target geometry and its associated materials parameters, the MoM code computes $\mathbf{Z}$ and $\mathbf{v}$ and then solves Eq. (1) to find $\mathbf{j}$, viz.

$$\mathbf{j} = \mathbf{Z}^{-1}(\boldsymbol{\eta})\mathbf{v} = \mathbf{Y}(\boldsymbol{\eta})\mathbf{v}\,, \tag{2}$$

where $\mathbf{Y}$ is the MoM admittance matrix for the target.

Now consider a vector of measurements $\mathbf{s}$ and MoM predictions $\mathbf{s}_p$ of the target's far-field (FF) scattering pattern at set of M observation angles and polarizations. The units of $\mathbf{s}$ and $\mathbf{s}_p$ are defined such that the magnitude squared of any element is equal to the FF target RCS. From Eq. (2), the MoM prediction at the m^{th} observation angle and polarization can be written as

$$s_{pm}(\boldsymbol{\eta}) = \mathbf{r}_m^T\mathbf{j} = \mathbf{r}_m^T\mathbf{Y}(\boldsymbol{\eta})\mathbf{v}_m = \mathbf{r}_m^T\mathbf{Z}^{-1}(\boldsymbol{\eta})\mathbf{v}_m\,, \tag{3}$$

where $\mathbf{r}_m$ is a (known) radiation vector relating the induced current to the far-field scattering pattern, and T denotes the matrix transpose. In general, this is not the same as the m^{th} measurement s_m, even under error-free measurement conditions. This is because the MoM model for the target is never perfect. To that end, the vector $\boldsymbol{\eta}$ corresponds to a set of N parameters that are chosen to represent the sources of the differences between the target measurements and its MoM model predictions. For obvious reasons, we will refer to these as Z-parameters.

In its most general form, the network model seeks to estimate a set of N Z-parameters $\boldsymbol{\eta}$ that brings the MoM scattering predictions $\mathbf{s}_p$ into satisfactory agreement with the scattering measurements $\mathbf{s}$:

$$s_m \approx s_{pm}(\boldsymbol{\eta}) = \mathbf{r}_m^T\mathbf{Z}^{-1}(\boldsymbol{\eta})\mathbf{v}_m, \quad m = 1, \ldots, M\,, \tag{4}$$

subject to constraints on the allowable solutions $\boldsymbol{\eta}$. This is a (constrained) nonlinear system of M equations and N unknowns.

Inasmuch as it is reasonable to assume the initial MoM predictions are not grossly in error, a solution to Eq. (1) can be found using one of many standard gradient-based iterative techniques. In particular, we use a modified Gauss-Newton method, wherein at the k^{th} iteration, Eq. (1) is expanded in a first-order Taylor series about the current values $\boldsymbol{\eta}_{(k)}$ of the Z-parameters;

$$\mathbf{s} \approx \mathbf{s}_{p(k)} + \mathbf{G}_{(k)}\Delta\boldsymbol{\eta}_{(k)}\,, \tag{5}$$

where $\mathbf{s}_{p(k)} = \mathbf{s}_p\left(\boldsymbol{\eta}_{(k)}\right)$ are the current values of the MoM scattering predictions, and $\mathbf{G}_{(k)}$ is the Jacobian matrix whose elements are given by

$$G_{mn(k)} = \left.\frac{\partial s_{pm}}{\partial \eta_n}\right|_{\boldsymbol{\eta}=\boldsymbol{\eta}_{(k)}} = -\mathbf{r}_m^T\mathbf{Y}\left(\boldsymbol{\eta}_{(k)}\right)\mathbf{Q}_n\left(\boldsymbol{\eta}_{(k)}\right)\mathbf{Y}\left(\boldsymbol{\eta}_{(k)}\right)\mathbf{v}_m\,, \tag{6}$$

with

$$\mathbf{Q}_n(\boldsymbol{\eta}) = \frac{\partial \mathbf{Z}(\boldsymbol{\eta})}{\partial \eta_n}\,. \tag{7}$$

A solution $\Delta\boldsymbol{\eta}_{(k)}$ is then found that satisfies the linear system of equations (5) to within some acceptable value in a least squares sense, viz.

$$\left\|\Delta\mathbf{s}_{(k)} - \mathbf{G}_{(k)}\Delta\boldsymbol{\eta}_{(k)}\right\|_2 < \varepsilon_{(k)}\,, \tag{8}$$

subject to the constraints on the allowable solutions, where $\Delta\mathbf{s}_{(k)} = \mathbf{s} - \mathbf{s}_{p(k)}$. This is used to update the MoM model Z-parameters according to

$$\boldsymbol{\eta}_{(k+1)} = \mathsf{P}_C\left(\boldsymbol{\eta}_{(k)} + \beta\Delta\boldsymbol{\eta}_{(k)}\right), \tag{9}$$

where $0 < \beta \leq 1$ to control the step size of the update and P_C is a projection onto any constraints. The process is then repeated until acceptable agreement between the measurements $\mathbf{s}$ and predictions $\mathbf{s}_p$ is achieved.

In general, the performance of the NM algorithm will depend on the number of unknown Z-parameters N relative to the number of independent measurements M. This is evident in the fact that linear system in Eq. (5) consists of M equations and N unknowns. Historically, model-based estimation algorithms require $M > N$ for good performance, because in that case the resulting system of equations is well-posed and stable and can be solved using standard (e.g., least squares) techniques. Unfortunately, in many applications, the number of measurements M is either limited or we seek to reduce it. Similarly, in order to ensure that the NM algorithm is robust with respect to the how the "as-built" measured target and its numerical model differ, we want to work in situations where the number of Z-parameters N is large. This is because we don't want to assume that we know *a priori* where the discrepancies between the model and the target lie. It is therefore very likely that we will be faced with an underdetermined problem ($M < N$) whose solution is not just ill-posed, but in fact non-unique. In this case, it is necessary to impose constraints and/or conditions upon the allowable solution in order to stabilize ("regularize") the linear system solver.

Two common regularization methods involve minimizing, or at least bounding, the ℓ_2 or ℓ_1 norms of the solution. Each results in a solution with very different characteristics. For the underdetermined problem, ℓ_2 minimization solvers produce solutions that tend to be "spread out" across all of the unknowns. Conversely, ℓ_1 minimization solvers (such as BP) produce "sparse" updates where a smaller fraction of the unknowns are significant.

It follows that for the purposes of locating defects (cracks, gaps, dents, bumps) on a target, an ℓ_1 minimization solver may be the better choice because while the locations of the defects aren't known, it is likely that there will be a relatively small number of them. (Of course, it is always good to incorporate a priori information about possible defect locations if available in order to keep the number of Z-parameters required to model them at a minimum.) ℓ_1 minimization is also more likely to provide a more compact (better resolved) estimate of the defects' location, thereby helping to overcome the limited resolution typical of low frequency measurements.

We chose the MATLAB code SPGL1 [9] as the ℓ_1 minimization linear system solver for the NM algorithm. This code achieves ℓ_1 minimization by solving the basis pursuits (BP) denoising problem, which is characterized as

$$\min_{\Delta\boldsymbol{\eta}} \left\|\Delta\boldsymbol{\eta}\right\|_1 \quad s.t. \quad \left\|\Delta\mathbf{s} - \mathbf{G}\Delta\boldsymbol{\eta}\right\|_2 < \varepsilon\,, \tag{10}$$

where ε is the desired accuracy of the linear solution at each Gauss-Newton iteration (see Eq. (1)). In order to accomplish this, the SPGL1 code uses a recasting of Eq. (10) known as the LASSO problem, which is defined as

$$\min_{\Delta\boldsymbol{\eta}} \left\|\Delta\mathbf{s} - \mathbf{G}\Delta\boldsymbol{\eta}\right\|_2 \quad s.t. \quad \left\|\Delta\boldsymbol{\eta}\right\|_1 < \tau\,. \tag{11}$$

SPGL1 begins with a small τ (typically zero), and with repeated iterations determines a $\Delta\boldsymbol{\eta}$ which satisfies Eq. (11). If this solution does not satisfy Eq. (10), τ is increased and the iterations are repeated.

Note that these BP iterations form an inner loop inside the NM Gauss-Newton iterations. In the current NM implementation of the SPGLI

code, the BP loop is stopped at the current value of τ when Eq. (11) is satisfied without having to refine the value of $\Delta\boldsymbol{\eta}$.

III. NETWORK MODEL SIMULATIONS

Numerical simulations of the NM algorithm defect detection performance were conducted using the EMCC version of the CARLOS-3D™ MoM code [7]. The code was modified to provide the matrices and vectors required to implement the NM algorithm Gauss-Newton iterations.

The structure used in the simulations was a 20" version of the PEC NASA almond target [10]. Two versions of the almond were created: a pristine "showroom" version with no defects which was used as the initial model for the MoM predictions, and an "slightly used" version with four defects that was used as the source of the "measured" data. Two of the defects (bump and edge dent) were relatively small and the other two (gouge and large dent) were relatively large. Fig. 1 and Fig. 2 show the meshes used in the MoM simulations of the two versions of the almond.

Far-field backscatter data for both versions of the almond were generated using the CARLOS-3D™ code for all three polarizations ($\theta\theta$, $\phi\phi$, and $\theta\phi = \phi\theta$) along five 360° azimuth cuts in 1° increments about the almond at frequencies of 3, 3.5, 3.7, and 4 GHz. The cuts were at elevations ranging from $\theta = -20°$ to +20° in 10° increments, where 0° elevation is defined as the plane of symmetry intersecting the side of the almond.

Data from three of the "slightly used" almond target azimuth cuts ($\theta = -20°$, 0°, +20°) were provided to the NM as the "measured" data $\mathbf{s}$. The corresponding cuts for the "showroom" target were provided to the NM as the predicted data $\mathbf{s}_p$.

In order to model the defects without having to perturb the shape of the "showroom" almond target, each of its facets was allowed to have unknown impenetrable complex-valued surface impedance. These impedance values comprised a total of $N = 8000$ unknown Z-parameters $\boldsymbol{\eta}$ which the NM estimated in order to bring the MoM predictions into agreement with the measurements. While only an approximation to the true defects, this choice of Z-parameters allowed the derivatives $\mathbf{Q}$ in Eq. (7) to be computed efficiently and in closed form. The initial values of the Z-parameter facet impedances for the "showroom" target were taken to be zero Ohms/square (PEC).

The NM impedance estimates were used then to locate the defects and predict the backscatter data at the other two elevations ($\theta = -10°$, +10°).

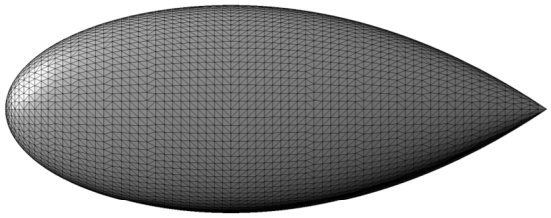

Fig. 1. MoM mesh for the "showroom" version of the 20" almond target (no defects).

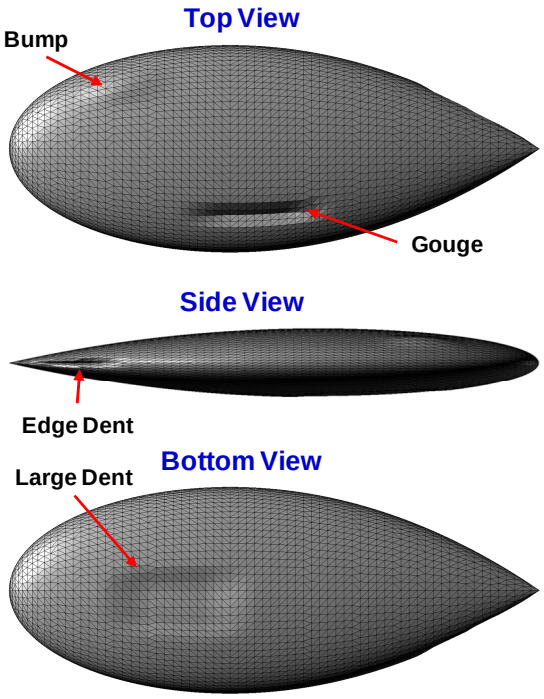

Fig. 2. MoM mesh for the "slightly used" version of the 20" almond target showing the four defects.

A. Single Frequency Defect Detection

Fig. 3 shows the absolute value of the estimated surface impedances found by the NM algorithm using the SPGL1 ℓ_1 minimization linear system solver using "measured" data at only a single frequency (4 GHz). The total number of independent measurements (based on Nyquist) for this case was $M = 255$. The estimates that differ substantially from zero (PEC) show a good correlation with the defect locations for the two

small defects (bump and edge dent). For the large dent defect, the NM estimates tend to correlate with its boundary rather than the entire extent of the defect. Finally, for the gouge defect, the non-zero NM impedance estimates correlate well with the defect location, but there are also a pair of additional "false alarm" artifacts adjacent to the gouge defect. These are likely due to the fact that we are using a surface impedance to approximate the defect, combined with using only single frequency data for the estimates.

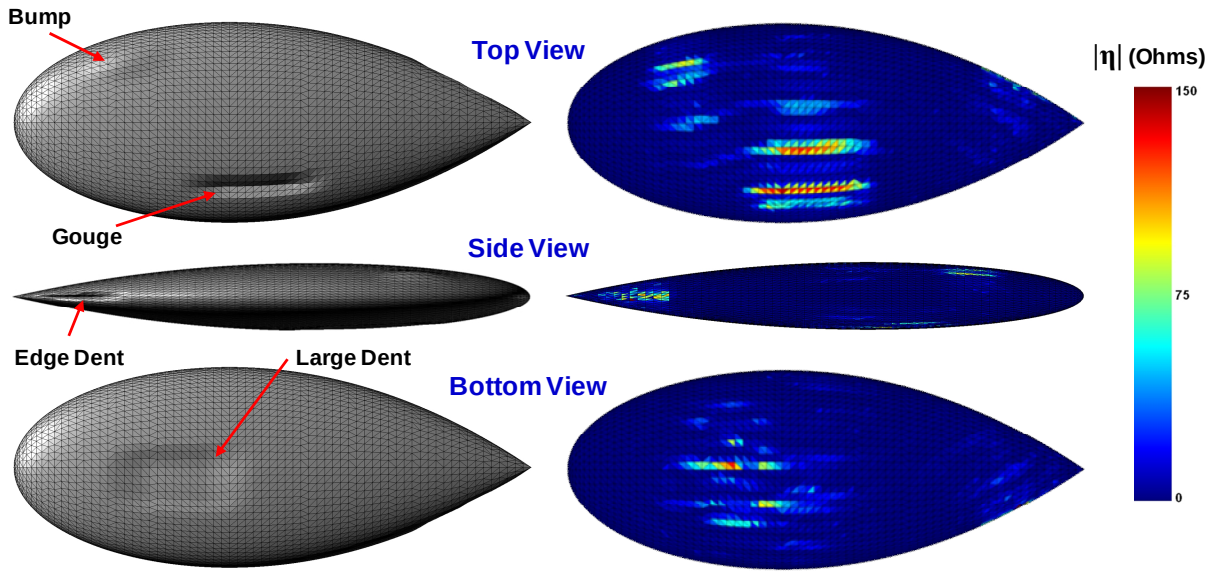

Fig. 3. Defects on the "slightly used" version of the almond target (left) compared to the BP single-frequency NM estimates of the facet surface impedances on the "showroom" version of the target (right).

Fig. 4 compares the NM estimates of the facet surface impedances obtained using the BP ℓ_1 minimization linear system solver to those obtained using a more traditional ℓ_2 minimization linear system solver, namely singular value decomposition (SVD). The estimates from each solver have been normalized to their respective peak values in order to better compare the two results. The figure clearly shows how ℓ_1 minimization results in a more sparse and localized estimate of the defect locations. It is worth noting the in both cases, the estimated impedances were almost purely reactive. This is not surprising because the defects do not contain any ohmic losses.

B. Multiple Frequency Defect Detection

In an attempt to reduce the "false alarm" artifacts in the NM impedance estimates, the results in Section III.A were repeated using the "measured" data at the other three frequencies (3.0, 3.5, and 3.7 GHz). The impedance estimates for all four frequencies were then averaged. The idea is that the false alarm artifacts will be uncorrelated with one another with sufficiently large changes in frequency.

Fig. 5 shows the absolute value of the averaged impedance estimates obtained from both the BP and SVD solvers. The results for each are shown on a scale that is normalized to the peak value of their respective averaged impedances. When compared to the 4 GHz single frequency estimates in Fig. 4, the results in Fig. 5 show that averaging the impedance estimates from multiple frequencies has reduced some of the artifacts, particularly for the SVD solver. That said, there remains a single, relatively large "false alarm" artifact associated with the gouge defect. In addition, frequency averaging does not appear to have substantially improved the detection of the large dent defect. It may be possible to improve the false alarm rejection by combining the multiple frequency results through some other method than averaging, such as M-out-of-N detection. Even better performance is potentially achievable by using all the frequencies jointly in the impedance estimation process.

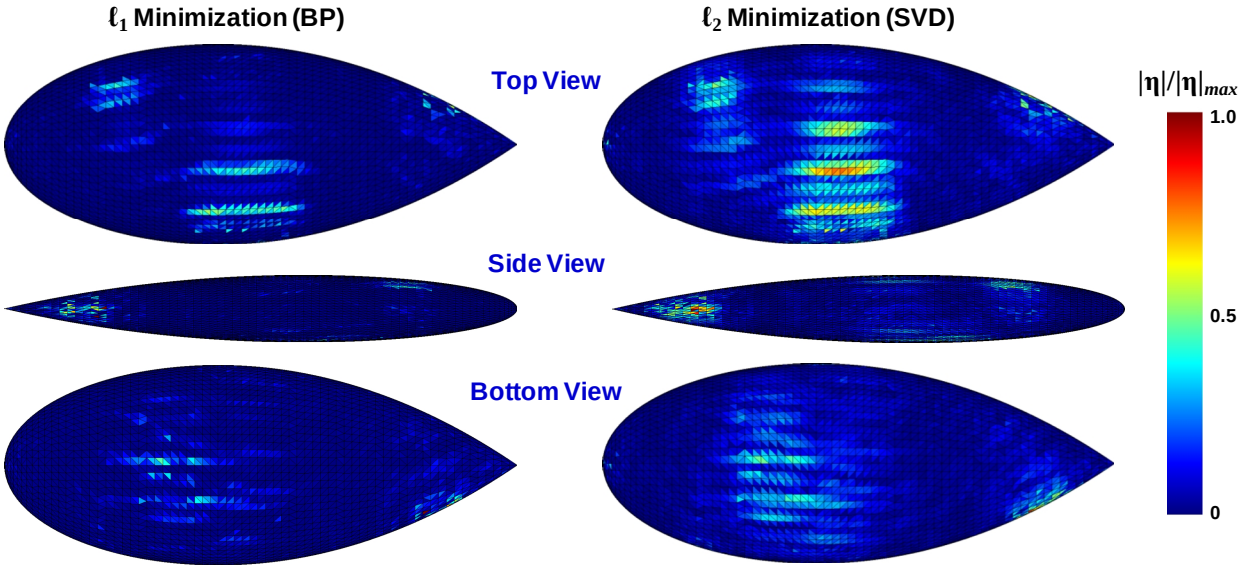

Fig. 4. Comparison of the BP (left) and SVD (right) single-frequency NM estimates of the facet surface impedances on the "showroom" version of the almond target. (Note that the images of the SVD results have been corrected from the original versions our AMTA paper [5].)

Fig. 5. Comparison of the BP (left) and SVD (right) frequency-averaged NM estimates of the facet surface impedances on the "showroom" version of the almond target.

C. Missing Data Interpolation

The single-frequency (4 GHz) NM impedance estimates were used to predict the RCS cuts of the "slightly used" target at the three "measured" and at two "unmeasured" elevation cuts. Plots of the mean RCS of the initial and final NM prediction error versus elevation angle for each of the five azimuth cuts are shown in Fig. 6, with the results from BP on the left and from SVD on the right. The prediction error is defined as the coherent difference between the "measured" data for the "slightly used" target and the MoM predictions for the "showroom" target.

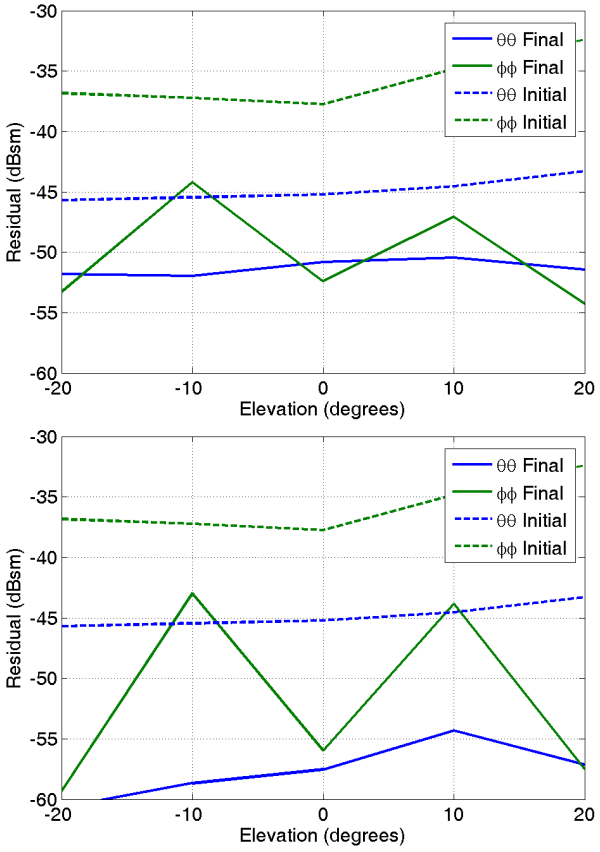

Fig. 6. Mean RCS versus elevation angle of the initial (dashed) and final (solid) NM prediction error obtained using the single-frequency (4 GHz) BP (top) and SVD (bottom) impedance estimates.

The plots show that the NM with BP solver has reduced the prediction error by 5-7 dB for θθ polarization and 15-20 dB for φφ polarization over the three azimuth cuts (θ = −20°, 0°, +20°) used to estimate the surface impedances. The corresponding reductions using the SVD solver are greater (10-15 dB for θθ polarization and 20-25 dB for φφ polarization). When one considers the two azimuth cuts (θ = −10°, +10°) that the were not part of the original "measured" data, the reductions are roughly the same as the measured cuts in θθ polarization over for both solvers. On the other hand, the reductions are less in φφ polarization, with BP performing 1-3 dB better than SVD.

IV. CONCLUSION

We have demonstrated the application of the iterative network model algorithm, combined with the basis pursuits (BP) ℓ_1 minimization technique, to the problem of locating unknown defects (dents, cracks, etc.) on a target from a limited set of RCS pattern measurements. The defects were modeled using an effective surface impedance. Numerical simulations of the NM algorithm performance were presented for the NASA almond target using the CARLOS-3D™ MoM code. The results showed that the use of a BP ℓ_1 minimization solver did a significantly better job of locating defects on the target relative to the more conventional ℓ_2 minimization (SVD) solver using data at a single frequency, although some artifacts were still present in the latter. Averaging the results from multiple frequencies further reduced the artifacts for both solvers. The results also showed that the estimated surface impedances could be used to accurately predict the target RCS at angles that were not part of the measured data.

As mentioned earlier, the approach described herein can be easily extended to include both near field and far field target measurements, so long as the near target illumination is known and can be modeled in the MoM code. An efficient technique for incorporating the illumination from an arbitrary antenna in MoM predictions is described in [11].

In future work, we plan on developing a parametric model for the frequency dependence of the defects that would allow us to use multiple frequencies jointly in the NM Gauss-Newton estimation algorithm. We expect this approach to work better for reducing false alarm artifacts relative to averaging the estimates obtain from applying the NM to each frequency individually.

V. REFERENCES

[1] J. F. Stach, "Numerical methods for measurement error mitigation," *Ant. Meas. Tech. Assoc. (AMTA) Proc.*, Williamsburg, VA, pp. 178-181, 1995.

[2] J. F. Stach, I. J. LaHaie, and E. I. LeBaron, "Multipath mitigation in compact RCS ranges using the network model and 2-D PML spectral estimation technique," *URSI North American Radio Science Meeting Dig.*, Montreal, CA, p. 731, 1997.

[3] J. F. Stach and J.W. Burns, "Mitigation of target illumination and multipath errors in ground plane RCS measurements," *Ant. Meas. Tech. Assoc. (AMTA) Proc.*, Montreal, Canada, pp. 67-71, 1998.

[4] C. M. Coleman, D. C. Love, M. A. Blischke, and I. J. LaHaie, "A technique for materials characterization from backscatter measurements," *Ant. Meas. Tech. Assoc. (AMTA) Proc.*, St. Louis, MO, pp. 116-121, 2007.

[5] I. J. LaHaie, S. M. Cossmann, and M. A. Blischke, "A model-based technique with ℓ_1 minimization for defect detection and RCS interpolation from limited data," *Ant. Meas. Tech. Assoc. (AMTA) Proc.*, Seattle, WA, pp. 139-144, 2012.

[6] F. Deek, M. El-Shenawee, "Microwave detection of cracks in buried pipes using the complex frequency technique," *Applied Computational Electromagnetics Society (ACES) Journal*, Vol. 25, No. 10, pp. 894-902, 2010.

[7] J. N. Putman and M. B. Gedera, "CARLOS-3D™: A general purpose three-dimensional method-of-moments scattering code," *IEEE Ant. Prop. Mag.*, Vol. 35, No. 2, pp. 69-71, 1993.

[8] R. F. Harrington, *Field Computations by Moment Methods*, Wiley-IEEE Press, New York, 1993.

[9] E. van den Berg and M. P. Friedlander, "Probing the Pareto frontier for basis pursuit solutions," *SIAM J on Scientific Computing*, Vol. 31, 0.2, pp. 890-912, 2008.

[10] A. C. Woo, et al., "Benchmark radar targets for the validation of computational electromagnetics programs," *IEEE Ant. Prop. Mag.*, Vol. 35, No. 1, pp. 84-89, 1993.

[11] I. J. LaHaie and M.A. Blischke, "Efficient Method for Representing Antenna Pattern Illumination in Method of Moments (MoM) Radar Cross-Section (RCS) Predictions," *Ant. Meas. Tech. Assoc. (AMTA) Proc.*, Denver, CO, pp. 41-45, 2011.

Ivan J. LaHaie received his BS degree in electrical engineering from Michigan State University in 1976, and his MS and Ph. D. degrees, also in electrical engineering, from the University of Michigan in 1977 and 1981, respectively. He joined the Environmental Research Institute of Michigan (ERIM) in 1980 and worked there for 30 years during its various incarnations as ERIM International, Veridian Systems, and General Dynamics Advanced Information Systems. He joined Integrity Applications Incorporated (IAI) in 2010, where he is currently a Principal Scientist in the Sensors and Analysis Sector. Dr. LaHaie's interests lie in the application of electromagnetics, inverse scattering, and signal processing techniques to problems in synthetic aperture radar (SAR) systems and phenomenology, unconventional RF and optical imaging, and radar cross-section (RCS) modeling, analysis, and measurements. Dr. LaHaie is a fellow of the Antenna Measurement Techniques Association (AMTA), a senior member of the Institute of Electrical and Electronics Engineers (IEEE), and a member of the Optical Society of America. He received the IEEE Aerospace and Electronic Systems Society Radar Systems Panel Award in 1991 and the AMTA Distinguished Achievement award in 2004.

Steven M. Cossmann received his BS and MS degrees in electrical engineering from Michigan State University in 2004 and 2006, respectively. He began working at General Dynamics Advanced Information Systems in 2006, and then moved to Integrity Applications Incorporated (IAI) in 2011, where he is currently a Systems Engineer in the Analytic Services Division. His primary interests are in applied and computational electromagnetics, radar cross-section (RCS) modeling and analysis, and inverse scattering.

Michael A. Blischke received his BS, MS, and Ph.D. in Electrical Engineering from Michigan State University in 1985, 1987, and 1989 respectively. He previously worked for Lockheed (later Lockheed Martin) beginning in 1989, and for ERIM International (later Veridian Systems, then General Dynamics Advanced Information Systems) beginning in 1998. He joined Integrity Applications Incorporated (IAI) in 2010, where he currently works performing design, analysis, and optimization in electromagnetics.

A Statistical Assessment of the Performance of FSV

G. Zhang[1], H. Sasse[2], L. Wang[1], and A. Duffy[2]

[1] School of Electrical Engineering and Automation
Harbin Institute of Technology, Harbin, 150001, China
zhang_hit@hit.edu.cn, wlx@hit.edu.cn

[2] School of Engineering
De Montfort University, Leicester, LE1 9BH, UK
hgs@dmu.ac.uk, apd@dmu.ac.uk

Abstract ─ This paper assesses the performance of the feature selective validation (FSV) method by applying probability density functions to the FSV point-by-point analysis. As an augmentation to confidence histograms, probability density functions offer two advantages: they (1) provide the users of FSV with more subtle information about the quality of the data comparison and (2) make a statistical analysis of the FSV results available. The application of probability density functions in the verification of FSV is presented in this paper, which provides a quantitative measure to support the qualitative conclusions drawn in early publications on the FSV method used as a foundation for IEEE Std. 1597.1.

Index Terms ─ Computational electromagnetics, EMC, feature selective validation, FSV, and statistical validity.

I. INTRODUCTION

With the publication of IEEE standard 1597.1 "standard for validation of computational electromagnetics computer modeling and simulation" [1], the feature selective validation (FSV) method has become a *de jure* standard for validation of electromagnetic simulation, particularly focusing on EMC. However, as the technique becomes more widely used [3-6], the need for certain enhancements becomes more apparent. In particular, the original formulation used six 'natural language' categories into which the FSV data was binned in order to help the interpretation between purely numerical results and the qualitative approach used by many practitioners. Unfortunately, this histogram approach only provides a coarse level of meta-representation and this lacks sufficient discrimination for more subtle usage, for example when comparing numerical modeling output as part of an optimization exercise. Continuous probability density functions (PDFs) offer the potential for greater precision in analysis over confidence histograms and this was demonstrated in a recent paper [2] but with only little detail. This paper addresses the issues that led to the development of the PDF approach, its implementation and interpretation and provides a more detailed investigation into the use of PDFs in the analysis of FSV comparisons, providing, for the first time a measure to verify the performance of FSV against one of the key design objectives, namely, to perform comparisons in the manner of a group of experts [7].

II. THE FSV METHOD

A. The FSV method

The FSV method was developed to validate electromagnetic models by quantifying the agreement between the reference and the numerical results. The details of this method can be found in [7] and [8]. In the FSV method, datasets under comparison are decomposed into DC, low- and high-frequency components first by use of the Fourier transform. Then three figures of merit are obtained to demonstrate data agreement from

Submitted On: June 26, 2013
Accepted On: Jan. 19, 2014

1054-4887 © 2013 ACES

different perspectives based on these components. The amplitude difference measure (ADM) shows the 'trend' difference, while the feature difference measure (FDM) quantifies the differences of fine details. Then the ADM and FDM are combined to give the global difference measure (GDM). These figures of merit can be further represented in three different ways: point-by-point results (ADMi, FDMi, and GDMi), single value results (ADMtot, FDMtot, and GDMtot), which are obtained by taking the mean of each point-by-point result, and confidence histograms (ADMc, FDMc, and GDMc), which are discussed below.

B. Natural language descriptors and confidence histograms

A very practical characteristic of FSV is that it provides quantitative and qualitative results depicted by six natural language descriptors (excellent, very good, good, fair, poor, and very poor). Table I outlines the relationship between quantitative results and these descriptors. The aforementioned confidence histogram is presented by counting the proportions of the point-by-point results that fall into the six categories (N.B., the process of linearization is discussed in section III).

Table I: FSV interpretation scale [1].

FSV value (quantitative)	FSV interpretation (qualitative)
Less than 0.1	Excellent
Between 0.1 and 0.2	Very Good
Between 0.2 and 0.4	Good
Between 0.4 and 0.8	Fair
Between 0.8 and 1.6	Poor
Greater than 1.6	Very Poor

However, the coarse categorization can mask some subtleties in the distribution of the FSV results. Figure 1 shows some typical results to be compared (for the sake of space, the confidence histogram for the GDM is presented in Fig. 3). Figure 2 shows histograms based on the distribution of the GDMi values of datasets given in Fig. 1 [8]. The first histogram, based on 6 bins, used in FSV as the standard GDMc, suggests only 1 local maximum (mode) at a GDM value of 0.45. While for the second histogram, with 30 bins, more local maxima (around GDM values of 0.3, 0.4, and 0.5) are revealed. So it is necessary to find an alternative indicator to show this information. Further, the histograms show their limitations when confronted with multiple comparisons. Specifically, we lack flexible tools in the cross-comparison of multiple histograms.

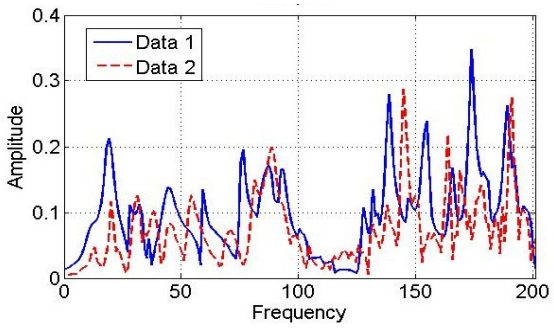

Fig. 1. Data sets for comparison [8].

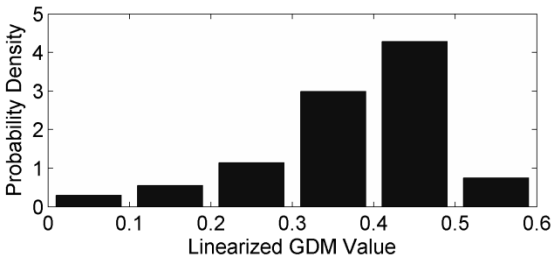

(a)

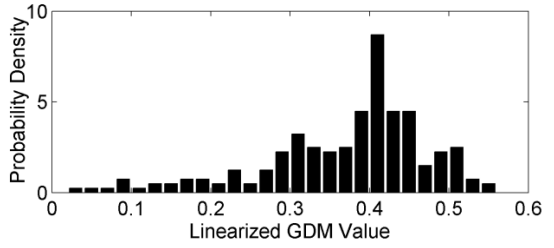

(b)

Fig. 2. Histogram of linearized GDMi value based on (a) 6 bins and (b) 30 bins.

III. EXTRACTING PROBABILITY DENSITY FUNCTIONS FROM FSV DATA

To solve the problems of histograms discussed in section II, a PDF, derived from the point-by-point data, is introduced to show the distribution of values in a more general way. As a result, the FSV distribution functions open up opportunities to apply statistical methods to the FSV results, giving rise to potentially revealing meta-analyses.

A. Method

The PDF is estimated based on a normal kernel function [9]. It is known that a probability density function $f(x)$ can be written as,

$$f(x) \equiv \frac{d}{dx}F(x) \equiv \lim_{h\to 0}\frac{F(x+h)-F(x-h)}{2h} \quad (1)$$

where $F(x)$ is the cumulative distribution function of the random variable x, and h is the "bandwidth". For a random sample of size n from the density f, X: $\{x_1, x_2, \ldots, x_n\}$, its empirical cumulative distribution function (ECDF) has the form,

$$\hat{F}(x) \equiv \frac{N\{X \le x\}}{n} \quad (2)$$

where $N\{X \le x\}$ represents the number of elements less than or equal to x in X. Then the form in equation (1) becomes

$$\hat{f}(x) = \frac{N\{x-h < X \le x+h\}}{2nh}, \quad (3)$$

which can also be rewritten as,

$$\hat{f}(x) = \frac{1}{nh}\sum_{i=1}^{n} K\left(\frac{x-x_i}{h}\right) \quad (4)$$

where

$$K(u) = \begin{cases} \frac{1}{2}, & -1<u<1, \\ 0, & \text{otherwise.} \end{cases}$$

The form in equation (4) is that of a Kernel density estimator with uniform Kernel function, K. The choice of Kernel bandwidth h controls the smoothness of the probability density curve, the detail of which can be found in [9]. To obtain smoother PDFs, a Gaussian Kernel function is adopted in this paper,

$$K_{\text{Gaussian}}(u) = \begin{cases} (1/\sqrt{2\pi})\exp(-u^2/2), & -1<u<1, \\ 0, & \text{otherwise.} \end{cases} \quad (5)$$

Due to the non-linear relationship between the quantitative results and the qualitative description in Table I, we need to pre-process the point-by-point results according to Table II, thereby reflecting the qualitative information linearly in PDFs.

B. Statistical analysis

By introducing PDFs, it becomes possible to analyze FSV results using statistics, which is familiar to most engineers. Generally, statistical moments can be applied to a single PDF result. The second moment, variance, provides information on the dispersion of a set of data. The third moment, Skewness, gives a measure of the symmetry of the shape of a distribution. The fourth moment, Kurtosis, is a measure of the flatness, or peakedness, of a distribution,

$$\text{Variance}=\sigma^2=\frac{1}{N}\sum_{i=1}^{N}(GDM(i)-\mu)^2 \quad (6)$$

$$\text{Skewness}=\frac{1}{N}\sum_{i=1}^{N}\frac{(GDM(i)-\mu)^3}{\sigma^3}, \quad (7)$$

$$\text{Kurtosis}=\frac{1}{N}\sum_{i=1}^{N}\frac{(GDM(i)-\mu)^4}{\sigma^4}, \quad (8)$$

where GDM(i) is the point-wise value of the FSV result (note that this also applies to the ADM(i) and FSM(i) results but only GDM(i) is shown because of space limitations). N is the number of points in the GDM, while μ and σ are the mean and standard deviation of GDM, respectively.

Table II: Piecewise linear conversion.

FSV value (point-by-point)	Linearized Value	FSV interpretation
X≤0.1	X	Excellent
0.1＜X≤0.2	X	Very Good
0.2＜X≤0.4	0.2+(X-0.2)/2	Good
0.4＜X≤0.8	0.3+(X-0.4)/4	Fair
0.8＜X≤1.6	0.4+(X-0.8)/8	Poor
1.6＜X≤3.2	0.5+(X-1.6)/16	Very Poor
X＞3.2	0.6	

For multiple comparisons, which is a strong motivation for the introduction of PDFs, statistical tests can provide widely recognized analysis methods. The Kolmogorov-Smirnov test (KS-test) [10] is used here for the following reasons: the KS-test is a non-parametric test, so it has the advantage of making no assumption on the distribution of data (important to ensure the generality of FSV); additionally, the KS-test is a robust test whose result is not affected by scale changing like the aforementioned linearizing procedure.

The KS-test aims to determine if the distributions of two datasets differ significantly. The null hypothesis is that the two datasets are from the same distribution. The alternative hypothesis is that they are from different distributions. The null hypothesis would be

rejected if the test statistic, D, is greater than the critical value decided by significance level. The statistic D is determined by the maximum vertical deviation between the two curves of the cumulative distribution functions (CDFs) of the datasets,

$$D = \max\left(\left|CDF_1(x) - CDF_2(x)\right|\right) \quad (9)$$

where $CDF_1(x)$ is the proportion of values less than or equal to x in the first data set and $CDF_2(x)$ is the proportion of values less than or equal to x in the second data set.

The critical value of statistic D [11] for different significance level can be decided by,

$$D_{Critical} = k \cdot \sqrt{\left(N_1 + N_2\right) / \left(N_1 \cdot N_2\right)} \quad (10)$$

where N_1 and N_2 is the length of datasets being compared. The value of k can be obtained from tables [11]. For 95 % confidence, k is 1.36, for 90 % confidence, k is 1.22.

IV. FSV PERFORMANCE VERIFICATION

A. Method

When FSV was introduced in [7] and [8], its validation was performed by comparing the confidence histograms of a survey of experts and FSV predictions. Figure 3 shows confidence histograms comparison of data sets shown in Fig. 1. By use of PDFs, the comparison can be shown in a more analytical way. Further, the discrepancy between them can be quantitatively represented by the result of the KS-test.

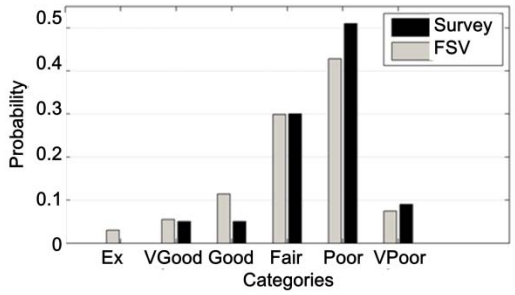

Fig. 3. Comparison of confidence histograms.

Due to the piecewise linear conversion of FSV results in Table II, the PDF results of visual assessment are calculated by transforming the qualitative results of FSV survey to typical quantitative values according to Table III. The survey results come from [8] with 50 experts surveyed.

Figures 4 and 5 outline the comparison of PDFs and CDFs between FSV prediction and visual assessment of data sets shown in Fig. 1, respectively. The single D value, 0.15, in Fig. 5 indicates the 'accuracy' of FSV when comparing the data sets in Fig. 1. According to the algorithm in equation (10), the $D_{Critical}$ for 90 % confidence is 0.17 with $N_1 = N_2 = 100$. In this case, the null hypothesis is accepted.

Table III: Typical values of FSV categories (mid-points in the linearized categories).

FSV Categories	Typical Values
Excellent	0.05
Very Good	0.15
Good	0.25
Fair	0.35
Poor	0.45
Very Poor	0.55

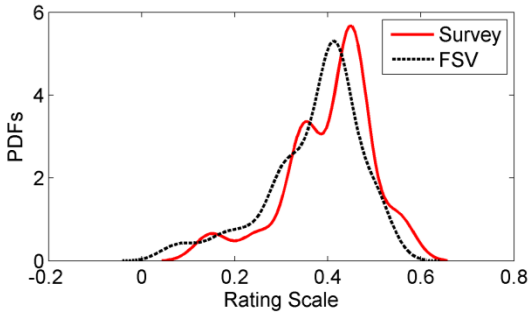

Fig. 4. Comparison of PDFs.

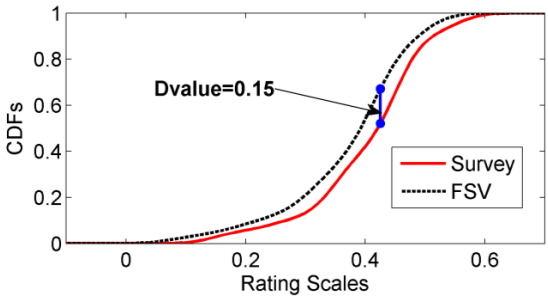

Fig. 5. Comparison of CDFs.

Further, the other 7 pairs of datasets from [8] are also analyzed. They are labeled as Data set 1 to 8 in turn considering data set in Fig. 1 is named Data set 5. The details follow.

B. Comparisons of xDM with survey results

It is known that FSV provides three types of measurement, ADM, FDM, and GDM. All the measurements can be given in the form of PDFs. Consequently, the discrepancy between these measurements and survey results can be shown by use of KS-test. By applying the typical values of FSV categories in Table III, the distributions of GDM of eight datasets are compared with their survey results in [8]. Table IV outlines the comparison result. It can be seen that most D values are smaller than the $D_{Critical}$ value, 0.17, except Data set 8, which means that it can be proposed that FSV results can mirror the assessment of experts in the majority of cases to a given level of accuracy in this case 90 % (or an inaccuracy of 1-in-10, which is about what the survey showed) .

Table IV: D values for different datasets.

Data set	D Value (GDM vs. Survey)
1	0.10
2	0.15
3	0.14
4	0.05
5	0.15
6	0.06
7	0.03
8	0.19

To evaluate the influence of typical value of FSV categories, the D values under different typical values for data sets are shown by boxplots in Fig. 7. As shown in Fig. 6, the typical values of FSV categories are linearly changed based on Table III, i.e., implementing a tolerance on the highly quantized visual results. For instance, the typical value for "Excellent" changes from 0 to 0.1 and, accordingly, the "Fair" value will change from 0.4 to 0.5. Consequently, the estimated PDFs will shift in the tolerance of FSV categories.

It can be seen from Fig. 7 that all the data sets have D values smaller than 0.17 with the change of typical values, including Data set 8. It is suggested that a new subtle survey is necessary to further verify the validity of FSV. Table V shows the comparison of D values when ADM and FDM are separately compared with survey results (using the typical values in Table III). D values of ADM and FDM for most of data sets are close to each. So it is reasonable to take the equal weighting of them when calculate GDM, as shown in equation,

$$GDM = \sqrt{ADM^2 + FDM^2}\,. \qquad (11)$$

It is also observed from Table V that neither ADM nor FDM can represent the discrepancy between data set as experts do not look at just trend or feature differences. But it works well when they are combined using equation (11), as shown in Table IV.

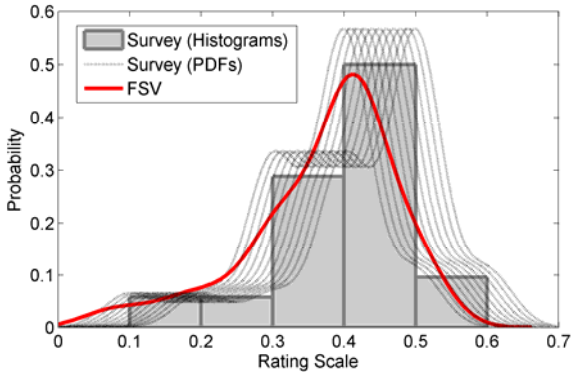

Fig. 6. Comparison of histograms and estimated PDFs given by different typical values of FSV categories.

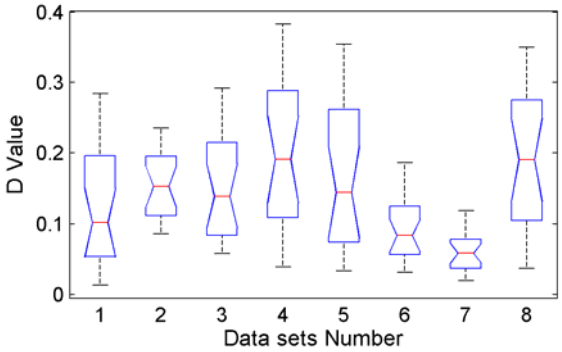

Fig. 7. Boxplots of data sets for different typical values of FSV categories.

Table V: D values for different comparisons.

Data set	D Value (ADM vs. Survey)	D Value (FDM vs. Survey)
1	0.14	0.12
2	0.07	0.16
3	0.35	0.33
4	0.11	0.77
5	0.31	0.45
6	0.26	0.24
7	0.13	0.10
8	0.34	0.48

Figure 8 (b) shows the results of Data set 2, the ADM is closer to survey results than FDM or GDM. It can be seen from Fig. 8 (a) that the difference between data set is mainly caused by a partial shift in axis X. Experts may visually correct this type of data and just focus on amplitude difference. So we can infer that experts pay little attention to the feature difference when they assess Data sets 2. In this case, how to decide the weight of FDM would be an interesting investigation in the future.

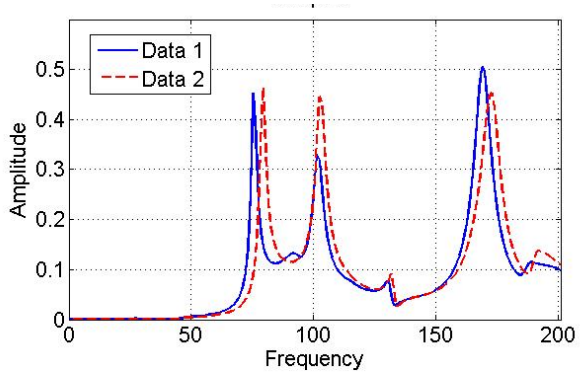

(a)

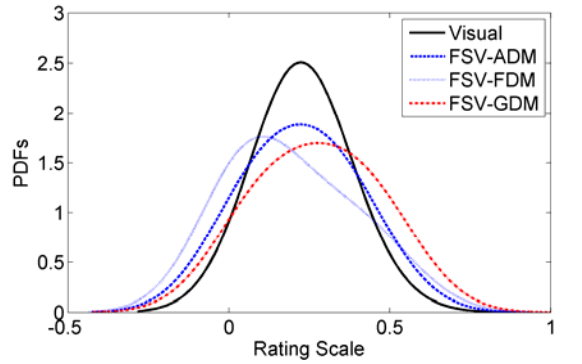

(b)

Fig. 8. (a) Data set 2 and (b) comparisons of its PDFs.

Figure 9 gives Data set 8 and the comparison of PDF results. It is indicated that the discrepancy between data sets is mainly caused by offset difference. So the ADM is much greater than the FDM and will dominate the GDM through equation (11). The equal weighting of ADM and FDM is also reasonable in this situation.

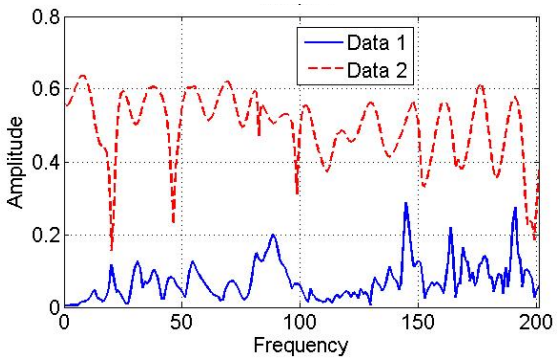

(a)

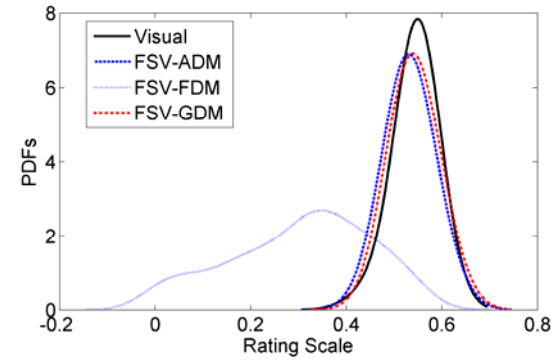

(b)

Fig. 9. (a) Data set 4 and (b) comparisons of its PDFs.

C. Comparison of statistical analysis

Table VI gives the comparison of the statistical analysis. The slight difference between mean values demonstrates that the FSV method can mirror the process of expert assessment. The mean value differences also indicate that, overall, experts tend to give more pessimistic assessment than FSV method for these data sets, which may provide a direction to the improvement of FSV. Data set 2 is an exception, as discussed in sub-section B, because experts intuitively correct the distortion caused by partial shift and give an optimistic assessment.

The comparison of variance shows that experts' assessment has tighter dispersion than FSV prediction. It means that FSV is more pessimistic in this. Again, comparisons of Skewness and Kurtosis show the general agreement between experts' assessment and FSV predication. It is noted that the variance of Data set 1's survey result is 0, so its Skewness and Kurtosis cannot be obtained.

To sum up, the PDFs and corresponding statistical analysis provide solid evidence to the validity of FSV method. And the introduction of PDFs makes it possible for the FSV to be a pre-statistical analysis method.

Table VI: Comparison of statistical analysis between FSV and experts assessment.

	Methods	1	2	3	4	5	6	7	8
Mean (GDMtot)	Survey	0.05	0.23	0.25	0.54	0.40	0.29	0.17	0.47
	FSV	0.03	0.27	0.20	0.54	0.37	0.28	0.16	0.41
Variance	Survey	0.0000	0.0048	0.0129	0.0006	0.0090	0.0138	0.0072	0.0037
	FSV	0.0009	0.0256	0.0069	0.0009	0.0106	0.0164	0.0140	0.0062
Skewness	Survey	-	1.0195	1.1188	-3.7500	-0.9285	0.1033	1.8939	-0.1585
	FSV	2.8684	0.0082	0.3778	0.4443	-1.0226	0.0385	0.9600	-1.0131
Kurtosis	Survey	-	4.9669	3.5826	15.0625	3.8481	2.5132	7.3729	2.4719
	FSV	14.6380	1.7572	3.0547	2.2734	3.9211	2.1639	3.0704	4.3879

V. CONCLUSION

This paper has discussed the introduction of PDFs as an enhancement to the presentation of FSV results. The performance of this indicator has been demonstrated in the verification of the performance of the FSV method itself. As the result of the introduction of PDFs, statistical analysis is employed to give quantitative results. By use of these analysis, the performance of FSV is verified when it is compared with experts' assessment. Further exploration with more data sets and more subtle rating scales would increase the statistical power of this observation, which needs more people to test this. Furthermore, the FSV method can be classified as a pre-statistical analysis method (or a data pre-conditioning method), which can provide greater flexibility for a wider range of computational electromagnetics practitioners.

ACKNOWLEDGMENT

This work was supported by National Natural Science Foundational of China under Grant No. 51077016.

REFERENCES

[1] *IEEE Standard for Validation of Computational Electromagnetics Computer Modeling and Simulations*, IEEE STD 1597.1-2008, pp. 1-41, 2008.

[2] G. Zhang, A. Duffy, H. Sasse, and W. Lixin, "The use of probability density functions to improve the interpretation of FSV results," *IEEE International Symposium on EMC*, U.S., pp. 685-689, 2012.

[3] A. Hastings, G. Palafox, and K. Tamhankar, "Assessment of feature selective validation (FSV) method for comparing modeled antenna patterns against measurements," *27th Annual Review of Progress in Applied Computational Electromagnetics (ACES)*, pp. 885-890, Virginia U.S., March 2011.

[4] A. Denton, A. Martin, and A. Duffy, "Quantifying EMC measurement accuracy using feature selective validation," *Applied Computational Electromagnetics Society (ACES) Journal*, vol. 23, no. 1, pp. 104-109, March 2008.

[5] A. Drozd, I. Kasperovich, C. Carroll, Jr., and A. Croneiser, "Antenna siting sensitivity study using the feature selective validation," *26th Annual Review of Progress in Applied Computational Electromagnetics (ACES)*, pp. 573-580, Tampere, Finland, April 2010.

[6] L. Hiltz and B. Archambeault, "Comparison of the modelled and measured antenna radiation pattern of a parabolic reflector using FSV," *25th Annual Review of Progress in Applied Computational Electromagnetics (ACES)*, pp. 173-177, California, U.S., March 2009.

[7] A. Duffy, A. Martin, A. Orlandi, G. Antonini, T. Benson, and M. Woolfson, "Feature selective validation (FSV) for validation of computational electromagnetics (CEM). Part I - The FSV method," *IEEE Transactions on Electromagnetic Compatibility*, vol. 48, pp. 449-459, Aug. 2006.

[8] A. Orlandi, A. Duffy, B. Archambeault, G. Antonini, D. Coleby, and S. Connor, "Feature selective validation (FSV) for validation of computational electromagnetics (CEM). Part II - Assessment of FSV performance," *IEEE Transactions on Electromagnetic Compatibility*, vol. 48, pp. 460-467, Aug. 2006.

[9] J. Simonoff, *Smoothing Methods in Statistics*, New York: Springer Verlag, 1996.
[10] F. Massey, "The Kolmogorov-Smirnov test for goodness of fit," *Journal of the American Statistical Association*, vol. 46, pp. 68-78, 1951.
[11] N. Smirnov, "Tables for estimating the goodness of fit of empirical distributions," *Annals of Mathematical Statistics*, vol. 19, pp. 279-281, 1948.

Gang Zhang received the B.Sc. in Electrical Engineering from China University of Petroleum, Dongying, China, in 2007, and M.Sc. degrees in Electrical Engineering from Harbin Institute of Technology (HIT), Harbin, China, in 2009. He is currently working toward the Ph.D. degree in HIT and Department of Engineering, De Montfort University, U.K., and involving in the research of Feature Selective Validation (FSV) method. His research interests include analysis of electromagnetic compatibility (EMC), electromagnetic simulation, and the validation of CEM.

Hugh Sasse graduated from The University of York in 1985. He has since has been working in the Machine Vision Group and later the Applied Electromagnetics Group at De Montfort University, Leicester and was awarded his PhD in 2010. His main interests are computer modeling of novel antenna structures and other communication channel components, with an emphasis on optimization of such structures.

Lixin Wang received the B.Sc. degree in Electrical Engineering from Nankai University, Tianjin, China, in 1988, and the M.Sc. and D.Sc. degrees in Electrical Engineering from Harbin Institute of Technology (HIT), Harbin, China, in 1991 and 1999, respectively.

He is currently a Professor of Power Electronic and Electric Drives at the HIT. He conducts research with Faults Online Monitoring and Diagnosis Laboratory, HIT, on a wide variety of topics including electromagnetic compatibility at the electronic system level, aircraft electromechanical fault diagnosis expert system and prediction and health management (PHM) of Li-ion battery.

Alistair Duffy was born in Ripon, U.K., in 1966. He received the B.Eng. (Hons.) degree in Electrical and Electronic Engineering and the M.Eng. degree from the University College, Cardiff, U.K., in 1988 and 1989, respectively. He received the Ph.D. degree from Nottingham University, Nottingham, U.K., in 1993 for his work on experimental validation of numerical modeling and the MBA from the Open University in 2003.

He is currently a Reader in electromagnetics at De Montfort University, Leicester, U.K. He is the author of over 150 articles published in journals and presented at international symposia. His research interests include CEM validation, communications cabling, and technology management.

Dr. Duffy is a Fellow of the Institution of Engineering and Technology (IET) and a Member of the International Compumag Society and the Applied Computational Electromagnetics Society. He is a member of the IEEE EMC Society Board of Directors and is the Chair of the IEEE EMC Society Standards Development and Education Committee.

Fast Multipole Method for Large-Scale Electromagnetic Scattering Problems on GPU Cluster and FPGA-Accelerated Platforms

V. Dang, Q. Nguyen, and O. Kilic

Department of Electrical Engineering and Computer Sciences
The Catholic University of America, Washington, DC 20064, USA
13dang@cardinalmail.cua.edu, 93nguyen@cardinalmail.cua.edu, and kilic@cua.edu

Abstract ─ The fast multipole method (FMM) for large-scale electromagnetic scattering problems is implemented on high performance computing (HPC) platforms and its performance is investigated in terms of accuracy, speedup, and scalability. The HPC platforms include a 13-node graphical processing unit (GPU) cluster, and a field programmable gate array (FPGA)-based high performance reconfigurable computer (HPRC). The details of the implementations and the performance achievements are shown and analyzed. We demonstrate a scalable parallelization while maintaining a good degree of accuracy.

Index Terms - Electromagnetic scattering, fast multipole method (FMM), FPGA, GPU, high performance reconfigurable computer (HPRC), iterative solvers, and method of moments.

I. INTRODUCTION

Modeling large-scale objects is a challenging problem in electromagnetics community due to the excessively heavy requirements of memory and computational resources. Since it has an important role in the research of target identification, or the stealth and anti-stealth technology, many numerical techniques have been developed over past two decades to reduce this burden without significant loss of accuracy, including adaptive integral method (AIM) [1], impedance matrix localization (IML) [2], and fast multipole method (FMM) [3]. Compared with the others, FMM is among the most suitable techniques for large-scale problems. It reduces the computational complexity of method of moments (MoM) from $O(N^3)$ to $O(N^{3/2})$ where N denotes the number of unknowns, whereas AIM and IML have the complexity of $O(N^{3/2}\log N)$ and $O(N^2\log N)$, respectively.

Many authors have investigated the parallelization of FMM and its multi-level version (MLFMA) [4-12] on CPU clusters in solving problems of hundreds of thousands to millions of unknowns. Others used FMM to solve large acoustic problems on multi-node GPU systems [13-14], or implemented MLFMA on GPUs, [15].

This paper is a continuation of our previous efforts [16, 17], and investigates the parallelization of FMM for electromagnetics structures on two HPC platforms. The first platform includes 13 nodes populated with a Nvidia Tesla M2090 GPU. The second platform is an FPGA-based SRC-7 system, which includes a single Altera Stratix EP4SE530 FPGA. In this paper, we enhance the GPU cluster implementation in [16] by the use of the two workload partitioning techniques among the computing nodes, namely group-based and direction-based distributions. The group-based distribution technique is applied for the calculation of the near components of the impedance matrix, while the direction-based distributions are used in the far component computation as will be discussed later in the implementation section. Our previous work in [16] utilized only the group-based approach, which resulted in more communication overhead. Regarding the FPGA platform, this paper provides an entire FMM implementation whereas our previous work in [17] utilized the FPGA only for the near component calculations of the impedance matrix. More details of the entire FMM implementation on FPGA is provided in the implementation section.

Submitted On: July 23, 2013
Accepted On: Jan. 19, 2014

1054-4887 © 2013 ACES

For the sake of validation of accuracy with analytical methods, the work presented here focuses on canonical problems such as scattering from a sphere. The work can easily be extended to real-life problems involving complicated structures.

The rest of the paper is organized as follows. Section II provides an overview of FMM. We present the implementation of FMM on HPC platforms in section III. Performance metrics for evaluation are presented in section IV. The experimental results are discussed in section V, followed by the conclusions in section VI.

II. OVERVIEW OF THE FAST MULTIPOLE METHOD (FMM)

The fundamental principles of FMM and its applications in electromagnetics have been well studied in literature [3-4]. In this section, we provide a brief overview to help our discussion on its parallel implementations discussed in section III.

Like in MoM, FMM solves for the linear equation system created in the form of $ZI = V$ where I represents the unknown currents, V depends on the incident field, and Z is the impedance matrix. The main idea in FMM is the grouping concept as shown in Fig. 1, where the N edges in the mesh of a given structure are categorized into M localized groups based on their proximity. According to this approach, two interaction types can be defined: near and far, as depicted in Fig. 1. These different types allow the system matrix to be split into two components, Z_{near} and Z_{far}, as shown in equation (1),

$$ZI = \left(Z_{near} + Z_{far}\right)I = V. \tag{1}$$

The near term comprises of interactions between spatially close edges, and is computed and stored in a similar manner to MoM [18]. The interactions between the remaining edges that are spatially far from each other constitute the far term. The advantage of separating the Z matrix into two components is that the Z_{far} matrix does not need to be computed and stored ahead of time. Instead it is factorized into radiation, T_1^E, T_2^E, receive, R_1^E, R_2^E and translation functions, T_L. Equation (2) depicts these functions based on the electric-field integral equation (EFIE) formulation,

$$Z_{far} = \frac{jk\eta}{4\pi}\left(\int d^2\hat{\mathbf{k}}\; R^E_{1,\mathbf{r}_{im}}\left(\hat{\mathbf{k}}\right).T_L\left(k,\hat{\mathbf{k}},\mathbf{r}_{mm'}\right).T^E_{1,\mathbf{r}_{i'm'}}\left(\hat{\mathbf{k}}\right) - \frac{1}{k^2}\int d^2\hat{\mathbf{k}}\; R^E_{2,\mathbf{r}_{im}}\left(\hat{\mathbf{k}}\right).T_L\left(k,\hat{\mathbf{k}},\mathbf{r}_{mm'}\right).T^E_{2,\mathbf{r}_{i'm'}}\left(\hat{\mathbf{k}}\right)\right), \tag{2}$$

where

$$T^E_{1,\mathbf{r}_{i'm'}}\left(\hat{\mathbf{k}}\right) = \int_S \mathbf{f_n}\left(\mathbf{r}_{i'm'}\right).e^{j\hat{\mathbf{k}}\cdot\mathbf{r}_{i'm'}}\,dS',$$
$$T^E_{2,\mathbf{r}_{i'm'}}\left(\hat{\mathbf{k}}\right) = \int_S \nabla'.\mathbf{f_n}\left(\mathbf{r}_{i'm'}\right).e^{j\hat{\mathbf{k}}\cdot\mathbf{r}_{i'm'}}\,dS', \tag{3}$$

$$R^E_{1,\mathbf{r}_{im}}\left(\hat{\mathbf{k}}\right) = \int_S \mathbf{f_n}\left(\mathbf{r}_{im}\right).e^{-j\hat{\mathbf{k}}\cdot\mathbf{r}_{im}}\,dS,$$
$$R^E_{2,\mathbf{r}_{im}}\left(\hat{\mathbf{k}}\right) = \int_S \nabla.\mathbf{f_n}\left(\mathbf{r}_{im}\right).e^{-j\hat{\mathbf{k}}\cdot\mathbf{r}_{im}}\,dS, \tag{4}$$

$$T_L\left(k,\hat{\mathbf{k}},\mathbf{r}_{mm'}\right) = \frac{k}{4\pi}\sum_{l=0}^{L}(-j)^{l+1}(2l+1)\, h_l^{(2)}\left(k\left|\mathbf{r}_{mm'}\right|\right)P_l\left(\hat{\mathbf{k}}\cdot\mathbf{r}_{mm'}\right). \tag{5}$$

In the equations above, the prime syntax denotes the source points, and i and m are indices that refer to the edges and groups in the mesh, respectively. The vector $\mathbf{r}_{ab}$ implies the direction from point b to a. The unit vector $\hat{\mathbf{k}}$ denotes the K possible field directions in κ space, $\mathbf{f}(\mathbf{r})$ denotes the associated basis function, $h_l^{(2)}(x)$ is the spherical Hankel function of the second kind, and $P_l(x)$ is the Legendre polynomial.

At this stage, the Z matrix is known and the unknown values for I can be solved for iteratively using equation (1). Each component of the voltage term V_i is calculated as in equation (6) using the matrix-vector multiplication (MVM),

$$V_i = \sum_{i'=1}^{N} Z_{ii'}I_{i'} = \sum_{i'=1}^{N} Z_{near,ii'}I_{i'} + \sum_{i'=1}^{N} Z_{far,ii'}I_{i'}, \tag{6}$$

where the near component is based on MoM and the far component is computed from equation (7) as,

$$\sum_{i'=1}^{N} Z_{far,ii'}I_{i'} = \frac{jk\eta}{4\pi}\left(\int d^2\hat{\mathbf{k}}\; R^E_{1,\mathbf{r}_{im}}\left(\hat{\mathbf{k}}\right).\sum_{m'\notin B_m} T_L\left(k,\hat{\mathbf{k}},\mathbf{r}_{mm'}\right).\sum_{i'\in G_{m'}} T^E_{1,\mathbf{r}_{i'm'}}\left(\hat{\mathbf{k}}\right)I_{i'} - \frac{1}{k^2}\int d^2\hat{\mathbf{k}}\; R^E_{2,\mathbf{r}_{im}}\left(\hat{\mathbf{k}}\right).\sum_{m'\notin B_m} T_L\left(k,\hat{\mathbf{k}},\mathbf{r}_{mm'}\right).\sum_{i'\in G_{m'}} T^E_{2,\mathbf{r}_{i'm'}}\left(\hat{\mathbf{k}}\right)I_{i'}\right), \tag{7}$$

where G_m denotes all elements in the m^{th} group, and B_m denotes all nearby groups of the m^{th} group.

The details of the parallelization of FMM will be discussed in the following section.

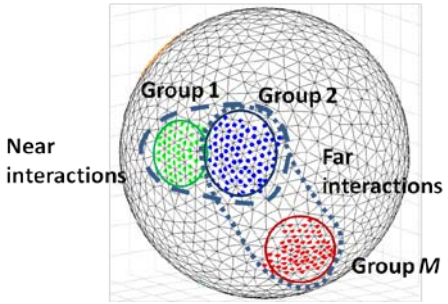

Fig. 1. Grouping in FMM (*N* edges, *M* groups).

III. HPC IMPLEMENTATION OF FMM

We consider two platforms for the parallel implementation of FMM; namely a GPU cluster and an FPGA-based HPRC system. In this section we first discuss the different architectures and programming models of these systems, and then provide the details of our HPC implementations on both platforms.

A. HPC architectures and programming models

The first platform utilized in our FMM implementation is the GPU cluster, which consists of 13 computing nodes. Each node has a dual 6-core 2.66 GHz Intel Xeon processor, 48 GB RAM along with one Nvidia Tesla M2090 GPU running at 1.3 GHz with 6 GB of GPU memory. The nodes are interconnected through the InfiniBand interconnection, as shown in Fig. 2. The cluster populates CUDA v4.2 and MVAPICH2 v1.8.1 (a well-known implementation of message passing interface (MPI)). Two parallel programming approaches of CUDA and MPI are combined to provide the use of GPU programming across the cluster.

The second platform is an SRC-7 MAPstation workstation, which consists of one general purpose microprocessor subsystem and one series J MAP reconfigurable processor subsystem, see Fig. 3. The microprocessor board, which is based on a dual-core 3.00 GHz Intel Xeon processor and 6 GB RAM, is connected to the MAP board through the series D SNAP interconnect. The SNAP card plugs into the memory DIMM slot on the microprocessor motherboard to provide a high data transfer rate between the boards. The MAP board is composed of one control FPGA (Altera Stratix EP2S130) and one user FPGA (Altera Stratix EP4SE530), which operate at 200 MHz. It also contains 16 on-board memory (OBM) banks with a total capacity of 64 MB, and two simultaneously accessible 1 GB global common memory (GCM) banks. SRC's proprietary Carte-C programming environment is used in the FPGA-based code development. The programming model offers a compromise between high-level languages (HLLs), e.g. C, and hardware description languages (HDLs), e.g. VHDL, to abstract underlying hardware design details and streamline the disparate design flows [19].

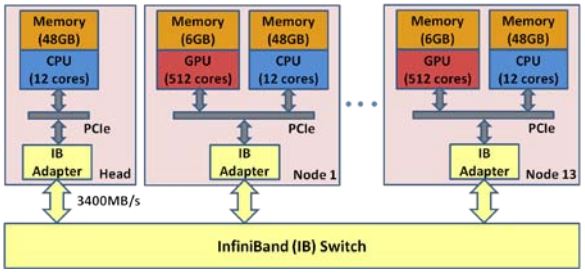

Fig. 2. System architecture of GPU cluster.

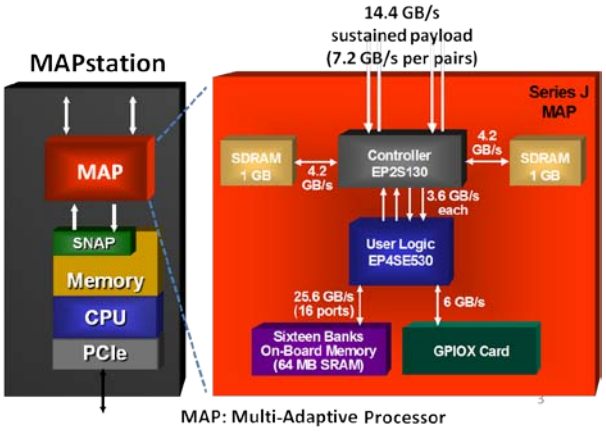

Fig. 3. System architecture of SRC MAPstation.

The two platforms utilize two different programming models. The CUDA used by the GPU follows the single program multiple data (SPMD) model [20], which allows data parallelism (wide parallelism). Under the SPMD scenario, thousands of threads execute the same program on different GPU cores, simultaneously operating on different data sets in parallel. On the other hand, FPGA programming mainly supports

task parallelism (deep parallelism) by utilizing pipelining technique. It is interesting to mention that data parallelism can also be allowed in FPGA programming. However, this depends on the availability of on-chip resources. The SRC's Carte programming environment allows the user full control of data utilization in terms of pipelining and parallelization, whereas with the CUDA environment the user is oblivious to how the GPU is scheduled. Thus, CUDA is very easy to use whereas Carte requires both software and hardware programming skills.

B. HPC implementations

The FMM algorithm comprises three main steps: pre-processing, processing, and post-processing (see Fig. 4). The pre-processing step involves reading the geometry mesh and dividing edges into localized groups. The processing step involves five tasks as shown in Fig. 4. The matrix components for near interactions, the radiation/receive functions, the translation matrix, and the V vector are calculated and stored. Iterative methods, such as biconjugate gradient stabilized method (BiCGSTAB) [21], are employed for solving the linear system. Finally, the electromagnetic quantities of interest, e.g. scattered fields, are calculated in the post-processing step. Based on our profiling results, the processing step consumes the most execution time in the algorithm. Hence, it is selected as the candidate for hardware parallelization, while the other steps are handled on the CPU.

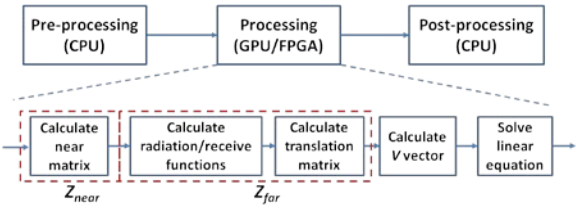

Fig. 4. FMM processing step flowchart.

B.1. GPU cluster implementation

The geometry mesh data resulting from the pre-processing step in Fig. 4 is transferred to the GPU memory once at the beginning of the processing step and the entire computation is performed on the GPU afterward. The parallelization of the processing step in GPU cluster implementation is performed at two levels: (i) among computing nodes using MPI library, and (ii) within GPU per node using CUDA programming model. The workload of computational tasks in the processing step, as shown in Fig. 4, are equally distributed to computing nodes such that each node holds the same amount of workload and the inter-node communication is minimized. Two partitioning techniques, which are defined as group-based distribution and direction-based distribution, are exploited to achieve the balanced workload distribution among the computing nodes. The first technique involves the uniform distribution of M groups among n computing nodes. The second technique, which was suggested in [5], involves the distribution of independent computation for each sample in κ space among the nodes. Within each node, the CUDA thread-block model is utilized to calculate the workload assigned to that node. The remaining parts of this section highlight the implementation details of each computational task in the processing step.

1) Near interaction calculations

Our earlier work [22] on implementing MoM on multiple GPUs is leveraged for the first task of the processing step (see Fig. 4), namely calculation of Z_{near}, which utilizes conventional MoM. Using the group-based partitioning technique, the rows of the Z_{near} matrix are assigned to the computing nodes with the assumption that each node has approximately an equal number of Z_{mn} elements, as shown in Fig. 5, where N_{group} denotes the average number of edges per group, and M_{node} is defined as the average number of groups per node [16]. At a given node, each sparse row is handled by a CUDA block in which a CUDA thread calculates one element, Z_{mn}, of that row. For further details of the GPU cluster implementation, the readers are referred to our previous work in [16-17].

2) Far interaction calculations

The second task is the calculation of the far interactions, which consists of the calculations of three functions: radiation, T^E, receive, R^E, and translation, T_L. As seen in equations (3) and (4), the radiation and receive functions are in the form of complex conjugate of each other. Thus their implementations are identical. In contrast to our

previous work in [16-17] in which the group-based partitioning was used for far interactions, the direction-based partitioning strategy is applied to the GPU implementation of this task due to the fact that each sample in κ space is completely independent of other samples. This efficient workload distribution guarantees the minimum communication at the end of the matrix-vector multiplication as discussed later in the next section. As shown in Fig. 6, following the κ space distribution, each node handles calculations of M groups for K_{node} ($\approx K/n$) directions. Given this amount of workload per node, the CUDA kernel is launched with $M \bullet K_{node}$ blocks such that each block performs N_{group} radiation/receive function calculations at a given direction and each thread evaluates a single function.

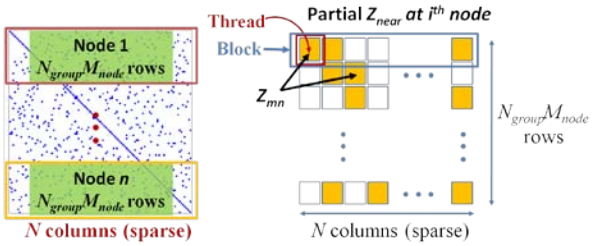

Fig. 5. Workload distribution and CUDA implementation of the Z_{near} matrix.

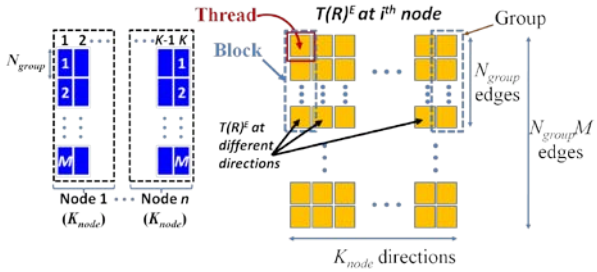

Fig. 6. Workload distribution and CUDA implementation of the radiation/receive functions.

The next task for the far interactions is the calculation of the translation matrix, T_L, which contains all the translation operators among far groups. The workload of the T_L matrix calculations is also distributed across the nodes following the direction-based technique since it has to be evaluated for the entire κ space. Each CUDA block is assigned to compute one sparse row of the T_L matrix for a given direction and each thread computes one element in that row, see Fig. 7.

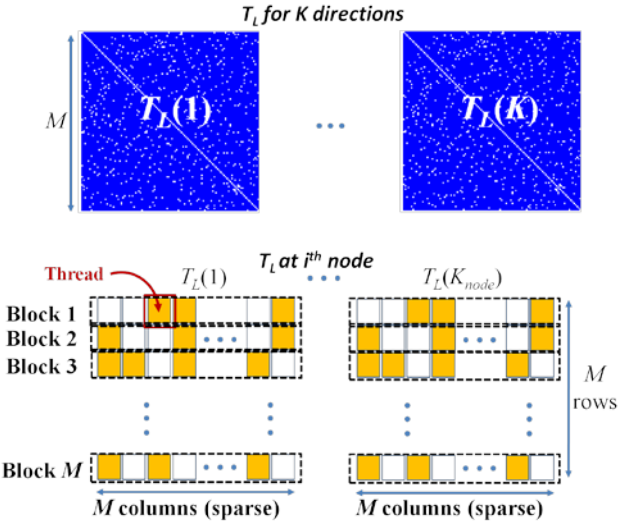

Fig. 7. Workload distribution and CUDA implementation of the translation matrix.

3) V vector calculations

The V vector calculations are simply the evaluations of incident electric fields at each triangle in the geometry mesh. The details of the computation, which render itself to parallel implementation can be found in [18].

4) Solution of the linear equation

The final task is the solution for the linear equation using iterative solver, i.e., BiCGSTAB algorithm [21]. In this algorithm, each iteration involves matrix-vector multiplications (MVMs), i.e., $Z.I$, which constitute the most time consuming part of the solution. The calculation of $Z_{far}I$ comprises three stages: aggregation, translation, and disaggregation, (the readers are referred to [3] for further details), while $Z_{near}I$ is simply a regular sparse MVM. This section only discusses the GPU cluster parallelization of $Z_{far}I$, as shown in Fig. 8. It should be noted that the other parts of the BiCGSTAB are also performed on GPU. They involve basic linear algebra operations leveraged from the CUBLAS library [23].

The unknown currents are distributed across the computing nodes using the group-based partitioning technique. During the iterative linear solution, each node calculates the estimated values

of its assigned unknowns and updates all nodes. In the aggregation stage, each node computes the radiated fields for all M groups for the K_{node} directions by multiplying the unknowns with their corresponding radiation functions, T^E, and accumulating within each group. The CUDA execution model assigns one group for a specific direction to each block in which each thread performs one multiplication. The CUDA kernel also requires parallel reductions within every block to sum the per-thread results to give the radiated fields for each group.

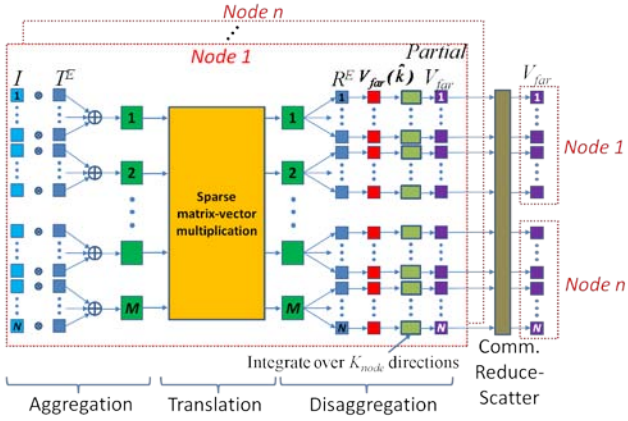

Fig. 8. Parallelization of the far MVM.

In the translation stage, the received fields for each associated direction are calculated from the multiplication of the translation matrix, T_L, and the radiated fields. Since the translation matrix is sparse, the CUDA implementation simply performs K_{node} normal sparse MVMs.

In the disaggregation stage, the received field quantities of all M groups are multiplied with the corresponding receive functions, R^E, and integrated over the partitioned κ space in each node. Similar to the aggregation stage, the CUDA kernel is invoked with M blocks each thread of which computes one disaggregation followed by the integration for one partial result of the far term V_i as presented in equation (6). Finally, at the end of the MVM, the partial results from all nodes are summed together and all nodes are updated. This is accomplished through the reduce-scatter communication.

The solution of the linear equation requires communication only at two steps: (i) before starting the MVM to update the estimated values for the unknowns among the nodes; (ii) after the disaggregation stage of the MVM to update the $Z_{far}I$ results among the nodes. Due to the efficient use of the group-based and direction-based distribution schemes, the inter-node communication overhead among the nodes is reduced. This overhead is further reduced as it is performed directly among GPU memory spaces using MVAPICH2's GPU-to-GPU feature.

B.2. FPGA implementation

The SRC-7 MAPstation contains a single user FPGA, thus in this paper the FPGA parallelization is performed on a single node. However, this work can be easily extended to work on a multi-node system using MPI librabry. As in the GPU implementation, the FPGA implementation in this work also focuses on the parallelization of the processing step of Fig. 4. However, only four tasks of the processing step, namely calculating matrix components for near interactions, calculating the radiation/receive functions, calculating the V vector, and iterative linear solution, are fully pipelined on FPGA. Due to its complex recursive computation relating to the evaluations of spherical Hankel functions and Legendre polynomials, as shown in equation (5), the remaining task, which is calculating the translation matrix, is not a good candidate for the FPGA implementation and thus is handled by the CPU. Since the on-board memory (OBM) is limited to a total capacity of 64 MB, the entire workload cannot fit on a single FPGA chip. Therefore, the workload of each computational task is equally divided in a group-wise manner into sequential chunks. Each chunk is then computed using the pipelining technique. Currently, the FPGA logic resource of our SRC-7 computer limits the number of pipelines in each task to one. In spite of that, our implementation can be modified with minimal effort to work with fewer chunks and more pipelines on larger resource FPGA systems. The remaining parts of this section highlight the FPGA implementation details of each computational task.

1) Near interaction calculations

The first task is the calculation of Z_{near}, see Fig. 4, which utilizes conventional MoM. Using the group-wise partitioning technique, the computation of Z_{near}'s rows are divided into

$N_{chunknear}$ chunks (see Fig. 9) where MAX_OBM is the maximum size of a single OBM bank. At the beginning of the calculation, the geometry mesh data is transferred from the CPU memory to the OBM. Per chunk, the row and column indices of the corresponding Z_{mn} elements are transferred to OBM followed by fully pipelined computations. The evaluation of each Z_{mn}, [18], is separated into two loops running concurrently. The first loop computes the elements under the integration sign. For the second loop, we leverage our earlier work in [22] on the integration implementation. The streaming technique is exploited, as shown in yellow blocks in Fig. 9, to enable computation and data transfer overlapped. Accordingly, each result of Z_{mn} is streamed out to CPU memory immediately as soon as it is computed. The process is continued for the rest of chunks.

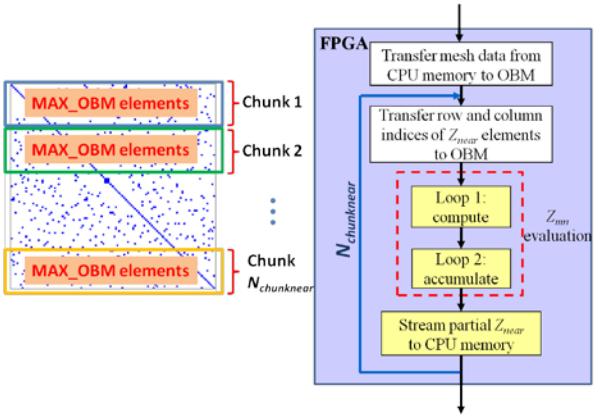

Fig. 9. Workload distribution and FPGA implementation of the Z_{near} matrix.

2) Far interaction calculations

The second task is the far interaction calculations. As mentioned before, for the FPGA implementation we only consider the radiation, T^E, and receive, R^E, functions, and their implementations are identical since they are complex conjugates of each other. For the sake of simplicity, the group-wise partitioning technique is also used to divide the radiation/receive functions to N_{chunk} chunks (see Fig. 10). The radiation/receive functions must be evaluated at all K directions. Before calculations, the group and direction data are transferred from the CPU memory to the OBM. Per chunk, the geometry mesh data is transferred to OBM before the fully pipelined computation starts. The use of streaming, as shown in yellow blocks in Fig. 10, allows the computations to continue while the data is being transferred out. The results are stored in the global-common memory (GCM) instead of the CPU memory to avoid the overhead of communication through SNAP card.

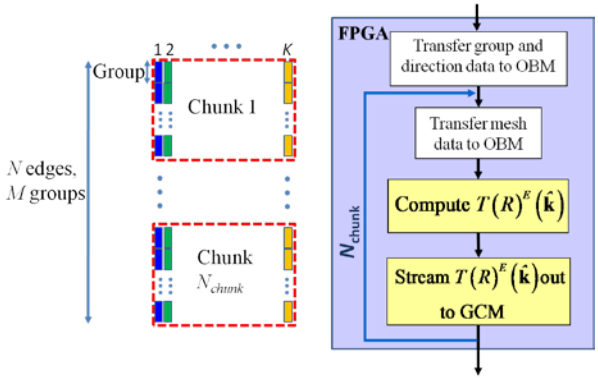

Fig. 10. Workload distribution and FPGA implementation of the radiation/receive functions.

3) V vector calculations

As in the GPU cluster implementation, the calculations of the V vector are parallelized on the hardware. The FPGA implementation details are not discussed in this paper due to its simplicity.

4) Solution of the linear equation

Similar to the GPU implementation, this section focuses on the $Z_{far}I$ matrix-vector multiplication (MVM) in BiCGSTAB algorithm. The calculation of $Z_{far}I$ comprises three stages: aggregation, translation, and disaggregation. The parallelization of far MVM follows the flowchart presented in Fig. 8, except one node is available to us in the HPRC system and is used to handle the entire computation. Thus, communication is not required at the end of the MVM. In terms of FPGA pipelining, it can be observed in equation (7) that these three stages are similar and involve multiplications and accumulations (integrations). Hence, a generic implementation, as shown in Fig. 11, can be applied to all stages. The symbols ***Input_A***, ***Input_B***, and ***Output_C*** are used to represent the input and output variables, and ***acc_length*** is the length of the accumulation for each stage (see Table I).

Before calculations, the ***Input_A*** is transferred to the OBM from the CPU memory. Using the group-wise partitioning technique, per chunk, the ***Output_C*** are then computed by multiplying each value of ***Input_A*** with its corresponding value of ***Input_B***, and accumulating on ***acc-length*** sequences. All computation loops are fully pipelined such that ***Input_B*** is streamed in from the GCM while ***Output_C*** are streamed out to the GCM.

Table I: General symbols for each stage in the far MVM.

	Aggrega-tion	***Translation***	***Disaggrega-tion***
Input_A	unknown currents	radiated fields of M groups	received fields of M groups
Input_B	radiation functions	translation matrix	receive functions
Output _C	radiated fields of M groups	received fields of M groups	$Z_{far}I$
acc-length	number of edges per group	number of elements per T_L matrix's row	K

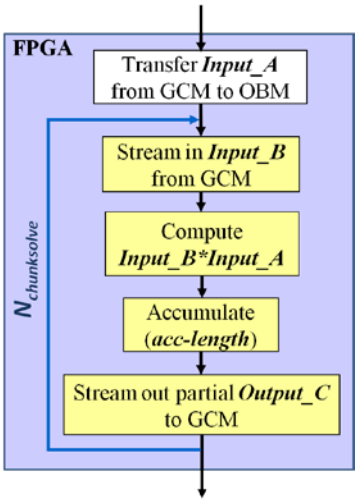

Fig. 11. Generic FPGA implementation of three stages of the far MVM.

IV. PERFORMANCE METRICS

In our performance analysis, we assume two models. The first model is the fixed-workload model (Amdahl's Law) [24] where the computational workload is fixed and equally distributed among the processing elements (PE) (i.e., computing nodes for GPU implementation and MAP cards for FPGA implementation) as the number of processing elements increases. The second model is the fixed-time model (Gustafson's Law) [24] where larger computational workloads (larger problem size) are used while maintaining the same performance as the number of processing elements is increased.

The performance of our HPC implementations is evaluated in reference to its single CPU implementation. In our analysis, we consider the computation time, T_{comp}, which is defined as the time spent on GPU or FPGA, as well as the total execution time, T_{total}, which is the sum of the computation time and the overhead, T_{comm}, which is associated with all communications between processing elements (GPUs or FPGAs) and CPUs, as given in equation (8),

$$T_{total}^{PE} = T_{comp}^{PE} + T_{comm}^{PE}. \tag{8}$$

Two metrics are investigated for performance comparisons between platforms: (i) speedup, and (ii) scalability. The speedup, S, is defined as the ratio of time required by a single CPU to carry out the total workload, $T^{CPU}(1,D)$, to the time required by multiple hardware processing elements for their associated workload, $T^{PE}(N_{PE},D_{PE})$ as in equation (9),

$$S(N_{PE}) = \frac{T^{CPU}(1,D)}{T^{PE}(N_{PE},D_{PE})}, \tag{9}$$

where D_{PE} is the workload for a single processing element, N_{PE} is the number of processing elements, D is the total workload assigned. In the fixed-workload model, the workload per element D_{PE} is adjusted with the number of processing elements, $D_{PE}=D/N_{PE}$. In the fixed-time model, the total workload D is adjusted with the number of processing elements, $D=D_{PE}*N_{PE}$.

Finally, the scalability factor, Ω, is defined as the normalized speedup of multiple processing elements in reference to a single processing element, as given by equation (10),

$$\Omega(N_{PE}) = \frac{S(N_{PE})}{S(1)}. \tag{10}$$

V. EXPERIMENTAL RESULTS

The implementation on both platforms is done using single precision. The implementation for

GPU is parallelized using up to 13 nodes, while the FPGA implementation is performed on a single node due to the available configuration in our lab. In reviewing our experimental results, first we verify the accuracy and then investigate the performance in terms of the two metrics: speedup and scalability.

A. Accuracy

We validate the accuracy of the implementation on both platforms by calculating the radar cross section (RCS) of a 5.4 λ diameter (58 K unknowns) PEC sphere illuminated by an x-polarized normally incident field. The RCS is compared with the results using Mie scattering. It can be observed from Fig. 12 that the two HPC results and the analytical solutions show a good agreement.

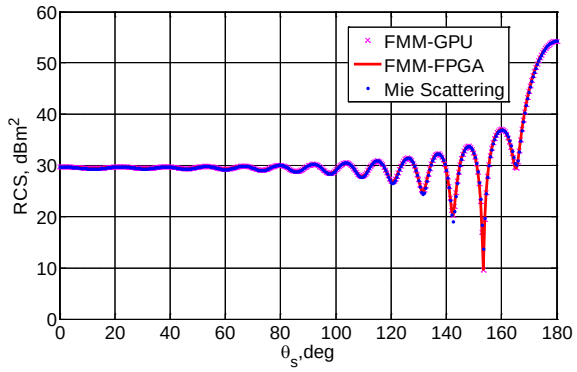

Fig. 12. RCS of a 5.4λ diameter PEC sphere.

B. Performance evaluation for GPU cluster

Two experiments are conducted with a PEC sphere following fixed-workload model and fixed-time model as discussed in section IV. In the fixed-workload model, the sphere diameter is chosen as d = 15.75 λ corresponding to 506 K unknowns. The size of the problem demands the use of at least 8 nodes to satisfy the required GPU memory. The speedup factor increases from 755 for 8 nodes to 1,152 for 13 nodes as observed in Fig. 13. Since each node processes less workload, the GPU execution time decreases as the number of nodes increases. The difference observed between the speedup of total execution time and computation time is due to the inter-node communication overhead.

In the fixed-time model, the sphere diameter for a single node is chosen as d = 7.45λ, which fully utilizes the single GPU memory with 113 K unknowns. As the number of nodes increases, the workload at each node remains constant enabling the solution for a 17.96 λ diameter sphere with 656 K unknowns for 13 nodes. We observe in Fig. 14 that the GPU implementation outperforms the CPU by achieving a speedup of 1,133 for 13 nodes.

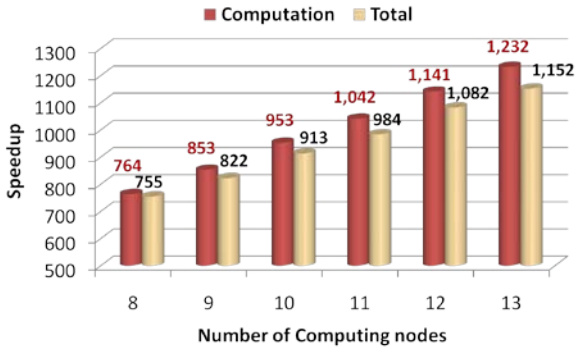

Fig. 13. Speedup of GPU cluster (Amdahl's Law, single CPU execution time ≈ 11 hours).

Finally, we compare the scalability of the GPU cluster implementation for both experiments. The scalabilities for the computation speedup and the total speedup in comparison to the linear theoretical scalability are demonstrated in Fig. 15 (fixed-workload model) and Fig. 16 (fixed-time model). It can be seen in both figures that the computation speedup scales identically to the theoretical linear expectation demonstrating our efficient hardware implementation. The total speedup scales closely to the theoretical expectation demonstrating our efficiency in reducing the inter-node communication overhead.

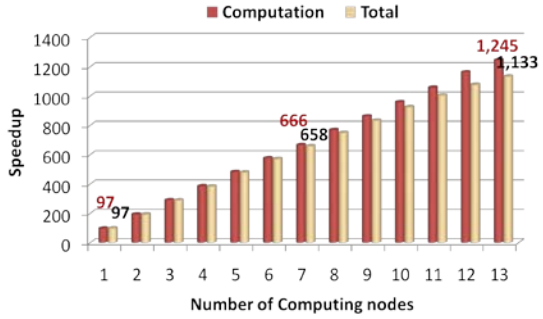

Fig. 14. Speedup of GPU cluster (Gustafson's Law, single CPU execution time ≈ 1.26 hours).

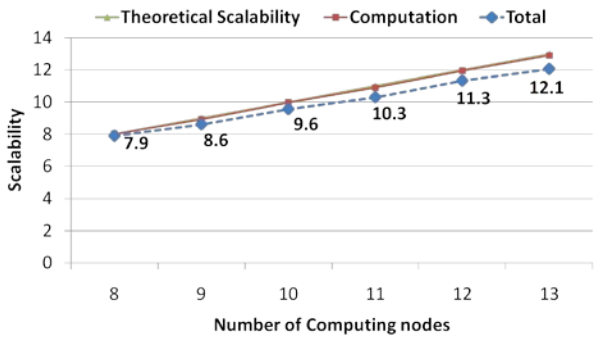

Fig. 15. Scalability of GPU implementation (fixed-workload model).

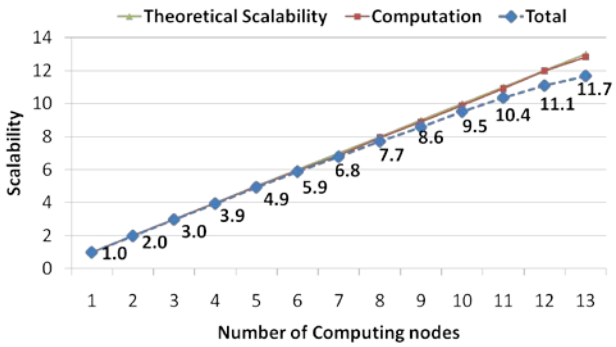

Fig. 16. Scalability of GPU implementation (fixed-time model).

C. Performance evaluation for FPGA workstation

Due to our available configuration of the SRC-7 MAPstation workstation, the experiment is carried out on a single FPGA fully utilizing its memory by choosing $d = 5.4\ \lambda$ (39 K unknowns). Therefore, our performance analysis is limited to the speedup of a single node, which is observed to be a factor of 2. For the same problem size, the GPU implementation achieves a total speedup factor of 77.5, outperforming the FPGA implementation. However, it should be noted that in the current FPGA implementation, due to the complex recursive nature as mentioned in section III.B.2, the translation matrix calculation task is handled on the CPU. This contributes to a decreased performance compared to that of GPU where all tasks are fully parallelized. Moreover, the FPGA system has significantly more limited resources in terms of clock speed and memory. In particular, the FPGA operates at 200 MHz whereas the GPU runs at 1.3 GHz, and the on-board memory of FPGA is limited to a total capacity of 64 MB compared with 6 GB of GPU memory. The memory limit results in the fact that each computational task can only be parallelized in a chunk-wise manner, which is part of the reason for the less impressive FPGA performance. This is despite the fact that the pipelining technique is efficiently utilized in each chunk.

VI. CONCLUSIONS

In this paper, the FMM algorithm is implemented on two HPC platforms, a 13-node GPU cluster and a single FPGA SRC workstation, for large-scale electromagnetic scattering problems. It is shown that for the same degree of accuracy, the GPU implementation outperforms the CPU implementation in terms of speedup by a factor of 1,133 for problem sizes with more than half million unknowns. Currently, the maximum problem size that can be handled by our GPU cluster implementation is limited by the GPU memory, which is 6 GB per node in our cluster. Larger problem sizes can be handled by the cluster by fully utilizing all available system resources including the CPU and GPU memories. We also observe that the GPU cluster implementation demonstrates a favorable scalability characteristic as the number of nodes increases, which proves a highly efficient parallelization scheme, which reduces the inter-node communication overhead. The paper also demonstrates a speedup factor of two for the FPGA implementation. Although, the comparison of performance in terms of speedup reveals that the GPU implementation surpasses the FPGA implementation, it should be noted that the FPGA system has significantly more limited resources than GPU in terms of frequency (200 MHz versus 1.3 GHz) and on-board memory (64 MB versus 6 GB). In the near future, when FPGA computers are equipped with larger resources and operate at higher frequencies, the authors believe a comparable performance with GPU can be achieved.

ACKNOWLEDGMENT

This material is based upon work supported by, or in part by, the U.S. Army Research Laboratory and the U.S. Army Research Office under contract/grant number W911NF-09-1-0123.

REFERENCES

[1] E. Bleszynski, M. Bleszynski, and T. Jaroszewicz, "AIM: Adaptive integral method for solving large-scale electromagnetic scattering and radiation problems," *Radio Science*, vol. 31, no. 5, pp. 1225-1251, 1996.

[2] F. Canning, "The impedance matrix localization (IML) method for moment-method calculations," *IEEE Antennas Propagat. Mag.*, vol. 32, no. 5, pp. 18-30, 1990.

[3] R. Coifman, V. Rokhlin, and S. Wandzura, "The fast multipole method for the wave equation: a pedestrian prescription," *IEEE Antennas Propagat. Mag.*, vol. 35, no. 3, pp. 7-12, June 1993.

[4] J. Song and W. Chew, "Multilevel fast multipole algorithm for solving combined field integral equations of electromagnetic scattering," *Microw. Opt. Tech. Lett.*, vol. 10, pp. 14-19, Sep. 1995.

[5] C. Waltz, K. Sertel, M. Carr, B. Usner, and J. Volakis, "Massively parallel fast multipole method solutions of large electromagnetic scattering problems," *IEEE Trans. Antennas Propag.*, vol. 55, no. 6, pp. 1810-1816, 2007.

[6] S. Velamparambil, J. Schutt-Aine, J. Nickel, J. Song, and W. Chew, "Solving large scale electromagnetic problems using a Linux cluster and parallel MLFMA," in *IEEE Antennas Propag. Soc. Int. Symp.*, vol. 1, pp. 636-639, 11-16 July 1999.

[7] S. Velamparambil and W. Chew, "Analysis and performance of a distributed memory multilevel fast multipole algorithm," *IEEE Trans. Antennas Propag.*, vol. 53, no. 8, pp. 2719-2727, August 2005.

[8] E.-L. Lu and D. Okunbor, "A massively parallel fast multipole algorithm in three dimensions," in *Proc. IEEE High Perform. Distrib. Comput. Int. Symp.*, pp. 40-48, August 1996.

[9] E.-L. Lu and D. Okunbor, "Parallel implementation of 3d FMA using MPI," in *Proc. MPI Developer's Conf.*, pp. 119-124, July 1996.

[10] S. Velamparambil, W. Chew, and M. Hastriter, "Scalable electromagnetic scattering computations," in *IEEE Antennas Propag. Soc. Int. Symp.*, vol. 3, pp. 176-179, 2002.

[11] G. Sylvand, "Performance of a parallel implementation of the FMM for electromagnetics applications," *Int. J. Numer. Meth. Fluids*, vol. 43, no. 8, pp. 865-879, Nov. 2003.

[12] O. Ergul and L. Gurel, "Efficient parallelization of the multilevel fast multipole algorithm for the solution of large-scale scattering problems," *IEEE Trans. Antennas Propag.*, vol. 56, no. 8, pp. 2335-2345, August 2008.

[13] M. López-Portugués, J. López-Fernández, J. Ranilla, R. Ayestarán, and F. Las-Heras, "Parallelization of the FMM on distributed-memory GPGPU systems for acoustic-scattering prediction," *J. Supercomput.*, vol. 64, no. 1, pp. 17-27, April 2013.

[14] M. López-Portugués, J. López-Fernández, J. Menéndez-Canal, A. Rodríguez-Campa, and J. Ranilla, "Acoustic scattering solver based on single level FMM for multi-GPU systems," *J. Parallel Distrib. Comput.*, vol. 72, no. 9, pp. 1057-1064, Sep. 2012.

[15] M. Cwikla, J. Aronsson, and V. Okhmatovski, "Low-frequency MLFMA on graphics processors," *IEEE Antennas Wireless Propag. Lett.*, vol. 9, pp. 8-11, 2010.

[16] Q. Nguyen, V. Dang, O. Kilic, and E. El-Araby, "Parallelizing fast multipole method for large-scale electromagnetic problems using GPU clusters," *IEEE Antennas Wireless Propag. Lett.*, vol. 12, pp. 868-871, July 2013.

[17] V. Dang, Q. Nguyen, O. Kilic, and E. El-Araby, "Fast multipole method for large-scale electromagnetic scattering problems using high performance computers," in *The 29th International Review of Progress in Applied Computational Electromagnetics (ACES 2013)*, Monterey, CA, USA, 24-28 March 2013.

[18] S. Rao, D. Wilton, and A. Glisson, "Electromagnetic scattering by surfaces of arbitrary shape," *IEEE Trans. Antennas Propag.*, vol. 30, no. 3, pp. 409-418, May 1982.

[19] E. El-Araby, O. Kilic, and V. Dang, "Exploiting FPGAs and GPUs for electromagnetics applications: interferometric imaging in random media case study," *The Applied Computational Electromagnetics Society (ACES) Journal*, vol. 27, no. 2, Feb. 2012.

[20] F. Darema, "The SPMD model: past, present and future," in *Proc. 8th European PVM/MPI Users' Group Meeting on Recent Advances in Parallel Virtual Machine and Message Passing interface,* Lecture Notes In Computer Science, vol. 2131, pp. 1, Sep. 2001.

[21] R. Barrett, M. Berry, T. Chan, J. Demmel, J. Donato, J. Dongarra, V. Eijkhout, R. Pozo, C. Romine, and H. van der Vorst, *Templates for the Solution of Linear Systems: Building Blocks for Iterative Methods*, Philadelphia, PA: SIAM, 1994.

[22] O. Kilic, E. El-Araby, Q. Nguyen, and V. Dang, "Bio-inspired optimization for electromagnetic structure design using full-wave techniques on GPUs," *Int. J. Numer. Model.*, vol. 26, no. 6, pp. 649-669, November/December 2013.

[23] NVIDIA Corporation, *CUDA Toolkit 4.2 CUBLAS Library,* Santa Clara, CA, Feb. 2012.

[24] K. Hwang and Z. Xu, *Scalable Parallel Computing: Technology, Architecture, Programming*, New York, NY: McGrawHill, 1998.

Vinh Dang *received his* B.Sc. (2003) and M. Eng. (2006) degrees in Electrical Engineering from the Posts and Telecommunications Institute of Technology and the University of Technology, in Vietnam, respectively. Prior to 2010, he was a Lecturer at the School of Electrical Engineering, International University. He is currently a PhD. candidate and a Graduate Research Assistant in the Department of Electrical Engineering and Computer Science, the Catholic University of America (CUA). His research interests include high performance computing, numerical electromagnetics with applications to radiation, scattering and remote sensing.

Quang Nguyen received his B.Sc. (2009) and M.Eng. (2011) degrees in Electrical Engineering from the International University, Vietnam, and the Catholic University of America, USA, respectively. He is currently a PhD. student and a Graduate Research Assistant in the Department of Electrical Engineering and Computer Science, Catholic University of America. His research interests include bio-inspired optimization methods, numerical electromagnetics with applications to radiation, scattering and remote sensing.

Dr. Ozlem Kilic is an Associate Professor in the Department of Electrical Engineering and Computer Science of the Catholic University of America. Prior to joining CUA, she was an Electronics Engineer at the U.S. Army Research Laboratory, Adelphi MD. Dr. Kilic has over five years of industry experience at COMSAT Laboratories as a Senior Engineer and Program Manager with specialization in satellite, link modeling and analysis. Her research interests include numerical electromagnetics, antennas, wave propagation, satellite communications systems, and microwave remote sensing. She is an Associate Editor of IEEE Antennas and Propagation Magazine and Applied Computational Electromagnetics Society Journal. She serves as Member at Large for USNC-URSI.

Computer Reconstructed Holographic Technique for Phase-less Near-Field Measurement

L. Zhiping[1], Z. Wang[2], and W. Jianhua[1]

[1] School of Electronics and Information Engineering
Beihang University, Beijing, 100191, China
lzp@buaa.edu.cn, wjh@buaa.edu.cn

[2] School of Automation and Electrical Engineering
University of Science and Technology, Beijing, 100083, China
wangzp@ustb.edu.cn

Abstract ─ A novel holographic near-field phase-less technique is presented. The measurement system is composed of the antenna under test, the reference antenna, the amplitude scanning measurement system, and the holographic reconstructed algorithm. The interference amplitude of the antenna under test with the reference antenna is measured by the amplitude scanning system. The complex near field of the antenna under test is reconstructed by a computer, where the measured interference is corrected by the multiplication with the virtual spherical reference wave and then filtered in Fourier transformation domain (e.g., plane wave angular spectrum) or the back-projected image space. The reconstruction method is rigorous without traditional Fresnel approximation. The novel technique requires the amplitude on one measurement surface and the computer reconstructed algorithm, while the previous phase less technique depends on two measurement surfaces or extra hardware to provide synthesized-reference-wave. The novel measurement method and reconstruction algorithm could be used in many applications as for the planar near field measurement for example. Simulated results are presented to demonstrate the complex field retrieval method and near-field to far field transformation.

Index Terms ─ Antenna measurements, hologram, near-field, and phase-less measurements.

I. INTRODUCTION

As well known the radiation characteristic of an antenna under test (AUT) is defined at far field distance and is therefore to be measured at the plane wave condition, which could be a physical or digital synthesis quiet zone. Far field range and compact range provide real plane wave where the pattern of the AUT [1] is measured directly. Near-field technique measures the radiation field in the near zone and calculates the radiation pattern [2, 3] employing post-processing near-field far field transformation (NFT) to obtain the synthesized plane wave. Although the phase error from the probe position can be corrected to some extent by employing some optical tracking device, it is very difficult to reduce the cable fluctuation phase error. The excessive cost of vector measurement and the phase accuracy restrict the application of near-field technique, especially for millimeter wave or sub millimeter bands. Phase less techniques are presented to overcome these difficulties, including planar [4, 5] and spherical measurements [6], where the costly phase measurement equipments are no longer required for the conventional NFT. The lack of phase information can be compensated by the additional amplitude on more measurement surfaces. The phase retrieval techniques rely on the wave propagation relationship between the measurement surfaces, e.g., Fourier angular spectrum for planar measurements, spherical modal expansion for spherical measurements. The amplitude scanning

Submitted On: March 29, 2013
Accepted On: Aug. 27, 2013

1054-4887 © 2013 ACES

measurements on more surfaces increase the burden of testing time and iterative reconstruction calculation, especially for electrically large or low side lobe AUTs.

Holography was firstly described by Dennis Gabor for the optical imaging systems. It is a two-step process: (1) recording the interference pattern (only amplitude) from the sum of wave fronts interacted with an object wave and a reference wave; (2) reconstruction of the object wave fronts from the recording. Gabor's holography was developed to the off-axis geometry for avoiding overlap by Emmett Leith and Juris Upatnieks in [7] and [8]. Based on these theories, the holographic near field phase less technique can be multiplied for antenna measurements. An off-axis reference antenna is included in the traditional near field measurement system. The interference amplitude of the AUT with the reference antenna is recorded by the amplitude scanning system. The complex near field of the AUT can be reconstructed by a computer with the measured interference amplitude, where the key process is how to separate and remove these unwanted terms including the reference wave and its complex conjugate. There are some ways such as Fresnel nonlinear phase approximation compensation [9] and synthesized-reference-wave [10-12] for the reference plane wave. Synthesized-reference required extra hardware including the directional coupler and a high quality flexible cable for the inner reference, and a variable attenuator and a phase shifter for the off-axis plane wave. There are some potential disadvantage for this method in the millimeter/submillimeter band because of the phase shifter's accuracy and the fluctuation error of the reference cables. This paper presents a novel near field computer reconstructed hologram (NFCRH), which will overcome the disadvantage in the synthesized-reference-wave holography. The complex near field of the antenna under test is reconstructed by computer, where the measured interference is just corrected by the multiplication with the virtual spherical reference wave and then filtered in the angular spectrum domain and the spatial domain.

In this paper the holographic near field phase less technique is presented for antenna measurements. Section II devotes the detailed concept and the rigorous reconstruction algorithm. Section III shows the simulated results of a medium antenna.

II. CONCEPT AND ALGORITHOM

As shown in Fig. 1, the signal from one coherent source is allocated to the antenna under test and reference antenna through a directional coupler, the interference field in the scanning area (planar, cylindrical, or spherical surface) is measured by a magnitude scanning probe. The control and process of measurement system is realized by a computer. The near-field amplitude and phase of the antenna under test is reconstructed by a virtual signal processing algorithm described in flow.

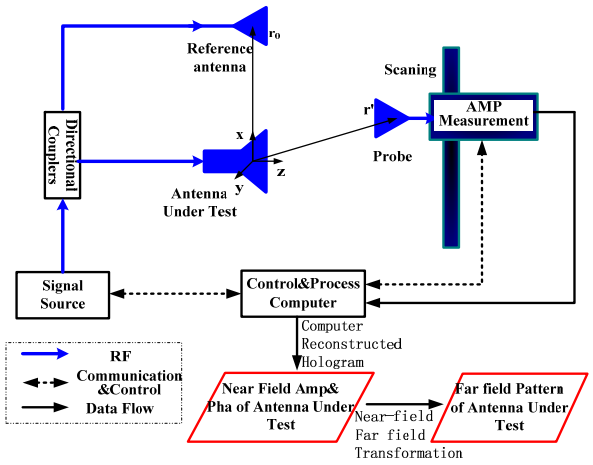

Fig. 1. Flowchart of holographic phaseless algorithm working with amplitude only data on one surface.

When the magnitude probe is scanning in near-field, the interference field in the scanning surface is summed coherently by the radiation field of test antenna and reference antenna, which can be expressed as,

$$E_g(\mathbf{r}') = A(\mathbf{r}')e^{j\phi(\mathbf{r}')} + Be^{-jk|\mathbf{r}_0-\mathbf{r}'|}/|\mathbf{r}_0-\mathbf{r}'|. \quad (1)$$

In which E_g is the interference field, $A(\mathbf{r}')$ and $\Phi(\mathbf{r}')$ is the amplitude and phase under test in any scanning position, separately. B is the unbalance factor between two channels. $e^{-jk|\mathbf{r}_0-\mathbf{r}'|}/|\mathbf{r}_0-\mathbf{r}'|$ is the reference spherical wave, $\mathbf{r_0}$, $\mathbf{r'}$ is the position vector of the probe and the reference source where the antenna under test is set to the zero position. k is the wave number in free space.

The amplitude obtained by the measurement system can be expressed as,

$$\begin{aligned}\left|E_{hf}(\mathbf{r}')\right|^2 &= [A(\mathbf{r}')e^{j\phi(\mathbf{r}')} + Be^{-jk|\mathbf{r}_0-\mathbf{r}'|}/|\mathbf{r}_0-\mathbf{r}'|]\times \\ &[A(\mathbf{r}')e^{j\phi(\mathbf{r}')} + Be^{-jk|\mathbf{r}_0-\mathbf{r}'|}/|\mathbf{r}_0-\mathbf{r}'|]^* \\ &= A^2(\mathbf{r}') + B^2/|\mathbf{r}_0-\mathbf{r}'|^2 \\ &+2BA(\mathbf{r}')/|\mathbf{r}_0-\mathbf{r}'|\cos[\phi(\mathbf{r}')+k|\mathbf{r}_0-\mathbf{r}'|]\ .\end{aligned} \tag{2}$$

The reconstruction step is implemented by a computer for the hologram. The reconstructed field E_r can be obtained when $|E_{hf}|^2$ is corrected by the multiplication with the virtual reference across the scanning surface,

$$\begin{aligned}E_r(\mathbf{r}') &= |\mathbf{r}_0-\mathbf{r}'|e^{-jk|\mathbf{r}_0-\mathbf{r}'|}\times\{A^2(\mathbf{r}') + B^2/|\mathbf{r}_0-\mathbf{r}'|^2 \\ &+2BA(\mathbf{r}')/|\mathbf{r}_0-\mathbf{r}'|\cos[\phi(\mathbf{r}')-k|\mathbf{r}_0-\mathbf{r}']\} \\ &= BA(\mathbf{r}')e^{-j[\phi(\mathbf{r}')+2k|\mathbf{r}_0-\mathbf{r}']} \\ &+[A^2(\mathbf{r}')|\mathbf{r}_0-\mathbf{r}'| + B^2/|\mathbf{r}_0-\mathbf{r}'|]e^{-jk|\mathbf{r}_0-\mathbf{r}'|} + A(\mathbf{r}')Be^{j\phi(\mathbf{r}')}.\end{aligned} \tag{3}$$

The reconstruction method is rigorous without Fresnel approximation [9]. Because the paraxial approximation is in conflict with the off-axis holography, the previous work using a spherical reference wave has been carried out with limited success [10]. Here a novel holographic near-field reconstruction technique is presented to overcome these limitations. The first two in equation (3) contain the space modulated carrier of reference signal, the off-axis design of reference signal leads to a higher spatial carrier, and makes the wave under test, the direct wave and the twin-wave reconstructed by holographic separable in spatial spectrum domain and the aperture back-projected. Both the amplitude and phase of the antenna under test are all low-frequency signals and varying slowly. They can be obtained through low-pass filtering. So we do Fourier transform for E_h, and then extract the low-frequency information. For a low gain antenna with the wide spatial spectrum it is not easy to separate the reconstructed spectrum. The holographic spectrum can be back-projected to the aperture where the reference source and under test is resolved by the imaging technique [13-16]. Finally, when the unwanted item have been filtered out the amplitude and phase of the antenna under test can be reconstructed by the inverse transform for the far field pattern.

III. SIMULATION RESULTS

Simulations have been done for a pyramidal horn as the antenna working at 15 GHz. The aperture field has been assumed to be a cosine function in the H-plane (oriented in the *x*-axis) with the dimensions a = 100 mm, and an uniform distribution in the E-plane (oriented in the *y*-axis) with the dimensions b = 70 mm. The near field amplitude and phase can be calculated by Rayligh-Sommerfeld formula [15] at a measurement plane (with the dimensions 800 mm × 800 mm, the sampling step 8 mm, which is less than λ/2, the distance 265 mm to the aperture under test). The antenna under test is set to zero position and the reference point source locates x = 175 mm and y = -360 mm. The interference amplitude of the antenna under test with the reference wave can be summed as the measurement value of the scanning probe.

The field reconstructed with hologram can be obtained using equation (3). These results can be transformed to angular spectrum by fast Fourier transformation (Fig. 2 (a)) where the spatial frequency is normalized to wave number, or back-projected to the aperture (Fig. 2 (b)) using near field imaging. The unwanted items can be separable and filtered out using low pass filter from the signal under test. In the angular spectrum domain these terms is separated in the k_x and k_y axis locations, while the imaging space is in the x and y axis. Because the reference antenna just locates at one point, it is easier to separate them in x and y space than in angular spectrum.

The complex near field reconstruction achieved by the angular and the image filter is show in Figs. 3 and 4, where the locations are the vertical and horizontal line in the measurement plane. These results show a high degree of agreement in the H-plane, however the level of agreement in the E-plane is reduced using angular filter. This is due to the point reference source location near to E-plane with a wider angular spectrum. The higher agreement has been obtained using image filter both in the E-plane and H-plane over the range ±asin (0.7) = ± 44.4°, which is near to the valid angle of NFT because those unwanted items can be removed more clearly due to the point source's spatial localization. Moreover, it can be seen that the calculated far field pattern is reconstructed from the complex near field. The accuracy of reconstructed far field can be reduced by the unbalance between the reference and test channels. The comparisons are shown in Figs. 5 and 6.

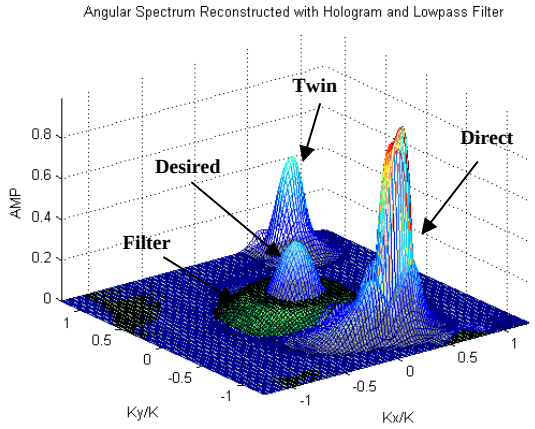

(a) Reconstructed and calculated angular spectrum of reconstructed field E_r.

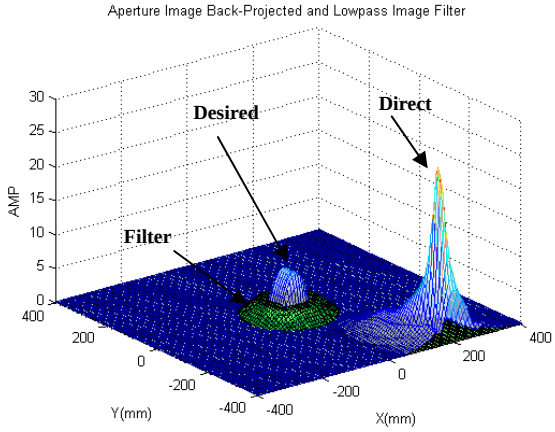

(b) Reconstructed and calculated aperture image of reconstructed field E_r.

Fig. 2. Calculated results for reconstruction and filtering.

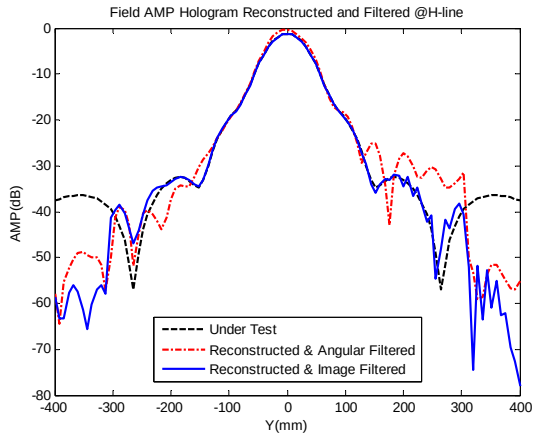

(a) Amplitude

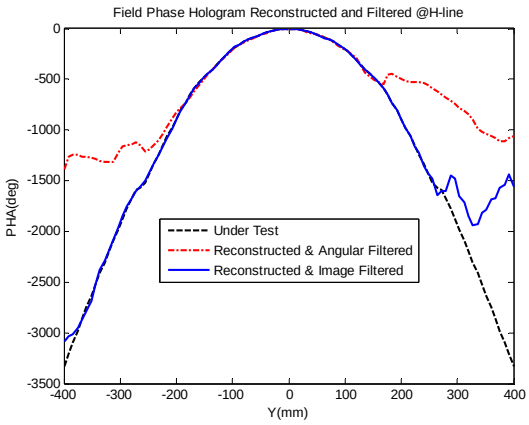

(b) Phase

Fig. 3. Near field amplitude and phase hologram reconstructed and angular/image filtered in the horizontal line.

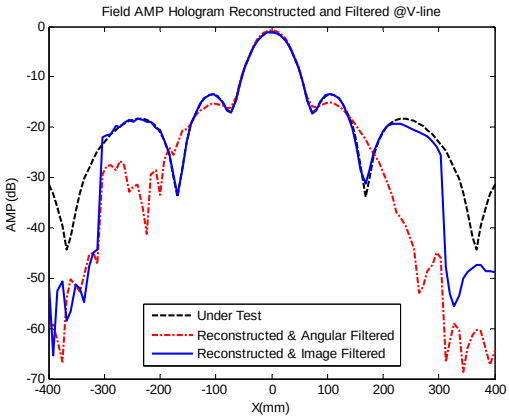

(a) Amplitude

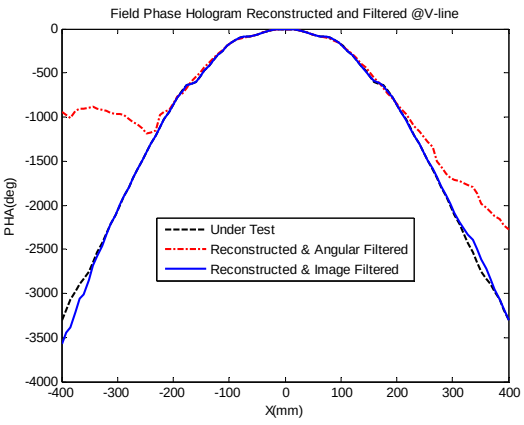

(b) Phase

Fig. 4. Near field amplitude and phase hologram reconstructed and angular/image filtered in the vertical line.

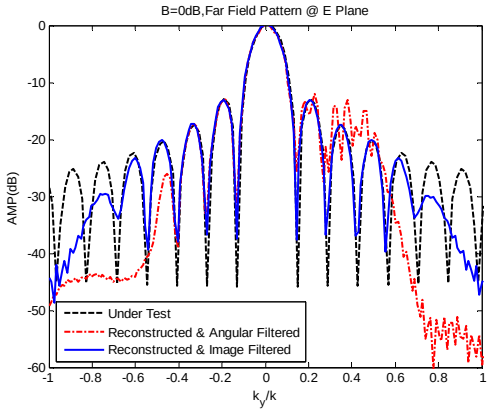

(a) E-Plane

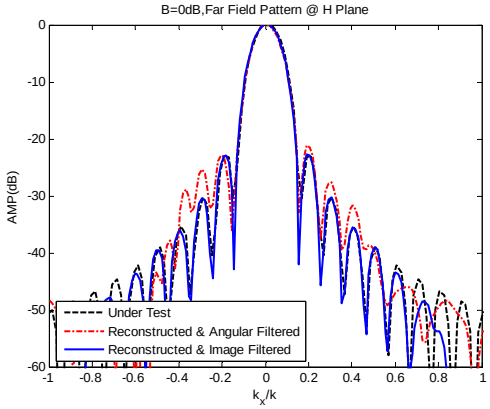

(b) H-Plane

Fig. 5. Calculated far field pattern from the reconstructed complex near field of the pyramidal horn under test in the E-and H-Planes (B = 0 dB).

IV. CONCLUSION

A holographic near-field phase less technique using the computer reconstruction algorithm to determine the complex near field and the far field pattern has been proposed in this paper. The innovation of the technique lays in the reference correction and the filter methods. In comparison with the previous technique, it does not require two measurement surfaces or extra hardware.

The effectiveness of the technique has been verified by numerical simulations using an aperture antenna with the medium gain. The results have been shown that the approach can provide the accurate near field and far field. The comparison of the filter methods show that the back-projected image filter more fits to the medium-gain antenna than angular spectrum filter. The accuracy of the reconstruction algorithm and filter methods has been confirmed by comparison of the results with the true value from the aperture.

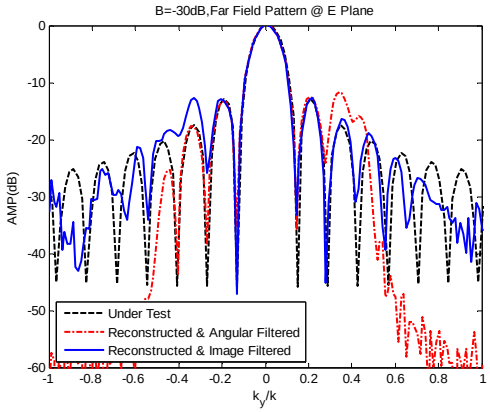

(a) E-Plane

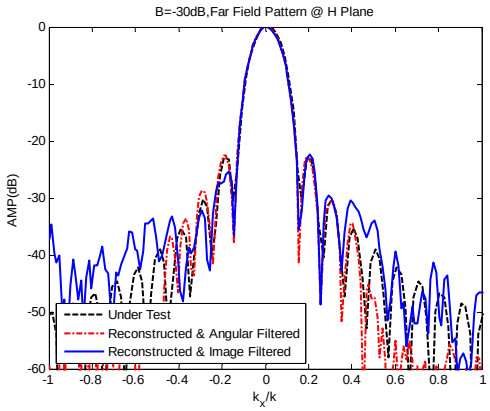

(b)H-Plane

Fig. 6. Calculated far field pattern from the reconstructed complex near field of the pyramidal horn under test in the E-and H-Planes (B = -30dB).

ACKNOWLEDGMENT

The paper is supported by the National Natural Science Foundation of China No. 61101003.

REFERENCES

[1] C. Balanis, *Modern Antenna Handbook*, John Wiley & Sons,Inc., 2008.

[2] A. Yaghjian, "An overview of near-field antenna measurements," *IEEE Trans. Antennas Propag.*, vol. 34, no. 1, pp. 30-45, 1986.

[3] E. Joy, "A brief history of the development of the near-field measurement technique at the Georgia Institute of the Technology," *IEEE Trans. Antennas Propag.*, vol. 36, no. 6, pp. 740-745, 1988.

[4] R. Yaccarino and Y. Rahmat-Samii, "Phaseless bi-polar planar near-field measurements and diagnostics of array antennas," *IEEE Trans. Antennas Propag.*, vol. 47, no. 3, pp. 574-583, 1999.

[5] S. Razavi and Y. Rahmat-Samii, "Resilience to probe-positioning errors in planar phaseless near-field measuremen," *IEEE Trans. Antennas Propag.*, vol. 58, no. 8, pp. 2632-640, 2010.

[6] C. Schmidt, S. Razavi, T. Eibert, and Y. Rahmat-Samii, "Phaseless spherical near-field antenna measurements for low and medium gain antennas," *Advances in Radio Science*, vol. 8, pp. 43-48, 2010.

[7] E. Leith and J. Upatnieks, "Wavefront reconstruction and communication theory," *J. Opt. Soc. Am.*, vol. 52, pp. 1123, 1962.

[8] E. Leith and J. Upatnieks, "Microscopy by wavefront reconstruction," *J. Opt. Society Amer.*, vol. 55, no. 5, pp. 569-570, 1965.

[9] J. Bennett, A. Anderson, P. McInnes, and A. Whittaker, "Microwave metrology of large antennas," *IEEE Trans. Antennas Propag.*, vol. 24, no. 3, pp. 295-303, 1976.

[10] D. Smith, M. Leach, and A. Sambell, "An indirect holographic method for determining antenna radiation patterns and imaging antenna fields," *Proc. IEEE Int. Antennas Propagat. Symp. Dig.*, San-Antonio, TX, vol. 4, pp. 706-709, June 16-21, 2002.

[11] D. Smith, M. Leach, M. Elsdon, and S. Foti, "Indirect holographic techniques for determining antenna radiation characteristics and imaging aperture fields," *IEEE Antennas Propag. Mag.*, vol. 49, no. 1, pp. 54-67, 2007.

[12] V. Schejbal, V. Kovarik, and D. Cermak, "Synthesized-reference-wave holography for determining antenna radiation characteristics," *IEEE Antennas Propag. Mag.*, vol. 50, no. 5, pp. 71-83, 2008.

[13] J. Fortuny, "Efficient Algorithms for Three-Dimensional Near-Field Synthetic Aperture Radar Imaging," *PhD Thesis, Germany: Faculty of Electrical Engineering University of Karslruhe*, 2001.

[14] Z. Li and G. He, "Two-dimensional near-field microwave imaging based on stolt-interpolation," *Chinese Journal of Radio Science*, vol. 22, no. 1, pp. 47-51, 2007. (in Chinese)

[15] F. Shen and A. Wang, "Fast-Fourier-transform based numerical integration method for the Rayleigh–Sommerfeld diffraction formula," *Applied Optics*, vol. 45, no. 6, pp. 1102-1110, 2006.

[16] L. Foged, L. Scialacqua, F. Mioc, M. Sabbadini, J. Quijano, and G. Vecchi, "Antenna diagnostics and measurement post processing using equivalent source technique," *27th Annual Review of Progress in Applied Computational Electromagnetics (ACES)*, pp. 459-463, April 2011.

Li Zhiping was born in Shanxi , China, 1979. He received his PhD in Electromagnetic Field and Microwave Technology from BeiHang University in 2008. He is a Lecture at the School of Electronics and Information Engineering BeiHang University. He studies Hologram CATR at Radio Laboratory of the Aalto University, Finland as a visiting researcher now. His research interests are Near-Field Measurement, Imaging, and CATR.

Wang Zhengpeng was born in Shandong Province, China in 1981. He received his B.Sc. degree in Electronic Science and Technology from Shandong University in 2004. He received his M.Sc. and PhD in Electromagnetic Field and Microwave Technology from BeiHang University in 2007 and 2012, respectively. He studied at Antenna and Applied Electromagnetic Laboratory in the University of Birmingham in 2009 and 2010 as a visiting researcher. He is now a postdoctoral fellowship as faculty member in University of Science and Technology Beijing. His research interests are reconfigurable filters, reconfigurable antennas and filtering antennas.

Wu Jianhua was born in Sichuan Province, China in 1977. He received his B.Sc. degree in Electronics Science and Technology from BeiHang University in 2000 and M.Sc. degree in Circuits and System in 2003. He is currently pursuing his PhD in Electromagnetic Field and Microwave Technology in BeiHang University. His research interests include compact antenna test range and microwave measurement system.

VFD Approach to the Computation TE and TM Modes in Elliptic Waveguide on TM Grid

A. Fanti, G. Montisci, G. Mazzarella, and G. A. Casula

Department of Electrical and Electronic Engineering
University of Cagliari, 09123, Piazza d'Armi, Cagliari, Italy
{alessandro.fanti, mazzarella, giorgiom, a.casula}@diee.unica.it

Abstract ― We describe here a vector finite difference approach (VFD) to the evaluation of eigenvalues and modes of elliptical waveguides. The FD is applied using a 2D elliptical grid in the waveguide section. A suitable Taylor expansion of the vector mode function allows to take exactly into account the boundary condition. To prevent the raising of spurious modes, our FD approximation results in a constrained eigenvalue problem, that we solve using a decomposition method. This approach has been evaluated comparing our results to known data for the elliptic case.

Index Terms - Elliptic waveguides, mode eigenvalues, and vector finite difference.

I. INTRODUCTION

The full-wave solution of waveguide problems can be faced both with general-purpose and specialized numerical techniques such as mode-matching (MM) [1] and methods of moments (MOM) [2]. The most effective of them is probably the mode-matching, since it exploit the modal structure of the field. However MM requires an accurate knowledge of the mode themselves to be implemented. More precisely, a quite large number of vector modes distribution and eigenvalues are needed and all the field modal functions must be known at the same set of points. The same type of information is also required in the analysis, using the method of moments (MoM), of thick-walled apertures [3-4] and slots [5]. Indeed, these apertures can be considered as stub waveguides, and the mode vectors of these guides are the natural basis functions for the MoM [6].

Apart from some simple geometries, where analytical evaluation of such mode vectors [7] is possible mode computation cannot be done in closed form, (or the closed-form solution is unsuitable for effective use), so, until now, many different numerical techniques have been proposed, and the most popular are based on FEM [8].

The most effective method to compute the field structure in a guide is the frequency-domain finite difference (FDFD) [9-10], i.e., the direct discretization of the vector eigenvalue problem [11-14]. Of course, for curved boundary, the standard rectangular grid is unfit, and a suitable curved grid should be used [15]. Moreover the vast majority of FDFD approach compute the Hertz potentials and then extract the vector mode functions using a numerical derivative. In this work we use an extension of vector generalization of FDFD approach presented in [16-17] to elliptic waveguides [18]. In order to improve both the accuracy and the computational effectiveness, a discretization grid fitting exactly the waveguide boundary is chosen. Both TE and TM modes are computed using an elliptic grid equivalent to the TM boundary condition [19] for scalar eigenvalue problem. For each grid point, a fourth-order Taylor approximations allow to replace the continuous eigenfunction problem with a discrete one. This leads to a matrix eigenvector problem, when additional conditions are added. These come out from the boundary conditions (which are included directly in the problem matrix), and the solenoidal or irrotational condition on mode vectors.

As a result, a matrix eigenvalue problem with linear constraints is obtained [20]. This is a known

Submitted On: June 27, 2013
Accepted On: Jan. 19, 2014

1054-4887 © 2013 ACES

linear algebra problems, which can be quite easily reduced to a standard eigenvalue problem [21], for which effective procedure exist.

II. DESCRIPTION OF THE TECHNIQUE

Each modes vector of a metallic waveguide $\vec{e}$ is an eigenfunction of the Helmholtz equation,

$$\begin{cases} \nabla_t^2 \vec{e} + k_t^2 \vec{e} = 0 \\ \vec{e} \times \vec{i}_n \big|_C = 0 \end{cases} \quad (1)$$

with additional condition, respectively (see Fig.1),

$$\nabla_t \cdot \vec{e} = 0 \quad \text{on C (TE modes)} \quad (2)$$

$$\nabla_t \times \vec{e} = 0 \quad \text{on C (TM modes),} \quad (3)$$

where C is the contour of the waveguide (see Fig. 1).

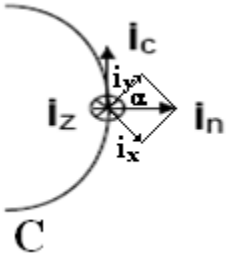

Fig. 1. Geometry of the waveguide contour.

Actually, in the MoM formulation, we need the modes of the surface magnetic current $\overrightarrow{M}$ equivalent to the transverse dielectric field $\vec{e}$. Therefore, we prefer a problem description in terms of the (two-dimensional) magnetic current $\overrightarrow{M}$ equivalent to the transverse field $\vec{e} = \vec{i}_z \times \overrightarrow{M}$. We can get from equation (1), for TM modes,

$$\begin{aligned} &\nabla_t^2 \vec{e} = \nabla_t \left(\nabla_t \cdot \vec{e} \right) = \nabla_t \left(\nabla_t \cdot \left(\vec{i}_z \times \overrightarrow{M} \right) \right) = \\ &-\nabla_t \left(\vec{i}_z \left(\nabla_t \times \overrightarrow{M} \right) \right) = -\left[\vec{i}_z \times \nabla_t \times \left(\nabla_t \times \overrightarrow{M} \right) \right] = \\ &\vec{i}_z \times \left[\nabla_t^2 \overrightarrow{M} - \nabla_t \left(\nabla_t \cdot \overrightarrow{M} \right) \right] \end{aligned} \quad (4)$$

$$\begin{aligned} &\nabla_t \times \vec{e} = \\ &\nabla_t \times \left[\vec{i}_z \times \overrightarrow{M} \right] = \vec{i}_z \left(\nabla_t \cdot \overrightarrow{M} \right) - \overrightarrow{M} \left(\nabla_t \cdot \vec{i}_z \right) + \\ &\left(\overrightarrow{M} \cdot \nabla_t \right) \vec{i}_z - \left(\vec{i}_z \cdot \nabla_t \right) \overrightarrow{M} = \vec{i}_z \left(\nabla_t \cdot \overrightarrow{M} \right) = 0. \end{aligned} \quad (5)$$

By equation (5), it follows that $\nabla_t \cdot \overrightarrow{M} = 0$. When substituted in equation (1), after replacing and collecting terms we get,

$$\begin{aligned} &\nabla_t^2 \vec{e} + k_t^2 \vec{e} = \\ &\vec{i}_z \times \left[\nabla_t^2 \overrightarrow{M} - \nabla_t \left(\nabla_t \cdot \overrightarrow{M} \right) \right] + k_t^2 \left(\vec{i}_z \times \overrightarrow{M} \right) = \\ &\vec{i}_z \times \left[\nabla_t^2 \overrightarrow{M} + k_t^2 \overrightarrow{M} \right]. \end{aligned} \quad (6)$$

The TM eigenvalue problem can therefore be rewritten as,

$$\nabla_t^2 \overrightarrow{M} + k_t^2 \overrightarrow{M} = 0 \quad (7)$$

with additional conditions. sentence,

$$\overrightarrow{M} \cdot \vec{i}_n \big|_C = 0 \quad (8)$$

$$\nabla_t \cdot \overrightarrow{M} = 0. \quad (9)$$

The dual procedure can be used to compute TE modes, and results in equations (7) and (8), while equation (9) must be replaced by,

$$\nabla_t \times \overrightarrow{M} = 0. \quad (10)$$

It is therefore clear that the only difference in computing $\vec{e}$ or $\overrightarrow{M}$ is the exchange of the additional conditions. We work, in the following, with $\overrightarrow{M}$ but the approach, using $\vec{e}$, is equivalent. It is worth noting that both, equations (9) and (10) are scalar equations (since $\overrightarrow{M}$ is transverse to the waveguide axis).

Vector FDFD approach to the solution of these problems is based on the replacement of equations (8), (9), and (10) with a discretized version. Therefore, $\overrightarrow{M}$ is evaluated only on the points of a elliptic grid (see Fig. 2) with spacing $\Delta u, \Delta v$, and the equations are replaced by difference equations. Also $\overrightarrow{M}$ is expressed in ellipitcal component so that equation (7) becomes,

$$\begin{aligned} &\left(\nabla_t^2 M \right)_u \overrightarrow{u_u} + \left(\nabla_t^2 M \right)_v \overrightarrow{u_v} = \\ &-k_t^2 \left(M_u \overrightarrow{u_u} + M_v \overrightarrow{u_v} \right). \end{aligned} \quad (11)$$

For each internal grid point (see Fig. 3), a fourth order Taylor approximation allows to evaluate the surface magnetic current in terms of the current samples at the neighboring points. The expression of the Laplace vector operator in elliptic coordinates [21] can be simplified if we let coordinates grid TE and TM $\vec{A} = h\vec{M}$, where

$h = \dfrac{1}{a_f\sqrt{\sinh^2 u + \sin^2 v}}$ is the common value of the scale factor, $2a_f$ being the inter-focal distance. The u component of $\nabla_t^2 \vec{M}$ then becomes,

$$\begin{aligned} &-\frac{1}{h^5}\cdot\frac{\partial h^2}{\partial u}\cdot\frac{\partial\left(A_u\right)}{\partial u}+\frac{1}{h^3}\frac{\partial^2\left(A_u\right)}{\partial u^2} \\ &+\frac{1}{h^5}\cdot\frac{\partial h^2}{\partial u}\cdot\frac{\partial\left(A_v\right)}{\partial v}-\frac{\partial h}{\partial v}\cdot\frac{1}{h^3}\cdot\frac{\partial\left(A_v\right)}{\partial u} \\ &+\frac{\partial h}{\partial v}\cdot\frac{1}{h^3}\cdot\frac{\partial\left(A_u\right)}{\partial v}+\frac{1}{h^5}\cdot\frac{\partial h^2}{\partial v}\cdot\frac{\partial\left(A_v\right)}{\partial u} \\ &-\frac{1}{h^5}\cdot\frac{\partial h^2}{\partial v}\cdot\frac{\partial\left(A_u\right)}{\partial v}+\frac{1}{h^3}\frac{\partial^2\left(A_u\right)}{\partial v^2}, \end{aligned} \tag{12}$$

and the v component,

$$\begin{aligned} &-\frac{1}{h^5}\cdot\frac{\partial h^2}{\partial v}\cdot\frac{\partial\left(A_u\right)}{\partial u}+\frac{1}{h^5}\cdot\frac{\partial h^2}{\partial v}\cdot\frac{\partial\left(A_v\right)}{\partial v} \\ &+\frac{1}{h^3}\cdot\frac{\partial^2\left(A_v\right)}{\partial v^2}+\frac{1}{h^3}\cdot\frac{\partial^2\left(A_v\right)}{\partial u^2} \\ &-\frac{1}{h^5}\cdot\frac{\partial h^2}{\partial u}\cdot\frac{\partial\left(A_v\right)}{\partial u}+\frac{1}{h^5}\cdot\frac{\partial h^2}{\partial u}\cdot\frac{\partial\left(A_u\right)}{\partial v}. \end{aligned} \tag{13}$$

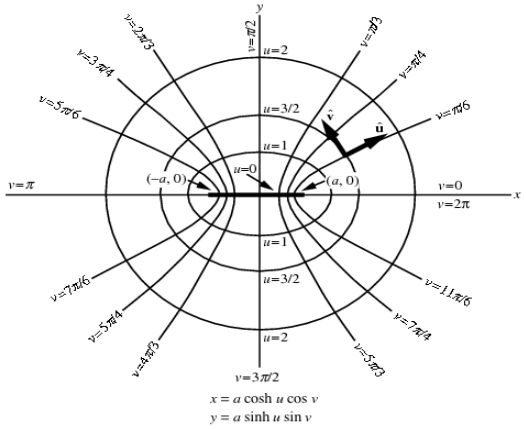

Fig. 2. Geometry of the elliptic cylindrical coordinates.

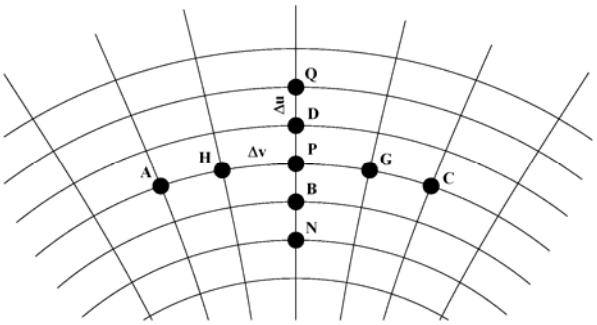

Fig. 3. Internal point of the elliptic cylindrical.

III. DISCRETIZATION OF THE EQUATIONS

For an internal point P as in Fig. 3 we can use a fourth-order Taylor expression. Letting,

$$\begin{aligned} A_i\left(u_p+\chi\right) &= A_{P,u}+\left.\frac{\partial A_u}{\partial u}\right|_P\cdot\chi+\left.\frac{1}{2}\frac{\partial^2 A_u}{\partial u^2}\right|_P\cdot\chi^2 \\ &+\left.\frac{1}{6}\frac{\partial^3 A_u}{\partial u^3}\right|_P\cdot\chi^3+\left.\frac{1}{24}\frac{\partial^4 A_u}{\partial u^4}\right|_P\cdot\chi^4 \end{aligned} \tag{14}$$

where i stands for both u and v, we have

$$A_{B,i}=A_i\left(u_p-\Delta u\right),\ A_{N,i}=A_i\left(u_p-2\Delta u\right)$$
$$A_{D,i}=A_i\left(u_p+\Delta u\right),\ A_{Q,i}=A_i\left(u_p+2\Delta u\right).$$

By combining these equations we find,

$$\begin{aligned} \left.\frac{\partial^2 A_u}{\partial u^2}\right|_P &= \frac{1}{14\Delta u^2}\cdot\begin{pmatrix}-A_{Q,u}-A_{N,u}\\+16A_{D,u}+16A_{B,u}\\-30A_{P,u}\end{pmatrix} \\ \left.\frac{\partial^2 A_v}{\partial u^2}\right|_P &= \frac{1}{14\Delta u^2}\cdot\begin{pmatrix}-A_{Q,v}-A_{N,v}\\+16A_{D,v}+16A_{B,v}\\-30A_{P,v}\end{pmatrix}. \end{aligned} \tag{15}$$

And similarly in v direction,

$$\begin{aligned} \left.\frac{\partial^2 A_v}{\partial v^2}\right|_P &= \frac{1}{14\Delta v^2}\cdot\begin{pmatrix}-A_{A,v}-A_{C,v}\\+16A_{G,v}+16A_{H,v}\\-30A_{P,v}\end{pmatrix} \\ \left.\frac{\partial^2 A_u}{\partial v^2}\right|_P &= \frac{1}{14\Delta v^2}\cdot\begin{pmatrix}-A_{A,u}-A_{C,u}\\+16A_{G,u}+16A_{H,u}\\-30A_{P,u}\end{pmatrix} \end{aligned} \tag{16}$$

for the second-order derivatives of equations (12) and (13). Also the first-order derivatives can be evaluated much in the same way as,

$$\begin{aligned}\frac{\partial A_u}{\partial u}&=\frac{8A_{D,u}+A_{N,u}-8A_{B,u}-A_{Q,u}}{12\Delta u}\\ \frac{\partial A_v}{\partial u}&=\frac{8A_{D,v}+A_{N,v}-8A_{B,v}-A_{Q,v}}{12\Delta u}\\ \frac{\partial A_u}{\partial v}&=\frac{8A_{C,u}+A_{H,u}-8A_{A,u}-A_{G,u}}{12\Delta v}\\ \frac{\partial A_v}{\partial v}&=\frac{8A_{C,v}+A_{H,v}-8A_{A,v}-A_{G,v}}{12\Delta v}.\end{aligned} \tag{17}$$

Equation (17) can be used also in equations (9) and (10) to get,

$$\begin{aligned}&\frac{1}{h^2}\cdot\left(\frac{\partial A_v}{\partial u}-\frac{\partial A_u}{\partial v}\right)=\frac{1}{12\Delta u h^2}\cdot\begin{bmatrix}8A_{D,v}+A_{N,v}\\ -8A_{B,v}-A_{Q,v}\end{bmatrix}-\\ &\frac{1}{12\Delta v h^2}\cdot\left[8A_{C,u}+A_{H,u}-8A_{A,u}-A_{G,u}\right]=0.\end{aligned} \tag{18}$$

In the same way, to discretize the condition of equation (9) (TM modes) we use equation (17) and get,

$$\begin{aligned}&\frac{1}{h^2}\cdot\left(\frac{\partial A_v}{\partial v}+\frac{\partial A_u}{\partial u}\right)=\\ &\frac{1}{h^2}\cdot\frac{8A_{C,v}+A_{H,v}-8A_{A,v}-A_{G,v}}{12\Delta v}+\\ &\frac{1}{h^2}\cdot\frac{8A_{D,u}+A_{N,u}-8A_{B,u}-A_{Q,u}}{12\Delta u}=0.\end{aligned} \tag{19}$$

For then points close to the boundary, such as P and B in Fig. 4, an approach different must be used to evaluate the u- derivatives since less than 2 grid points (D is not a grid point) are present outside. Therefore, both the equation for P and B require the mode vector at N.K.S.

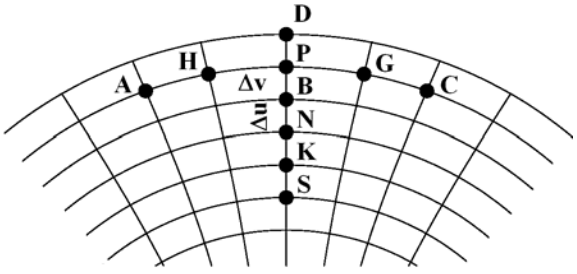

Fig. 4. Boundary point of the elliptic cylindrical.

Since $A_{k,i}=A_i\left(u_p-3\Delta u\right)$, $A_{s,i}=A_i\left(u_p-4\Delta u\right)$, $A_{K,i}$, $A_{S,i}$, $A_{B,i}$, and $A_{N,i}$ we can evaluate the derivatives by a suitable linear combination as,

$$\left.\frac{\partial^2 A_u}{\partial u^2}\right|_P=\frac{1}{12\Delta u^2}\cdot\begin{pmatrix}6A_{B,u}+4A_{N,u}\\ -A_{k,u}-9A_{P,u}\end{pmatrix} \tag{20}$$

$$\left.\frac{\partial^2 A_v}{\partial u^2}\right|_P=\frac{1}{12\Delta u^2}\begin{pmatrix}-104A_{B,v}+114A_{N,v}\\ -64A_{K,v}+11A_{S,v}\\ -43A_{P,v}\end{pmatrix}. \tag{21}$$

In equation (20) we have also included the BC $A_{D',u}=0$. In the same way, the condition of equations (9) and (10) becomes,

$$\begin{aligned}&\frac{1}{h^2}\cdot\left(\frac{\partial A_v}{\partial u}-\frac{\partial A_u}{\partial v}\right)=\\ &\frac{1}{12h^2\Delta u}\begin{pmatrix}-16A_{K,v}+36A_{N,v}\\ -48A_{B,v}+3A_{S,v}-25A_{P,v}\end{pmatrix}-\\ &\frac{1}{12h^2\Delta v}\cdot\left(8A_{C,u}+A_{H,u}-8A_{A,u}-A_{G,u}\right)=0\end{aligned} \tag{22}$$

$$\begin{aligned}&\frac{1}{h^2}\cdot\left(\frac{\partial A_v}{\partial v}+\frac{\partial A_u}{\partial u}\right)=\\ &\frac{1}{12h^2\Delta v}\cdot\left(8A_{C,v}+A_{H,v}-8A_{A,v}-A_{G,v}\right)+\\ &\frac{1}{12h^2\Delta u}\begin{pmatrix}-16A_{K,u}+36A_{N,u}\\ -48A_{B,u}+3A_{S,u}-25A_{P,u}\end{pmatrix}.\end{aligned} \tag{23}$$

The elliptical framework has different singular points, i.e., the foci and the points on the inter-focal segment, which require a different treatment, since the field are not regular there. For the focus of the ellipse (Fig. 5) we need the integral form of the eigenvalue equation. By integrating the first term of equation (7) on the surface S of Fig. 5,

$$\int_S \nabla_t^2\vec{M}\cdot dS=-k_t^2\int_S\vec{M}\cdot dS \tag{24}$$

wherein the Laplace operator is equal to,

$$\begin{aligned}\nabla_t^2\vec{M}&=\nabla_t\left(\nabla_t\cdot\vec{M}\right)-\nabla_t\times\nabla_t\times\vec{M}\\ &=\nabla_t\left(\nabla_t\cdot\vec{M}\right).\end{aligned} \tag{25}$$

Substituting in equation (7) we get,

$$\int_S \nabla_t \left(\nabla_t \cdot \vec{M}\right) \cdot dS = -k_t^2 \int_S \vec{M} dS \qquad (26)$$

and use of the theorem of the gradient [19] results in,

$$\int_S \nabla_t \left(\nabla_t \cdot \vec{M}\right) dS = \int_C (\nabla_t \cdot \vec{M}) \vec{i_n}\, dl =$$

$$\int_C \nabla_t \vec{M} \cdot \vec{i_n} \cdot dl = \int_C \frac{1}{h^2} \cdot \frac{\partial M_u}{\partial u} \cdot \vec{i_n} dl + \int_C \frac{1}{h^2} \cdot \frac{\partial M_v}{\partial v} \cdot \vec{i_n} dl. \qquad (27)$$

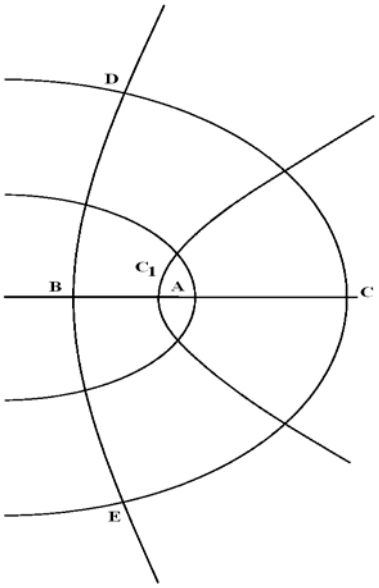

Fig. 5. Focus A of the ellipse.

The line integrals are divided in 4 parts (see Fig. 5). We describe here in details only the evaluation of the part over C_1. Letting $Q = \left(a, \frac{\Delta v}{2}\right)$ and $R = \left(\frac{\Delta u}{2}, 0\right)$, we have,

$$\int_{C_1} \frac{1}{h^2} \cdot \frac{\partial M_u}{\partial u} \cdot \vec{i_n} \cdot dl = \int_o^{\frac{\Delta u}{2}} \frac{1}{h^2} \cdot \frac{\partial M_u}{\partial u} \cdot \vec{i_n} \cdot h \cdot du =$$

$$\frac{1}{h} \cdot \vec{i_n}\Big|_{x_p} \cdot \int_o^{\frac{\Delta u}{2}} \frac{\partial M_u}{\partial u} \cdot du =$$

$$= \frac{-\vec{i_x}}{4h(Q)} \cdot \begin{bmatrix} M_u(A) + M_u(B) + M_u(C) \\ + M_u(D) + M_u(A)/2 \\ + M_u(B)/2 \end{bmatrix}, \qquad (28)$$

and

$$\int_{C_1} \frac{1}{h^2} \frac{\partial M_v}{\partial v} \vec{i_n} dl = \frac{1}{h} \vec{i_n} \frac{\partial M_v}{\partial v}\Big|_Q \int_0^{\frac{\Delta u}{2}} du =$$

$$\frac{1}{h(Q)} \left(-\vec{i_x}\right) \left(\frac{M_v(B) - M_v(A)}{\Delta v}\right) \frac{\Delta u}{2}. \qquad (29)$$

The same approach can be used for points on the inter-focal segment.

IV. SOLUTION OF CONSTRAINED EIGENVALUE PROBLEM

The discretized version of equation (1) for TM modes are obtained collecting equation (7) and the constraint in equations (8) and (9) to get a constrained eigenvalue problem. In the same way, equation (7) and the constraint of equations (8) and (10) are equivalent to the TE problems. Both can be written as,

$$\begin{cases} Ax = \lambda x \\ C^T x = 0 \end{cases} \qquad (30)$$

when, $\mathbf{A}$ is the discrete Laplace operator, including the boundary condition, and $\mathbf{C}$ is the discrete form of the constraint (2) or (3), $\mathbf{A}$ is a (2n, 2n) matrix, and $\mathbf{C}$ is (2n, m) with n > m and $\lambda = -k_t^2$. Following [20], we can solve equation (30) by letting $x = Q \cdot y$, where Q is the orthogonal (2n, 2n) matrix obtained by the QR factorization of the matrix C. Inserting $x = Q \cdot y$ in the first of equation (30), and pre-multiplying by Q^T we get,

$$A \cdot Q \cdot y = \lambda \cdot Q \cdot y \Rightarrow Q^T \cdot A \cdot Q \cdot y =$$

$$= \lambda \cdot Q^T \cdot Q \cdot y = \lambda y,$$ which can be recast as $By = \lambda y$, where $B = Q^T \cdot A \cdot Q$ is a (2n, 2n) matrix. This matrix can then be partitioned as,

$$B \cdot y = \lambda \cdot y \qquad \Rightarrow \begin{vmatrix} B_{11} & B_{12} \\ B_{21} & B_{22} \end{vmatrix} \cdot \begin{vmatrix} u \\ v \end{vmatrix} = \lambda \cdot \begin{vmatrix} u \\ v \end{vmatrix}. \qquad (31)$$

Now $C = Q \cdot R$, and the constraint becomes analogously $R^T \cdot y = 0$. Since R is partitioned into an invertible T_1 and a null matrix, both $n \cdot n$ then,

$$R^T \cdot y = 0 \qquad \Rightarrow \begin{vmatrix} T_1 & 0 \end{vmatrix} \cdot \begin{vmatrix} u \\ v \end{vmatrix} = 0. \qquad (32)$$

So the constraint can be expressed as $u = 0$ [23]. Therefore, we need to extract the eigenvalues of B_{22},

$$B_{22} \cdot v = \lambda v \tag{33}$$

where B_{22} is a (n, n) matrix. Therefore, we still needs the eigenvalues of an $n \cdot n$ matrix which, at variance of the scalar case, is a full one. After the eigenvalues and eigenvectors of B_{22} are computed (by standard routines) the actual eigenvectors x can be computed $x = Q \cdot \begin{vmatrix} 0 \\ v \end{vmatrix}$.

V. NUMERICAL RESULTS

The high-order VFD elliptic waveguide described in the previous section has been extensively validated, to assess its accuracy and effectiveness. It is well-known that an analytical solution is known for elliptic waveguide [18] but its effectiveness is very poor, so that it is unsuitable for our comparison. Therefore, we have chosen to test our data on the cut-off frequencies against the data of Zhang and Chen [24], which are very accurate but quite hard to compute, and the data of Tsogkas et.al. reported [25], which is the most recent paper on the topic. We have chosen a set of waveguide with a minor axis equal to 4 (in arbitrary units) and different eccentricities ex. The discretization step Δv has been always set to 1°, while different values of Δu has been used for each test. The resulting eigenvalue problem has been solved using standard MATLAB routines, on a PC with two Intel Xeon E5504 CPUs @ 2.00 GHz, 48 GB RAM, OS: MS Windows 7 Professional.

The main results of our validation are collected in Figs. 7 and 8. From them it appears that our VFD approach is able to give a very high accuracy, with a difference (with respect to the accurate data of [24]), which is smaller than 0.01%. On the other hand, the recent approach proposed in [25] has an accuracy around 1%. The results reported in Fig. 9, show also that the accuracy of our VFD is essentially independent from the eccentricity. The computation time of the VFD approach is the sum of the matrix filling time and the time needed to extract eigenvalue and eigenvectors of the full matrix. The latter is high since we deal with full matrices so that the total time is essentially equal to it. For example, for a grid with Du = 0.0065 and 72000 points, the filling matrix time is 6,10 sec and the time to extract eigenvalue and eigenvectors is 800 sec.

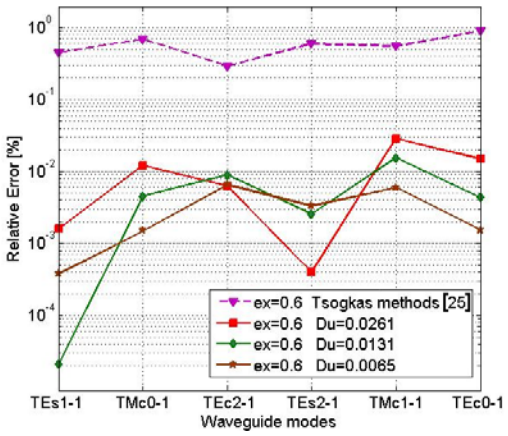

Fig. 7. Relative error on the cut-off frequency of the first modes of an elliptic waveguide ex = 0.6.

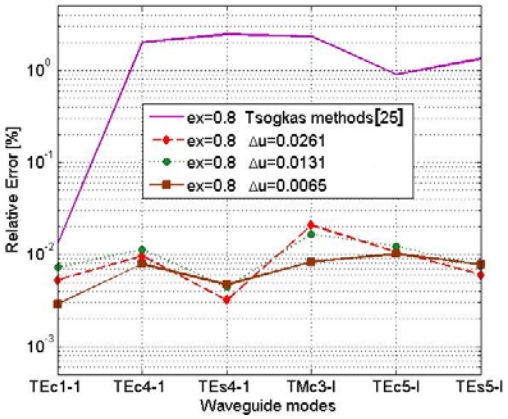

Fig. 8. Relative error on the cut-off frequency of the first modes of an elliptic waveguide ex = 0.8.

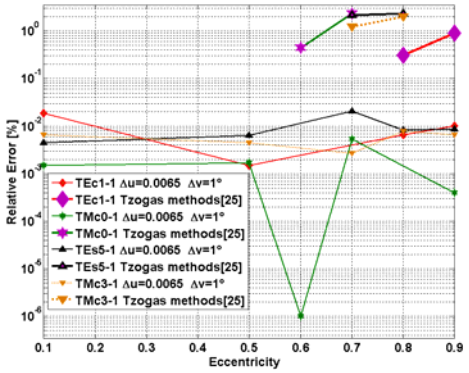

Fig. 9. Relative error on the cut-off frequency of the proposed VFD approach for different eccentricities.

VI. CONCLUSION

A new approach to the VFD computation of modes of an elliptic waveguide has been presented. We describe here a high vector finite difference frequency domain approach to the mode computation for both TE and TM modes. The main idea is the use of a discretization grid tailored to the waveguide boundary.

ACKNOWLEDGMENT

Alessandro Fanti, "Gratefully acknowledges Sardinia Regional Government for the financial support (P.O.R. Sardegna F.S.E. Operational Programme of the Autonomous Region of Sardinia, European Social Fund 2007-2013 - Axis IV Human Resources, Objective l.3, Line of Activity l.3.1 "Avviso di chiamata per il finanziamento di Assegni di Ricerca").

REFERENCES

[1] L. Prkna, M. Hubalek, and J. Ctyroky, "Vectorial eigenmode solver for bent waveguides based on mode matching," *IEEE Photonics Technology Letters*, vol. 16, no. 9, pp. 2057-2059, Sep. 2004.

[2] X. Zhu, D. Chen, and S. Wang, "A multistrip moment method technique and its application to the post problem in a circular waveguide," *IEEE Trans. Microw. Theory Tech.*, vol. 39, no. 10, pp. 1762-1766, Oct. 1991.

[3] G. Mazzarella and G. Montisci, "Effect of the longitudinal component of the aperture electric field on the analysis of waveguide longitudinal slots," *IEEE Transactions on Antennas and Propagation*, vol. 59, pp. 4334-4337, 2011.

[4] L. Deias, G. Mazzarella, and A. Mereu, "A new analysis method for thick planar EBG," *IEEE Proc. Int. Conf Antennas and Propagation Society International Symposium*, US, 5-8 July 2008.

[5] S. Rengarajan, "Compound radiating slot in a broad wall of a rectangular waveguide," *IEEE Transactions on Antennas Propagation*, vol. 37, pp. 1116-1124, 1989.

[6] G. Mazzarella and G. Montisci, "Accurate characterization of the interaction between coupling slots and waveguide bends in waveguide slot arrays," *IEEE Trans. Microw. Theory Tech.*, vol. 48, pp. 1154-1157, September 2000.

[7] P. Alinikula and K. Kunz, "Analysis of waveguide aperture coupling using the finite-difference time-domain method," *IEEE Microw. Guided Wave Lett.*, vol. 1, no. 8, pp. 189-191, Aug. 1991.

[8] M. Matthys, M. Botha, and D. Davidson, "Investigation of an explicit, residual-based, a posteriori error indicator for the adaptive finite element analysis of waveguide structures," *Applied Computational Electromagnetics Society (ACES) Journal*, vol. 21, no. 1, pp. 63-71, March 2006.

[9] R. Collin, *Field Theory of Guided Waves*, 2nd ed., IEEE Press, N.Y.

[10] T. Weiland, "Three dimensional resonator mode computation by finite difference method," *IEEE Trans. Magn.*, vol. 21, pp. 2340-2343, 1985.

[11] J. Hwang, "A compact 2-D FDFD method for modeling microstrip structures with nonuniform grids and perfectly matched layer," *IEEE Trans. Microw. Theory Tech.*, vol. 53, no. 2, pp. 653-659, Feb. 2005.

[12] D. White and J. Koning: "Computing solenoidal eigenmodes of the vector Helmholtz equation: a novel approach," *IEEE Trans. Magnetics*, vol. 38, no. 5, pp. 3420-3425, Sep. 2002.

[13] N. Thomas, P. Sewell, and T. Benson, "A new full-vectorial higher order finite-difference scheme for the modal analysis of rectangular dielectric waveguides," *Journal of Lightwave Technology*, vol. 25, no. 9, pp. 2563-2570, Sept. 2007.

[14] P. Lüsse, P. Stuwe, J. Schüle, and H.-G. Unger, "Analysis of vectorial mode fields in optical waveguides by a new finite difference method," *Journal of Lightwave Technology*, vol. 12, no. 3, pp. 487-494, March 1994.

[15] G. Hadley and R. Smith, "Full-vector waveguide modeling using an iterative finite-difference method with transparent boundary conditions," *Journal of Lightwave Technology*, pp. 465-469, March 1995.

[16] A. Fanti and G. Mazzarella, "A finite difference polar-Cartesian grid approach for mode computation in rounded-end waveguides," *Applied Computational Electromagnetics Society (ACES) Journal*, vol. 26, no. 9, pp. 768-775, Sep. 2011.

[17] A. Fanti, G. Mazzarella, G. Montisci, and G. Casula, "Computation of the modes of elliptic waveguides with a curvilinear 2D frequency-domain finite-difference approach," *Progress In Electromagnetics Research M*, vol. 26, pp.69-84, 2012.

[18] L. Chu, "Electromagnetic waves in elliptic hollow pipes of metal," *Journal. Appl. Phys.*, vol. 9, pp. 583-591, Sep. 1938.

[19] A. Fanti and G. Mazzarella, "Finite difference single grid evaluation of TE and TM modes in metallic waveguides," *IEEE Proc. I nt. Conf. Loughborough Antennas and Propagation Conference*, UK, pp. 517-520, 08-09 Nov. 2010.

[20] W. Gander, G. Golub, and U. Matt, "A constrained eigenvalue problem," *Linear Algebra*

and its Applications," vol. 114-115, pp. 815-839, March-April 1989.
[21] P. Halmos, *Linear Algebra Problem Book*, The Mathematical Association of America.
[22] J. Bladel, *Electromagnetic Fields*, Wiley Interscience, New York.
[23] G. Golub and C. Loan, *The Matrix Computations*, The Johns Hopkins University Press, 3rd ed., pp. 621.
[24] Sh. Zhang and Y. Chen, "Eigenmodes sequence for an elliptical waveguides with arbitrary ellipticity," *IEEE Trans. Microwave Theory and Techniques*, vol. 43, no. 1, pp. 227-230, Jan. 1995.
[25] G. Tsogkas, J. Roumeliotis, and S. Savaidis, "Cutoff wavelengths of elliptical metallic waveguides," *IEEE Trans. Microw. Theory Tech.*, vol. 57, no. 10, pp. 2406-2415, Oct. 2009.

Alessandro Fanti received the Laurea degree in electronic engineering and Ph.D. degree in electronic engineering and computer science from the University of Cagliari, Cagliari, Italy, in 2006 and 2012, respectively. He currently holds a post-doc scholarship for design of microwave components. His research activity involves the use of numerical techniques for modes computation of guiding structures.

Giorgio Montisci received the Laurea degree (summa cum laude) in electronic engineering and Ph.D. degree in electronic engineering and computer science from the University of Cagliari, Cagliari, Italy, in 1997 and 2000, respectively. Since November 2000, he is Assistant Professor of electromagnetic field at the Dipartimento di Ingegneria Elettrica ed Elettronica, University of Cagliari, teaching courses in electromagnetics and microwave engineering. His research activity is mainly focused on analysis and design of waveguide slot arrays, microwave holographic techniques for the diagnostic of large reflector antennas, numerical methods in electromagnetics, and printed antennas. He is author or coauthor of about 30 papers in international journals and Reviewer for EM Journals.

Giuseppe Mazzarella graduated Summa with Laude in Electronic Engineering from the Università "Federico II" of Naples in 1984 and obtained the Ph.D. in Electronic Engineering and Computer Science in 1989. In 1990, he became Assistant Professor at the Dipartimento di Ingegneria Elettronica at the Università "Federico II" of Naples. Since 1992, he is with the Dipartimento di Ingegneria Elettrica ed Elettronica of the Università di Cagliari, first as associate professor and then, since 2000, as full professor, teaching courses in Electromagnetics, Microwave, Antennas and Remote Sensing. His research activity has focused mainly on: efficient synthesis of large arrays of slots, power synthesis of array factor, microwave holography techniques for the diagnostic of large reflector antennas, use of evolutionary programming for inverse problems solving. He is author (or co-author) of about 50 papers in international journals, and is a reviewer for many EM journals.

Giovanni Andrea Casula received the Laurea degree (summa cum laude) in electronic engineering and Ph.D. degree in electronic engineering and computer science from the University di Cagliari, Cagliari, Italy, in 2000 and 2004, respectively. Since March 2006, he is an Assistant Professor of electromagnetic field and microwave engineering at the Dipartimento di Ingegneria Elettrica ed Elettronica, University of Cagliari. His current research interests are in the field of synthesis, analysis and design of wire, patch, and slot antennas. Dr. Casula serves as reviewer for several international journals and is a member of the Italian Electromagnetic Society (SIEm).

A Thin Dielectric Approximation for Calculation of Electromagnetic Scattering from 3-D Homogeneous Chiral Bodies

X. Deng[1], Y. Tian[1], J. Wang[2] , C. Gu[3], and Y. Zhou [3]

[1] Department of Electronic Information, Jiangsu University of Science and Technology, Zhenjiang 212003, China
dengxiaoqiao_521@163.com, yubo.tian@163.com

[2] State Key Laboratory of Millimeter Waves, School of Information Science and Engineering, Southeast University, Nanjing 210016, China
wangjian.seu@hotmail.com

[3] College of Electronic and Information Engineering, Nanjing University of Aeronautics and Astronautics, Nanjing 210016, China
gucq0138@sina.com, iamrealzyg@yahoo.com.cn

Abstract ─The full current thin dielectric sheet (TDS) approximation is considered for the problem of electromagnetic (EM) scattering by a three-dimensional (3-D) homogeneous thin chiral dielectric sheet. This approximation leads to surface integral equations (SIE) instead of the traditional volume integral equations (VIE). The surface of the thin dielectric region is modeled by triangle cells. Consequently, the number of unknowns is reduced by only surface meshes being utilized to discretize the dielectric geometry. Modified Rao-Wilson-Glisson (RWG) and pulse functions simultaneously for basis and testing functions are employed to approximate the tangential and normal currents in the dielectric layer. Then these SIEs are solved numerically using the conventional method of moments (MoM). The results by this approach show agreement with other methods while it greatly reduces the number of unknowns.

Keywords ─ Electromagnetic (EM) scattering, method of moments (MoM), pulse basis functions, Rao-Wilson-Glisson (RWG) basis functions, surface integral equations (SIE), thin dielectric sheet (TDS), and volume integral equations (VIE).

I. INTRODUCTION

Over recent years, many works have been contributed in an effort to develop efficient numerical techniques to solve the electromagnetic (EM) problems related to three-dimensional (3-D) chiral materials [1-4]. In [1], the finite-difference time-domain (FDTD) method was extended for chiral bodies. In [2], the transition matrix (T-matrix) method has been modified for chiral scatterer. However, each of these methods has certain limitations. In solving problems involving dispersive materials, time domain methods rely on the Z-transform of analytical expressions that describe dispersion properties of a material. The convergence problem restricts T-matrix's application. Extensive literatures in this area show a continuous interest in the method of moments (MoM) technique for solving EM problems related to chiral bodies [3, 4]. The MoM based on surface integral equation (SIE) method has been applied to deal with chiral problems [3]. For complex bodies consisting of inhomogeneous chiral media, the generalizing volume integral equation (VIE) method involving MoM has been extended to solve the EM scattering [4]. As we all well know, volumetric formulations have been widely used in calculating the electromagnetic scattering from arbitrarily shaped, inhomogeneous, dielectric bodies, however, it is also well known that

Submitted On: Sept. 4, 2012
Accepted On: Jan. 19, 2014

1054-4887 © 2013 ACES

burdened with the discretization of the object and the surrounding space, the number of unknowns of VIE rapidly grows with the size of the object, this results in larger memory requirement and longer solution time in solving the corresponding matrix equation, it limits the application of the simulation in the case of large and open radiation problems. The VIE is suitable for inhomogeneous dielectric structures. However, both VIE and general SIE only work well for relatively thick dielectric materials. They tend to suffer from unfavorable convergence problems when the dielectric is thin, especially less than one tenth of a wavelength in dielectric.

By the way, more and more nonmetallic structures have replaced metallic ones to reduce the weight or the radar cross section (RCS), especially in the construction of radome, so that an investigation of a thin dielectric layer is very important. For a very thin dielectric, a method called impedance boundary condition (IBC) algorithm has been extensively applied to analyze the thin and lossy dielectric coating problems [5]. In this way, the geometry is modeled by surface meshes for the SIE instead of volume meshes for the VIE. The unknown quantity is then greatly reduced, and the resultant SIE based on the IBC is then solved by MoM using the popular RWG basis. The algorithm can greatly facilitate the solving of EM scattering problems involving thin dielectric. Although the IBC method has a high computational efficiency, there still have some constraints of the algorithm because of its plane wave approximation. Another method for solving thin dielectric sheet problems is the thin dielectric sheet (TDS) approximation [6]. In this approximation, the algorithm adopts the assumption that the induced volume current remains constant and very small in the normal direction because the thickness of the dielectric sheet is relatively small compared to the wavelength, then only the tangential field component is considered, that is the contribution from the normal polarization current was ignored. In order to improve the accuracy of the equivalent model of TDS, a modified TDS approximation referred as the full current TDS approximation [7, 8] takes both tangential and normal currents into account, and the normal currents are described by the additional vector pulse basis functions in the algorithm. It can handle the EM scattering problem of TDS more efficiently. The full current TDS approximation is then extended to deal with the scattering problem for multilayer dielectric sheets and coating objects [9, 10].

As a generalization work of the previous methods, the main contribution of this paper therefore is that the full current TDS approximation strategy is extended and applied to the scattering problems for thin chiral dielectric sheet. The rest of the paper is organized as follows. Section 2 gives a concise introduction to the full current TDS formulations derived from VIE equations to describe electromagnetic scattering involving thin chiral dielectric sheet. In section 3, The MoM solution procedure and matrix evaluation are described. Numerical examples are demonstrated and discussed in section 4. Last but not least, some concluding remarks are given in section 5.

II. FORMULATION

A. TDS surface integral formulation

Let us consider a thin homogeneous bi-isotropic sheet, as illustrated in Fig. 1. The geometry is assumed to be illuminated by a plane wave incident fields $\mathbf{E}^{inc}, \mathbf{H}^{inc}$. The expressions of electric and magnetic fields inside the bi-isotropic region are relatively complex due to the introduction of bi-isotropic constitutive relations, namely,

$$\mathbf{D} = \varepsilon \mathbf{E} + \xi \mathbf{H} \tag{1}$$

$$\mathbf{B} = \mu \mathbf{H} + \zeta \mathbf{E}, \tag{2}$$

where ε and μ are the permittivity and permeability, respectively, ξ and ζ are bi-isotropic parameters. $\mathbf{E}$, $\mathbf{H}$, $\mathbf{D}$, and $\mathbf{B}$ are the complex-valued phasors of the electric field, magnetic field, displacement vector, and magnetic induction intensity, respectively. And the $\mathbf{D}$ and $\mathbf{B}$ can be also written as,

$$\mathbf{D} = \varepsilon \mathbf{E} + (\chi_r - i\kappa_r)\sqrt{\varepsilon\mu}\mathbf{H} \tag{3}$$

$$\mathbf{B} = \mu \mathbf{H} + (\chi_r + i\kappa_r)\sqrt{\varepsilon\mu}\mathbf{E}, \tag{4}$$

where κ_r and χ_r are chirality parameter and tellegen parameter, respectively. A bi-isotropic medium with $\chi_r = 0$ and $\kappa_r = 0$ is an ordinary magneto-dielectic medium, the one with $\chi_r = 0$ and $\kappa_r \neq 0$ then is called chiral medium, while the one with $\chi_r \neq 0$ and $\kappa_r = 0$ is named Tellegen medium.

In the paper, we only study the chiral problem as a special case. However, the method is applicable to any thin bi-isotropic media situation.

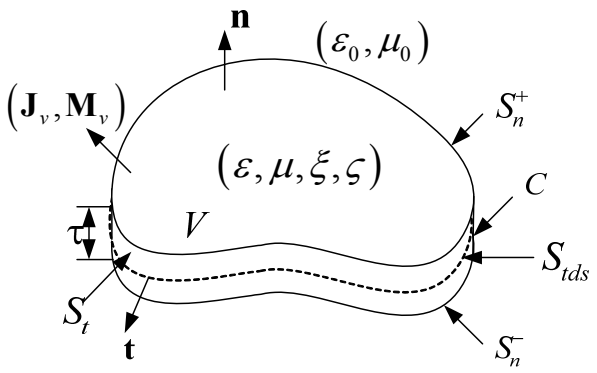

Fig. 1. Configuration of a thin chiral sheet.

Then $\mathbf{E}$, $\mathbf{H}$ can be expressed as,

$$\mathbf{E} = \alpha_1 \mathbf{D} + \alpha_2 \mathbf{B} \tag{5}$$

$$\mathbf{H} = \alpha_3 \mathbf{D} + \alpha_4 \mathbf{B}, \tag{6}$$

where the parameters $\alpha_i (i = 1,2,3,4)$ are given by equations (26) to (29) in the appendix.

The polarization volume electric/magnetic current density in the chiral dielectric are defined by,

$$\mathbf{J}_v = i\omega\beta_1 \mathbf{D} + i\omega\beta_2 \mathbf{B} \tag{7}$$

$$\mathbf{M}_v = i\omega\beta_3 \mathbf{D} + i\omega\beta_4 \mathbf{B}, \tag{8}$$

where the parameters $\beta_i (i = 1,2,3,4)$ are given by equations (30) to (33) in the appendix.

Inside the thin dielectric medium, the incident electric field, scattered electric field, and total electric field satisfy,

$$\mathbf{E}^{inc}(\mathbf{r}) = \mathbf{E} - \mathbf{E}_{die}^{scat}(\mathbf{r}), \quad \mathbf{r} \in V \tag{9}$$

where $\mathbf{E}_{die}^{scat}$ stands for the scattered electric field from the TDS, $\mathbf{r}$ denotes the field point. Similarly, by electric-magnetic duality in Maxwell theory, the relationships among the incident magnetic field, scattered magnetic field, and total magnetic field in the thin sheet can be expressed as,

$$\mathbf{H}^{inc}(\mathbf{r}) = \mathbf{H} - \mathbf{H}_{die}^{scat}(\mathbf{r}), \quad \mathbf{r} \in V \tag{10}$$

where $\mathbf{H}_{die}^{scat}$ stands for the scattered magnetic field from the TDS. Scattering electric and magnetic fields from the dielectric region are written as,

$$\mathbf{E}_{die}^{scat}(\mathbf{r}) = -i\omega\mu_0 \int_v G(\mathbf{r},\mathbf{r}')\mathbf{J}_v(\mathbf{r}')dV' + \frac{\nabla}{i\omega\varepsilon_0}\int_v G(\mathbf{r},\mathbf{r}')\left(\nabla' \cdot \mathbf{J}_v(\mathbf{r}')\right)dV' - \nabla \times \int_v G(\mathbf{r},\mathbf{r}')\mathbf{M}_v(\mathbf{r}')dV' \tag{11}$$

$$\mathbf{H}_{die}^{scat}(\mathbf{r}) = -i\omega\varepsilon_0 \int_v G(\mathbf{r},\mathbf{r}')\mathbf{M}_v(\mathbf{r}')dV' + \frac{\nabla}{i\omega\mu_0}\int_v G(\mathbf{r},\mathbf{r}')\left(\nabla' \cdot \mathbf{M}_v(\mathbf{r}')\right)dV' - \nabla \times \int_v G(\mathbf{r},\mathbf{r}')\mathbf{J}_v(\mathbf{r}')dV' \tag{12}$$

where $G(\mathbf{r},\mathbf{r}')$ is the scalar Green's function in free space which is defined by $G(\mathbf{r},\mathbf{r}') = \frac{e^{ik_0|\mathbf{r}-\mathbf{r}'|}}{4\pi|\mathbf{r}-\mathbf{r}'|}$. The thickness of dielectric layer is quite limited compared to the wavelength, so the fields vary very little with respect to the normal direction. Volume integral can be replaced by the surface integral at the middle section, as,

$$\int_v dV' \approx \tau \int_{S_{tds}} dS'. \tag{13}$$

Thus, the volume integrals degenerate to surface integrals and the number of unknowns is evidently reduced because only surface meshes are utilized to discretize the geometry. In addition, to transform the volume integrals in equations (11) and (12) to surface integrals, it is necessary to decompose the $\mathbf{D}$ and $\mathbf{B}$ into tangential and normal components within the TDS, that is,

$$\mathbf{D} = \mathbf{D}_t + \mathbf{D}_n \tag{14}$$

$$\mathbf{B} = \mathbf{B}_t + \mathbf{B}_n. \tag{15}$$

According to [7],

$$\nabla \cdot (\beta_i \mathbf{D}) = \nabla\beta_i \cdot \mathbf{D} + \beta_i \nabla \cdot \mathbf{D} = \nabla\beta_i \cdot \mathbf{D}, \quad (i = 1,2) \tag{16}$$

and take equations (7), (8), (13), and (16) into equations (11) and (12), the integrals in equations (11) and (12) then can be approximated as,

$$\begin{aligned}\mathbf{E}_{die}^{scat}(\mathbf{r}) = {} & \omega^2\mu_0\tau\int_{S_{tds}} G(\beta_1\mathbf{D})dS' + \frac{\nabla}{\varepsilon_0}\oint_{S_t+S_n^+ +S_n^-} G\Delta\beta_1\mathbf{n}'\cdot\mathbf{D}dS' \\ & + \omega^2\mu_0\tau\int_{S_{tds}} G(\beta_2\mathbf{B})dS' + \frac{\nabla}{\varepsilon_0}\oint_{S_t+S_n^+ +S_n^-} G\Delta\beta_2\mathbf{n}'\cdot\mathbf{B}dS' \\ & - i\omega\tau\beta_3\int_{S_{tds}} \nabla G\times\mathbf{D}dS' - i\omega\tau\beta_4\int_{S_{tds}} \nabla G\times\mathbf{B}dS'\end{aligned} \tag{17}$$

$$\mathbf{H}_{die}^{scat}(\mathbf{r}) = \omega^2\varepsilon_0\tau\int_{S_{tds}} G(\beta_3\mathbf{D})dS' + \frac{\nabla}{\mu_0}\oint_{S_t+S_n^+ +S_n^-} G\Delta\beta_3\mathbf{n}'\cdot\mathbf{D}dS' + \omega^2\varepsilon_0\tau\int_{S_{tds}} G(\beta_4\mathbf{B})dS' + \frac{\nabla}{\mu_0}\oint_{S_t+S_n^+ +S_n^-} G\Delta\beta_4\mathbf{n}'\cdot\mathbf{B}dS' - i\omega\tau\beta_1\int_{S_{tds}}\nabla G\times\mathbf{D}dS' - i\omega\tau\beta_2\int_{S_{tds}}\nabla G\times\mathbf{B}dS' \quad (18)$$

where S_n^+, S_n^-, S_t, S_{tds} denote top, bottom, side, and middle surfaces, respectively, and $\mathbf{n}'$ is the unit normal vector directing out of the TDS at the interfaces. Take equations (14) and (15) into equations (17) and (18), the formulas (34) and (35) for $\mathbf{E}_{die}^{scat}$ and $\mathbf{H}_{die}^{scat}$ can be further obtained. Then the TDS SIEs are obtained by taking equations (34) and (35) into equations (9) and (10).

B. MoM solution

Because the electric flux in equation (14) is decomposed into normal and tangential parts, it can be specified by two sets of basis functions numerically. It is the same to magnetic intensity in equation (15). As a result, to solve the TDS SIEs by the MoM, four sets of basis functions are employed. For TDS, the modified RWG basis [7] is used for the tangential current since charge is enforced to exist at the edges between air-dielectric interfaces, and the pulse basis [7-8] is used for the normal current. The difference between the modified RWG basis and the conventional RWG basis [11] is that the former defines half basis functions at the edges. The electric flux and magnetic intensity are approximated by four sets of basis functions as follows,

$$\mathbf{B}_t \approx \sum_{d=1}^{N_d} B_d\mathbf{f}_d(\mathbf{r}) \quad (19)$$

$$\mathbf{B}_n^+ \approx \sum_{n=1}^{N} B_n\mathbf{P}_n(\mathbf{r}), \quad (20)$$

$$\mathbf{D}_t \approx \sum_{d=1}^{N_d} D_d\mathbf{f}_d(\mathbf{r}), \quad (21)$$

$$\mathbf{D}_n^+ \approx \sum_{n=1}^{N} D_n\mathbf{P}_n(\mathbf{r}), \quad (22)$$

where N_d is the number of total edges (including shared and boundary edges) and N is the total number of triangles T_n of the TDS. $\mathbf{f}_d(\mathbf{r})$ is the modified RWG basis defined as,

$$\mathbf{f}_d(\mathbf{r}) = \begin{cases} \dfrac{l_d}{2A_d^{\pm}}\boldsymbol{\rho}_d^{\pm} & \mathbf{r}\in T_d^{\pm} \\ 0 & otherwise \end{cases} \quad (23)$$

where l_d is the length of the edge and $A_d^{\pm}$ is the area of the corresponding triangle $T_d^{\pm}$. It should be noted that for half basis, only A_d^+ is defined at the boundary edges of an open surface. $\mathbf{P}_n(\mathbf{r})$ is the vector pulse basis of triangles, defined as,

$$\mathbf{P}_n(\mathbf{r}) = \begin{cases} \mathbf{n}_n & \mathbf{r}\in T_n \\ 0 & \mathbf{r}\notin T_n \end{cases} \quad (24)$$

where $\mathbf{n}_n$ is the unit normal vector of the triangle T_n.

To convert the TDS SIEs into matrix equations, by Galerkin's testing procedure, we test the TDS SIEs with the modified RWG basis and pulse basis. The matrix equation $[Z][I]=[V]$ can be written as,

$$\begin{bmatrix} Z_{TT}^{DD} & Z_{TN}^{DD} & Z_{TT}^{DB} & Z_{TN}^{DB} \\ Z_{NT}^{DD} & Z_{NN}^{DD} & Z_{NT}^{DB} & Z_{NN}^{DB} \\ Z_{TT}^{BD} & Z_{TN}^{BD} & Z_{TT}^{BB} & Z_{TN}^{BB} \\ Z_{NT}^{BD} & Z_{NN}^{BD} & Z_{NT}^{BB} & Z_{NN}^{BB} \end{bmatrix}\begin{bmatrix} D_d \\ D_n \\ B_d \\ B_n \end{bmatrix} = \begin{bmatrix} V_t^E \\ V_n^E \\ V_t^H \\ V_n^H \end{bmatrix} \quad (25)$$

where the subscript *TT* denotes the interaction between tangential current, *TN* and *NT* denotes the interaction between tangential and normal current, *NN* denotes the interaction between normal current. The superscript alphabet *D* and *B* involves electric current and magnetic current, respectively. V_t^E and V_t^H denote the excitation from incident tangential electric and magnetic fields, and V_n^E and V_n^H denote the excitation from incident normal electric and magnetic fields. B_d and D_d are $N_d\times 1$ unknown matrices, and D_n and B_n are $N\times 1$ unknown matrices. The elements of $[Z]$ are given in the appendix.

III. NUMERICAL RESULTS

In this section, three examples are investigated. Only chiral problems are considered as a special case, so $\chi_r = 0$ in the following examples. The first example is a dielectric sphere shell under the illumination of a plane wave incident from the direction where $(\theta,\varphi)=(0^\circ,0^\circ)$ at 0.2 GHz. The sphere is with inner radius 1.0 m, outer radius 1.05m, and $\varepsilon_r = 2.6$, $\mu_r = 1$, $\kappa_r = 0$. It is modeled

by 1866 triangles. Figure 2 (a) and (b) show the total RCS at $\varphi = 0^{\circ}$ and $\varphi = 90^{\circ}$. The circle lines by our proposed TDS SIE agree well with the solid lines by the Mie series.

In the second example, we consider a thin chiral plate as an example. In order to demonstrate the validity and advantages of our method, the results calculated by VIE are also given for comparison. The dimension of the chiral plate is $1m \times 0.5m \times 0.05m$ (in x, y, and z dimensions, respectively), and the constitutive parameters are $\varepsilon_r = 2.6$, $\mu_r = 1$, and $\kappa_r = 0$, 0.1, 0.3, 0.5, 0.7. The structure is illuminated by a plane wave incident from the direction where $(\theta, \varphi) = (180^{\circ}, 0^{\circ})$. It is modeled by 400 triangles for the TDS SIE and 1369 tetrahedrons for VIE. Figure 3 shows the normalized co-polarized and cross-polarized bistatic RCS ($\sigma_{\theta\theta}/\lambda_0^2$ and $\sigma_{\phi\theta}/\lambda_0^2$) for scattering angle $\varphi = 0^{\circ}$ calculated by our code and VIE. In order to show more clearly, the curves calculated by VIE are plotted only when $\kappa_r = 0.5$. From Fig. 3, we can conclude that they are in good agreements. Small discrepancy exists due to the approximation of TDS formulations. We also can see that there are big differences among $\sigma_{\phi\theta}$ with different κ_r. The cross-polarized RCS $\sigma_{\phi\theta}$ of the TDS with $\kappa_r = 0$ is very small and can be ignored when compared with those with $\kappa_r \neq 0$. With the increase of κ_r, the cross-polarized RCS is gradually increasing up covering the observed angles ranges from 120^{o} to 180^{o}. It confirms that the truth of one distinct manifestation of "chirality" is the existence of a cross-polarization component in the field scattered by a chiral object [12].

Finally, the TDS approximation is applied to calculate $\sigma_{\theta\theta}/\lambda_0^2$ and $\sigma_{\phi\theta}/\lambda_0^2$ of a thin chiral circular cylinder shell with radius 0.6 m, thickness 0.05 m, and height 0.2 m. The constitutive parameters are $\varepsilon_r = 2.6$, $\mu_r = 1$, and $\kappa_r = 0.0$, 0.2, 0.4, 0.6. The structure is illuminated by a plane wave incident from the direction where $(\theta, \varphi) = (0^{\circ}, 0^{\circ})$. Figure 4 (a) and (b) show the normalized co-polarized and cross-polarized bistatic RCS ($\sigma_{\theta\theta}/\lambda_0^2$ and $\sigma_{\phi\theta}/\lambda_0^2$) for scattering angle $\varphi = 0^{\circ}$, respectively. It is modeled by 480 triangles for the TDS SIE and 1038 tetrahedrons for VIE. The results when $\kappa_r = 0.2$ calculated by VIE (solid lines) are plotted for comparison. We can see from Fig. 4, the RCS results calculated by our code are in good agreements with those by VIE. It further confirms that the cross-polarization component in the field scattered by a chiral object is existing. It shows the superiority of the method used in the paper over VIE on the treatment of TDS.

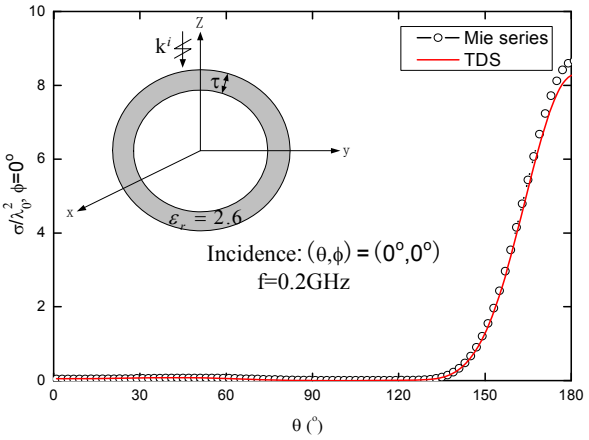

(a)

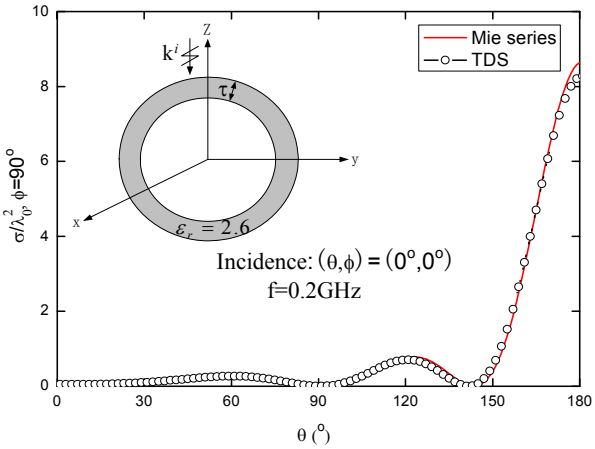

(b)

Fig. 2. Normalized total scattering cross section of a dielectric sphere shell in free space characterized by $\varepsilon_r = 2.6$, $\mu_r = 1$, $\kappa_r = 0$; (a) RCS at $\varphi = 0^{\circ}$ and (b) RCS at $\varphi = 90^{\circ}$.

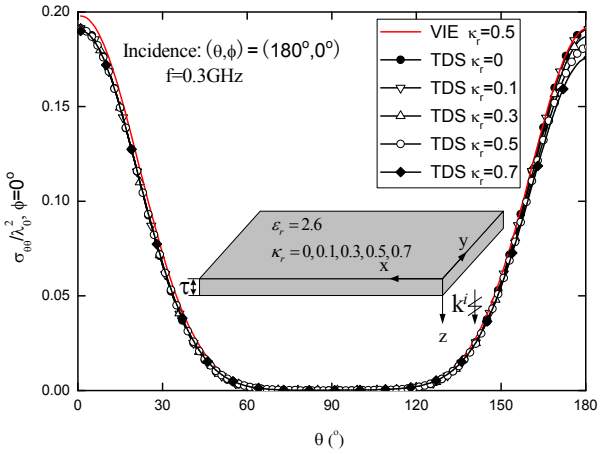

(a)

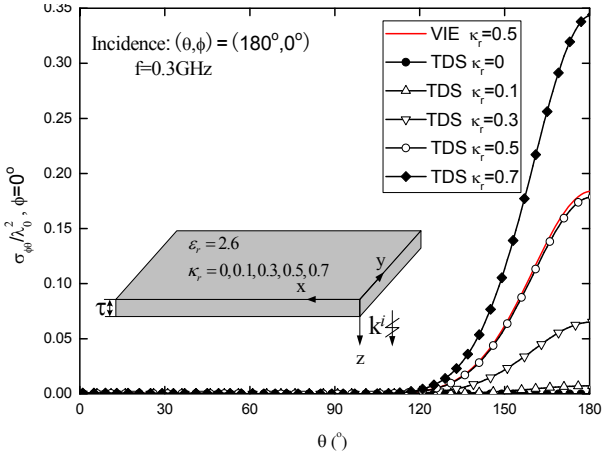

(b)

Fig. 3. Normalized scattering cross section of a thin chiral plate in free space characterized by $\varepsilon_r = 2.6$, $\mu_r = 1$, and $\kappa_r = 0, 0.1, 0.3, 0.5, 0.7$; (a) co-polarized and (b) cross-polarized components.

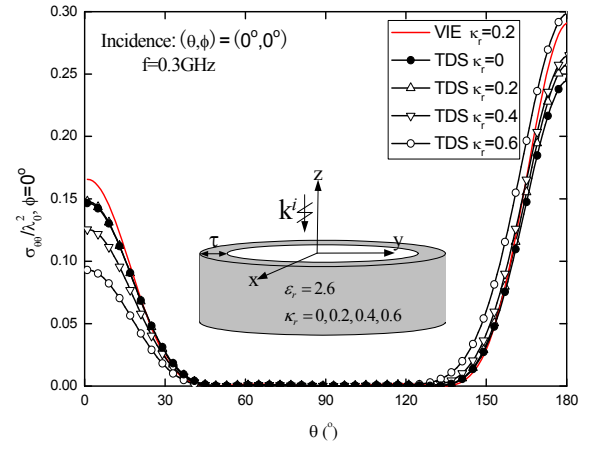

(a)

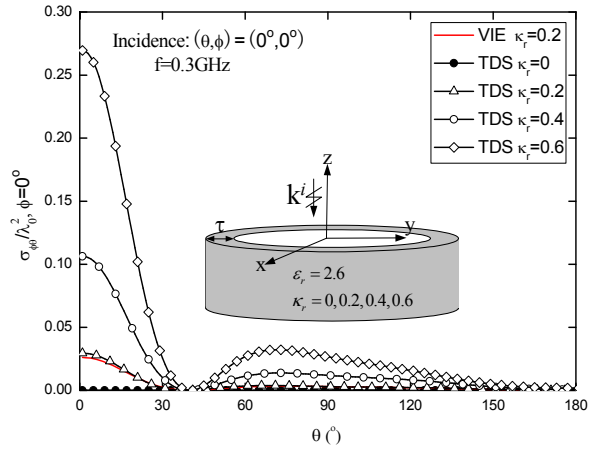

(b)

Fig. 4. Normalized scattering cross section of a chiral circular cylinder shell in free space characterized by $\varepsilon_r = 2.6$, $\mu_r = 1$, and $\kappa_r = 0, 0.2, 0.4, 0.6$; (a) co-polarized and (b) cross-polarized components.

IV. CONCLUSION

The TDS SIE method used in the paper leads to SIE instead of the traditional VIE. Consequently, the number of unknowns is reduced by only surface meshes being utilized to discretize the thin chiral dielectric sheet. Apparently, the approach in the paper needs fewer unknowns compared with VIE. In addition, it is easier for meshing. Modified RWG and pulse functions for basis and testing functions are employed to approximate the tangential and normal currents in the thin chiral dielectric layer. Finally, the TDS method are verified by Mie series and VIE by considering different shapes, and the simulation results show good agreements. Obviously, it is more advantageous to solve some thin sheet problems by TDS SIE than VIE. We further confirm that the truth of one distinct manifestation of "chirality" is the existence of a cross-polarization component in the field scattered by a chiral object in the paper.

The TDS approximation in the paper can deal with thin electric, chiral, and bi-isotropic media effectively. In spite of this, the method has its limitations because it is an approximate method. Scattering or radiation problems of a TDS coating metal are also of practical interest, the task is currently in progress and it will be reported later.

ACKNOWLEDGMENT

The work is supported by the National Nature Science Foundation of China under Grant No. 61071019, the Joint Funding projects of the Aerospace Science Foundation Office of China No. 2008ZA52006, the Innovation Program for Graduate Education of Jiangsu Province under Grant No. CXLX13_092.

APPENDIX

In this appendix, the parameters in equations (5), (6), (7), and (8) are given as,

$$\alpha_1 = \frac{\mu}{\varepsilon\mu - \zeta\xi} \tag{26}$$

$$\alpha_2 = \frac{-\xi}{\varepsilon\mu - \zeta\xi}\ , \tag{27}$$

$$\alpha_3 = \frac{-\zeta}{\varepsilon\mu - \zeta\xi}\ , \tag{28}$$

$$\alpha_4 = \frac{\varepsilon}{\varepsilon\mu - \zeta\xi}, \tag{29}$$

$$\beta_1 = \frac{\mu(\varepsilon - \varepsilon_0) - \zeta\xi}{\varepsilon\mu - \zeta\xi}\ , \tag{30}$$

$$\beta_2 = \frac{\xi\varepsilon_0}{\varepsilon\mu - \zeta\xi}, \tag{31}$$

$$\beta_3 = \frac{\zeta\mu_0}{\varepsilon\mu - \zeta\xi}\ , \tag{32}$$

$$\beta_4 = \frac{\varepsilon(\mu - \mu_0) - \zeta\xi}{\varepsilon\mu - \zeta\xi}\ . \tag{33}$$

Let us now consider the integrals in equations (17) and (18). According to [8], when τ is close to 0, the formulations (17) and (18) then can be approximated as,

$$\begin{aligned}\mathbf{E}_{die}^{scat}(\mathbf{r}) &= \omega^2\mu_0\tau\int_{S_{tds}} G(\beta_1\mathbf{D})dS' \\ &+\frac{\nabla}{\varepsilon_0}\left[\begin{array}{l}\tau\int_C G\Delta\beta_{1t}\mathbf{t}'\cdot\mathbf{D}_t dl' + \int_{S_n^+} G_T\Delta\beta_{1n}^+\mathbf{n}'\cdot\mathbf{D}_n^+ dS' \\ -\tau\int_{S_n^-} G\Delta\beta_{1n}^-\nabla_t'\cdot\mathbf{D}_t dS' - \int_{S_n^-} G\Delta\beta_{1n}^-\mathbf{n}'\cdot\mathbf{D}_n^+ dS'\end{array}\right] \\ &+\omega^2\mu_0\tau\int_{S_{tds}} G(\beta_2\mathbf{B})dS' \\ &+\frac{\nabla}{\varepsilon_0}\left[\begin{array}{l}\tau\int_C G\Delta\beta_{2t}\mathbf{t}'\cdot\mathbf{B}_t dl' + \int_{S_n^+} G_T\Delta\beta_{2n}^+\mathbf{n}'\cdot\mathbf{B}_n^+ dS' \\ -\tau\int_{S_n^-} G\Delta\beta_{2n}^-\nabla_t'\cdot\mathbf{B}_t dS' - \int_{S_n^-} G\Delta\beta_{2n}^-\mathbf{n}'\cdot\mathbf{B}_n^+ dS'\end{array}\right] \\ &-i\omega\tau\beta_3\int_{S_{tds}}\nabla G\times\mathbf{D}dS' - i\omega\tau\beta_4\int_{S_{tds}}\nabla G\times\mathbf{B}dS'\end{aligned}$$

$$\begin{aligned}\mathbf{H}_{die}^{scat}(\mathbf{r}) &= \omega^2\varepsilon_0\tau\int_{S_{tds}} G(\beta_3\mathbf{D})dS' \\ &+\frac{\nabla}{\mu_0}\left[\begin{array}{l}\tau\int_C G\Delta\beta_{3t}\mathbf{t}'\cdot\mathbf{D}_t dl' + \int_{S_n^+} G_T\Delta\beta_{3n}^+\mathbf{n}'\cdot\mathbf{D}_n^+ dS' \\ -\tau\int_{S_n^-} G\Delta\beta_{3n}^-\nabla_t'\cdot\mathbf{D}_t dS' - \int_{S_n^-} G\Delta\beta_{3n}^-\mathbf{n}'\cdot\mathbf{D}_n^+ dS'\end{array}\right] \\ &+\omega^2\varepsilon_0\tau\int_{S_{tds}} G(\beta_4\mathbf{B})dS' \\ &+\frac{\nabla}{\mu_0}\left[\begin{array}{l}\tau\int_C G\Delta\beta_{4t}\mathbf{t}'\cdot\mathbf{B}_t dl' + \int_{S_n^+} G_T\Delta\beta_{4n}^+\mathbf{n}'\cdot\mathbf{B}_n^+ dS' \\ -\tau\int_{S_n^-} G\Delta\beta_{4n}^-\nabla_t'\cdot\mathbf{B}_t dS' - \int_{S_n^-} G\Delta\beta_{4n}^-\mathbf{n}'\cdot\mathbf{B}_n^+ dS'\end{array}\right] \\ &-i\omega\tau\beta_1\int_{S_{tds}}\nabla G\times\mathbf{D}dS' - i\omega\tau\beta_2\int_{S_{tds}}\nabla G\times\mathbf{B}dS'\end{aligned} \tag{35}$$

here $G_T(\mathbf{r},\mathbf{r}') = G(\mathbf{r},\mathbf{r}'+\tau n')$, representing the contribution from the sources on the interface S_n^+. Note that $\mathbf{D}_n^-$ and $\mathbf{B}_n^-$ have been replaced by $\nabla_t\cdot\mathbf{D}_t$, $\mathbf{D}_n^+$ and $\nabla_t\cdot\mathbf{B}_t$, $\mathbf{B}_n^+$. And $\Delta\beta_{it} = \Delta\beta_{in}^+ = \Delta\beta_{in}^- = \beta_i\ (i = 1,2,3,4)$.

Then evaluations of the submatrices of the impedance matrix in equation (25) are,

$$Z_{TT,qd}^{DD} = \alpha_1 I_{tt1} - \omega^2\mu_0\tau\beta_1 I_{tt2} - \frac{\tau\beta_1}{\varepsilon_0} I_{tt3} + i\omega\tau\beta_3 I_{tt4} \tag{36}$$

$$Z_{TT,qd}^{DB} = \alpha_2 I_{tt1} - \omega^2\mu_0\tau\beta_2 I_{tt2} - \frac{\tau\beta_2}{\varepsilon_0} I_{tt3} + i\omega\tau\beta_4 I_{tt4}\ , \tag{37}$$

$$Z_{TT,qd}^{BD} = \alpha_3 I_{tt1} - \omega^2\mu_0\tau\beta_3 I_{tt2} - \frac{\tau\beta_3}{\varepsilon_0} I_{tt3} + i\omega\tau\beta_1 I_{tt4}\ , \tag{38}$$

$$Z_{TT,qd}^{BB} = \alpha_4 I_{tt1} - \omega^2\mu_0\tau\beta_4 I_{tt2} - \frac{\tau\beta_4}{\varepsilon_0} I_{tt3} + i\omega\tau\beta_2 I_{tt4}\ , \tag{39}$$

$$Z_{TN,qn}^{DD} = \alpha_1 I_{tn1} - \omega^2\mu_0\tau\beta_1 I_{tn2} - \frac{\beta_1}{\varepsilon_0} I_{tn3} + i\omega\tau\beta_3 I_{tn4}\ , \tag{40}$$

$$Z_{TN,qn}^{DB} = \alpha_2 I_{tn1} - \omega^2\mu_0\tau\beta_2 I_{tn2} - \frac{\beta_2}{\varepsilon_0} I_{tn3} + i\omega\tau\beta_4 I_{tn4}\ , \tag{41}$$

$$Z_{TN,qn}^{BD} = \alpha_3 I_{tn1} - \omega^2\mu_0\tau\beta_3 I_{tn2} - \frac{\beta_3}{\varepsilon_0} I_{tn3} + i\omega\tau\beta_1 I_{tn4}\ , \tag{42}$$

$$Z_{TN,qn}^{BB} = \alpha_4 I_{tn1} - \omega^2\mu_0\tau\beta_4 I_{tn2} - \frac{\beta_4}{\varepsilon_0} I_{tn3} + i\omega\tau\beta_2 I_{tn4}\ , \tag{43}$$

$$Z_{NT,md}^{DD} = \alpha_1 I_{nt1} - \omega^2\mu_0\tau\beta_1 I_{nt2} - \frac{\tau\beta_1}{\varepsilon_0} I_{nt3} + i\omega\tau\beta_3 I_{nt4}\ , \tag{44}$$

$$Z_{NT,md}^{DB} = \alpha_2 I_{nt1} - \omega^2\mu_0\tau\beta_2 I_{nt2} - \frac{\tau\beta_2}{\varepsilon_0} I_{nt3} + i\omega\tau\beta_4 I_{nt4}\ , \tag{45}$$

$$Z_{NT,md}^{BD} = \alpha_3 I_{nt1} - \omega^2\mu_0\tau\beta_3 I_{nt2} - \frac{\tau\beta_3}{\varepsilon_0} I_{nt3} + i\omega\tau\beta_1 I_{nt4}\ , \tag{46}$$

$$Z_{NT,md}^{BB} = \alpha_4 I_{nt1} - \omega^2 \mu_0 \tau \beta_4 I_{nt2} - \frac{\tau \beta_4}{\varepsilon_0} I_{nt3} + i\omega\tau\beta_2 I_{nt4}, \quad (47)$$

$$Z_{NN,mn}^{DD} = \alpha_1 I_{nn1} - \omega^2 \mu_0 \tau \beta_1 I_{nn2} - \frac{\beta_1}{\varepsilon_0} I_{nn3} + i\omega\tau\beta_3 I_{nn4}, \quad (48)$$

$$Z_{NN,mn}^{DB} = \alpha_2 I_{nn1} - \omega^2 \mu_0 \tau \beta_2 I_{nn2} - \frac{\beta_2}{\varepsilon_0} I_{nn3} + i\omega\tau\beta_4 I_{nn4}, \quad (49)$$

$$Z_{NN,mn}^{BD} = \alpha_3 I_{nn1} - \omega^2 \mu_0 \tau \beta_3 I_{nn2} - \frac{\beta_3}{\varepsilon_0} I_{nn3} + i\omega\tau\beta_1 I_{nn4}, \quad (50)$$

$$Z_{NN,mn}^{BB} = \alpha_4 I_{nn1} - \omega^2 \mu_0 \tau \beta_4 I_{nn2} - \frac{\beta_4}{\varepsilon_0} I_{nn3} + i\omega\tau\beta_2 I_{nn4}, \quad (51)$$

where

$$I_{tt1} = \int_{\partial T_q} \mathbf{f}_q \cdot \mathbf{f}_d ds, \quad (52)$$

$$I_{tt2} = \int_{\partial T_q} \int_{\partial T_d} G \mathbf{f}_q \cdot \mathbf{f}_d ds' ds, \quad (53)$$

$$I_{tt3} = \int_{\partial T_q} \int_C \mathbf{f}_q \cdot \nabla G\left(\mathbf{r}, \mathbf{r}' \in S_n^-\right) dl' ds - \int_{\partial T_q} \nabla_t' \cdot \mathbf{f}_d \int_{\partial T_d} \mathbf{f}_q \cdot \nabla G\left(\mathbf{r}, \mathbf{r}' \in S_n^-\right) ds' ds, \quad (54)$$

$$I_{tt4} = \int_{\partial T_q} \mathbf{f}_q \cdot \int_{\partial T_d} \nabla G \times \mathbf{f}_d ds' ds, \quad (55)$$

$$I_{tn1} = \int_{\partial T_q} \mathbf{f}_q \cdot \mathbf{n}_n ds, \quad (56)$$

$$I_{tn2} = \int_{\partial T_q} \mathbf{f}_q \cdot \int_{\partial T_d} G \mathbf{n}_n ds' ds, \quad (57)$$

$$I_{tn3} = \int_{\partial T_q} \mathbf{f}_q \cdot \nabla \int_{\partial T_d} G(\mathbf{r}, \mathbf{r}' \in S_n^+) \mathbf{n}' \cdot \mathbf{n}_n ds' ds - \int_{\partial T_q} \mathbf{f}_q \cdot \nabla \int_{\partial T_d} G(\mathbf{r}, \mathbf{r}' \in S_n^-) \mathbf{n}' \cdot \mathbf{n}_n ds' ds, \quad (58)$$

$$I_{tn4} = \int_{\partial T_q} \mathbf{f}_q \cdot \int_{\partial T_d} \nabla G \times \mathbf{n}_n ds' ds, \quad (59)$$

$$I_{nt1} = \int_{\partial T_m} \mathbf{n}_m \cdot \mathbf{f}_d ds, \quad (60)$$

$$I_{nt2} = \int_{\partial T_m} \mathbf{n}_m \cdot \int_{\partial T_d} G \mathbf{f}_d ds' ds, \quad (61)$$

$$I_{nt3} = \int_{\partial T_m} \mathbf{n}_m \cdot \nabla \int_C G(\mathbf{r}, \mathbf{r}' \in S_n^-) \mathbf{t}' \cdot \mathbf{f}_d dl' ds - \int_{\partial T_m} \mathbf{n}_m \cdot \nabla \int_{\partial T_d} G(\mathbf{r}, \mathbf{r}' \in S_n^-) \nabla_t' \cdot \mathbf{f}_d ds' ds, \quad (62)$$

$$I_{nt4} = \int_{\partial T_m} \mathbf{n}_m \cdot \int_{\partial T_d} \nabla G \times \mathbf{f}_d ds' ds, \quad (63)$$

$$I_{nn1} = \int_{\partial T_m} \mathbf{n}_m \cdot \mathbf{n}_n ds, \quad (64)$$

$$I_{nn2} = \int_{\partial T_m} \mathbf{n}_m \cdot \int_{\partial T_n} G \mathbf{n}_n ds' ds, \quad (65)$$

$$I_{nn3} = \int_{\partial T_m} \mathbf{n}_m \cdot \nabla \int_{\partial T_n} G(\mathbf{r}, \mathbf{r}' \in S_n^+) \mathbf{n}' \cdot \mathbf{n}_n ds' ds - \int_{\partial T_m} \mathbf{n}_m \cdot \nabla \int_{\partial T_n} G(\mathbf{r}, \mathbf{r}' \in S_n^-) \mathbf{n}' \cdot \mathbf{n}_n ds' ds, \quad (66)$$

$$I_{nn4} = \int_{\partial T_m} \mathbf{n}_m \cdot \int_{\partial T_n} \nabla G \times \mathbf{n}_n ds' ds. \quad (67)$$

Consider $\mathbf{t}' \cdot \mathbf{f}_d = 1$, $\mathbf{n}' \cdot \mathbf{n}_n = 1$ and $\int_s \mathbf{f} \cdot \mathbf{n} ds = 0$, then the above formulas become simple and easy to handle. It should note that $G(\mathbf{r}, \mathbf{r}' \in S_n^+) = G_T(\mathbf{r}, \mathbf{r}')$, representing the contribution from the sources on the interface S_n^+ . Consider,

$$\mathbf{n}(\mathbf{r}) \cdot \nabla G(\mathbf{r}, \mathbf{r}') = \frac{\partial G}{\partial n} \approx \frac{1}{\tau}\left[G\left(\mathbf{r} \in S_n^+, \mathbf{r}'\right) - G\left(\mathbf{r} \in S_n^-, \mathbf{r}'\right)\right] \quad (68)$$

then the integrations in equations (62) and (66) can be transformed to more simple forms, and then just integral of the Green's function needs to be treated, rather than that of the gradient of Green's function. After all these matrix elements have been evaluated, and then B_d , D_d , D_n , and B_n can be solved by direct or iterative matrix solvers.

REFERENCES

[1] V. Demir, A. Elsherbeni, and E. Arvas, "FDTD formulations for scattering from three dimensional chiral objects," *20th Annual Review of Progress in Applied Computational Electromagnetics (ACES)*, Syracuse, NY, April 2004.

[2] Y. Zhang, A. Bauer, and E. Li, "T-Matrix analysis of multiple scattering from parallel semi-circular channels filled with chiral media in a conducting plane," *Progress In Electromagnetics Research*, vol. 53, pp. 299-318, 2009.

[3] D. Worasawate, J. Mautz, and E. Arvas, "Electromagnetic scattering from an arbitrarily shaped three-dimensional homogeneous chiral body," *IEEE Trans. Antennas Propag.*, vol. 51, no. 5, pp. 1077-1084, May 2003.

[4] M. Hasanovic, C. Mei, J. Mautz, and E. Arvas, "Scattering from 3-D inhomogeneous chiral bodies of arbitrary shape by the method of moments," *IEEE Trans. Antennas Propag.*, vol. 55, no. 6, pp. 1817-1825, June 2007.

[5] T. Senior and J. Volakis, "Derivation and application of a class of generalized bound conditions," *IEEE Trans. Antennas Propag.* , vol. 37, pp. 1566-1572, 1989.

[6] R. Harrington and J. Mautz, "Impedance sheet approximation for thin dielectric shells," *IEEE Trans. Antennas Propag.*, vol. 23, no. 4, pp. 531-534, 1975.

[7] I. Chiang and W. Chew, "Thin dielectric sheet simulation by surface integral equation using modified RWG and pulse bases," *IEEE Trans. Antennas Propag.*, vol. 54, no. 7, pp. 1927-1934, July 2006.

[8] I. Chiang and W. Chew, "A coupled PEC-TDS surface integral equation approach for electromagnetic scattering and radiation from composite metallic and thin dielectric objects,"

IEEE Trans. Antennas Propag., vol. 54, no. 11, pp. 3511-3516, Nov. 2006.

[9] S. He, Z. Nie, S. Yan, and J. Hu, "Multi-layer TDS approximation used to numerical solution for dielectric objects," *Asia-Pacific Microwave Conference Proceedings*, APMC, 2008.

[10] S. He, Z. Nie, and J. Hu, "Numerical solution of scatter from thin dielectric-coated conductors based on TDS approximation and EM boundary conditions," *Progress In Electromagnetics Research*, vol. 93, pp. 339-354, 2009.

[11] S. Rao, D. Wilton, and A. Glisson, "Electromagnetic scattering by surfaces of arbitrary shape," *IEEE Trans. Ante nnas Propag.*, vol. 30, pp. 409-418, May 1982.

[12] A. Dmitrenko, A. Mukomolov, and V. Fisanov, "Scattering of electromagnetic waves on a magneto dielectric with chiral properties," *Russian Physics Journal*, vol. 39, no. 8, pp. 781-785, 1996.

Novel Monolayer Windmill Structure Left-Handed Metamaterial

H. Xiong, J.–S. Hong, and D.–L. Jin

School of Physical Electronics
University of Electronic Science and Technology of China,Chengdu, 610054, China
xiong1226han@126.com

Abstract ─ In this paper, a simple structure made of periodic arrays of windmill structure, printed on only one side of a dielectric substrate, is introduced. Simulation and measurement were carried out for one layer of infinite left-handed material (LHM) slab using monolayer windmill structure. The results showed that by carefully adjusting the dimensions of the windmill structure, magnetic and electric resonances can be coexistent in a frequency range where there are both negative magnetic and electric responses. To further verify the left-handed (LH) properties of this structure metamaterial, effective medium parameters were retrieved and a refraction phenomenon based on a wedge-shaped model was demonstrated. Equivalent circuits for the magnetic and electric resonance were also offered to give a qualitative explanation of the LH behaviours.

Index Terms ─ Double negative (DNG), left-handed material (LHM), monolayer, and negative refractive index (NRI).

I. INTRODUCTION

Artificial electromagnetic structures, called metamaterials, can be engineered to exhibit exotic electric and magnetic properties not realizable in nature. In 1968, Veselago [1] initially assumed a material with negative permittivity and permeability simultaneously and theoretically demonstrated the abnormal electromagnetic properties. However, research work in this area did not draw much attention in the engineering and physics communities because there are no such materials in natural world. His work was neglected for almost 30 years. In 1999, Pendry et al. [2] showed that negative ε can be realized by using conducting wires and negative μ by split-ring resonators (SRRs). Smith et al. [3] constructed a real structure composed of conducting wires and SRRs, and demonstrated its negative ε and μ at microwave frequencies. Subsequently, a great variety of left-handed metamaterials (LHMs) were proposed, such as split-triangle resonator (STRs) [4], multi-gap split-ring [5], SRR pairs [6, 7], single split-ring resonators [8], ferromagnetic host and wire array [9], etc. The above methods of realizing LHMs enrich greatly the content of LHMs. Nevertheless, there is an annoying problem for the LHMs realized by the above methods. Most of the above-mentioned LHMs share one thing in common that they print the metallic patterns on both sides of the substrates. It not only increases the complicacy of fabrication when the operating frequency increased to high frequency such as terahertz frequency but also increases the difficulty to add lumped active elements (for example, varactor diodes) on such structures to control their left-handed properties, because modern commercial components are generally designed for surface mount.

In this paper, a simple metamaterial structure based on the windmill is proposed and investigated experimentally and numerically at microwave frequency range. Although it derives from the bi-layered chiral metamaterial [10, 11], unlike the structure in [10] that requires the electromagnetic waves normal to the planes of the printed boards, this paper's proposed structure requires electromagnetic waves travel along the planes of the thin dielectric sheet. Compared with the conjugated gammadions structure [11], this monolayer windmill metamaterial structure is more easily manufactured.

Submitted On: Oct. 26, 2012
Accepted On: Jan. 1, 2014

1054-4887 © 2013 ACES

II. UNIT-CELL DESIGN AND SIMULATION

A unit cell of the single-sided windmill structure is shown in Fig. 1, where the metallic strips are printed on one side of t = 0.6 mm thick FR4 substrate with the relative permittivity of 4.4 and $\tan\delta_s$ = 0.02. The metallization is copper with a thickness of 0.017 mm. The other geometrical dimensions are as follows, in millimetres: L = 5, a = 2.05, b = 0.3, c = 0.2, d = 2.4, g = 0.6. The Y structure has been demonstrated to have LH behaviours in some frequency ranges [12]. So for this paper, in response to the magnetic field, the capacitance between four adjacent L-shaped structures (seen the loop in Fig. 4 (a)) and their own self-inductance form an equivalent L–C loop, which can provide a negative permeability. In response to the electric field, the metal thin strips which, parallel to the electric field can provide a negative permittivity. So LH behaviours are expected for this structure.

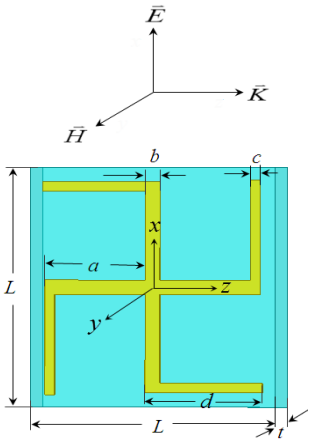

Fig. 1. Geometry of one unit cell of the windmill structure metamaterial.

In order to verify our speculation, the numerical simulations were performed for one layer of the windmill structure LHM slab by HFSS. A theoretical model based on an artificial waveguide with the transverse boundaries of two ideal magnetic conductors and two ideal electric conductor planes is employed. This enables the model to be equivalent to an infinite layer medium illuminated by a parallel incident plane wave. To be specific, input/output ports are imposed in z-direction, and perfectly electric conducting (PEC) and perfectly magnetic conducting (PMC) boundary conditions are imposed in x– and y–directions (perpendicular to the plane of the windmill structure), respectively. There are many methods to retrieve constitutive parameters of metamaterials [13-15]. Most of them use scattering parameters to obtain the impedance z and effective refractive index n and then calculating $\mu = nz$ and $\varepsilon = n/z$. In this paper, we use a standard algorithm [15] extracted from the scattering parameters. Figure 2 gives the simulated magnitudes of S_{11} and S_{21} parameters, as well as the retrieved real parts (solid curves) and imaginary parts (dashed curves) of effective permeability, permittivity, and refractive index. Figure 2 (a) shows that there is a transmission peak at 10.4 GHz, which indicates an LH passband. As clearly shown in Fig. 2 (b) and (c), there are obviously an electric resonance and a magnetic resonance. In Fig. 2 (b) and (c) show that the effective the effective permittivity is negative in 9.28 GHz–12 GHz while the frequency range of negative effective permeability is 10.2 GHz–10.7 GHz, much narrower than the negative electric permittivity. In the frequency range where both the effective permittivity and permeability are negative, an LH band is expected. Figure 2 (d) depicts the extracted effective refractive index of the metamaterial at various frequencies. Clearly, as the frequency increases, the effective index of refraction changes from positive to negative then to positive. The refractive index varies from n = -2.95 + j0.85 at 10.1 GHz to n = -0.018 + j2.54 at 11.35 GHz. So as the grey area shows, the windmill structure is double negative between 10.2 GHz and 10.7 GHz, and the negative index bandwidth is 500 MHz.

Please note that in Fig. 2 (c) and (d), the negative reflective region (shaded region) is much wider than the negative permeability region. This can be explained as follows. A wider negative n' frequency band is observed due to the dispersion of fabricated prototype. Since the real part of n (n') is given by $n' = \varepsilon'z' - \varepsilon''z''$ from $n = \varepsilon z$ and z = sqrt(μ/ε), the imaginary parts of the permittivity (ε'') and the permeability (μ'') also accounts for n'. Therefore, a negative real part of n can be accomplished without having ε' and μ' simultaneously negative. The amplitude of Im (n) is relatively small compared to the real part, which

suggests a low loss in the proposed left-handed metamaterial.

To further verify the LH properties and obtain a direct image of the negative refraction of the EM wave for the windmill structure, we utilize a wedge–shaped configuration, which is stacked by our designed single slab planar metamaterials with an inclined angle of 45°in simulation. Similarly to [16] described methods, it stacked one unit cell along the *y*-axis in the simulation. For the wedge model, 7 unit cells are used along the *x*–axis and the *z*–axis, respectively. The refraction interface has a staircase pattern with one unit cell step in the *x*–direction and the *z*–direction, which can be referred to as a wedge angle of 45°. All the unit cells are positioned between two conducting plates with the absorber boundary conditions at the side faces.

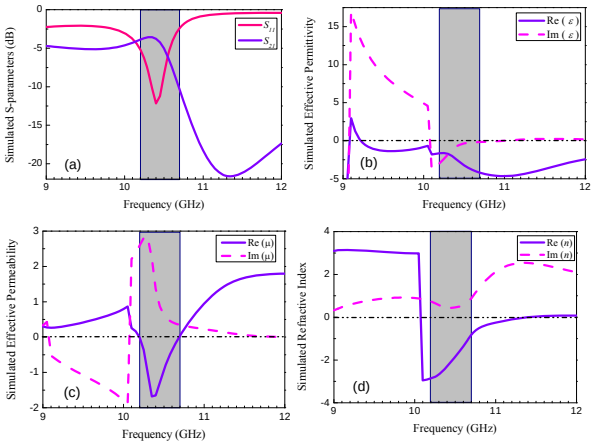

Fig. 2. (a) Simulated magnitudes of $S_{11}$and S_{21} parameters; real (solid curves) and imaginary (dashed curves) of the effective, (b) relative permittivity, (c) relative permeability, and (d) index of refraction.

Figure 3 shows the phenomenon of refraction of the EM radiation at the interface between designed metamaterial and vacuum. The typical electric field distributions at 10.4 GHz and 9 GHz are presented in Fig. 3 (a) and (b), in which the negative and the positive refractive behaviors are demonstrated clearly, respectively. The unambiguous negative refraction phenomenon is observed in the LH transmission passband, which has been ascertained from the retrieved effective parameter procedures as discussed above. The arrow lines indicate the transmission direction of the refracted waves, while the dashed lines are along the surface normal.

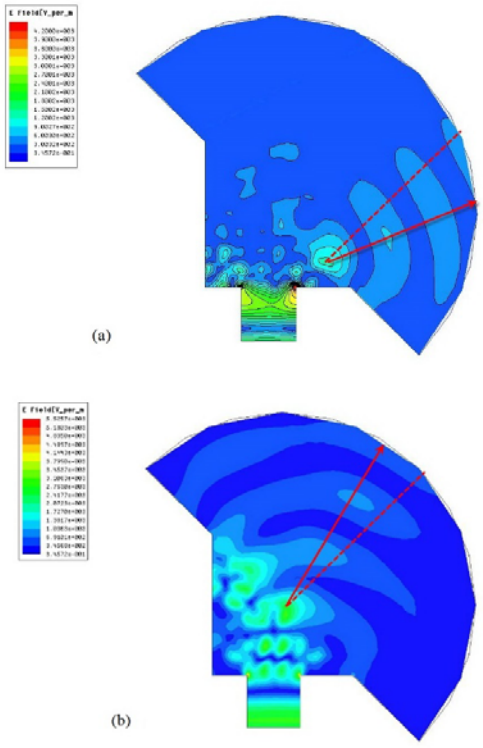

Fig. 3. The distribution of the electric field in the wedge-shaped configuration at different frequency points; (a) the negative refraction at 10.4 GHz and (b) the positive refraction at 9 GHz.

III. EQUIVALENT CIRCUIT MODEL AND PARAMETRIC STUDY

Negative effective permittivity and permeability can be obtained by electric and magnetic resonances, respectively. Both the electric and magnetic resonances are equivalent to L–C resonant circuits. The windmill structure has an intrinsic relation with the Jerusalem cross [17-19]. We start with the equivalent circuit model in Fig. 4 when the proposed LHM responds to incident electromagnetic waves. The wires along the electric field **E**-direction of the incident electromagnetic wave excite the electric response and produce negative permittivity ε up to the plasma frequency. The linear arrow in Fig. 4 (a) denotes the equivalent current of electric resonance. In Fig. 4 (a), both *A* and *B* are

equivalent to *A*' and *B*' for periodicity. Equivalent L–C circuit of electric resonance is given in Fig. 4 (b), where L_e is the inductance of the cross bar and C_e is the capacitance between four L-shaped gaps. Due to anti-parallel currents induced by the magnetic field of the incident electromagnetic wave, The four L–shaped structures perpendicular the magnetic field **H** direction act as magnetic resonators, providing negative permeability μ. The corresponding equivalent current is denoted by the circular arrow. According to the orientation of the equivalent current, the equivalent circuit of magnetic resonance can be illustrated by Fig. 4 (c), where L_m and C_m are, respectively the equivalent mutual inductance and capacitance around one windmill structure. The similar formulas for L_e, C_e, L_m, and C_m can be found in references [16, 17]. Figure 5 (a)–(d) present the relations between the electromagnetic resonance and geometric parameters. It is shown that the electric resonance f_e and the magnetic resonance f_m are proportional to *1/a, b, 1/c*, and *1/d*, for the parallel incidence case.

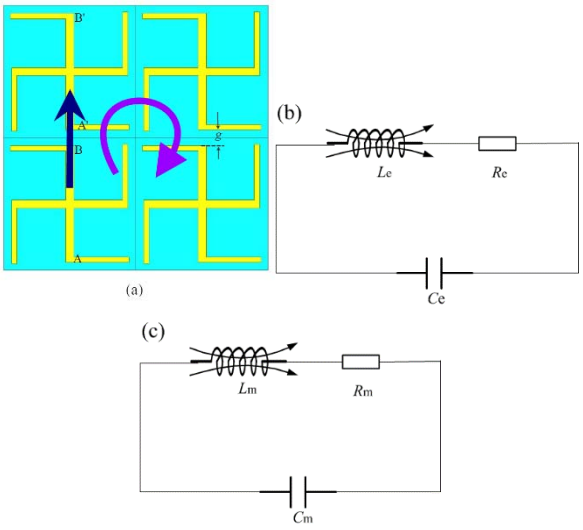

Fig. 4. Equivalent circuit description of the proposed LHM; (a) illustration of equivalent current in windmill structure, (b) equivalent circuit of the electric resonance, and (c) equivalent circuit of the magnetic resonance.

IV. EXPERIMENTAL VERIFICATION

The expected behaviour has been confirmed experimentally by measuring the transmission and reflection properties of the proposed metamaterial using the waveguide method [20]. Because the waveguide measurement method is easy to carry out, and there no tough requirements for the material sample. In the experiment, the slab like sample being placed in the middle of the waveguide makes the higher order incident evanescent modes significantly attenuated prior to reaching the sample under test. The transmission properties of a slab like sample are firstly measured to verify the existence of the pass band due to the double negative property. The geometrical dimensions of the fabricated sample are the same as the simulation. The sample under measurement contains 3 unit cells in the *z* direction, 2 unit cells in *x* direction, and 35 unit cells in the *y* direction. There is no need for spacers between stacked layers in *y*-direction, which makes the setup easier [21]. The measurement setup consists of two coaxial-to-waveguide adapters connected to a BJ100 standard waveguide and an Agilent E8361A network analyser. The experimental setup is shown in Fig. 6. Using the recorded scattering parameters, the constitutive effective parameters are retrieved. Figure 7 (a)–(d) illustrate the experimented parameters. There exist some discrepancies between measured date and the simulated results. This could be due to the fabrication error as the design we used.

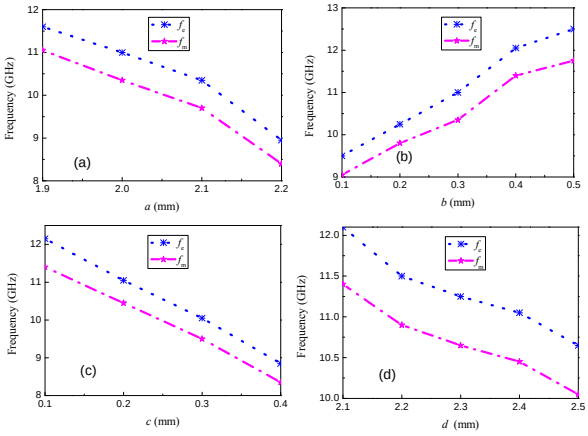

Fig. 5. Magnetic resonance frequency and electric resonance frequency versus; (a) wire length "*a*", (b) wire width "*b*", (c) wire width "*c*", and (d) wire length "*d*".

Fig. 6. Photograph of the experimental setup.

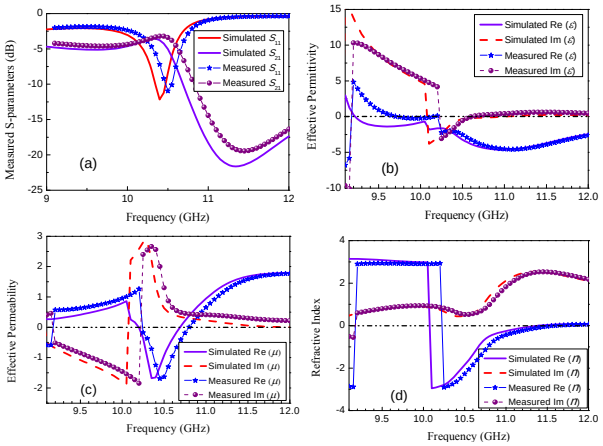

Fig. 7. Comparison between simulation and measurement result of (a) S_{11} and S_{21} parameters, (b) permittivity, (c) permeability, and (d) index of refraction.

V. CONCLUSION

In summary, we studied the LH properties of the monolayer windmill structure by simulation and experiment in the microwave frequency regime. The windmill structure metamaterial simultaneously shows an electric and magnetic response to incident EM wave, and the LH transmission passband is expected. The negative refraction is demonstrated by simulating the wedge-shaped model. Furthermore, the design parameters and their relation to the magnetic and electric resonances have been investigated. The simplicity of structure makes the LHM easy to fabricate, which may be useful for potential applications in the future.

ACKNOWLEDGMENT

This work was supported by the National Natural Science Foundation of China (No.61172115 and No.60872029), the High-Tech Research and Development Program of China (No. 2008AA01Z206), the Aeronautics Foundation of China (No.20100180003)and the Fundamental Research Funds for the Central Universities of China (Grant No.ZYGX2012YB019).

REFERENCES

[1] V. Veselago, "The electrodynamics of substances with simultaneously negative values of ε and μ," *Sov. Phys. Uspekhi*, vol. 10, pp. 509-514, 1968.

[2] J. Pendry, A. Holden, D. Robbins, and W. Stewart, "Magnetism from conductors and enhanced nonlinear phenomena," *IEEE Trans. Microwave Theory Tech.*, vol. 47, pp. 2075-2084, 1999.

[3] D. Smith, W. Padilla, D. Vier, S. Nemat-Nasser, and S. Schultz, "Composite medium with simultaneously negative permeability and permittivity," *Phys. Rev. Lett.*, vol. 84, pp. 4184-4187, 2000.

[4] M. Abessolo, N. Aknin, and A. El Moussaoui, "A new left-handed metamaterial structure based on split-triangle resonators (STRs)," *Appl. Comp. Electro. Society (ACES) Journal*, vol. 26, no. 11, pp. 945-952, Nov. 2011.

[5] H. Xiong, J. Hong, D. Jin, and Z. Zhang, "A novel structure for a broadband left-handed metamaterial," *Chin. Phys. B*, vol. 21, no. 9, pp. 094101, 2012.

[6] J. Liu, W. Shao, and B. Wang, "A dual-band metamaterial design using double SRR structures," *Appl. Comp. Electro. Society (ACES) Journal*, vol. 26, no. 6, pp. 459-463, June 2011.

[7] Y. Cheng, H. Yang, Y. Nie, R. Gong, and Z. Cheng, "Investigation of negative index properties of planar metamaterials based on split-ring pairs," *Appl. Phys. A: Mater.*, vol. 103, pp. 989-994, 2011.

[8] M. Tang, S. Xiao, D. Wang, J. Xiong, K. Chen, and B. Wang, "Negative index of reflection in planar metamaterial composed of single split-ring resonators," *Appl. Comp. Electro. Society (ACES) Journal*, vol. 26, no. 3, pp. 250-258, March 2011.

[9] Y. Huang, G. Wen, T. Li, and K. Xie, "Positive-negative-positive metamaterial consisting of ferrimagnetic host and wire array," *Appl. Comp. Electro. Society (ACES) Journal*, vol. 25, no. 8, pp. 696-702, August 2010.

[10] Y. Ye, X. Li, F. Zhuang and S. Chang, "Homogeneous circular polarizers using a bilayered chiral metamaterial," *Appl. Phys. Lett.*, vol. 99, pp. 031111, 2011.

[11] D. Zarifi, M. Soleimani, and V. Nayyeri, "Dual- and multiband chiral metamaterial structures with strong optical activity and negative refraction index," *IEEE Antennas Wireless Propagation Lett.*, vol. 11, pp. 334-337, 2012.

[12] N. Wongkasem, A. Akyurtlu, K. Marx, Q. Dong, J. Li, and W. Goodhue, "Development of chiral negative refractive index metamaterials for the terahertz frequency regime," *IEEE Trans. Antennas Propag.*, vol. 55, pp. 3052-3062, 2007.

[13] A. Houck, J. Brock, and I. Chuang, "Experimental observations of a left-handed material that obeys Snell's law," *Phys. Rev. Lett.*, vol. 90, pp. 137401, 2003.

[14] X. Chen, T. Grzegorczyk, B. Wu, J. Pacheco Jr., and J. Kong, "Robust method to retrieve the constitutive effective parameters of metamaterials," *Phys. Rev. E*, vol. 70, pp. 016608, 2004.

[15] D. Smith, D. Vier, T. Koschny, and C. Soukoulis, "Electromagnetic parameter retrieval from inhomogeneous metamaterials," *Phys. Rev. E*, vol. 71, pp. 036617, 2005.

[16] Z. Dong, S. Zhu, H. Liu, J. Zhu, and W. Cao, "Numerical simulations of negative-index refraction in wedge-shaped metamaterials," *Phys. Rev. E*, vol. 72, pp. 016607, 2005.

[17] M. Hosseinipanah and Q. WU, "Equivalent circuit model for designing of Jerusalem cross-based artificial magnetic conductors," *Radio Engineering*, vol. 18, pp. 544-550, 2009.

[18] M. Hosseini and M. Hakkak, "Characteristics estimation for Jerusalem cross-based artificial magnetic conductors," *IEEE Antennas Wireless Propag. Lett.*, vol. 7, pp. 58-61, 2008.

[19] J. Wang, S. Qu, Z. Xu, Z. Fu, H. Ma, and Y. Yang, "A broad-band three-dimensional isotropic left-handed metamaterial," *J. Phys. D: Appl. Phys.*, vol. 42, pp. 155413, 2009.

[20] H. Chen, J. Zhang, Y. Bai, Y. Luo, L. Ran, Q. Jiang, and J. Kong, "Experimental retrieval of the effective parameters of metamaterialsbased on a waveguide method," *Opt. Express*, vol. 14, pp. 12944-12949, 2006.

[21] N. Amiri, K. Forooraghi, and Z. Atlasbaf, "A wideband uniplanar polarization independent left-handed metamaterial," *IEEE Antennas Wireless Propag. Lett.*, vol. 10, pp. 524-527, 2011.

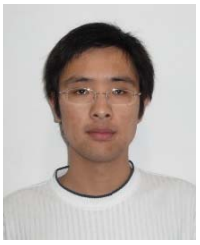

Han Xiong was born in HuBei. He received his M.Sc. from Yunnan Normal University in 2010. Now, he is a doctor in Radio Physics in the University of Electronic Science and Technology of China now. His research interests include antenna technology and metamaterials.

Jing-Song Hong received the B.Sc. degree in electromagnetics from Lanzhou University, China, in 1991, and the M.Sc. and Ph.D. degrees in Electrical Engineering from the University of Electronic Science and Technology of China (UESTC), in 2000 and 2005, respectively. He is now a Professor with UESTC. From 1991 to 1993, he was a Circuit Designer with the Jingjiang Radar Factory, Chengdu, China. From 1993 to 1997, he was a Testing Engineer with SAE Magnetics (HK) Ltd, Guangdong, China. From 1999 to 2002, he was a Research Assistant with the City University of Hong Kong. His research interest includes the use of numerical techniques in electromagnetics and the use of microwave methods for materials characterization and processing.

Da-Lin Jin is a gradute student major in Radio Physics in the University of Electronic Scienceand Technology of China now. Her research interests include antenna technology and metamaterial technique.

Measurements on Long and Rigid Objects for Radar Field Probe

P. S. P. Wei (Retired)

The Boeing Company, Seattle, Washington
paxwei3@gmail.com

Abstract – As a novel concept for field probes, radar cross section (RCS) measurements on long rigid objects rotated within a small angular range in and out of the broadside condition are reported. The rotation was maintained either in a horizontal (H) plane or in a vertical (V) plane containing the center of the quiet-zone (QZ). Processing the RCS data by DFT yields a spectrum, which is recognized as the field distribution along that object. This spectrum compares extremely well to traditional field-probes taken earlier by translating a sphere across the QZ in H- or V-direction. Preliminary results at several S-band frequencies are presented and discussed.

Keywords – Compact range, field distribution, large targets, and RCS measurements.

I. INTRODUCTION

For accurate radar cross section (RCS) measurements, it is important to perform the field probe in the target zone as a function of frequency, polarization, and the locations. Traditionally, one can translate a calibration object (e.g., a sphere) across the test zone, and to analyze the response with respect to the field uniformity or the variation thereof. Such a method is usually time consuming and costly. Besides, the probe and its supporting structure (if large) may often contaminate the very field being probed.

While searching for a suitable calibration object for the cross-polarized channels in the Boeing 9-77 compact range, we studied dielectric strings stretched tightly across the range at 45° from horizontal and near broadside to the radar. The lower end of the string was anchored to the floor while the upper end was tied to the upper turntable (UTT). Rotating the UTT would produce a pattern from the string as a function of the aspect-angle. It dawned on us that when we processed the data by the digital Fourier transform (DFT), it would generate a response spectrum, which was related to the incident wave-field distribution along that string at 45° from horizontal [1, 2].

Of practical interest regarding field probes, the two major orientations are *horizontal* and *vertical* intersecting at the quiet-zone (QZ) center. The problem and challenge for the experiments are to assemble such long and rigid targets, mounting it to the range and maneuvering it for the desired motion. To validate the concept, some preliminary measurements were taken (among others) from a 60-ft steel rod supported *horizontally* [3], and a 40-ft aluminum cylinder plus a blue rope supported *vertically* [4]. The results are analyzed in connection with the feasibility of the new concept.

II. HORIZONTAL MEASUREMENTS

The 60-ft long rod (diameter 1.74 inches) was assembled by connecting six 10-ft long steel conduits together. The five joints were each made by fastening the ends of two adjacent conduits with screws to a short cylindrical stem inserted inside the conduits. The screw-heads were kept flush to the outer surface. The outside of the joints were wrapped with conducting aluminum tape. The two ends of the long rod were each covered by a flat circular plate and then painted. The long rod, weighing 75 pounds, was supported by eight pairs of strings (non-flashing) from the UTT at eight attachment points evenly distributed along its length, as depicted in Fig. 1.

Figure 2 shows the typical azimuth dependence of the radar echoes at 2.4 GHz from the 60-ft long rod. Data have been collected in the range of $\pm$ 20°, but only those within $\pm$ 5° are

Submitted On: Feb. 23, 2013
Accepted On: Aug. 27, 2013

1054-4887 © 2013 ACES

plotted here. The main peak is very narrow. The side-lobes are asymmetric. Note that the VV trace (red) is shifted down by -10 dB to avoid overlap, and that it is very similar to the HH trace (blue).

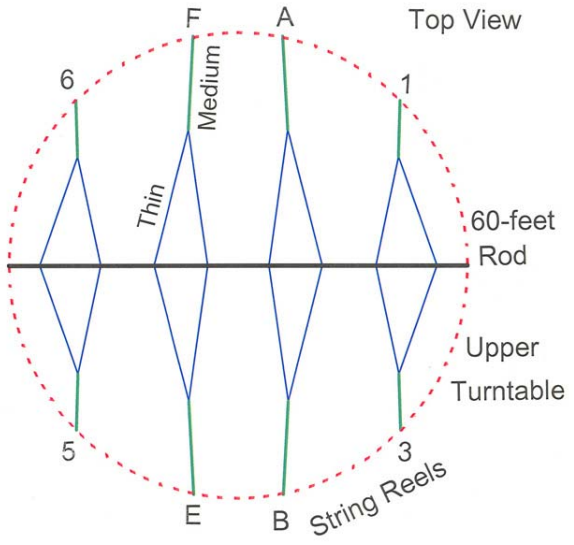

Fig. 1. Schematic of the 60-ft rod supported horizontally by eight string-reels (where A, B, E, F represent high-capacity and 1, 3, 5, 6 represent low-capacity string-reels) from the UTT (of diameter 60 feet, represented by a circle of red dashes).

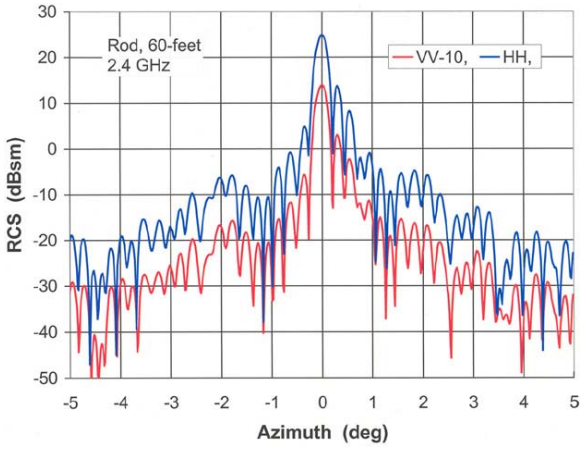

Fig. 2. Azimuth patterns in radar echoes at 2.4 GHz measured from the 60-ft long rod supported horizontally by strings.

Figure 3 shows the Fourier transform spectra using the 2.4 GHz data (of I and Q). The central portion within $\pm$ 800 bins exhibits a plateau at about 35 dB above the noise floor. We recognize that the intensity variation on the plateau is of interest. Though the plateau is fairly flat at the center, it drops off quickly on the two sides. The fast oscillating wiggles near bins $\pm$ 750 are commonly known as the Gibb's phenomenon due to truncation of the rod.

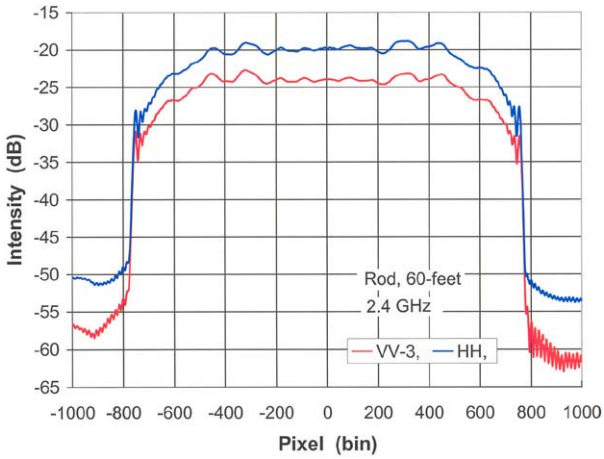

Fig. 3. Typical Fourier transform spectra from the azimuth measurements of the 60-ft rod at 2.4 GHz, (with HH in blue, VV in red and shifted down by -3 dB).

Figure 4 shows extended plots of the two ends, with computed points in symbols. The next step is to calibrate the bin number to distance along the rod. The appropriate formula taken from [1, 2] is as follows,

$$R / \lambda = J * (D_a - 1) / (2W * A * N) \qquad (1)$$

where R is the cross-range distance, $\lambda = c / F$ is the radar wavelength, J is the bin number measured from zero, N = power of 2, zero-padded, is the total size of the data set, D_a is the number of measured data points, A is the UTT-angle swept (in radian), c is the speed of light, and W = 1 here, is a conversion factor which relates the UTT-angle to the actual out-of-plane angle for the rotation (if needed). In equation (1), we find that R and J have a unique relationship, once all the other parameters are known.

For easy comparison with the horizontal field probes using the 14-inch sphere recorded in 1996, we plot the results on similar scales in Fig. 6, i.e., the ordinate in 5 dB/div., the abscissa in 60 inch/div. By aligning Figs. 5 and 6, we can readily discern their strong resemblance, curve by curve,

wiggle by wiggle, per polarization and per frequency. Thus, the 60-ft rod provided the same horizontal field probe results, even at a higher resolution and over a wider coverage area. The close agreement validates the new method of performing field probes as proposed earlier [1, 2]. Furthermore, it is nice to know that the wave-field at the Boeing 9-77 compact range on three arbitrarily chosen frequencies has not changed with time.

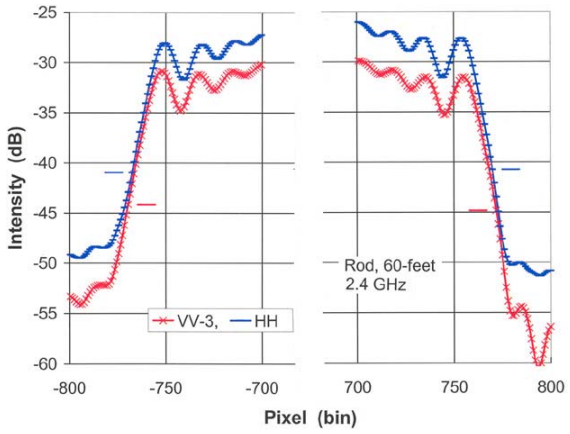

Fig. 4. Extended view of the two ends of the Fourier transform spectra at 2.4 GHz. For calibration of pixel bin versus cross-range distance, the points at -13 dB down from the outermost peaks (denoted by short bars) are taken as end points.

Figure 5 shows the new results from the 60-ft rod of the field distribution represented by the Fourier transform spectra for both HH and VV polarizations at 3 frequencies. The ordinate scale (y-axis) is for the HH trace (blue) at 2.0 GHz, while the HH for 2.4 and 2.8 are shifted down successively by -10 dB. The VV traces (red) are each shifted down by -3 dB from the corresponding HH. We see that the features in Figs. 5 and 6 match each other remarkably well as a function of cross-range distance, per frequency and per polarization.

III. VERTICAL MEASUREMENTS

The configuration of test geometry for moving an object in a vertical plane using the high-capacity string-reels at the 9-77 compact range is shown in Fig. 7 (a) (schematic) and (b) (photograph). The 40-ft aluminum rod (4-inch diameter) supported by a blue rope through its center was the first target for measurement. The angular motion of the rod with respect to the pivot (on top) was achieved by pulling on the weight either by the pair of strings A and F from the front side, or by the pair of strings B and E from the back side. Figure 1 shows the relative placements of the string-reels.

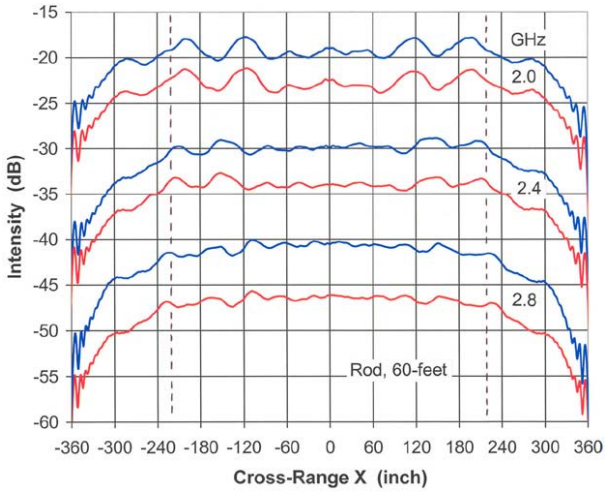

Fig. 5. Fourier transform spectra for the 60-ft rod after calibration of the cross-range distance and at three representative frequencies (2.0 GHz, 2.4 GHz, and 2.8 GHz). Dashed lines mark the boundary of ± 220 inches for easy comparison with the earlier results (see Fig. 6).

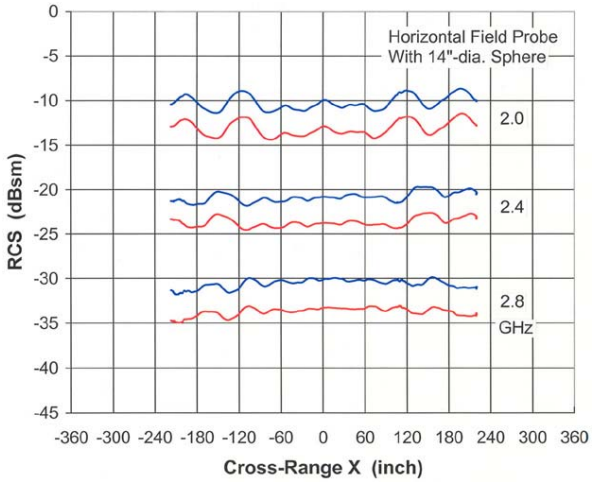

Fig. 6. Horizontal field probes measured in 1996 at three frequencies by translating a 14-inch sphere supported by strings within the distance of ± 220 inches [7].

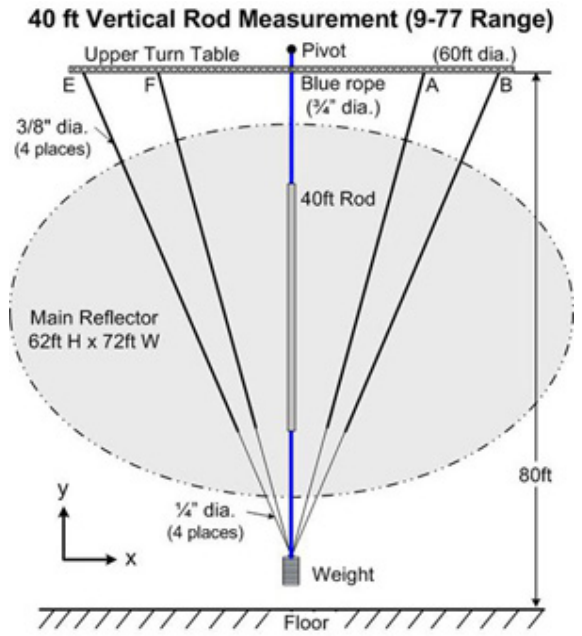

(a)

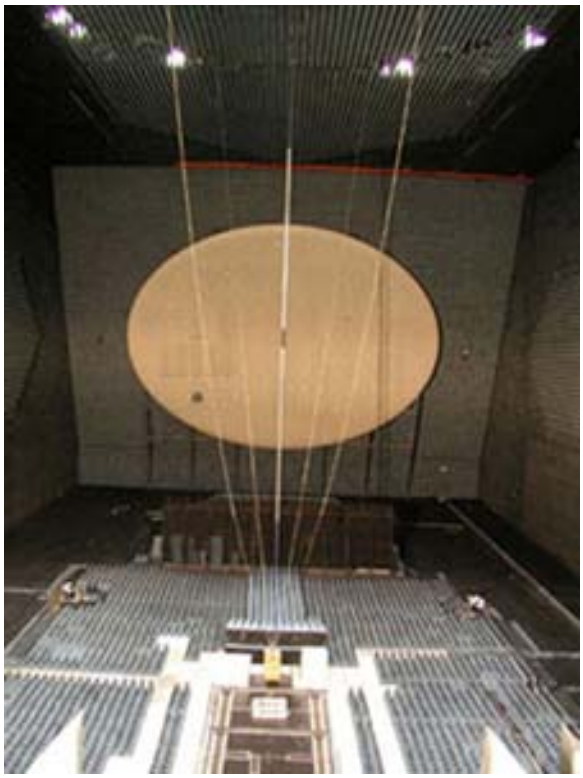

(b)

Fig. 7. (a) Schematic diagram of the test geometry for the vertical measurements and (b) photograph of the test geometry for vertical measurements (as viewed from the back).

The RCS data thus collected as a function of the translation distance of the lower end of the rod along Z (proportional to the out-of-plane tilt angle) were studied and analyzed. The second target was a separate piece of blue rope (dielectric, of 0.75 inch diameter before being stretched). The artesian coordinates (Fig. 7 (a)) are defined according to the right-handed system with the X-axis pointing east, Y-axis pointing up vertically, and the Z-axis pointing out from the page (away from the main reflector, down-range, to the south).

Figures 8 and 9 show the measured radar echoes at 2.4 GHz on the 40-ft rod and on the long blue rope, respectively. They look very similar, except in [dBsm] scale. In Fig. 9, the difference in peak RCS for the blue rope, (VV-HH) at 2.4 GHz, was found to be 6.002 dB. With reference to the wave equations for thin dielectric strings, the ratio of $(T_E / T_H)^2$ for the vertical string gives rise to a simple expression of $\{(\varepsilon_o+1)^2 / 4\}$, where ε_o = 2.99 can be estimated as the dielectric constant of the rope [5, 6]. Also in Fig. 9, the peak RCS for the rope in VV at 2.4 GHz was measured at 7.124 [dBsm]. Though the ka value at 0.479 (for the original radius of 0.375 inch) was moderate, not thin, let us assume that the equation for $S_{vv} = (T_E)^2 = [(L / 2) (\pi)^{1/2} (\varepsilon_o-1) (ka)^2]^2$ may still apply [5, 6]. By using L = 37.66 feet = 11.486 meter, and ε_o = 2.99, we can estimate the ka to be 0.335, or a = 0.262 inch as the "effective" radius of the rope (for wave scattering) after being stretched by a heavy weight.

A retro-reflecting ring was taped to the lower edge of the rod (Y= -20 ft) to facilitate monitoring of its motion by precision optical monitoring system (POMS). The (x, y, z) positions of the marker, recorded along with the radar data, were analyzed. The increments in dz versus z are shown in Fig. 10. Proper application of the DFT algorithm requires that the input data set must be equally spaced. In reality, however, the tilting motion of a vertically positioned object by pulling the strings tied to its lower end was not as smooth as we would have liked. To show how badly the sampling was, we subjected the as-measured raw data (2.4 GHz, VV) to DFT, and we obtained the arbitrary shaped spectra (in black) for the two cases in Fig. 11 (40-ft rod) and Fig. 12 (blue rope). Re-sampling of the raw data in regular steps of 0.20 inch (for increasing z from -60 to 60 inches) was performed by two methods:

a) Linear interpolation using the two nearest neighbors at each z position.

b) Spline interpolation using four data points at each prospective location, (aka cubic spline fit).

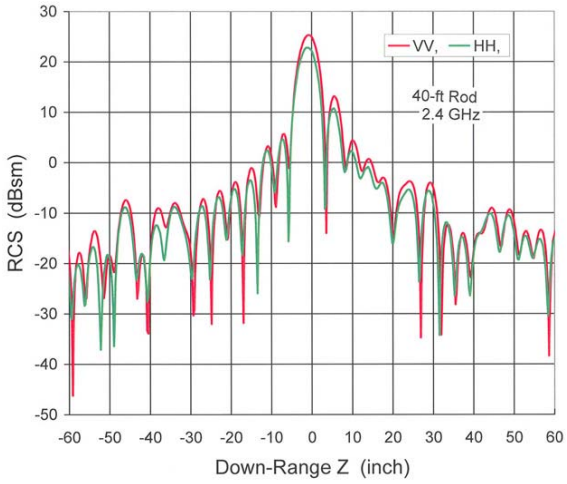

Fig. 8. Radar responses from the vertical 40-ft rod at 2.4 GHz versus distance z. The pattern reached its peak within a narrow range in z when the rod was at broadside to the wave-front.

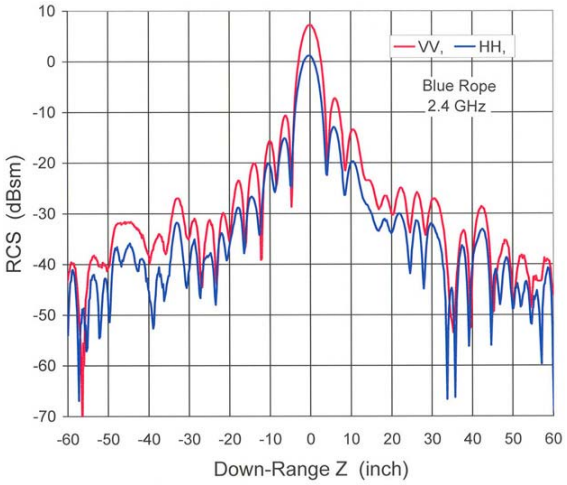

Fig. 9. Radar responses from the vertical blue rope at 2.4 GHz versus distance z. Though similar to Fig. 8 above, the HH scattering from the dielectric rope was weaker than its VV by 6 dB.

In the DFT spectra from the linearly interpolated data for the 40-ft rod (Fig. 11, in green) and for the blue rope (Fig. 12, in blue), we see that the spectra now show an interesting feature consisting of a plateau at about 40 dB above the noise level. The DFT spectra from the spline interpolated data are also plotted (in red) for the two cases. For clarity, the DFT spectra are displaced on the amplitude scale by dB values as noted in the graph. Upon closer inspection, we see that the red spectra exhibit more (or better) fine structures than those from the linearly interpolated data (in green or in blue). Thus, the spline interpolation method was chosen for further analysis in the present work.

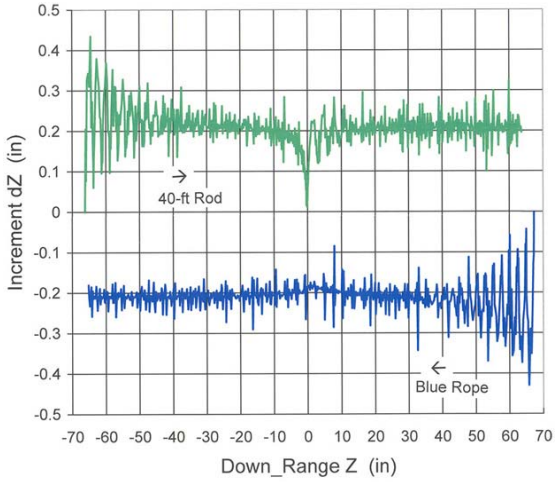

Fig. 10. Motion of z-increments versus z for the 40-ft rod (green) and the blue rope (blue). The direction of motion is indicated by an arrow. Note the swinging motion at the beginning of a run, as well as the hesitation near the broadside at z = 0.

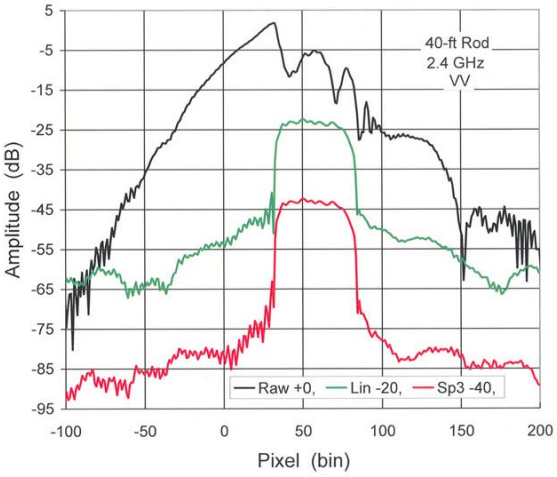

Fig. 11. DFT spectra of the as-measured raw data (black, arbitrarily shaped) and re-sampled data for the 40-ft rod. The stepped plateau was of prime interest in the present work. The cubic spline fit (red) showed more details than the linear interpolation (green).

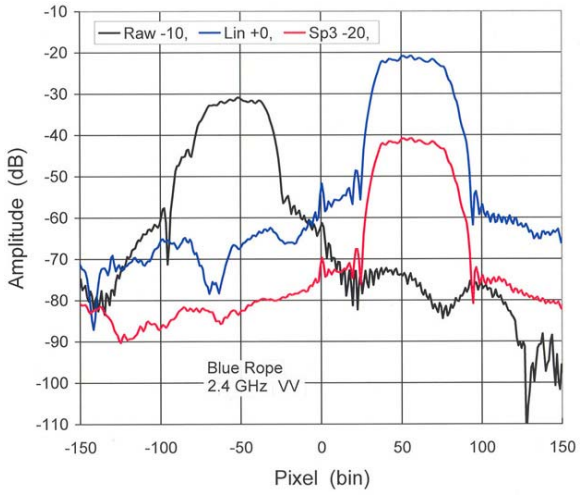

Fig. 12. DFT spectra of as-measured raw data (black) and re-sampled data for the blue rope (otherwise similar to Fig. 11 above).

Calibration of vertical distance Y was facilitated by the Gibb's phenomenon due to the finite length of the 40-ft rod in Fig. 11, plus the small peak at zero pixel due to the pivot of rotation in Fig. 12. The pivot for the swinging motion of the targets was about 4 feet above the UTT (see Fig. 7 (a)). Figure 13 shows the same data at 2.4 GHz (both HH and VV) re-plotted as a function of the abscissa in the calibrated vertical distance Y (in feet). The ripples across the plateau represent the variation in field as sampled from the vertical objects by their small angular motions in a plane containing the YZ-axes. While the 40-ft rod showed abrupt cutoffs, the blue rope by its nearly floor-to-ceiling length (< 80 ft) would actually sample the field tapered much beyond the nominal quiet zone boundary (Y = $\pm$ 14 ft) in the vertical dimension. Except for some minor difference, the field distributions within $\pm$ 14 feet from the center are qualitatively similar as sampled from the two objects, and for each of the two polarizations.

In Figs. 14 and 15, we compare the results of field distributions at three frequencies obtained by the two objects plotted with the same scales. While the VV spectra for both objects are plotted in red, the HH spectra are plotted separately for the 40-ft rod (in green) and the blue rope (in blue) for easy distinction. The abscissae are Y-distance in 10 feet per division. The ordinates are in 3-dB per division, which was calibrated to the [dBsm] scale for the 2.0 GHz VV-case only. The VV traces for the 2.4 GHz and 2.8 GHz are each shifted down by -6 dB from the previous VV trace.

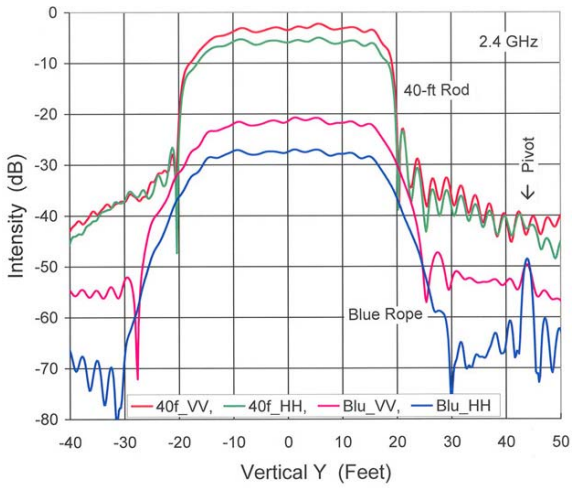

Fig. 13. DFT spectra versus calibrated distance Y for the 40-ft rod and the blue rope at 2.4 GHz for both VV and HH polarizations.

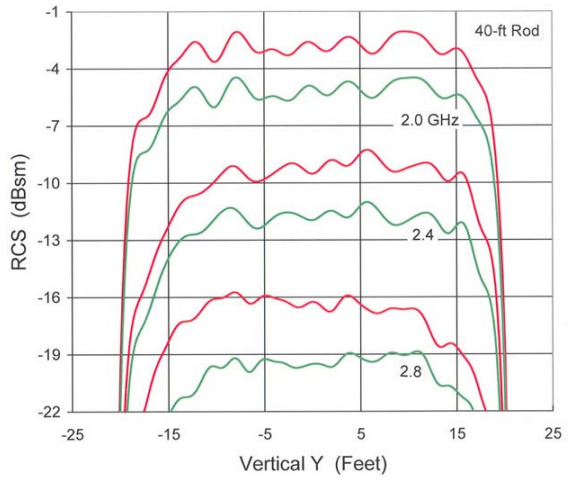

Fig. 14. FFT spectra versus vertical distance from the 40-ft rod at selected frequencies and polarization [VV (red) and HH (green)]. The cutoffs were due to the finite length of the rod.

In Fig. 14, the HH traces are each shifted down by -2 dB from the respective VV at the same frequency. Yet, in Fig. 15, since the HH scattering from the dielectric blue-rope is -6 dB weaker than the corresponding VV, the HH traces are each shifted up by 4 dB from the respective VV, so as to match the appearance of Fig. 14. We see in Figs. 14 and 15 that the DFT spectra obtained from the two different vertical objects (a metal rod

and a dielectric rope) are remarkably similar per frequency and per polarization, but varying in magnitude [dBsm].

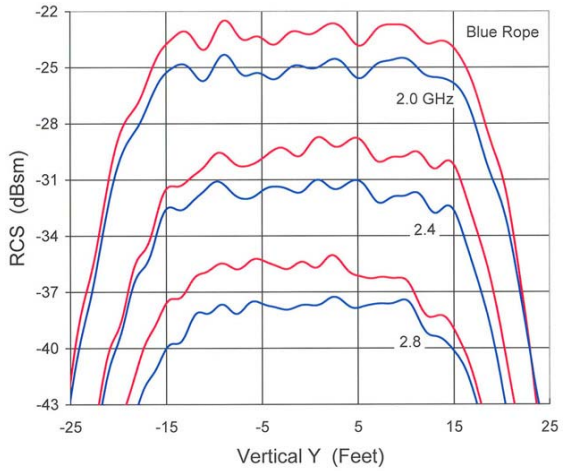

Fig. 15. FFT spectra from the blue rope versus frequency and polarization [VV (red) and HH (blue)]. The results showed a wider field distribution tapering out from the quiet zone boundary. Different only in RCS scale (dBsm) for the two vertical objects, the features of Figs. 14 and 15 (as a representation of field distribution) looked extremely similar.

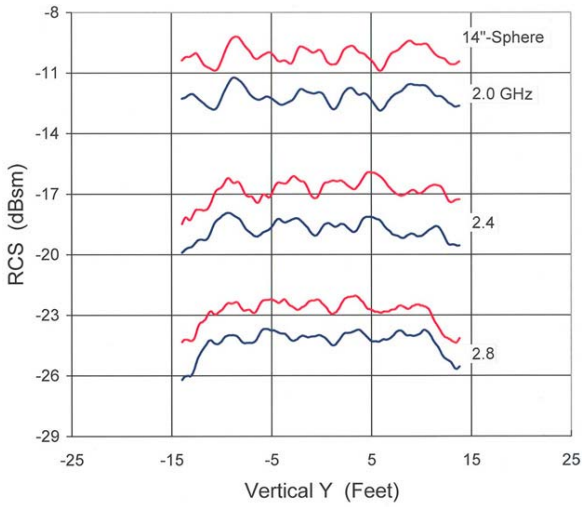

Fig. 16. Vertical field probes by a calibration sphere versus frequency and polarization recorded in 1996 [7]. The quiet zone boundary in the vertical dimension was specified as ± 14 ft, (or ± 168 inches).

For comparison with the new results shown in Figs. 14 and 15, we revisit the field probes measured by translating a sphere supported by strings in the vertical direction through the QZ center, (data collected in 1996). In Fig. 16 (which is plotted with the same scales), we see that the field distributions are very comparable with the new results. It is comforting to know that the radar wave-field has remained about the same with time.

IV. SUMMARY AND CONCLUSION

The measurements described in this paper took a group effort by dedicated colleagues (named in the references) several years to accomplish. To them I am deeply grateful. We conclude that the new method of performing field probes by the angular motion of a long rigid object, in either the horizontal or vertical plane, has been successfully demonstrated and validated. Further research should shed new light on radar measurements.

REFERENCES

[1] P. Wei and E. Knott, "The long string as a field probe," *Proc. 27th AMTA*, pp. 136-141, 2005.

[2] E. Knott and P. Wei, "The long string as a field probe," *IEEE Ant. and Prop. Mag.* , vol. 47, no. 6, pp. 22-27, Dec. 2005.

[3] P. Wei, A. Reed, C. Ericksen, J. Doty, and R. Schuessler, "Field probe from the angular response of a rigid body," *U.S. Patent 7,498,977 issued to the Boeing Company*, March 2009.

[4] P. Wei, A. Reed, C. Ericksen, J. Doty, and R. Schuessler, "Determining characteristics of a radar cross section (RCS) test range," *U.S. Patent 8,098,194 issued to the Boeing Company*, Jan. 2012.

[5] P. Wei, A. Reed, and E. Knott, "Study of wires and strings of finite sizes," *Proc. 20th AMTA*, pp. 221-226, 1998.

[6] E. Knott, A. Reed, and P. Wei, "Broadside echoes from wires and strings," *Microwave Journal*, vol. 42, Horizon House, pp. 102, Jan. 1999.

[7] P. Wei, A. Reed, C. Ericksen, and M. Bushbeck, "Study of RCS measurements from a large flat plate," *Proc. 7th AMTA*, pp. 3-8, 2005. Some typical field-probe results are included in Appendix A: Fig. A1, horizontal; Fig. A2, vertical.

[8] M. Agatonovic, Z. Marinkovic, and V. Markovic, "Application of ANNs in evaluation of microwave pyramidal absorber performance," *Applied Computational Electromagnetics Society (ACES) Journal*, vol. 27, no. 4, pp. 326-333, April 2012.

[9] S. Makino, Y. Konishi, H. Nishikawa, S. Morita, S. Kuroda, and Y. Inasawa, "Far-field RCS prediction from measured near-field data including metal

ground bounce," *21st Annual Review of Progress in ACES*, Honolulu, Hi, 2005.

Pax S. P. Wei received his B.Sc. from the National Taiwan University in 1960, his M.Sc. from University of Illinois in 1963, and his PhD in chemical physics from the California Institute of Technology in Pasadena, CA in 1968. After two years at the Bell Telephone Labs in Murray Hill, NJ, he joined the Boeing Company in Seattle, WA in 1969. There he performed research in low energy electron diffraction (LEED), optical spectroscopy on laser-produced plasmas and electrical discharge, and polarimetric radar target signature analysis. Dr. Wei started to work on RCS measurements from 1991; his interest was in radar response from simple geometric shapes for calibration and uncertainty analysis. He retired from the Boeing Company in 2010.

Planar Metamaterial for Matched Waveguide Termination

J. Li[1], F. Wang[2], G. Wen[1], Y. Huang[1], and W. Zhu[3]

[1] Centre for RFIC and System Technology, School of Communication and Information Engineering
University of Electronic Science and Technology of China, Chengdu, 611731, China
yongjunh@uestc.edu.cn

[2] Department of Communication, Chengdu Electromechanical College, Chengdu 611730, China
qifly@126.com

[3] Advanced Computing and Simulation Laboratory (AχL), Department of Electrical and Computer Systems Engineering, Monash University, Clayton, Victoria 3800, Australia
weiren.zhu@monash.edu

Abstract ─ We present the design, fabrication, and characterization of a novel matched waveguide termination based on planar artificial metamaterial. This matched termination is realized by recent developed planar metamaterial absorber, which can be designed to near-completely absorb the propagating electromagnetic energy at the edge of a shorted rectangular waveguide. Theoretical discussions, numerical simulations and microwave experiments are employed to illustrate the matched characteristics of the proposed waveguide termination. As an example, a matched waveguide termination with standing wave ratio of 1.23 is experimentally demonstrated at microwave frequency. Our result yields a promising approach to design of novel waveguide terminations by techniques of metamaterials.

Index Terms - Metamaterial absorber, waveguide, and termination.

I. INTRODUCTION

Matched waveguide termination, as a kind of important component, has been widely employed in waveguide systems to assist microwave measurements. The main functionality of such component is to absorb the electromagnetic field energy at the end of waveguides so as to eliminate the influences by waves reflecting at the edge. The origins of matched waveguide terminations could be traced to mid-20th century. Since that time, a great many approaches were developed to make matched terminations by, for examples, inductive and capacitive iris pairs [1], long sizes of tuners and dissipative elements [2], double-slug transformers and lossy dielectric loads [3], short-circuiting plungers and dissipative elements [4], and sliding loads by sections of lossless and lossy dielectrics [5]. Nowadays, the most commonly used waveguide matched terminations are built by merging the tapered wedges or slabs of lossy materials into waveguides (see [6]).

Unfortunately, all the existed matched waveguide terminations have the same disadvantage of large dimensions, restricting the possibility for integration application. Moreover, the present techniques of waveguide terminations are mainly focused on microwave frequencies, hardly suitable for terahertz and optical applications, such as silicon waveguide and nanophotonic integration. On the other hand, microwave absorbers have been rapidly developed in the past half century. Variety of absorbers was reported, such as dielectric absorbers, magnetic absorbers, ferrites, and ferroelectrics [7]. In particular, recent planar microwave absorbers, owning to the advantage of ultra-subwavelength thicknesses, have attracted considerable attention in design of communication radio frequency devices and antennas, some of which can be found in [8-11].

In the past decade, artificial structured

Submitted On: Sept. 4, 2012
Accepted On: Jan. 19, 2014

1054-4887 © 2013 ACES

materials, termed metamaterials [12–16], have gained extensive research interests. Theoretically predicted by Veselago [17] and experimentally realized by Smith et al. [18, 19], metamaterials enable a fantastic approach to control electromagnetic wave propagating inside such media by properly designing the "meta-atoms". Due to the excellent flexibility introduced by design of metamaterials, various novel applications have been considered such as super-lens [20], invisibility cloaks [21], enhanced antennas [22], etc. Besides, there is another important application, using metamaterials to design planar absorber so called metamaterial absorber (MA) [23]. Such MA is impedance-matched with free space while exhibits high loss, which is able to absorb incident electromagnetic wave energy near perfectly [24]. It is commonly known that, for the conventional absorbers, the electromagnetic wave energy is transformed into heat in the absorbing materials. For the MA, the energy is mainly consumed by the metal metamaterial resonators, due to the high-strength resonance characteristics [25]. Moreover, the absorbing frequency band can be easily operated from microwave to terahertz and optical frequencies by scaling the geometrical sizes [26, 27] and the bandwidth can also be widened by various techniques [28–31].

Recently, in our previous works we have demonstrated that the rectangular waveguide can be used to experimentally demonstrate the absorptivity of MAs [32], giving an alternative method to analyze the configurations of MAs compared with the free space measurement method [33]. Most importantly, this method provides a fire-new approach to design the matched terminations, especially for the rectangular waveguide applications. Comparing with conventional matched waveguide terminations [1–6], the newly metamaterial-based termination exhibits high-flexible design tolerance by using various metamaterial configurations. In this paper, we present a novel design of the planar matched terminations for rectangular waveguide applications, for the first time to our knowledge, by using metamaterials. Such matched termination is realized by designing a metamaterial absorber that suitable for shorted rectangular waveguide, which matches the characteristic impedance of waveguide and can absorb incident electromagnetic (EM) energy. As an example, a matched waveguide termination operated at X-band (8 GHz – 12 GHz) is designed, fabricated, and characterized by means of numerical simulation and microwave experiment. This paper is arranged as follows: section II gives a briefly discussions on the theoretical relationship between absorptivity and effective constitutive parameters; a metamaterial absorber is numerically designed in section III, and its application as matched terminations is demonstrated in section IV.

II. THEORY

We start by considering electromagnetic wave propagating at an interface between medium 1 and medium 2, the material properties of which are characterized by the relative permittivity $\varepsilon_{r,i}$ and relative permeability $\mu_{r,i}$, where i = 1, 2 denotes each medium. Fresnel equations give the reflections of s-polarized and p-polarized waves to be,

$$R_s = \left| \frac{\eta_2 \cos\theta - \eta_1 \sqrt{1-(n_1 \sin\theta / n_2)^2}}{\eta_2 \cos\theta + \eta_1 \sqrt{1-(n_1 \sin\theta / n_2)^2}} \right|^2 \quad (1a)$$

$$R_p = \left| \frac{\eta_2 \sqrt{1-(n_1 \sin\theta / n_2)^2} - \eta_1 \cos\theta}{\eta_2 \sqrt{1-(n_1 \sin\theta / n_2)^2} + \eta_1 \cos\theta} \right|^2 , \quad (1b)$$

where $\eta_i = \sqrt{\mu_{r,i}\mu_0 / \varepsilon_{r,i}\varepsilon_0}$ is the characteristic impedance and $n_i = \sqrt{\mu_{r,i}\varepsilon_{r,i}}$ is the refractive index. For sake of simplicity, we restrict our discussion on the normal incident wave (i.e., the incident angle $\theta = 0$) and medium 1 is free space with $\varepsilon_{r,i} = \mu_{r,i} = 1$. Equation (1) is therefore reduced to be,

$$R = R_s = R_p = \left| \frac{\eta_2 - \eta_1}{\eta_2 + \eta_1} \right|^2 = \left| \frac{\sqrt{\mu_{r,2}} - \sqrt{\varepsilon_{r,2}}}{\sqrt{\mu_{r,2}} + \sqrt{\varepsilon_{r,2}}} \right|^2 . \quad (2)$$

If we consider the metamaterial absorbers that consisted of electric-inductance-capacitor (ELC) resonators and backed metallic plate [23], in which case zero transmissivity is achieved, and thus the absorptivity could be simply expressed as,

$$A = 1 - R = 1 - \left| \frac{\sqrt{\mu_{r,2}} - \sqrt{\varepsilon_{r,2}}}{\sqrt{\mu_{r,2}} + \sqrt{\varepsilon_{r,2}}} \right|^2 . \quad (3)$$

Equation (3) reveals the relationship between the absorptivity and effective material parameters ε_r and μ_r of metamaterial. By properly designing the geometry of metamaterial's unit cells and the coupling strength between those units and the metallic plate layers, one can successfully achieve the conditions of $\varepsilon(\omega) = \mu(\omega)$ and large loss tangents $\tan\delta_\varepsilon$ and $\tan\delta_\mu$. The MAs can, therefore, impedance-match with free space and absorb the electromagnetic waves completely.

III. NUMERICAL DESIGN OF METAMATERIAL ABSORBER

Before discussing the proposed planar matched waveguide termination, we first numerically design an MA with nearly complete absorption, the unit cell of which is shown in the insert of Fig. 1. The designed structure is similar to [23], made up of metallic ELC resonator (constructed by copper line with width of 0.2 mm and thickness of 0.017 mm, and the electric conductivity of copper is 5.8×10^7 S/m) on one side of the FR4 substrate and metallic ground plane on the other side.

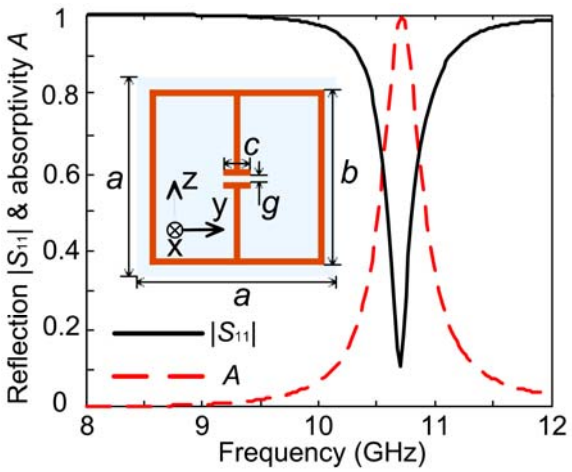

Fig. 1. Simulated reflection and absorptivity of the MA unit cell. The inset is the schematic representation of the MA unit cell with dimensional parameters: $a = 5$ mm, $b = 3.3$ mm, $c = 1$ mm, and $g = 0.2$ mm. The substrate is FR4 with relative dielectric constant $\varepsilon_r = 4.0(1 + 0.02i)$ and thickness of 0.8 mm.

In our simulation, perfect ***E*** boundaries along the *z*-axis and perfect ***H*** boundaries along the *y*-axis are applied to mimic a transverse electromagnetic (TEM) wave propagating to the periodically arranged unit cells. Through strict numerical calculation by Ansoft HFSS software, a group of geometrical parameters are obtained, as listed in the caption of Fig. 1. It is seen that, there is a reflection dip centered at 10.7 GHz (see the black solid line). Due to existence of the ground plane on the other side of the substrate, no EM power can be transmitted through the structure. Since the surface of the metamaterial is smooth enough compare to the wavelength of incident wave, the influence of scattering is negligible. Therefore, the absorptivity of the MA comes to be $A = 1-|S_{11}|^2$. The red dashed line in Fig. 1 indicates that more than 99.9 % EM energy is absorbed by the MA at the resonant frequency.

The surface current distributions on the ELC resonant and the ground plane are shown in Fig. 2 to reveal the resonant mechanism at resonance frequency 10.7 GHz. For EM wave normal incidence, the electric currents on the ELC pattern are symmetrical and thus provide the electric response. The antiparallel currents between the ELC cell and the ground plane show that a magnetic response is induced by the incident EM wave. The electric response and magnetic response appeared simultaneously at the given frequency so that enables the MA to absorb the incident electric and magnetic fields completely.

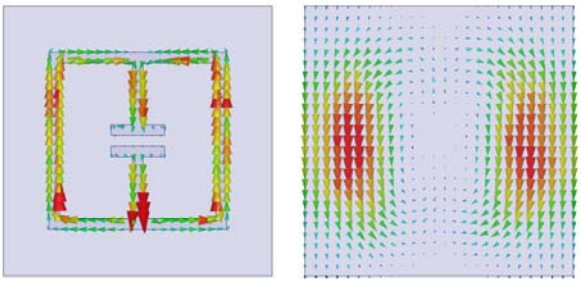

Fig. 2. The surface current densities on the metamaterial unit cell and ground plane at resonant frequency 10.7 GHz.

As analyzed in [23], the near-perfect absorption is mainly arisen from two aspects. The first one is that the metamaterial provides electric and magnetic resonances and enhances the local EM field. The other aspect is the losses in the coppers and substrate material. Both of the structure resonance and material losses provide the

impedance-match and absorption properties. In the following section, we show the application of the proposed metamaterial absorber as a planar matched waveguide termination operated at microwave X-band.

IV. MATCHED WAVEGUIDE TERMINATION

The above-mentioned MA shows near-perfect absorption to the normal incident EM wave, it is expected that similar MA is also useful for rectangular metallic waveguides where the incident waves are restricted into transverse electric mode. In such a way, MA can be applied as a planar matched waveguide termination. As shown in Fig. 3, the fabricated matched waveguide termination is 22.86 × 10.16 mm^2 in size to fit the transverse size of the X-band rectangular waveguide and the other dimensional parameters are all the same as shown in the above section except the period space a = 4.5 mm.

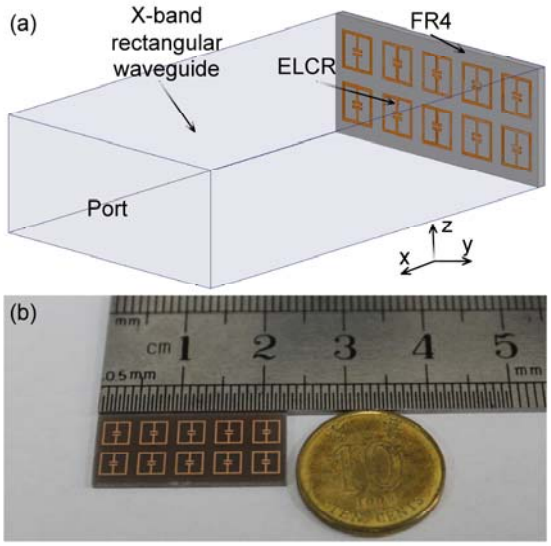

Fig. 3. (a) Schematic representation of the X-band matched rectangular waveguide termination based on the metamaterial and (b) fabricated metamaterial sample.

The performance of a matched waveguide termination is characterized by the standing wave ratio (SWR), commonly defined as the amplitude ratio of a partial standing wave at an antinode (maximum) to an adjacent node. For ideal case that free of any reflection, no standing wave is formed and thus SWR equals to 1. The measurement is performed by a vector network analyzer (Agilent N5230A) and coaxial-to-rectangular-waveguide transition. Figure 4 shows the measured SWR compared with the numerical result. It is seen that the matched termination exhibits a narrow matched band of about 80 MHz (SWR < 1.5) centered at 10.62 GHz with the dip value of SWR about 1.23. Comparing the measured and simulated results, there is a little shift of the matched band, mainly due to the fabrication tolerance. The reflection of the MA in rectangular waveguide is also in good agreement with that in free space, which verifies the equal effectiveness in both cases. Surface current distributions are further investigated in Fig. 5, where same resonance characteristics are found compared with that in Fig. 2.

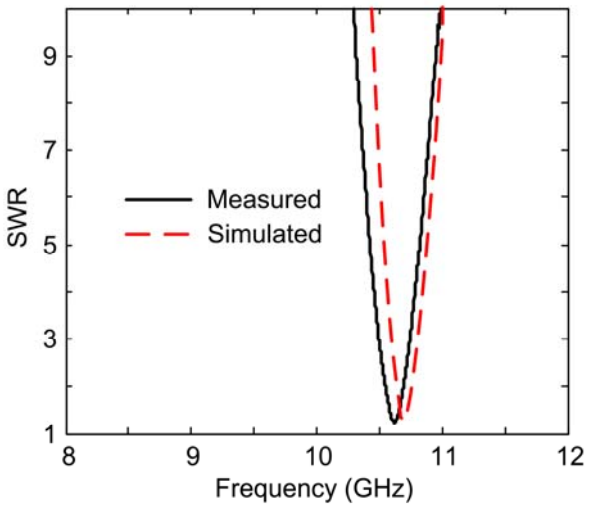

Fig. 4. Measured and simulated SWR of the proposed matched waveguide termination.

Moreover, the measured and simulated input impedance characteristics are presented in Fig. 6 to further show the impedance-match properties. In both measurement and simulation, the reference planes are chosen as close as possible to the metamaterial plane. The comparison shows a good agreement between the numerical and measured results near the resonant frequency. The measured result indicates a considerable mismatch which, leads to a big SWR at the design frequency (the circle of SWR = 1.5 is also shown in Fig. 6). To miniaturize the mismatch or SWR, some methods should be explored which, will be discussed in the next of this paper.

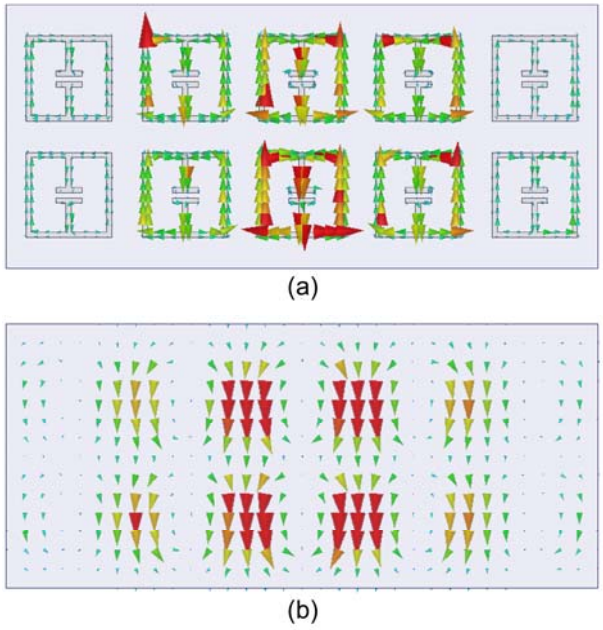

Fig. 5. The surface current densities on the metamaterial unit cells and the shorted wall at resonant frequency 10.7 GHz.

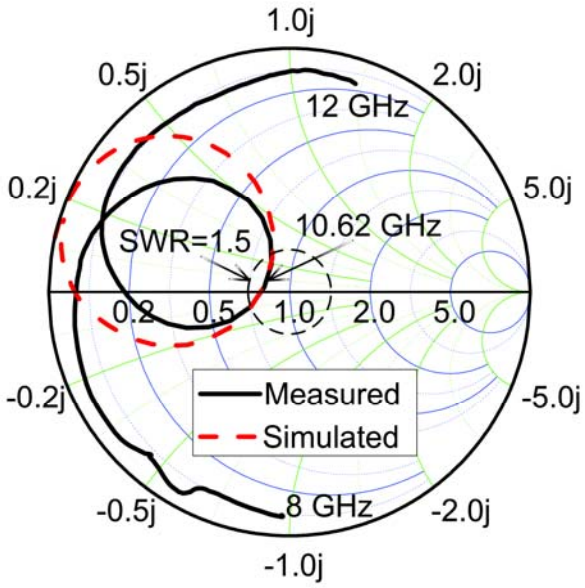

Fig. 6. Measured and simulated input impedances of the metamaterial based matched termination.

The performance of the above matched termination can be further improved to near perfect impedance-match by turning the thickness of the substrate or changing the substrate material with other loss values, as the same optimization method of MAs which, have been discussed in [23]. Here we give an optimized result of the proposed matched termination by adjusting the thickness of the substrate. Figure 7 shows the simulated SWR characteristics of the matched termination with different thicknesses of the substrates range from 0.8 mm to 1.0 mm. It can be known that the matched termination keeps a reasonable matched performance along the whole considered range (the SWR curves have a matched frequency band of wider than 70 MHz for SWR < 1.5). When the thickness of the substrate increases, the SWR first decreases and trends to the optimum value of 1.035 at 10.7 GHz and then arises back to the 1.23 at 10.7 GHz (see the inset figure of Fig. 7). In this case, the optimized thickness of the substrate is 0.9 mm. The optimized result shows a very well impedance-match characteristic, similar to the conventional matched waveguide terminations [1-6].

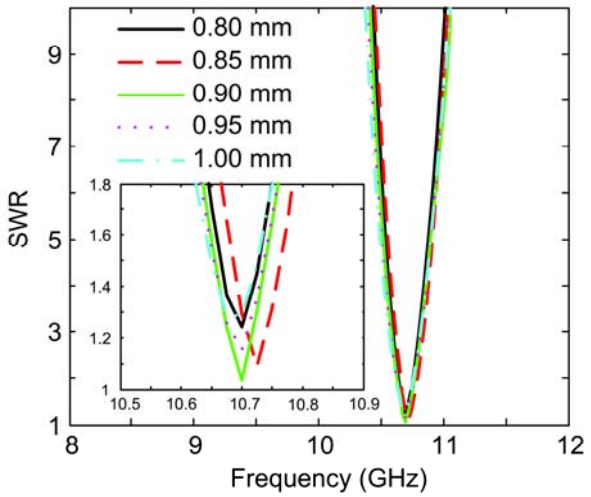

Fig. 7. Simulated SWR characteristics at different thickness of the substrate. The inset figure is the amplified SWR characteristics near the resonance frequency.

As a concluding remark, we would like to note that the unit cell of MA proposed in this paper is only for example, and it can be replaced by any other configurations reported in [34, 35]. Although our work is only focusing on microwave frequency, it can be expected that the behavior presented in this paper is quite general and can be also useful for THz or even optical range. Moreover, the narrow bandwidth can be widened by variety of techniques [26-31].

V. CONCLUSION

In this paper, a novel schematic design of X-band planar matched waveguide termination based on the metamaterial has been discussed for the first time to our knowledge. The measured and simulated results demonstrated that the proposed inclusion exhibited a narrow matched frequency band of about 80 MHz (SWR < 1.5) centered at 10.62 GHz. It was also shown that such near perfect matched characteristic could be optimized by adjusting the thickness of substrate. We expect that the matched frequency band can be operated from microwave to terahertz, and even optical frequencies by changing the structure sizes and the bandwidth can be enlarged by using some broadband techniques. It opens the way to design and fabricate the novel matched termination for waveguide by using the very interested metamaterials. It also has the broad applications in microwave engineering areas, for example, it can be used in design of traveling-wave antennas or leaky-wave antennas as matched terminations.

ACKNOWLEDGMENT

This work was partially supported by the National Natural Science Foundation of China (Grant No. 61371047), the Research Fund for the Doctoral Program of Higher Education of China (Grant No. 20110185110014), and the Fundamental Research Funds for the Central Universities (Grant No. E022050205). Y. Huang gratefully acknowledges the Scholarship Award for Excellent Doctoral Student granted by Ministry of Education of China (Grant No. A03003023901006) and the Excellent Doctoral Student Training Program support by University of Electronic Science and Technology of China. W. Zhu also gratefully acknowledges the Australian Research Council for financial support within the frame of the Discovery Grant scheme under grant DP110100713.

REFERENCES

[1] R. Fellers and R. Weidner, "Broad-band wave-guide admittance matching by use of irises," *Proc. of the I.R.E*, vol. 35, no. 10, pp. 1080-1085, 1947.

[2] R. Grantham, "A reflectionless wave-guide termination," *Rev. Sci. Instr*., vol. 22, no. 11, pp. 828-834, 1951.

[3] R. Ellenwood and W. Ryan, "A UHF and microwave matching termination," *Proc. of the I.R.E*, vol. 41, no. 1, pp. 104-107, 1953.

[4] J. Smidt, "A reflectionless wave guide termination," *Appl. Sci. Res*, vol. 3, pp. 465-476, 1954.

[5] M. Wood, "Tunable low-reflection waveguide termination," *Electro. Lett.*, vol. 18, no. 4, pp. 174-175, 1982.

[6] R. Collin, *Foundations for Microwave Engineering*, Wiley-Interscience, New York, 2001.

[7] V. Petrov and V. Gagulin, "Microwave absorbing materials," *Inorganic Materials*, vol. 37, no. 2, pp. 93-98, 2001.

[8] E. Hashsish, "Design of wideband thin layer planar absorber," *Journal of Electromagnetic Waves and Applications*, vol. 16, no. 2, pp. 227-241, 2002.

[9] L. Folgueras, E. Nohara, R. Faez, and M. Rezende, "Dielectric microwave absorbing material processed by impregnation of carbon fiber fabric with polyaniline," *Materials Research*, vol. 10, no. 1, pp. 95-99, 2007.

[10] V. Levcheva, I. Arestova, B. Nikolov, and P. Dankov, "Characterization and modeling of microwave absorbers in the RF and antenna projects," *Telfor Journal*, vol. 1, no. 2, pp. 57-60, 2009.

[11] S. Pandi, B. Narayanan, and V. Mcginn, "Analysis and design of planar multi-layered parabolic absorber for low-power applications," *Electromagnetics*, vol. 31, pp. 448-459, 2011.

[12] J. Valentine, S. Zhang, T. Zentgraf, E. Ulin-Avila, D. A. Genov, G. Bartal, and X. Zhang, "Three-dimensional optical metamaterial with a negative refractive index," *Nature*, vol. 455, pp. 376-379, 2008.

[13] Y. Huang, G. Wen, T. Li, and K. Xie, "Positive-negative-positive metamaterial consisting of ferrimagnetic host and wire array," *Applied Computational Electromagnetic Society (ACES) Journal*, vol. 25, no. 8, pp. 696-702, August 2010.

[14] W. Zhu, I. Rukhlenko, and M. Premaratne, "Light amplification in zero-index metamaterial with gain inserts," *Appl. Phys. Lett*., vol. 101, pp. 031907, 2012.

[15] Y. Huang, G. Wen, Y. Yang, and K. Xie, "Tunable dual band ferrite-based metamaterials with dual negative refractions," *Appl. Phys. A*, vol. 106, pp. 79-86, 2012.

[16] Y. Huang, G. Wen, T. Li, L. Li, and K. Xie, "Design and characterization of tunable terahertz metamaterials with broad bandwidth and low loss," *IEEE Antennas and Wireless Propagation Letters*, vol. 11, pp. 264-267, 2012.

[17] V. Veselago, "The electrodynamics of substances with simultaneously negative values of ε and μ," *Soviet Phys. Uspekhi*., vol. 10, pp. 509-514, 1968.
[18] D. Smith, W. Padilla, D. Vier, S. Nemat-Nasser, and S. Schultz, "Composite medium with simultaneously negative permeability and permittivity," *Phys. Rev. Lett*., vol. 84, no. 18, pp. 4184-4187, 2000.
[19] R. Shelby, D. Smith, and S. Schultz, "Experimental verification of a negative index of refraction," *Science*, vol. 292, pp. 77-79, 2001.
[20] J. Pendry, "Perfect cylindrical lenses," *Opt. Express*, vol. 11, pp. 755-760, 2003.
[21] D. Schurig, J. Mock, B. Justice, S. Cummer, J. Pendry, A. Starr, and D. Smith, "Metamaterial electromagnetic cloak at microwave frequencies," *Science*, vol. 314, pp. 977-980, 2006.
[22] M. Fallah, A. Heydari, A. Mallahzadeh, and F. Kashani, "Design and SAR reduction of the vest antenna using metamaterial for broadband applications," *Applied Computational Electromagnetic Society (ACES) Journal*, vol. 26, no. 28, pp. 141-152, February 2011.
[23] Tao, H., C. M. Bingham, A. C. Strikwerda, D. Pilon, D. Shrekenhamer, N. I. Landy, K. Fan, X. Zhang, W. J. Padilla, and R. D. Averitt, "Highly flexible wide angle of incidence terahertz metamaterial absorber: Design, fabrication, and characterization," *Phys. Rev. B*, vol. 78, p. 241103(R), 2008.
[24] C. Watts, X. liu, and W. Padilla, "Metamaterial electromagnetic wave absorbers," *Adv. Mater.*, vol. 24, pp. OP98-Op120, 2012.
[25] Q. Wen, Y. Xie, H. Zhang, Q. Yang, Y. Li, and Y. Liu, "Transmission line model and fields analysis of metamaterial absorber in the terahertz band," *Opt. Express*, vol. 17, pp. 20256-20265, 2009.
[26] W. Zhu and X. Zhao, "Metamaterial absorber with random dendritic cells," *Eur. Phys. J. Appl. Phys.*, vol. 50, pp. 21101, 2010.
[27] W. Zhu, X. Zhao, B. Gong, L. Liu, and B. Su, "Optical metamaterial absorber based on leaf-shaped cells," *Appl. Phys. A*, vol. 102, pp. 147-151, 2011.
[28] J. Zhong, Y. Huang, G. Wen, H. Sun, P. Wang, and O. Gordon, "Single-/dual-band metamaterial absorber based on cross-circular-loop resonator with shorted stubs," *Appl. Phys. A*, vol. 108, pp. 329-335, 2012.
[29] W. Zhu, Y. Huang, I. Rukhlenko, G. Wen, and M. Premaratne, "Configurable metamaterial absorber with pseudo wideband spectrum," *Opt. Express*, vol. 20, no. 6, pp. 6616-6621, 2012.
[30] F. Ding, Y. Cui, X. Ge, Y. Jin, and S. He, "Ultra-broadband microwave metamaterial absorber," *Appl. Phys. Lett*., vol. 100, pp. 103506, 2012.
[31] Y. Cui, K. Fung, J. Xu, H. Ma, Y. Jin, S. He, and N. Fang, "Ultra broadband light absorption by a sawtooth anisotropic metamaterial slab," *Nano Lett*., vol. 12, pp. 1443-1447, 2012.
[32] Y. Huang, G. Wen, J. Li, J. Zhong, P. Wang, Y. Sun, O. Gordon, and W. Zhu, "Metamaterial absorbers realized in X-band rectangular waveguide," *Chin. Phys. B*, vol. 21, pp. 117801, 2012.
[33] Y. Cheng and H. Yang, "Design, simulation, and measurement of metamaterial absorber," *J. Appl. Phys.*, vol. 108, pp. 034906, 2010.
[34] D. Schurig, J. Mock, and D. Smith, "Electric-field-coupled resonators for negative permittivity metamaterials," *Appl. Phys. Lett.*, vol. 88, pp. 041109, 2006.
[35] W. Padilla, M. Aronsson, C. Highstrete, M. Lee, J. Taylor, and R. Averitt, "Electrically resonant terahertz metamaterials: Theoretical and experimental investigations," *Phys. Rev. B*, vol. 75, pp. 041102, 2007.

Jian Li received the B.Sc. and M.Sc. degrees in Communication Engineering from UESTC in 2007 and 2010, respectively, and is currently working toward a Ph.D. degree in UESTC. His research interests include including RF, Microwave, and Millimeter wave Integrated Circuits and system. His is also interested in electromagnetic metamaterial and its applications in substrate integrated waveguide.

Fei Wang was born in Sichuan, China, in 1978. He received his B.S degree in Management from Nanjing University of Aeronautics and Astronautics in 2002 and received his M.S degree in Computing Science from Sichuan University in 2006. He is currently working with the Department of Communication, Chengdu Electromechanical College. His research activities include wireless communication and system, electromagnetic metamaterials design and simulations.

Guangjun Wen was born in Sichuan, China, in 1964. He received his M.Sc. and Ph.D. degrees in Chongqing University of China in 1995 and UESTC in 1998, respectively. He is currently a professor and doctor supervisor in UESTC.

His research and industrial experience covers a broad spectrum of electromagnetics, including RF, Microwave, Millimeter wave Integrated Circuits and Systems design for Wireless Communication, Navigation, Identification, Mobile TV applications, RFIC/MMIC/MMMIC device modeling, System on Chip (SoC) and System in Package (SiC) Design, RF/Microwave/Millimeter wave Power source Design, "The Internet of things" devices and system, RFID system and networks, antennas, as well as model of electromagnetic metamaterial and its application in microwave engineering area.

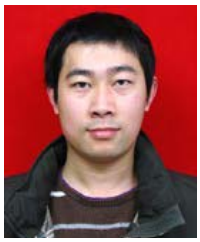

Yongjun Huang received the B.Sc. degree in Mathematics from Neijiang Normal University of China in 2007, M.S. degree in Communication Engineering from University of Electronic Science and Technology of China (UESTC) in 2010, and is currently working toward a Ph.D. degree in UESTC. His research activities are electromagnetic metamaterial and its application in microwave engineering area, FDTD and CAD analysis for the metamaterial model and characteristics.

Weiren Zhu received the B.Sc. and Ph.D degrees in Applied Physics and Material Physics & Chemistry from Northwestern Polytechnical University, in 2006 and 2011, respectively. Then he worked as a Postdoctoral Fellow at Nonlinear Physics Centre, the Australian National University, and now he is a Research Fellow at Advanced Computing and Simulation Laboratory, Monash University. His research interests include electromagnetic metamaterials, plasmonics, and nonlinear optics.

UWB Monopole Antenna with WLAN Frequency Band-Notched Performance by using a Pair of E-Shaped Slits

N. Ojaroudi, M. Ojaroudi, and N. Ghadimi

Young Researchers Club
Ardabil Branch, Islamic Azad University, Ardabil, Iran
n.ojaroudi@yahoo.com, m.ojaroudi@iauardabil.ac.ir, noradin.ghadimi@gmail.com

Abstract ─ In this paper an ultra-wideband monopole antenna with frequency band-stop performance is designed and manufactured. The proposed antenna consists of square radiating patch with two E-shaped slits and a ground plane with a protruded T-shaped strip inside the rectangular slot. In the proposed structure, by inserting a rectangular slot with a T-shaped strip protruded inside the slot on the ground plane, additional resonance is excited and hence, much wider impedance bandwidth can be produced, especially at the higher band. In order to create band-rejected function we use two E-shaped slits in the square radiating patch. The fabricated antenna has the frequency band of 3 GHz to over 12.7 GHz with a rejection band around 5 GHz – 6 GHz. Good VSWR and radiation pattern characteristics are obtained in the frequency band of interest. Simulated and measured results are presented to validate the usefulness of the proposed antenna structure for UWB applications

Index Terms ─ Band-notched function, E-shaped slit, microstrip-fed monopole antenna, protruded T-shaped strip, and ultra-wideband (UWB) communications.

I. INTRODUCTION

Communication systems usually require smaller antenna size in order to meet the miniaturization requirements of radio-frequency (RF) units [1]. It is a well-known fact that planar monopole antennas present really appealing physical features, such as simple structure, small size, and low cost. Due to all these interesting characteristics, planar monopoles are extremely attractive to be used in emerging UWB applications, and growing research activity is being focused on them. Consequently, a number of planar monopoles with different geometries have been experimentally characterized [2-3].

The frequency range for UWB systems between 3.1GHz–10.6 GHz will cause interference to the existing wireless communication systems for example the wireless local area network (WLAN) for IEEE 802.11a operating in 5.15GHz–5.35 GHz and 5.725GHz–5.825 GHz bands, so the UWB antenna with a band-notch function is required. Lately to generate the frequency band-notch function, modified planar monopoles several antennas with band-notch characteristic have been reported [4-10]. In [6-8], different shapes of the slots (i.e., W-shaped, L-shaped, and folded trapezoid) are used to obtain the desired band notched characteristics. Single and multiple [9] half-wavelength U-shaped slots are embedded in the radiation patch to generate the single and multiple band-notched functions, respectively. and automatic design methods have been developed to achieve band-notch performance [10].

In this paper, a simple method for designing a novel and compact microstrip-fed monopole antenna with band-notched characteristic for UWB applications has been presented. In the proposed antenna, for bandwidth enhancement we use a rectangular slot with a T-shaped strip protruded inside the rectangular slot on the ground plane. Also by using two E-shaped slits with variable dimensions beside the square radiating patch a band-stop performance can be created. The presented monopole antenna has a small size of 12×18 mm^2. The size of the designed antenna is smaller than the UWB antennas with band-notched function reported recently, which has at least a

Submitted On: Sept. 25, 2012
Accepted On: Jan. 19, 2014

1054-4887 © 2013 ACES

size reduction of 15 % with respect to the previous similar antenna [7-10]. Good return loss and radiation pattern characteristics are obtained in the frequency band of interest. Simulated and measured results are presented to validate the usefulness of the proposed antenna structure for UWB applications.

II. ANTENNA DESIGN

The presented small monopole antenna fed by a microstrip line is shown in Fig. 1, which is printed on an FR4 substrate of thickness 1.6 mm, permittivity 4.4, and loss tangent 0.018. The basic monopole antenna structure consists of a cross-shaped radiating patch, a feed line, and a ground plane. The patch is connected to a feed line of width W_f and length L_f. The width of the microstrip feed line is fixed at 2 mm, as shown in Fig. 1. On the other side of the substrate, a conducting ground plane is placed. The proposed antenna is connected to a 50 Ω SMA connector for signal transmission.

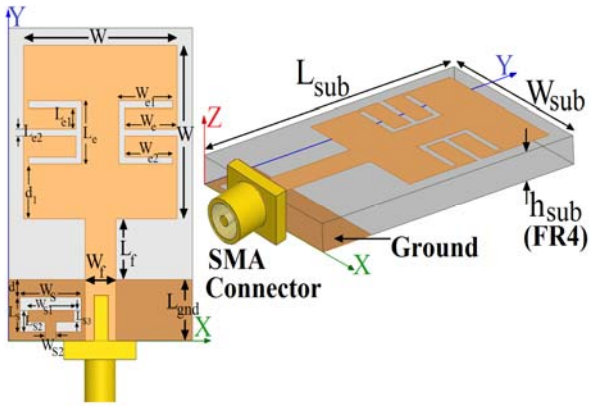

(a) (b)

Fig. 1. Geometry of the proposed antenna, (a) side view and (b) bottom view.

Regarding defected ground structures (DGS), creating slots in the ground plane provides an additional current path. Moreover, this structure changes the inductance and capacitance of the input impedance, which in turn leads to change the bandwidth. The DGS applied to a microstrip line causes a resonant character of the structure transmission with a resonant frequency controllable by changing the shape and size of the slot [2]. Therefore, by cutting a rectangular slot with a T-shaped strip protruded inside the rectangular slot on the ground plane and carefully adjusting its parameters, much enhanced impedance bandwidth may be achieved. As illustrated in Fig. 1, the E-shaped slits are placed in the radiating patch and is also symmetrical with respect to the longitudinal direction. This structure can perturb the resonant response and also acts as a half-wave resonant structure [3]. At the notched frequency, the current flows are more dominant around the slits, and they are oppositely directed between the slit edges [3]. As a result, the desired high attenuation near the notch frequency can be produced.

The optimized values of presented monopole antenna design parameters are as follows: W_{sub} = 12 mm, L_{sub} = 18 mm, h_{sub} = 1.6 mm, W_f = 2 mm, L_f = 3.5 mm, W = 10 mm, W_S = 4 mm, L_S = 2 mm, W_{S1} = 1 mm, L_{S1}= 1 mm, W_{S2} = 3 mm, L_{S2} = 11.5 mm, W_{S3} = 1 mm, W_e = 12 mm, L_e = 0.5 mm, W_{e1} = 0.25 mm, L_{e1} = 0.5 mm, W_{e2} = 3 mm, L_{e2} = 3.5 mm, d = 1.5 mm, d_1 = 3.5 mm, and L_{gnd} = 3.5 mm.

III. RESULTS AND DISCUSSIONS

The proposed microstrip monopole antenna with various design parameters were constructed, and the numerical and experimental results of the input impedance and radiation characteristics are presented and discussed. The proposed microstrip-fed monopole antenna was fabricated and tested. The parameters of this proposed antenna are studied by changing one parameter at a time and fixing the others. Ansoft HFSS simulations are used to optimize the design and agreement between the simulation and measurement is obtained [11].

The configuration of the presented monopole antenna was shown in Fig. 1. Geometry for the ordinary square patch antenna (Fig. 2 (a)), with a rectangular slot with a T-shaped strip protruded inside the rectangular slot on the ground plane (Fig. 2 (b)), and the proposed antenna (Fig. 2 (c)) structures are compared in Fig. 2. The VSWR characteristics for structures that were shown in Fig. 2 are compared in Fig. 3. As shown in Fig. 3, it is observed that the upper frequency bandwidth is affected by using the rectangular slot with a T-shaped strip protruded inside the rectangular slot on the ground plane and the notch frequency bandwidth is sensitive to the E-shaped slits on the

radiating patch [12]. Also it is found that by using the T-shaped strip protruded inside the rectangular slot on the ground plane, the third resonance occur at around 12 GHz in the simulation. The input impedance of the proposed slot antenna structure that studied in Fig. 1, on a Smith chart is shown in Fig. 4.

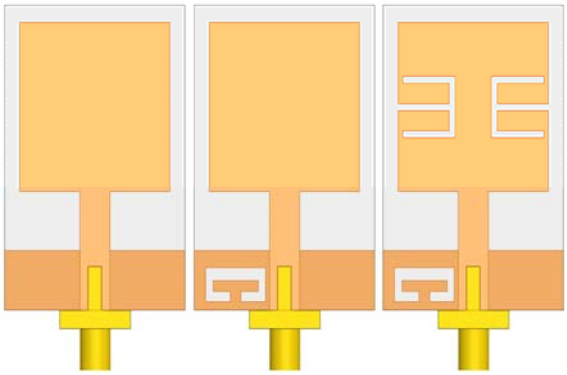

(a) (b) (c)

Fig. 2. (a) Basic structure (ordinary square monopole antenna), (b) antenna with a pair of H-shaped slots in the ground plane, and (c) the proposed antenna.

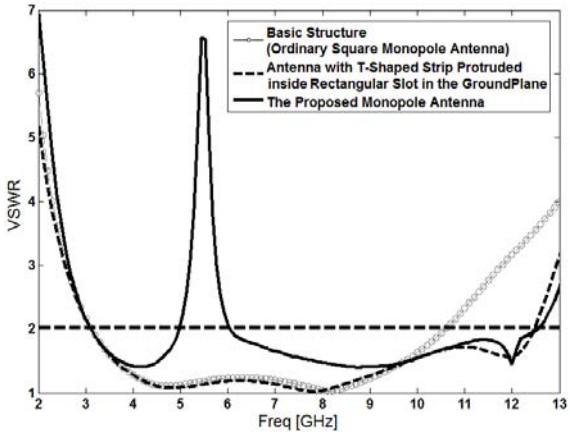

Fig. 3. Simulated VSWR characteristics for the monopole antennas shown in Fig. 2.

In order to understand the phenomenon behind this additional resonance and band notch performance, the simulated current distribution on the ground plane for the square antenna with a T-shaped strip protruded inside the rectangular slot on the ground plane at the new resonance frequency of 12 GHz are presented in Fig. 5 (a). It can be observed that in Fig. 5 (a), the current concentrated on the edges of the interior and exterior of T-shaped strip protruded inside the rectangular slot at 12 GHz [13].

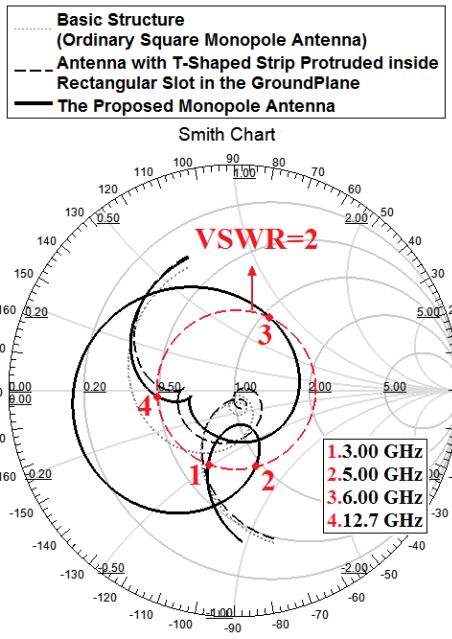

Fig. 4. The simulated input impedance on a Smith chart of the proposed antenna structure shown in Fig. 1.

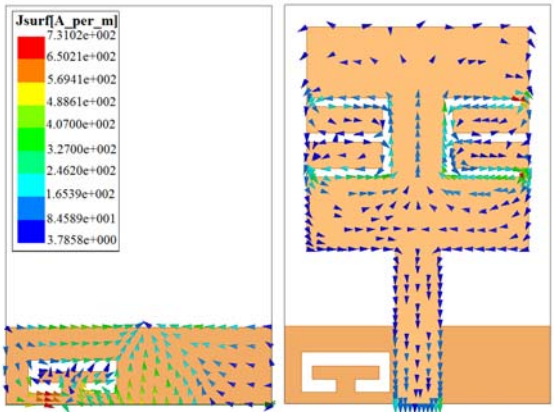

(a) (b)

Fig. 5. Simulated surface current distributions on the ground plane (a) for the square monopole antenna with two H-shaped slot at 11.2 GHz and (b) for the proposed antenna at 5.5 GHz.

Therefore the antenna impedance changes at this frequency due to the resonance properties of the proposed structure. Also, to understand the

phenomenon behind this band-notch performance, the simulated current distribution on the radiating patch for the proposed antenna at the notch frequency (5.5 GHz) is presented in Fig. 5 (b). It can be observed that in Fig. 5 (b), the current is concentrated on the edges of the interior and exterior of the E-shaped slits at 5.5 GHz. Therefore the antenna impedance changes at this frequency due to the band-notch properties of the proposed structure.

Figure 6 shows the simulated VSWR curves with different values of W_e. As shown in Fig. 6, when the interior width of the E-shaped slits increases from 3.0 mm to 4.5 mm, the center of the notched frequency decreases from 6.7 GHz to 4.1 GHz. From these results, we can conclude that the notched frequency is controllable by changing the interior width of the E-shaped slits in the radiating patch.

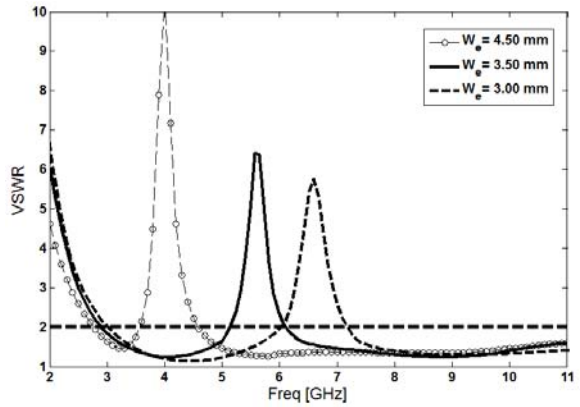

Fig. 6. Simulated VSWR characteristics for the proposed antenna with different values of L_P.

The proposed antenna with optimal design was built and tested. The measured and simulated VSWR characteristic of the proposed antenna was shown in Fig. 7. The fabricated antenna has the frequency band of 3 GHz to over 12.7 GHz with a rejection band around 5 GHz–6 GHz. However, as shown in Fig. 7, there exists a discrepancy between measured data and the simulated results. This discrepancy between measured and simulated results is mostly due to a number of parameters such as the fabricated antenna dimensions as well as the thickness and dielectric constant of the substrate on which the antenna is fabricated, the wide range of simulation frequencies and also the effect of SMA and its connector, because in the simulation the mismatch, which is made by the adapter and connector, are not considered, but in practice the effect of the coaxial cable, which is connected to the SMA at the input of the antenna is considerable, especially the additional inductance which is produced by the length of its inner conductor, is not negligible [8]. In other words, in a physical network analyzer measurement, the feeding mechanism of the proposed antenna is composed of an SMA connector and a microstrip line (the microstrip feed-line is excited by an SMA connector), which are connected to network analyzer through a coaxial cable, whereas the simulated results are obtained by using the Ansoft simulation software high-frequency structure simulator (HFSS), in which by default, the antenna is excited by a wave port that it is renormalized to a 50 Ω full port impedance at all frequencies, therefore this discrepancy between measured data and the simulated results could be due to the effect of the SMA port [8]. In order to confirm the accurate return loss characteristics for the designed antenna, it is recommended that the manufacturing and measurement process need to be performed carefully, besides, SMA soldering accuracy and FR4 substrate quality needs to be taken into consideration.

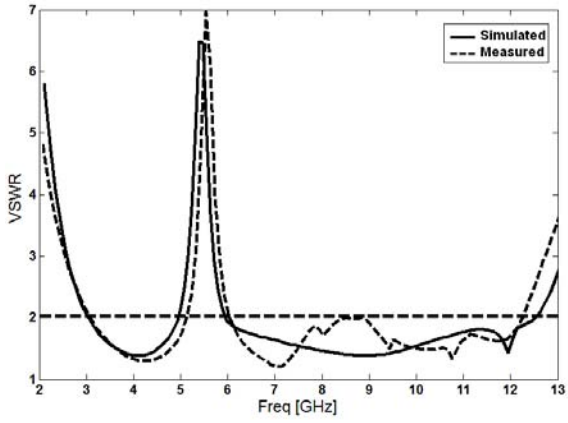

Fig. 7. Measured and simulated VSWR characteristics for the proposed antenna.

Figure 8 illustrates the measured radiation patterns, including the co-polarization and cross-polarization, in the H-plane (x-z plane) and E-plane (y-z plane). It can be seen that the radiation patterns in the x-z plane are nearly omni-directional for the three frequencies [14-15].

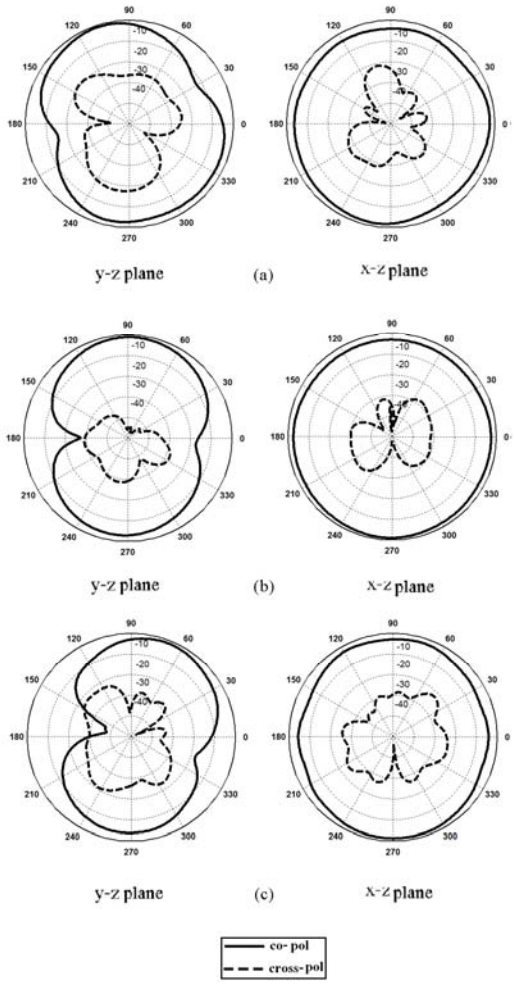

Fig. 8. Measured radiation patterns of the proposed antenna at (a) 4 GHz, (b) 7 GHz, and (c) 10 GHz.

Figure 9 shows the effects of the E-shaped slits and the protruded T-shaped strip on the maximum gain in comparison to the same antenna without them. It can be observed in Fig. 9 that by these structures, a sharp decrease of maximum gain in the notched frequency band at 5.5 GHz is shown. For other frequencies outside the notched frequency band, the antenna gain with the filter is similar to those without it [16].

IV. CONCLUSION

A new small printed monopole antenna (PMA) with frequency-notch function for UWB applications is presented, in this paper. The proposed antenna can operate from 3 GHz to 12.7 GHz with WLAN rejection band around 5 GHz–6 GHz. In order to enhance the bandwidth we cut a rectangular slot with a T-shaped strip protruded inside the rectangular slot in the ground plane and also by using two E-shaped slits in the radiating patch, a frequency band-notch function can be achieved. The designed antenna has a small size of 12×18 mm^2. Simulated and experimental results show that the proposed antenna could be a good candidate for UWB applications.

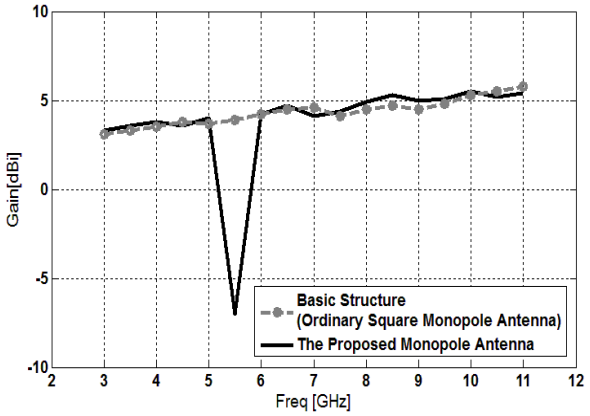

Fig. 9. Maximum gain comparisons for the ordinary square monopole antenna (simulated), and the proposed antenna (measured).

ACKNOWLEDGMENT

The authors are thankful from Microwave Technology (MWT) company staffs for their beneficial and professional help (www.microwave-technology.com).

REFERENCES

[1] H. Schantz, *The Art and S cience of Ultra Wideband Antennas*, Artech House 2005.

[2] J. Jung, W. Choi, and J. Choi, "A compact broadband antenna with an L-shaped notch," *IEICE Trans. Commun*., vol. E89-B, no. 6, pp. 1968-1971, June 2006.

[3] A. Ghazi, M. Azarmanesh, and M. Ojaroudi, "Muti-resonance square monopole antenna for ultra-wideband applications," *Progress In Electromagnetics Research C*, vol. 14, pp. 103-113, 2010.

[4] L. Lizzi, G. Oliveri, and A. Massa, "Planar monopole UWB antenna with WLAN-band notched characteristics," *Progress In Electromagnetic Research B*, vol. 25, pp. 277-292, 2010.

[5] M. Tang, S. Xiao, T. Deng, D. Wang, J. Guan, B. Wang, and G. Ge, "Compact UWB antenna with multiple band-notches for WiMAX and WLAN,"

IEEE Trans. Antennas and Propag., vol. 59, no. 4, pp. 1372-1376, 2011.

[6] N. Ojaroudi and M. Ojaroudi, "Dual band-notched monopole antenna with multi-resonance characteristic for UWB wireless communications," *Progress In Electromagnetics Research C*, vol. 40, pp. 188-199, 2013.

[7] M. Abdollahvad, G. Dadashzadeh, and D. Mostafa, "Compact dual band-notched printed monopole antenna for UWB 2 application," *IEEE Antennas Wireless Propag. Let t.*, vol. 9, pp. 1148-1151, 2010.

[8] M. Ojaroudi, M., "Printed monopole antenna with a novel band-notched folded trapezoid for ultra-wideband applications," *Journal of Electromagnetic Waves and Application (JEMWA)*, vol. 23, pp. 2513-2522, 2009.

[9] M. Ojaroudi, Gh. Ghanbari, N. Ojaroudi, and Ch. Ghobadi, "Small square monopole antenna for UWB applications with variable frequency band-notch function," *IEEE Antennas and Wireless Propagation Letters*, vol. 8, pp. 1061-1064, 2009.

[10] T. Dissanayake and K. Esselle, "Prediction of the notch frequency of slot loaded printed UWB antennas," *IEEE Trans. Antennas and Propag.*, vol. 55, no. 11, pp. 3320-3325, 2007.

[11] Ansoft High Frequency Structure Simulation (HFSS), Ver. 13, Ansoft Corporation, 2010.

[12] T.-G. Ma and S.-J. Wu, "Ultrawideband band-notched folded strip monopole antenna," *IEEE Trans. Antennas Propag.*, vol. 55, no. 9, pp. 2473-2479, 2007.

[13] N. Ojaroudi and M. Ojaroudi, "An UWB slot antenna with band-stop notch," *ICET Microw. Antennas Propag.*, vol. 10. pp. 831-835, 2013.

[14] M. Ojaroudi and N. Ojaroudi, "Ultra-wideband small rectangular slot antenna with variable band-stop function," *IEEE Trans. Antennas Propag*., vol. 62, pp. 490-494, 2014.

[15] M. Ojaroudi and N .Ojaroudi, "Ultra-wideband slot antenna with frequency band-stop operation," *Microw. Opt. Technol. Lett* ., vol. 55, pp. 2020-2023, 2013.

[16] N. Ojaroudi and M. Ojaroudi, "Novel design of dual band-notched monopole antenna with bandwidth enhancement for UWB applications," *IEEE Antennas Wireless Propag. Lett.*, vol. 12, pp. 698-701, 2013.

Nasser Ojaroudi was born in 1986 in Germi, Iran. He received his B.Sc. degree in Electrical Engineering from Azad University, Ardabil Branch. From 2011, he is working toward the M.Sc. degree in Telecommunication Engineering at Shahid Rajaee Teacher Training University. Since March 2008, he has been a Research Fellow in the Microwave Technology Company (MWT), Tehran, Iran. His research interests include monopole antenna, slot antennas, microstrip antennas for radar systems, ultra-wideband (UWB) and small antennas for wireless communications, microwave passive devices and circuits, and microwave/millimeter systems.

Mohammad Ojaroudi was born in 1984 in Germi, Iran. He received his B.Sc. degree in Power Electrical Engineering from Azad University, Ardabil Branch and M.Sc. degree in Telecommunication Engineering from Urmia University. From 2010, he is working toward the Ph.D. degree at Shahid Beheshti University. Also from July 2013 he has been working, as a research visitor in University of Tennessee, Knoxville, USA. From 2007 until now, he is a Teaching Assistant with the Department of Electrical Engineering, Islamic Azad University, Ardabil Branch, Iran.

Since March 2009, he has been the Chief Executive Officer (CEO) in the Microwave Technology Company (MWT), Tehran, Iran. From 2012, Dr. Ojaroudi is a member of the IEEE Transaction on Antennas and Propagation (APS) reviewer group and the Applied Computational Electromagnetic Society. His research interests include analysis and design of microstrip antennas, design and modeling of microwave structures, radar systems, and electromagnetic theory. He is author and coauthor of more than 150 journal and international conferences papers. His papers have more than 600 citations with 13 h-index.

Noradin Ghadimi was born in ardabil-Iran in 1985, and received the B.Sc. degree in Electrical Engineering from the Islamic Azad University, Ardabil Branch, Ardabil, Iran, in 2009 and the M.Sc. degree in Electrical Engineering from the Islamic Azad University Ahar Branch, Ahar, Iran, in 2011. His research interests include Power System Protection, modeling and analysis of Distributed Generations, renewable energy and communications systems.

Design of an Array Feed Offset Parabolic Reflector Antenna by Using Electromagnetic Simulations and Measured Results

N. Michishita[1], J. Shinohara[1], Y. Yamada[1], M. T. Islam[2], and N. Misran[2]

[1] National Defense Academy, 1-10-20 Hashirimizu, Yokosuka, Japan
yyamada@nda.ac.jp

[2] Universiti Kebangsaan Malaysia, 43600 Bangi, Selangor Darul Ehsan, Malaysia
tariqul@ukm.my

Abstract ─ Offset parabolic reflector antennas are well-known for their very simple configurations and are widely used. However, low antenna gain sometimes results in inconvenient operation. In order to increase the antenna gain, an array feed is generally employed to correct the antenna aperture distribution. However, accurate and low-loss realization methods for array feeds were not studied sufficiently. In this work, radiation pattern synthesis is first performed at the array feed to achieve uniform aperture distribution. As a result of this synthesis, the array excitation coefficients are determined. Further, accurate design methods for corporate feed line networks to obtain the required excitation coefficients and low feeder loss through electromagnetic simulations are described. Finally, the designed array feed is fabricated, and the measured radiation patterns are compared with the calculated results. Moreover, the array feed is combined with the fabricated offset reflector, and the antenna radiation patterns and gains are obtained. An increase in the antenna gain is ensured.

Index Terms – Array feed, electromagnetic simulation, offset parabolic reflector, and radiation pattern synthesis.

I. INTRODUCTION

Offset parabolic reflector antennas are well-known for their very simple configuration and ease of installation. Currently, these antennas are widely used as satellite broadcasting receivers [1] and vehicle mounted uses for satellite communications [2]. Previously, an important review of this type of antenna was reported [3], and an example of a shaped beam obtained by weighted array feeds [4] was cited. Recently, simple design formulas for linear array feeds were reported [5]. As for the array feeds, examples of the fabrication of a small-number array [6] and a large-number array [7] were reported. In the case of a small-number array, it was reported that the error in the corporate feed design and feeder loss results in 1 to 2 dB of array feed loss. For realizing appropriate and low-loss array feeds, accurate design of array excitations, arrangement of corporate feed lines, and accurate fabrication are required.

In this paper, an accurate and low-loss realization method for array feeds is described. First, the radiation pattern of an array feed is determined in order to increase the antenna gain of the offset reflector antenna. The excitation coefficients of the array elements are obtained through radiation pattern synthesis of the array feed in order to achieve uniform illumination of the offset antenna aperture. Further, corporate feed line network designs are performed by using a commercial electromagnetic simulator called FEKO. The main feature of the proposed feed line network is a coplanar feeder line arrangement for achieving a single feed point. Feed lines of appropriate lengths and power dividing ratios are designed on the basis of the accurate simulation results of the array excitations. In order to ensure design accuracies, an actual array feed is fabricated. Finally, the radiation patterns are

Submitted On: March 20, 2013
Accepted On: Jan. 1, 2014

1054-4887 © 2013 ACES

measured by using a combination of the fabricated array feed and the offset reflector.

II. DESIGN OF AN ARRAY FEED

A. Array excitation coefficients for a shaped beam

The antenna configuration is shown in Fig. 1. The offset parabolic reflector is fed by an array feed. The antenna aperture illumination $E_a(\rho)$ is determined from the simple relation to the radiation pattern $E_f(\theta_f)$ of the array feed as follows,

$$E_a(\rho) = \frac{1}{2f} E_f(\theta_f) \cos^2(\theta/2) \cdot \quad (1)$$

For achieving uniform illumination on the aperture plane, $E_f(\theta_f)$ must satisfy the following expression,

$$E_f(\theta_f) = \frac{2f}{\cos^2(\theta/2)} . \quad (2)$$

The shape of $E_f(\theta_f)$ given by equation (2) is shown in Fig. 2. The strengths are normalized by the value at the angle θ_u. The required $E_f(\theta_f)$ has the shape of a slope. This shape is quite different from those of the ordinal radiators.

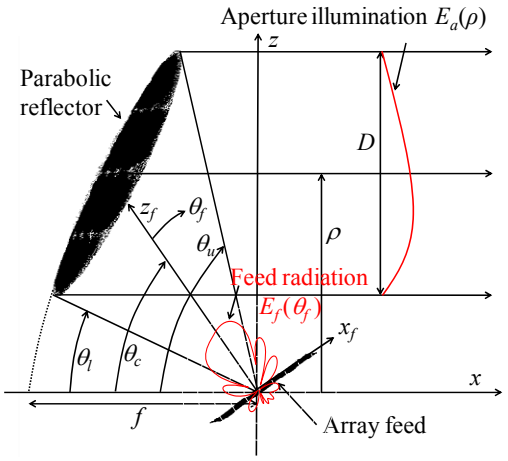

Fig. 1. Antenna configuration.

For achieving the radiation pattern in Fig. 2, the array feed configuration shown in Fig. 3 is used. A planar array configuration is employed. The array is composed of three column arrays and six row patches. Radiation pattern synthesis is performed in the column array, and $E_f(\theta_f)$ is achieved in the z_f-x_f plane. The three column arrays are used to form a radiation pattern in the z_f-y_f plane. The three column arrays have the same excitation values in order to adequately illuminate the reflector.

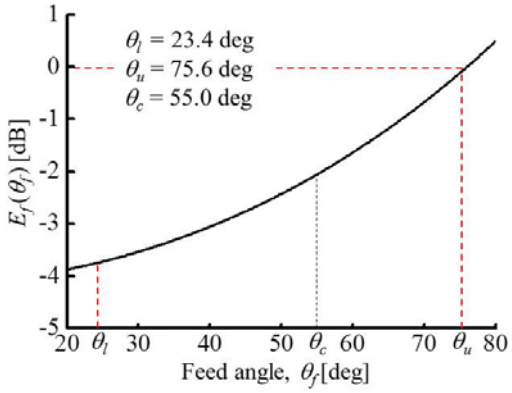

Fig. 2. Feed radiation pattern for achieving uniform $E_a(\rho)$.

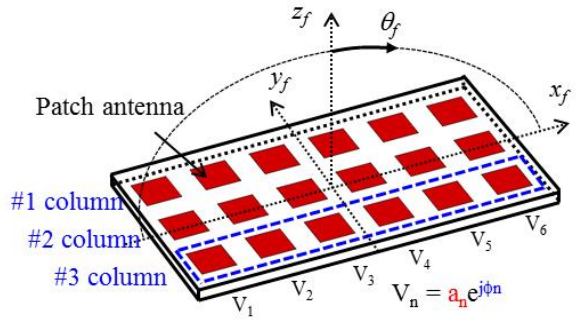

Fig. 3. Configuration of an array feed.

Radiation pattern synthesis is performed by determining the array excitation coefficients, which are denoted as $V_n = a_n e^{j\phi n}$. The excitation coefficients of the array elements are determined through the least mean square method [8]. The above calculation is performed using the following expression,

$$[V] = ([B]^H[T_0][B])^{-1}[B]^H[T_0][A] \quad (3)$$

where [V] is the excitation coefficient vector, and [A] is the radiation pattern vector that corresponds to the objective radiation pattern in Fig. 2. $[T_0]$ is a weighting matrix, which emphasizes the important direction in the radiation pattern, and [B] denotes the contributions of [V] to the array radiation pattern.

The synthesized radiation pattern ([F]) and [A] are shown in Fig. 4 (a). At [A], the reflector exists between angles θ_l and θ_u. Near the edges of the

reflector, the radiation levels are decreased by approximately -10 dB in order to suppress the spillover from the reflector. In all the radiation regions, [F] is well-designed with regard to [A]. The radiation pattern in the z_f-y_f plane is shown in Fig. 4 (b). At the reflector edges, the radiation levels are suppressed by approximately -10 dB.

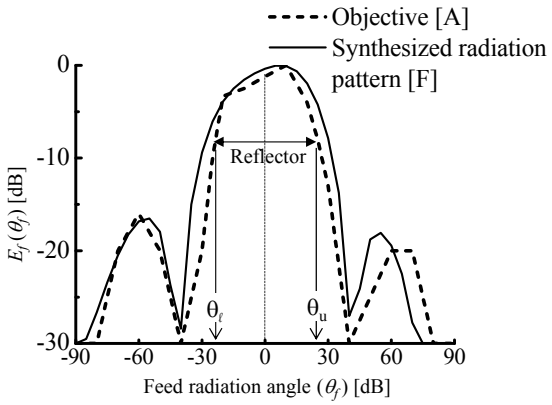

(a) Feed pattern for uniform $E_a(\rho)$.

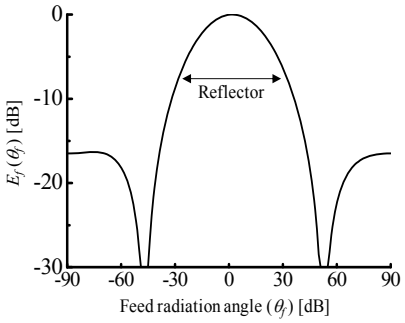

(b) Radiation pattern in the z_f-y_f plane.

Fig. 4. Feed radiation patterns.

The excitation coefficients designed using equation (3) are shown in Fig. 5. The amplitudes are symmetrical on both sides of the array. The phases are rotationally symmetrical around the center of the array. In the excitation phases, there are very steep changes at the two end elements. The maximum value obtained is 160°.

B. Accurate design of the excitation coefficients

The design concept of the feed lines is illustrated in Fig. 6. Regarding the previous example, the radiation elements and feed lines are formed on a single plate in a 4 × 4 array antenna [9]. The objective of this configuration is to design a low-loss feeding network. The presence of a single feed point and the conformation of the series feed network within the column arrays are effective in reducing the feed network losses. Moreover, the conformation of the radiation elements and feed lines on a single plate allows for easy fabrication. The patch antennas and feed lines are formed on a Teflon substrate having electric constants of ε_r = 2.6 and tanδ = 0.0018 and a thickness of 0.8 mm. The frequency in this case is selected as 11 GHz, by considering the use of broadcasting satellite (11 GHz to 12 GHz). Then, the patch size is 8 mm^2. The λ/2 patch separation is 13.6 mm. In this configuration, the design of a four-port power divider at the feed point and the series feed network is sensitive for feed line parameters. Accurate feed line design is performed through try and error process by an electromagnetic simulator.

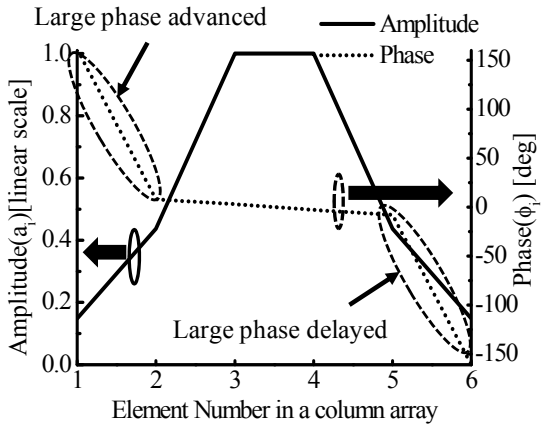

Fig. 5. Excitation coefficients of the feed array.

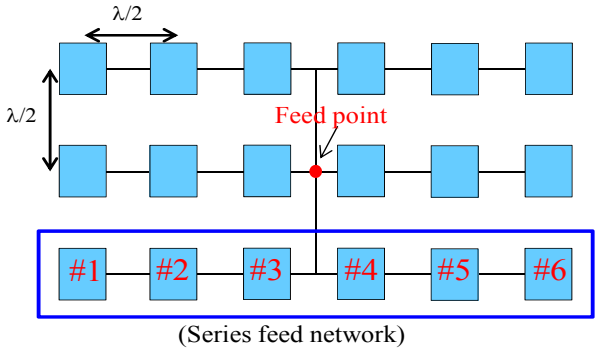

Fig. 6. Design concept of the feed lines.

The actual series feed configuration is shown in Fig. 7. The phase distribution in Fig. 5 is achieved by adjusting the feed line length. At the

line length between P_1 and P_2, a very large phase lead is required. For this, the feed line length has to be very short when compared with the patch spacing. Therefore, a line length of one wavelength is added. The amplitude distribution is achieved by obtaining the appropriate power ratios at the power dividers. As shown in Fig. 7, D_3 denotes the power divider, and P_1 through P_6 denote the power ratios in Fig. 5. Z_T denotes the terminal resistance corresponding to the edge impedance of the patch antenna, and it is set to 127 Ω. Although the patch antennas should be attached to the terminal points, they are replaced by Z_T for design convenience. At the final stage shown in Fig. 12, the patch antennas are attached to the terminals, and certain corrections are mainly added to the line lengths. Z_0 denotes the common feeder line impedance, and it is set to 100 Ω. Z_i denotes the feeder line impedance. Z_A is used to equally divide the source power to the half branches of the array antenna.

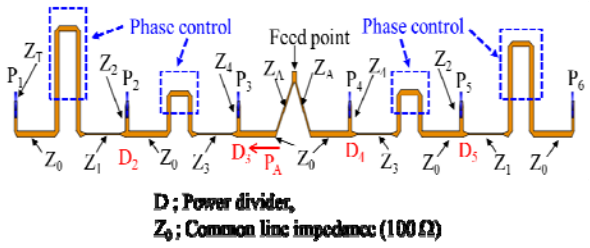

Fig. 7. Series feed configuration.

The fundamental design of a power divider (D_3) is performed on the basis of the following equation,

$$\sqrt{P_A} : \sqrt{P_1 + P_2} = \frac{1}{Z_0} : \frac{1}{Z_3} \tag{4}$$

where P_A is the sum of P_1, P_2, and P_3. The relation of P_1:P_2:P_3 = 0.02:0.19:1.0 is determined from the amplitude relation in Fig. 5. The remaining power dividers, namely, D_2, D_4, and D_5, are designed in a similar manner. The calculated results of all the line impedances are shown in Fig. 8. The values of P_1 and P_6 are very small because Z_1 is very large. The amplitudes and phases of the terminal currents are shown in Fig. 9. These values correspond to the excitation coefficients. The obtained amplitudes and phases of the configuration in Fig. 7 agree very well with the objective values.

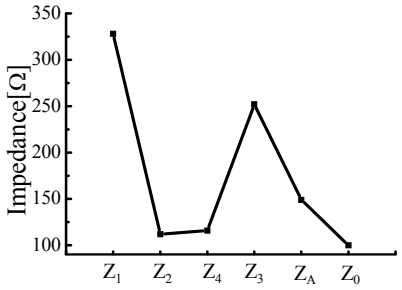

Fig. 8. Impedance.

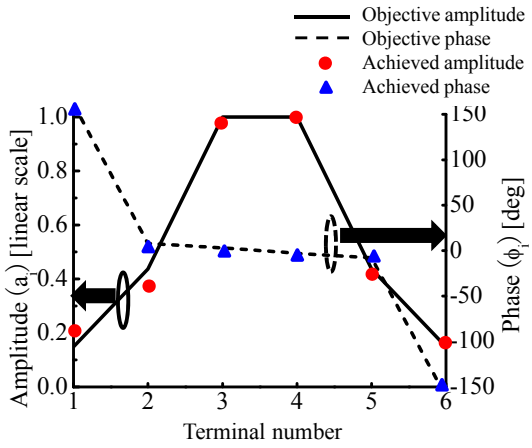

Fig. 9. Terminal currents.

Further, the feed line configuration between the column arrays is shown in Fig. 10. The feed lines to the six central patches are considered for design easiness. In order to achieve the same excitation phase in the column arrays, the feed line lengths are adjusted at the phase control sections. Similar amplitude excitations of the three column arrays are designed at the power divider. At the power divider, a power ratio of P_1:P_2:P_3:P_4 = 2:1:1:2 is obtained by taking into account the same amplitude in the three column arrays. Modifications of the line impedances Z_B and Z_C are required because the line configuration around the power divider is rather complicated. As a result, Z_B = 128 Ω and Z_C = 109 Ω are obtained. In order to ensure the design results, the terminal currents in Fig. 10 are redrawn in Fig. 11. The same magnitudes and phases are realized between the column arrays.

C. Array feed characteristic

The final array feed configuration is shown in Fig. 12. Patch antennas are added to the feed-line

network design, as shown in Figs. 7 and 10. The current amplitudes are shown. Almost the same amplitudes are achieved in the three column arrays.

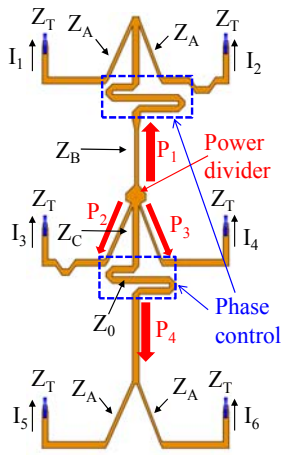

Fig. 10. Feed line design between the columns.

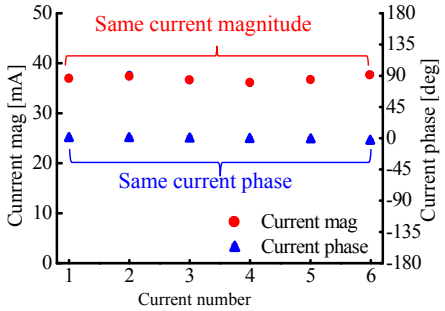

Fig. 11. Terminal currents.

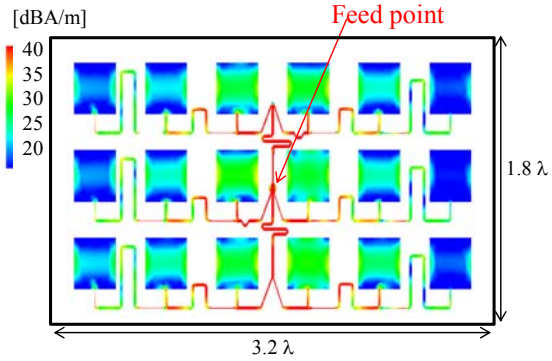

Fig. 12. Array feed configuration.

The excitation coefficients obtained for the patch antennas are shown in Fig. 13. The deviations in the amplitudes and phases between the column arrays are rather small. Excellent excitation coefficients are obtained in the array feed.

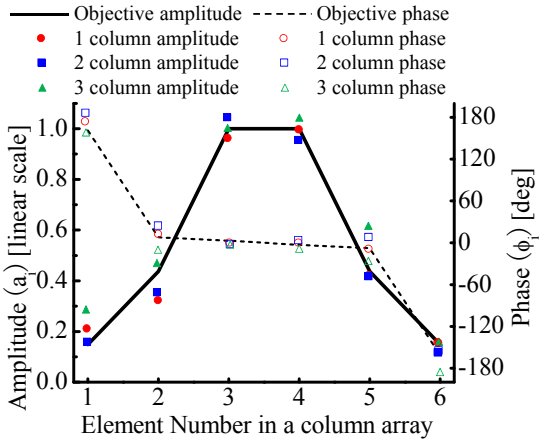

Fig. 13. Excitation coefficient.

In order to measure the realized electrical characteristics, an array feed is fabricated as shown in Fig. 14. Patch antennas and feed lines are fabricated by using a cutting machine. Almost the same shape is achieved as shown in Fig. 12. First, the return loss less than -10 dB is obtained in 9.5 GHz to 10.5 GHz. The center frequency shift from the calculated frequency (11 GHz) is due to the difference of the dielectric constant.

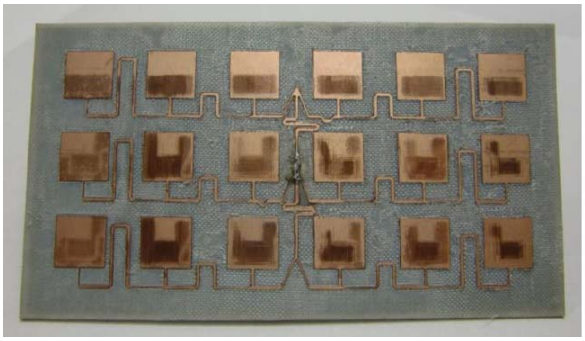

Fig. 14. Fabricated array feed

The radiation patterns of the array feed are shown in Fig. 15. The z_f-x_f plane is shown in Fig. 15 (a). The measured and calculated results agree very well with each other. The maximum electric field level is 12.2 dBi. In order to estimate the feeder loss, the conductivity of the metal is set to infinity, and tanδ of the dielectric substrate is set to zero in the calculations. Then, the feeder loss is estimated to be 0.2 dB. Through this agreement, accurate excitation coefficients are ensured. The z_f-y_f plane is shown in Fig. 15 (b). The measured pattern is broader than the calculated one. This

pattern degradation is due to the slight phase difference between the column arrays.

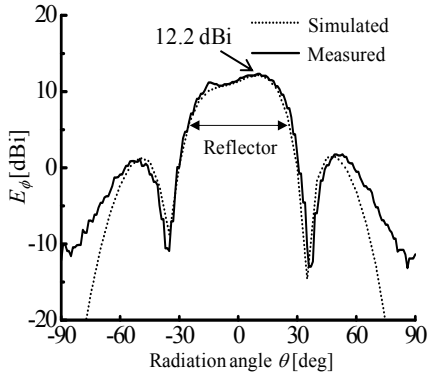

(a) z_f-x_f plane.

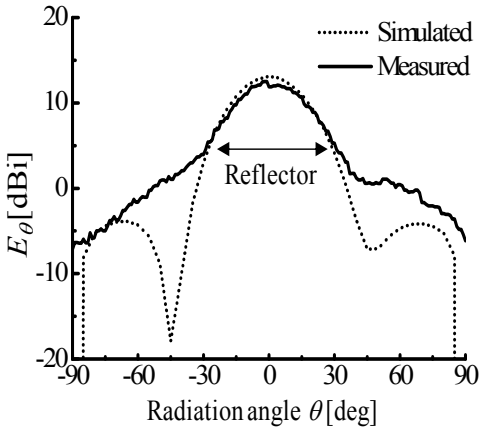

(b) z_f-y_f plane.

Fig. 15. Radiation pattern of the array feed.

III. CHARACTERISTICS OF THE FABRICAED ANTENNA

The fabricated array feed is combined with the fabricated offset parabolic reflector, as shown in Fig. 16 [10]. The reflector is composed of a carbon FRP material. The array feed functions in the horizontal polarization. The radiation angles are denoted as θ and ϕ. The main beam direction is along the x axis, which corresponds to $\theta = 90°$. First, electromagnetic simulations are performed. The simulation parameters are listed in Table I. Although the antenna diameter is only 9.1 times the wavelength, rather large calculation resources are required. The electric near-field distributions are shown in Fig. 17. The radiated electric fields from the array feed are well-concentrated in the reflector region. Regarding the reflected electric fields from the reflector, the electric field intensity for a plane wave is almost constant over the aperture plane.

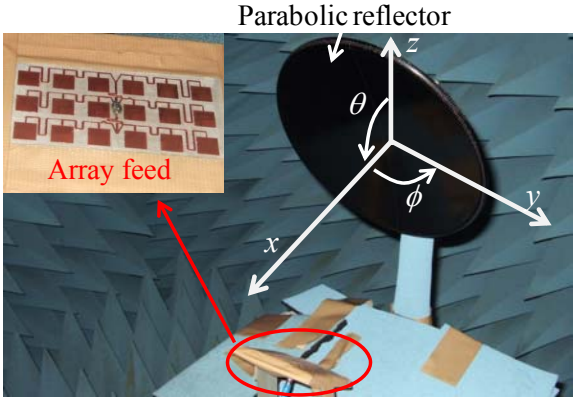

Fig. 16. Fabricated OPA.

The effect of radiation pattern synthesis is ensured through the uniform intensity of the plane wave. At the upper and lower edges of the reflector, appreciable spillover levels are observed.

Table I: Simulation parameters.

Computer	Memory	16 GB
	Clock time	3.2 GHz
Simulator	FEKO Suite 6.0	MoM
Frequency		11 GHz
Antenna diameter		248 mm
Focal length		218 mm
Mesh size		0.02 mm (array feed) 8.30 mm (reflector)
Number of meshes		15498
Simulation memory		7.9 GB
Simulation time		6.9 hours

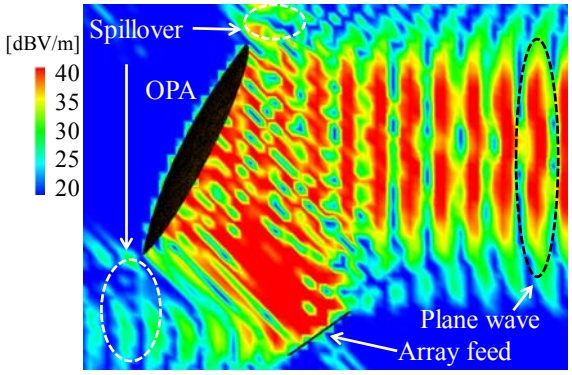

Fig. 17. Electric near-field distribution.

Finally, the measured radiation characteristics are compared with the calculated results. The wide-angle radiation patterns are shown in Fig. 18. In the *x-y* plane shown in Fig. 18 (a), the measured results for the main beam shape is in good agreement with the calculated results. In the *x-z* plane shown in Fig. 18 (b), the measured results for the main beam and side lobes are in good agreement with the calculated results. In particular, appreciable spillovers are observed in the zenith direction ($\theta = 0°$) and reflector backward direction ($\theta = 90°$).

The near-axis radiation patterns are shown in Fig. 19. In the *x-y* plane shown in Fig. 19 (a), the measured antenna gain of 26.0 dBi is only 0.4 dB lower than the calculated results. The measured side lobes are larger than the calculated levels by more than 5 dB. These increases correspond to the radiation pattern distortion shown in Fig. 15 (b). In the *z-x* plane shown in Fig. 19 (b), the measured and calculated results agree very well with each other. Excellent radiation pattern synthesis in this plane is ensured. In order to estimate the aperture efficiency, the antenna loss budgets are summarized in Table II. For uniform aperture distribution, the actual antenna gain is 26.8 dBi taking into account the losses. Further, the measured gain of 26.0 dBi corresponds to 83.2 % antenna aperture efficiency. High aperture efficiency is ensured.

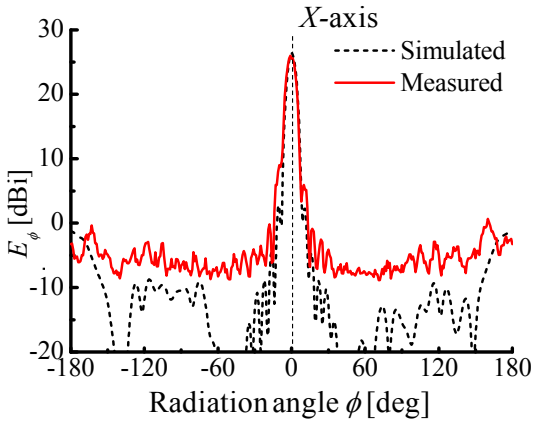

(a) *x-y* plane.

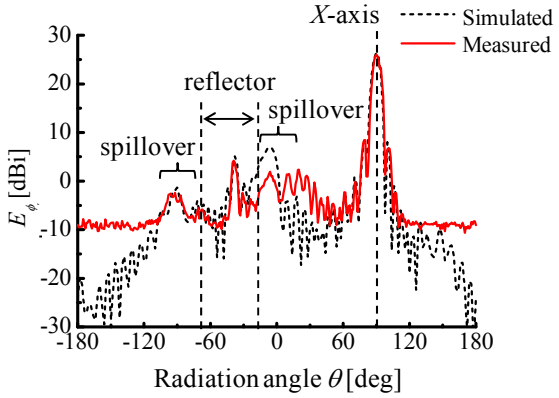

(b) *z-x* plane.

Fig. 18. Wide-angle radiation pattern.

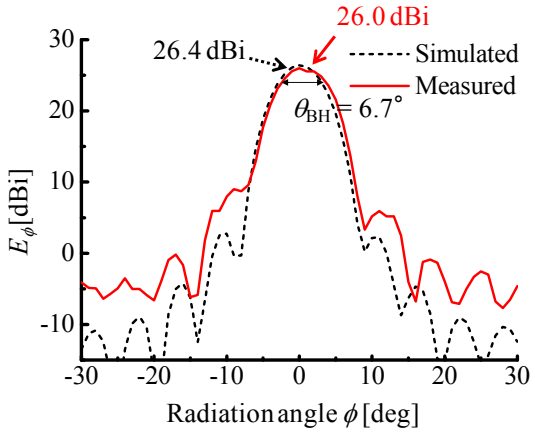

(a) *x-y* plane.

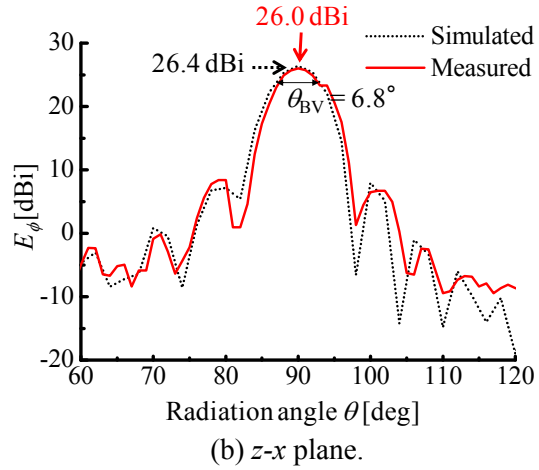

(b) *z-x* plane.

Fig. 19. Near-axis radiation pattern.

Table II: Antenna loss budgets.

		Gain	Aperture Efficiency (η_{ap})
Uniform aperture distribution		28.2 dBi	100%
Losses	Spill over	1.2 dB	
	Feed loss	0.2 dB	
Actual gain		26.8 dBi	100%
Measured gain		26.0 dBi	83.2%

IV. CONCLUSION

Radiation pattern synthesis of an array feed is performed in order to achieve uniform aperture illumination for the offset antenna. The design of the important excitation coefficients of the array feed is successfully performed through accurate electromagnetic simulations. The design accuracies are ensured through the measured results of the fabricated array feed. Moreover, the antenna radiation characteristics are obtained by combining the array feed with a parabolic reflector. An increased antenna aperture efficiency of 83.2% is ensured from the measured antenna gain.

REFERENCES

[1] K. Miwa, M. Tanaka, T. Naito, and Y. Endo, "A new FRP parabolic antenna for satellite broadcasting system," *ITE Technical Report*, vol. 8, no. 7, pp. 7-12, May 1984.

[2] http://www42.tok2.com/home/fleet7/FilmScanner/NegaScanJGSDFe.html, Antennas of TASCOM －X.

[3] A. Rudge and N. Adatia, "Offset-parabolic-reflector antennas: A review," *Proc. IEEE*, vol. 66, pp. 1592-1618, 1978.

[4] C. Han, "A multifeed offset reflector antenna for the Intelsat V communication satellite," *Proc. 7th European Microwave Conf.*, pp. 343-347, 1977.

[5] S. Lee and Y. Samii, "Simple formulas for designing an offset multibeam parabolic reflector," *IEEE Trans. Antennas and Propag.*, vol. 29, no. 3, pp. 472-478, 1981.

[6] J. Huang and Y. Samii, "Fan beam generated by a linear-array fed parabolic reflector," *IEEE Trans. Antennas and Propag.*, vol. 38, no. 7, pp. 1046-1052,1990.

[7] Y. Samii, J. Huang, B. Lopez, M. Lou, E. Im, S. Durden, and K. Bahadori, "Advanced precipitation radar antenna: Array-fed offset membrane cylindrical reflector antenna," *IEEE Trans. Antennas and Propag.*, vol. 53, no. 8, pp. 2503-2515, 2005.

[8] J. Shinohara, Y. Yamada, N. Michishita, M. Islam, and N. Misran, "Design of an array feed offset parabolic reflector antenna used for a simple earth station," *Int. Conf. Space Science and Commun.*, Paper ID 81, 2011.

[9] A. Mallahzadeh and M. Taherzadeh, "Investigation of a proposed ANN-based array antenna diagnosis technique on a planar microstrip array antenna," *ACES Journal*, vol. 26, no. 8, pp. 667-678, Aug. 2011.

[10] J. Shinohara, N. Michishita, Y. Yamada, M. Islam, and N. Misran, "Measured electrical characteristics of an array feed offset parabolic reflector antenna," ISAP'12, POS2-19, pp. 1104-1107, 2012.

Naobumi Michishita received his B.E., M.E., and D.E. degrees in Electrical and Computer Engineering from Yokohama National University in 1999, 2001, and 2004, respectively. In 2004, he joined the Department of Electrical and Electronic Engineering, National Defense Academy, as a research associate. From 2006 to 2007, he was a visiting scholar at the University of California, Los Angeles. In 2004 and 2005, he received the Young Engineer Award from the IEEE AP-S Japan Chapter and IEICE, respectively. His current research interests include metamaterial antennas and electromagnetic analysis. He is a member of IEEE.

Junichi Shinohara graduated from the Department of Electronic Engineering, National Defense Academy, in 2008. He belongs to the Japan Ground Self-Defense Force. He completed his master's program in engineering at the National Defense Academy in 2013. He has been engaged in research on parabolic reflector antennas. He is now an instructor in the JGSDF signal school as a Second Lieutenant.

Yoshihide Yamada graduated from the Nagoya Institute of Technology and received his BS and MS degrees in electronics in 1971 and 1973, respectively. In 1989, he received his DE degree from the Tokyo Institute of Technology. In 1973, he joined the Electrical Communication Laboratories at the Nippon Telegraph and Telephone Corporation (NTT). Until

1984, he was engaged in research and development (R&D) related to reflector antennas for terrestrial and satellite communications. Beginning in 1985, he engaged in R&D for base station antennas for mobile radio systems. In 1993, he moved to NTT Mobile Communications Network Inc. (NTT DoCoMo). In 1995, he was temporarily transferred to YRP Mobile Telecommunications Key Technology Research Laboratories Co., Ltd. In 1996, he was a guest professor at the Cooperative Research Center at Niigata University as well as a lecturer at the Science University of Tokyo. In 1998, he took a position as a professor at the National Defense Academy. His current research interests include very-small normal-mode helical antennas, reflector antennas, and radar cross sections.

He is a fellow member of IEICE; a member of JSST of Japan; a member of ACES; and a senior member of IEEE AP, VT, and COMM.

Mohammad Tariqul Islam received his B.Sc. and M.Sc. degrees in Applied Physics and Electronics in 1998 and 2000, respectively, from the University of Dhaka, Dhaka, Bangladesh and a Ph.D degree in telecommunication engineering from the Universiti Kebangsaan Malaysia (UKM) in 2006. He is currently a professor at the Institute of Space Science (ANGKASA), UKM, Malaysia. He has been very promising as a researcher and a recipient of several international gold medals, the Best Invention in Telecommunication award, and a special award from Vietnam for his research and innovation. He has filed six patent applications. He has authored and co-authored 102 international journal papers, 90 international and local conference papers, and 3 books. Thus far, his publications have been cited 560 times, and the H-index is 15 (Source: Scopus). He has been awarded “Best Researcher Award” in 2010 and 2011 at UKM. He served as a faculty member at the Multimedia University (MMU), Malaysia, from May 2007 until May 2008. His research interests concern enabling technology for RF, antenna technology, electromagnetic absorption, and radio astronomy instruments. He is currently handling many research projects from the Ministry of Science, Technology, and Innovation (MOSTI) and the Ministry of Higher Education, Malaysia (MOHE).

Norbahiah Misran received her B.Eng. degree in Electrical, Electronic, and System Engineering from Universiti Kebangsaan Malaysia in 1999. She completed her Ph.D. degree in Communication Engineering at the Queen’s University of Belfast, United Kingdom, in 2004. She started her career as a tutor at the Department of Electrical, Electronic, and System Engineering, Universiti Kebangsaan Malaysia in 1999. She has been as a lecturer since 2004 and was appointed as an associate professor in 2009. Since 2012, she has been a professor at Universiti Kebangsaan Malaysia as well as an associate senior research fellow at the Institute of Space Science, Universiti Kebangsaan Malaysia. Her current research interests include RF device design, particularly microstrip antenna technology, and reflect array antennas. She is also involved in engineering education research.

UWB Slot Antenna with Band-Stop Operation by Using H-Shaped Parasitic Structures for UWB Applications

M. Ojaroudi, N. Ojaroudi, and N. Ghadimi

Young Researchers Club
Ardabil Branch, Islamic Azad University, Ardabil, Iran
m.ojaroudi@iauardabil.ac.ir, n.ojaroudi@yahoo.com, noradin.ghadimi@gmail.com

Abstract ─ A novel ultra wideband (UWB) printed slot antenna with band-notched performance is designed and manufactured. In order to increase the impedance bandwidth of the slot antenna, we use a rectangular slot with an H-shaped parasitic structure inside the rectangular slot on the feed-line that with this structure UWB frequency range can be achieved. Additionally, by using a square ring radiating stub with a rotated H-shaped parasitic structure inside the square ring, a frequency band-stop performance has been obtained. The designed antenna has a small size of 20×20 mm^2 while showing the radiation performance in the frequency band of 2.97 GHz to over 12.39 GHz with a band rejection performance in the frequency band of 5.01 GHz to 5.98 GHz. Simulated and experimental results obtained for this antenna show that it exhibits good radiation behavior within the UWB frequency range.

Index Terms - Microstrip slot antenna, H-shaped parasitic structure, and ultra wideband application.

I. INTRODUCTION

In UWB communication systems, one of key issues is the design of a compact antenna while providing wideband characteristic over the whole operating band. Consequently, a number of printed microstrip with different geometries have been experimentally characterized [1-2], and automatic design methods have been developed to achieve the optimum planar shape [3]. Moreover, other strategies to improve the impedance bandwidth have been investigated [4-5].

The federal communication commission (FCC)'s allocation of the frequency range 3.1 GHz – 10.6 GHz for UWB systems and it will cause interference to the existing wireless communication systems, such as, the wireless local area network (WLAN) operating in 5.15 GHz – 5.35 GHz and 5.725 GHz – 5.825 GHz bands, so the UWB antenna with a single band-stop performance is required [6-11]. The easiest and most common technique is embedding a narrow slot into the radiating patch of the antenna and change the current flows on it, as used in [8, 9]. In [8, 9] different shapes of the slots (i.e., square ring and folded trapezoid) are used to obtain the band notch function. Single and multiple band notch functions are achieved by cutting single and multiple half-wavelength U-shaped slits in the radiating patch. On the other hand, another method to avoid this frequency interference is the use of reconfigurable antennas. The reconfigurable structure provides switchable band notch characteristic and whenever there is no coexisting system, the antenna can use the whole UWB spectrum. In [10] RF MEMS are used for notching the WLAN band while in [11] PIN diodes are used for the same reason.

A novel and compact microstrip-fed slot antenna with additional resonance and band-notched characteristics for UWB applications has been presented. This letter focuses on a rectangular slot antenna for UWB applications, which combines the square ring radiating stub approach with a rotated H-shaped parasitic structure inside the square ring, and the microstrip feed-line with a rectangular slot with an H-shaped parasitic structure inside the rectangular slot that achieves a fractional bandwidth of more than 120 %. In the proposed structure, first by cutting a rectangular slot with an H-shaped parasitic structure inside the rectangular slot on the

Submitted On: July 27, 2012
Accepted On: Dec. 24, 2013

1054-4887 © 2013 ACES

microstrip feed-line, additional resonance is excited and hence, much wider impedance bandwidth can be produced, especially at the higher frequencies. In order to generate a single band-notch function, for the first time, we use a rotated H-shaped parasitic structure inside the square ring radiating stub. In the slot antenna design, by reducing the antenna size, the impedance matching at lower frequencies becomes poor and the bandwidth is degraded [3-4]. The distinctive point of the proposed antenna is that although it has small size with respect to the antennas introduced in [2-5], (43 % smaller than the antenna in [4]), it has wider impedance bandwidth in the frequency band of 2.97 GHz to 12.39 GHz with a rejection bands around 5.01 GHz – 5.98 GHz, which has a frequency bandwidth increment of 13 % with respect to the previous similar antenna [8-11], and also, the impedance matching at lower frequencies is very well obtained. Unlike other band-notched UWB antennas reported in the literature to date [6-9], this structure has an ordinary square radiating stub configuration. Simulated and measured results are presented to validate the usefulness of the proposed antenna structure for UWB applications.

II. ANTENNA DESIGN

The presented slot antenna fed by a 50 Ω microstrip line is shown in Fig. 1, which is printed on a FR4 substrate of thickness 0.8 mm, permittivity 4.4, and loss tangent 0.018. The basic antenna structure consists of a square radiating stub, a 50 Ω microstrip feed-line, and a ground plane with a rectangular slot. The square radiating stub has a width W. The radiating stub is connected to a feed line of width W_f and length L_f, as shown in Fig. 1. On the other side of the substrate, a conducting ground plane with a rectangular slot is placed. The proposed antenna is connected to a 50 Ω SMA connector for signal transmission.

In this study, based on electromagnet coupling theory (ECT), the H-shaped parasitic structure inside the rectangular slot in the microstrip feed-line is playing an important role in the broadband characteristics of this antenna, because it can adjust the electromagnetic coupling effects between the feed line and the parasitic element, and improves its impedance bandwidth without any cost of size or expense [5]. As illustrated in Fig. 1, the rotated H-shaped parasitic structure is placed inside the square ring radiating patch and is also symmetrical with respect to the longitudinal direction. The rotated H-shaped parasitic structure perturbs the resonant response and also acts as a parasitic half-wave resonant structure electrically coupled to the square ring radiating stub [7]. At the notch frequency, the current flows are more dominant around the parasitic element, and they are oppositely directed between the parasitic element and the square ring radiating stub [8-9]. As a result, the desired high attenuation near the notch frequency can be produced.

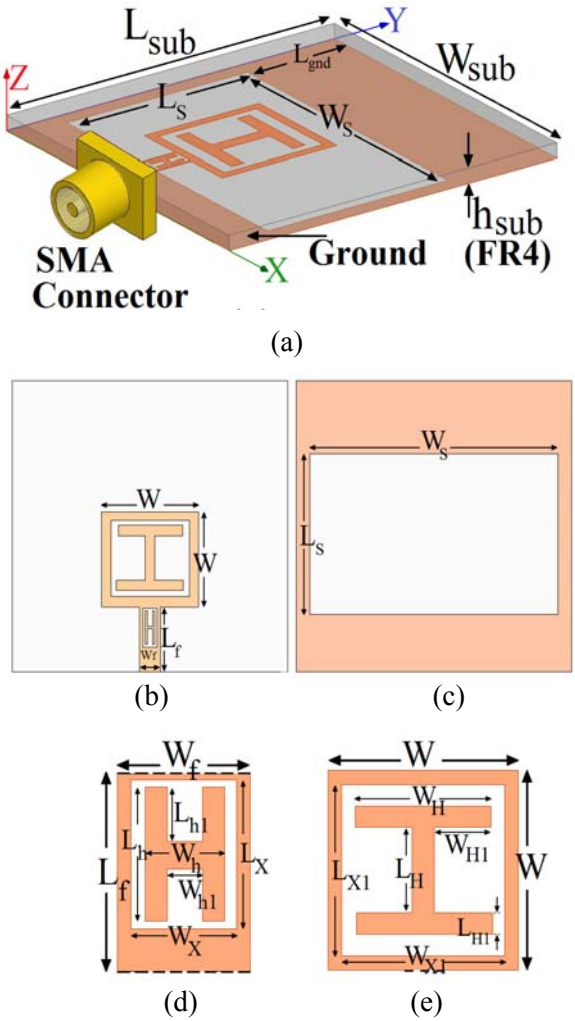

Fig. 1. (a) Geometry of the proposed square slot antenna, (b) top layer, (c) bottom layer, (d) a rectangular slot with an H-shaped parasitic structure on the feed-line, and (e) rotated H-shaped parasitic structure inside the square ring radiating stub.

In this work, we start by choosing the aperture length L_S. We have a lot of flexibility in choosing this parameter. The length of the aperture mostly affects the antenna bandwidth. As L_S decreases, so does the antenna BW and vice versa. Next step, we have to determine the aperture width W_S. The aperture width is approximately $\lambda_S/2$, where λ_S is the slot wavelength that depends on a number of parameters such as the slot width as well as the thickness and dielectric constant of the substrate on which the slot is fabricated. The last and final step in the design is to choose the length of the radiating patch W. A good starting point is to choose it to be equal to $W = \lambda_m/4$, where λ_m is the guided wavelength in the microstrip line [4]. The important step in the design is to choose L_{notch} (the length of the filter) and $L_{resonance}$ (the length of the resonator). L_{notch} is set to band-stop resonate at $0.5\lambda_{notch}$, where $L_{notch1} = L_{X1}+W_{X1}+2L_{H1}+L_H$, λ_{notch} correspond to notched band frequency wavelength (5.5 GHz), and $L_{resonance}$ is set to resonate at $0.25\lambda_{resonance}$, where $L_{resonance}=L_h+2L_{h1}+Wh$, $\lambda_{resonance}$ correspond to third resonance frequency wavelength (10.2 GHz).

The optimal dimensions of the designed antenna are as follows: W_{sub} = 20 mm, L_{sub} = 20 mm, h_{sub} = 0.8 mm, W_S = 18 mm, L_S = 11 mm, W_f = 1.5 mm, L_f = 4 mm, W = 7 mm, W_X = 1.1 mm, L_X = 2.8 mm, W_{X1} = 6 mm, L_{X1} = 6 mm, W_h = 0.7 mm, L_h = 2.4 mm, W_{h1} = 0.3 mm, L_{h1} = 1 mm, W_H = 5 mm, L_H = 4.5 mm, W_{H1} = 2.25 mm, L_{H1} = 0.5 mm, and L_{gnd} = 6 mm.

III. RESULTS AND DISCUSSIONS

In this section, the planar slot antenna with various design parameters were constructed, and the numerical and experimental results of the input impedance and radiation characteristics are presented and discussed. The parameters of this proposed antenna are studied by changing one parameter at a time and fixing the others. The simulated results are obtained using the Ansoft simulation software high-frequency structure simulator (HFSS) [12].

Figure 2 shows the structure of various antennas used for simulation studies. VSWR characteristics for ordinary square slot antenna (Fig. 2 (a)), with a rectangular slot with an H-shaped parasitic structure inside the rectangular slot on the feed-line (Fig. 2 (b)), and the proposed antenna structure (Fig. 2 (c)) are compared in Fig 3.

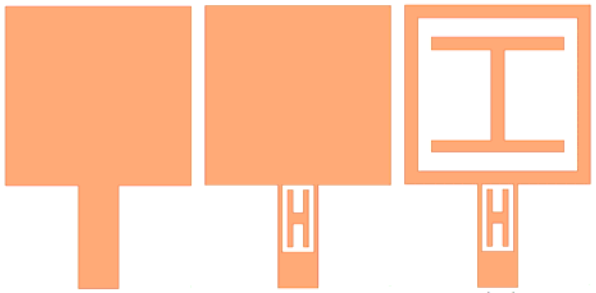

Fig. 2. Radiating stub and microsrtip feed-line of (a) the ordinary slot antenna, (b) the antenna with a rectangular slot with an H-shaped parasitic structure on the microstrip feed-line, and (c) the proposed antenna.

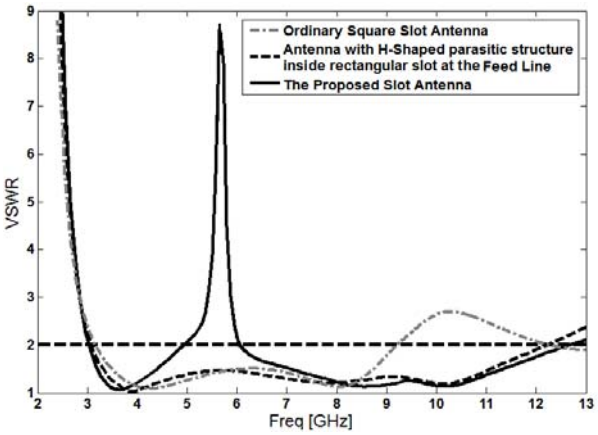

Fig. 3. VSWR characteristics for the various antenna structures shown in Fig. 2.

It is found that by inserting the rectangular slot with an H-shaped parasitic structure inside the rectangular slot on the feed-line, the antenna can create the third resonant frequency at 10.2 GHz and hence the impedance bandwidth is effectively improved at the upper frequency [13]. Also as shown in Fig. 3, in this structure, the rotated H-shaped parasitic is used in order to generate the frequency band-stop performance. Also the input impedance of the various slot antenna structures that shown in Fig. 2, on a Smith chart is shown in Fig. 4.

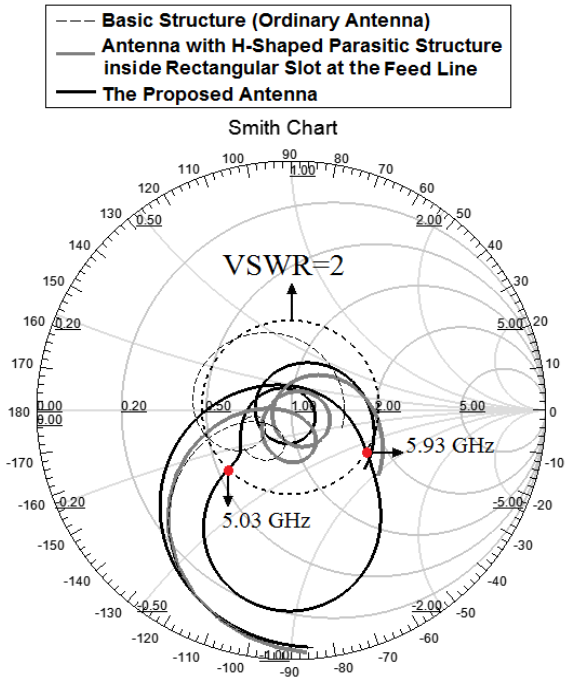

Fig. 4. The simulated input impedance on a Smith chart of the various slot antenna structures shown in Fig. 2.

In order to understand the phenomenon behind this new additional resonance performance, the simulated current distribution on the radiating patch and feed-line for the square antenna with a rectangular slot with an H-shaped parasitic structure inside the rectangular slot on the feed-line at new resonance frequency (10.2 GHz) is presented in Fig. 5 (a). It can be observed in Fig. 5 (a) that the current concentrated on the edges of the interior and exterior of the H-shaped parasitic structure at 10.2 GHz. Therefore, the antenna impedance changes at these frequencies due to the resonant properties of the H-shaped parasitic structure. In addition, by inserting the rotated H-shaped parasitic structure the band notch performance is created [14-15]. It can be observed on Fig. 5 (b) that the current concentrated on the edges of the interior and exterior of the rotated H-shaped parasitic structure inside the square ring radiating stub at the notch frequency (5.5 GHz). This figure shows that the electrical current for the new resonance frequency (5.5 GHz) does change direction along the coupled rotated H-shaped parasitic structure, due to the band notch properties of the proposed structure.

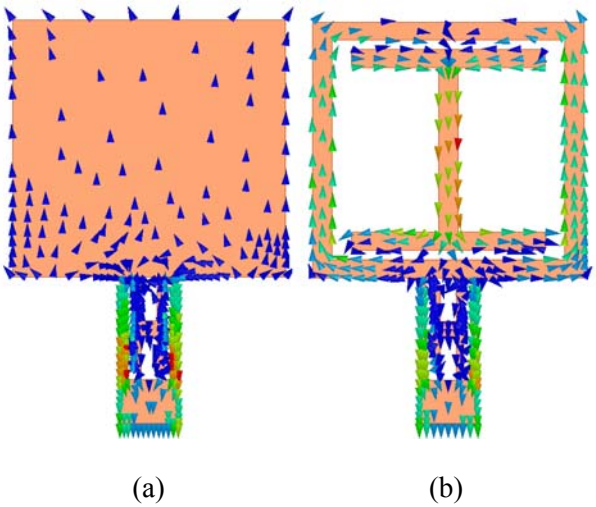

Fig. 5. Simulated surface current distributions on the radiating stub and microstrip feed-line for (a) the square antenna with a rectangular slot with an H-shaped parasitic structure on the microstrip feed-line antenna at 10.2 GHz and (b) the proposed antenna at 5.5 GHz.

The proposed antenna with optimal design was built and tested. Figure 6 shows the measured and simulated VSWR characteristics of the proposed antenna. The fabricated antenna satisfies the VSWR < 2 requirement from 2.97 GHz to over 12.39 GHz with a band rejection performance in the frequency band of 5.01 GHz to 5.98 GHz. As shown in Fig. 6, there exists a discrepancy between measured data and the simulated results this could be due to the effect of the SMA port. In order to confirm the accurate VSWR characteristics for the designed antenna, it is recommended that the manufacturing and measurement process need to be performed carefully.

Figure 7 shows the measured radiation patterns including the co-polarization and cross-polarization in the *H*-plane (*x-z* plane) and *E*-plane (*y-z* plane). The main purpose of the radiation patterns is to demonstrate that the antenna actually radiates over a wide frequency band. It can be seen that the radiation patterns in *x-z* plane are nearly omni-directional for the three frequencies [16].

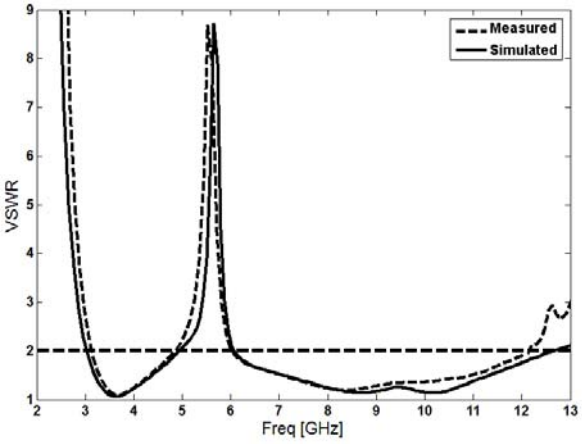

Fig. 6. Measured and simulated VSWR characteristics for the proposed antenna.

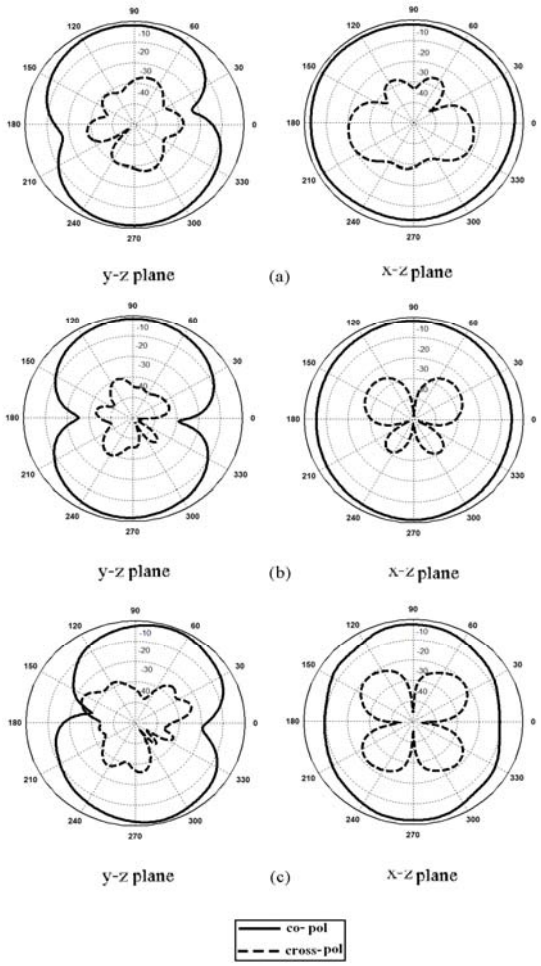

Fig. 7. Measured radiation patterns of the proposed antenna, (a) 4 GHz, (b) 8 GHz, and (c) 12.2 GHz.

IV. CONCLUSION

In this letter, a novel compact printed slot antenna (PSA) has been proposed for UWB applications. The fabricated antenna satisfies the VSWR < 2 requirement from 2.97 GHz to over 12.39 GHz with a band rejection performance in the frequency band of 5.01 GHz to 5.98 GHz. By cutting a rectangular slot with an H-shaped parasitic structure inside the slot on the microstrip feed-line, additional resonance is excited and hence, much wider impedance bandwidth can be produced, especially at the higher band, also by inserting a rotated H-shaped parasitic structure inside the square ring radiating stub the band notch performance is generated. The proposed antenna has a simple configuration and is easy to fabricate. Experimental results show that the proposed antenna could be a good candidate for UWB applications.

ACKNOWLEDGMENT

The authors are thankful to Microwave Technology (MWT) company staff for their beneficial and professional help (www.microwave-technology.com).

REFERENCES

[1] J. Sze and K. Wong, "Bandwidth enhancement of a microstrip line-fed printed wide-slot antenna," *IEEE Trans. Antennas Propag.*, vol. 49, pp. 1020-1024, 2001.

[2] M. Ojaroudi, N. Ojaroudi, and Y. Ebazadeh, "Dual band-notch small square monopole antenna with enhanced bandwidth characteristics for UWB applications," *Appl. Comp. Electro. Society (ACES) Journal*, vol. 27, no. 5, pp. 420-426, May 2012.

[3] A. Valizade, Ch. Ghobadi, J. Nourinia, N. Ojaroudi, and M. Ojaroudi, "Band-notch slot antenna with enhanced bandwidth by using Ω-shaped strips protruded inside rectangular slots for UWB applications," *Appl. Comp. Electro. Society (ACES) Journal*, vol. 27, no. 10, pp. 816-822, October 2012.

[4] M. Ojaroudi and A. Faramarzi, "Multiresonance small square slot antenna for ultra-wideband applications," *Microwave and Optical Tech. Lett.*, vol. 53, no. 9, pp. 2145-2149, Sep. 2011.

[5] M. Ojaroudi, S. Yzdanifard, N. Ojaroudi, and R. Sadeghzadeh, "Band-notched small square-ring antenna with a pair of T-shaped strips protruded inside the square ring for UWB applications," *IEEE Antennas Wireless Propag. Lett.*, vol. 10, pp. 227-230, 2011.

[6] M. Partovi, N. Ojaroudi, and M. Ojaroudi, "Small slot antenna with enhanced bandwidth and band-notched performance for UWB applications," *Appl. Comp. Electro. Society (ACES) Journal*, vol. 27, no. 9, pp. 772-778, Sep. 2012.

[7] B. Siahkal-Mahalle, M. Ojaroudi, and N. Ojaroudi, "Enhanced bandwidth small square monopole antenna with band-notched functions for UWB wireless communications," *Appl. Comp. Electro. Society (ACES) Journal*, vol. 27, no. 9, pp. 759-765, Sep. 2012.

[8] G. Zhang, J. Hong, B. Wang, and G. Song, "Switched band-notched UWB/ WLAN monopole antenna," *Appl. Comp. Electro. Society (ACES) Journal*, vol. 27, no. 3, pp. 256-260, March 2012.

[9] X. Ma, W. Shao, and G. He, "A novel dual narrow band-notched CPW-fed UWB slot antenna with parasitic strips," *Appl. Comp. Electro. Society (ACES) Journal*, vol. 27, no. 7, pp. 581-586, July 2012.

[10] Z. Zhou, L. Li, and J. Hong, "A novel compact monopole antenna with triple high quality rejected bands for UWB applications," *Appl. Comp. Electro. Society (ACES) Journal*, vol. 27, no. 8, pp. 654-659, August 2012.

[11] A. Valizade, Ch. Ghobadi, J. Nourinia, and M. Ojaroudi, "A novel design of reconfigurable slot antenna with switchable band notch and multiresonance functions for UWB applications," *IEEE Antennas and Wireless Prop. Lett.*, vol. 11, no. 1, pp. 1166-1169, 2012.

[12] Ansoft High Frequency Structure Simulation (HFSS), Ver. 13, Ansoft Corporation, 2011.

[13] N. Ojaroudi and M. Ojaroudi, "An UWB slot antenna with band-stop notch," *IET Microw. Antennas Propag.*, vol. 10. pp. 831-835, 2013.

[14] N. Ojaroudi and M. Ojaroudi, "Dual band-notched monopole antenna with multi-resonance characteristic for UWB wireless communications," *Progress in Electromagnetics Research C*, vol. 40, pp. 188-199, 2013.

[15] M. Ojaroudi and N. Ojaroudi, "Ultra-wideband small rectangular slot antenna with variable band-stop function," *IEEE Trans. Antennas Propag*., vol. 62, pp. 490-494, 2014.

[16] N. Ojaroudi and M. Ojaroudi, "Novel design of dual band-notched monopole antenna with bandwidth enhancement for UWB applications," *IEEE Antennas Wireless Propag. Lett.*, vol. 12, pp. 698-701, 2013.

Mohammad Ojaroudi was born in 1984 in Germi, Iran. He received his B.Sc. degree in Power Electrical Engineering from Azad University, Ardabil Branch and M.Sc. degree in Telecommunication Engineering from Urmia University. From 2010, he is working toward the Ph.D. degree at Shahid Beheshti University. Also from July 2013 he has been working, as a research visitor in University of Tennessee, Knoxville, USA. From 2007 until now, he is a Teaching Assistant with the Department of Electrical Engineering, Islamic Azad University, Ardabil Branch, Iran. Since March 2009, he has been the Chief Executive Officer (CEO) in the Microwave Technology Company (MWT), Tehran, Iran. From 2012, Dr. Ojaroudi is a member of the IEEE Transaction on Antennas and Propagation (APS) reviewer group and the Applied Computational Electromagnetic Society. His research interests include analysis and design of microstrip antennas, design and modeling of microwave structures, radar systems, and electromagnetic theory. He is author and coauthor of more than 150 journal and international conferences papers. His papers have more than 600 citations with 13 h-index.

Nasser Ojaroudi was born in 1986 in Germi, Iran. He received his B.Sc. degree in Electrical Engineering from Azad University, Ardabil Branch. From 2011, he is working toward the M.Sc. degree in Telecommunication Engineering at Shahid Rajaee Teacher Training University. Since March 2008, he has been a Research Fellow in the Microwave Technology Company (MWT), Tehran, Iran. His research interests include monopole antenna, slot antennas, microstrip antennas for radar systems, ultra-wideband (UWB) and small antennas for wireless communications, microwave passive devices and circuits, and microwave/millimeter systems.

Noradin Ghadimi was born in Ardabil-Iran in 1985, and received the B.Sc. degree in Electrical Engineering from the Islamic Azad University, Ardabil Branch, Ardabil, Iran, in 2009 and the M.Sc. degree in Electrical Engineering from the Islamic Azad University Ahar Branch, Ahar, Iran , in 2011. His research interests include power system protection, modeling and analysis of distributed generations, renewable energy and communications systems.

2013 INSTITUTIONAL MEMBERS

DTIC-OCP LIBRARY
8725 John J. Kingman Rd, Ste 0944
Fort Belvoir, VA 22060-6218

AUSTRALIAN DEFENCE LIBRARY
Northcott Drive
Canberra, A.C.T. 2600 Australia

BEIJING BOOK CO, INC
701 E Linden Avenue
Linden, NJ 07036-2495

DARTMOUTH COLLEGE
6025 Baker/Berry Library
Hanover, NH 03755-3560

DSTO EDINBURGH
AU/33851-AP, PO Box 830470
Birmingham, AL 35283

SIMEON J. EARL – BAE SYSTEMS
W432A, Warton Aerodome
Preston, Lancs., UK PR4 1AX

ENERGY KEN LIBRARY
PO Box 300613
Jamaica, NY, 11430

ENGINEERING INFORMATION, INC
PO Box 543
Amsterdam, Netherlands 1000 Am

ETSE TELECOMUNICACION
Biblioteca, Campus Lagoas
Vigo, 36200 Spain

GA INSTITUTE OF TECHNOLOGY
EBS-Lib Mail code 0900
74 Cherry Street
Atlanta, GA 30332

TIMOTHY HOLZHEIMER
Raytheon
PO Box 1044
Rockwall, TX 75087

HRL LABS, RESEARCH LIBRARY
3011 Malibu Canyon
Malibu, CA 90265

IEE INSPEC
Michael Faraday House
6 Hills Way
Stevenage, Herts UK SG1 2AY

INSTITUTE FOR SCIENTIFIC INFO.
Publication Processing Dept.
3501 Market St.Philadelphia, PA
19104-3302

LIBRARY – DRDC OTTAWA
3701 Carling Avenue
Ottawa, Ontario, Canada K1A OZ4

LIBRARY of CONGRESS
Reg. Of Copyrights
Washington DC, 20559

LINDA HALL LIBRARY
5109 Cherry Street
Kansas City, MO 64110-2498

MISSOURI S&T
400 W 14th Street
Rolla, MO 56409

MIT LINCOLN LABORATORY
244 Wood Street
Lexington, MA 02420

NATIONAL CHI NAN UNIVERSITY
Lily Journal & Book Co, Ltd
20920 Glenbrook Drive
Walnut, CA 91789-3809

JOHN NORGARD
UCCS
20340 Pine Shadow Drive
Colorado Springs, CO 80908

OSAMA MOHAMMED
Florida International University
10555 W Flagler Street
Miami, FL 33174

NAVAL POSTGRADUATE SCHOOL
Attn:J. Rozdal/411 Dyer Rd./ Rm 111
Monterey, CA 93943-5101

NDL KAGAKU
C/0 KWE-ACCESS
PO Box 300613 (JFK A/P)
Jamaica, NY 11430-0613

OVIEDO LIBRARY
PO BOX 830679
Birmingham, AL 35283

DAVID PAULSEN
E3Compliance
1523 North Joe Wilson Road
Cedr Hill, TX 75104-1437

PENN STATE UNIVERSITY
126 Paterno Library
University Park, PA 16802-1808

DAVID J. PINION
1122 E Pike Street #1217
SEATTLE, WA 98122

KATHERINE SIAKAVARA
Gymnasiou 8
Thessaloniki, Greece 55236

SWETS INFORMATION SERVICES
160 Ninth Avenue, Suite A
Runnemede, NJ 08078

YUTAKA TANGE
Maizuru Natl College of Technology
Maizuru, Kyoto, Japan 625-8511

TIB & UNIV. BIB. HANNOVER
Welfengarten 1B
Hannover, Germany 30167

UEKAE
PO Box 830470
Birmingham, AL 35283

UNIV OF CENTRAL FLORIDA
4000 Central Florida Boulevard
Orlando, FL 32816-8005

UNIVERSITY OF COLORADO
1720 Pleasant Street, 184 UCB
Boulder, CO 80309-0184

UNIVERSITY OF KANSAS – WATSON
1425 Jayhawk Blvd 210S
Lawrence, KS 66045-7594

UNIVERSITY OF MISSISSIPPI
JD Williams Library
University, MS 38677-1848

UNIVERSITY LIBRARY/HKUST
Clear Water Bay Road
Kowloon, Honk Kong

CHUAN CHENG WANG
8F, No. 31, Lane 546
MingCheng 2nd Road, Zuoying Dist
Kaoshiung City, Taiwan 813

THOMAS WEILAND
TU Darmstadt
Schlossgartenstrasse 8
Darmstadt, Hessen, Germany 64289

STEVEN WEISS
US Army Research Lab
2800 Powder Mill Road
Adelphi, MD 20783

YOSHIHIDE YAMADA
NATIONAL DEFENSE ACADEMY
1-10-20 Hashirimizu
Yokosuka, Kanagawa,
Japan 239-8686